Efficient and accurate calibration for radio interferometers

Kazemi, Sanaz

rijksuniversiteit
groningen

Efficient and Accurate Calibration for Radio Interferometers

Proefschrift

ter verkrijging van het doctoraat in de
Wiskunde en Natuurwetenschappen
aan de Rijksuniversiteit Groningen
op gezag van de
Rector Magnificus, dr. E. Sterken,
in het openbaar te verdedigen op
vrijdag 22 november 2013
om 09.00 uur

door

Sanaz Kazemi

geboren op 19 september 1984
te Esfahan, Iran

Promotores:	Prof. dr. S. Zaroubi
	Prof. dr. A.G. de Bruyn
Copromotor:	Dr. S. Yatawatta

Beoordelingscommissie:	Prof. dr. W. Brouw
	Prof. dr. A.J. van der Veen
	Prof. dr. A. Leshem

ISBN 978-90-367-6521-3
ISBN 978-90-367-6522-0 (electronic version)

Contents

Chapter 1

Introduction

In this chapter, we briefly review the historical development of radio interferometers, some basic terms and concepts, and some fundamental mathematical concepts. The importance of signal processing, and application of EM (Expectation Maximization) algorithm (Dempster et al., 1977) in radio interferometry is discussed. The aim of this thesis and a brief outline of the next chapters is also presented in the last section of this chapter.

1.1 Radio interferometry

An introduction to radio interferometry is given by Thompson et al. (2001). A radio interferometer is an array of two or more radio receivers which coherently observe the same astronomical object. The spacing between the receivers is referred to as the "baseline" (Fig. 1.2). Signals of every pair of receivers get combined with each other in a correlator to make a coherent signal for the corresponding baseline. Cross-correlation in fact decreases the noise level in signal, because noise of different receivers are un-correlated. There are two significant advantages in the usage of radio interferometers in comparison with the traditional single element radio telescopes. An interferometer superimposes the signals of different baselines and achieves a high level of sensitivity. Moreover, its angular resolution scales inversely with the size of its longest baseline. Therefore, the array could improve the resolution up to that of a single dish telescope with a diameter as large as the size of the interferometer's longest baseline.

1.1.1 Invention

After several unsuccessful attempts that have been made since 1860s to detect radio emissions from stellar objects, in 1933, Karl Jansky, an American electrical engineer with Bell Telephone Laboratories, constructed the first radio antenna receiver with the purpose of locating sources of telephone interference. He discovered a daily repeated radio signal with an unknown origin in his records and hence he was able to trace to the center of the Milky Way Galaxy. Following his work, in 1935, Grote Reber, another American electrical engineer, built the first 9 meter diameter dish-shaped radio telescope. After 1945, major radio astronomical research groups were formed in England, Australia, and The Netherlands. The first radio interferometer was constructed by Martin Ryle in 1946. The interferometer had the same design as a Michelson optical interferometer

(invented by Albert Michelson at 1887). It consisted of only two steerable elements (dipole antennas) whose distance could vary between 17 m and 240 m. This interferometer quickly became famous for the discovery of new objects which showed extremely high velocities. Solar observations which were carried out by Ruby Payne-Scott at roughly the same time (1948) also played a very important role in early radio interferometry. She used the sea interferometer for her observations which was a single receiver interferometer made during World War II in Australia. The instrument has been installed for radar at several costal locations near Sidney. The interferometry technique was performed via its every single receiver absorbing the direct radiation of different sources, plus their reflections from the sea. These discoveries stablished the application of interferometric arrays in radio astronomy with the goal of improving the resolution of observations obtained by single element telescopes.

1.1.2 Developments

By the early 1960s, advances were made in the design of radio interferometers, as well as in the principles of interferometry. In 1964, the "One-Mile" array at Cambridge University started to operate. The array was used for the first time for the aperture synthesis technique which mixes signals from different receivers to produce images having the same angular resolution as a single receiver with the size of the longest baseline. From that time, the main goal in the design of radio synthesis arrays was to construct extremely long baselines, as well as a large number of receivers, in order to increase the resolution, and the sensitivity, respectively. In 1969, the first large synthesis array, Westerbork Radio Synthesis Telescope (WSRT), was built in the Netherlands. After that, in 1971, the 5-km Ryle aperture synthesis radio telescope, was built at Cambridge University. This interferometer was the first in generating subarcsecond images of radio galaxies and quasars. Following those, from 1980s, radio interferometers such as the Very Large Array (VLA) [1], the Very Long Baseline Array (VLBA) [2], the LOw Frequency ARray (LOFAR) (van Haarlem et al., 2013), the Murchison Widefield Array (MWA) (Lonsdale et al., 2009), the Precision Array to Probe Epoch of Reionization (PAPER) (Parsons et al., 2010), the 21-cm Array (21CMA)[3], the Hydrogen Epoch of Reionization Array (HERA)[4], and, currently under development, the Square Kilometre Array (SKA)[5] were designed.

Although there is always a limit in sensitivity that can be achieved using a radio interferometer (the achievable sensitivity is limited by the receiver's collecting area), there has been always a great attempt to achieve their sensitivity limit in the smallest time scale possible. The reason is that optical telescopes have always had the advantage of operating in real-time (the optical astronomer can directly see what is being observed through the telescope). However, radio signals are invisible, and only after they are transfered to computer and have been processed via various software they can result into images. Reducing the time between observations (data collection from the instrument) and imaging procedures is one of the main challenges in the radio astronomy, because then the instrument can be instantly steered away from unexpected events or errors.

Minimizing the time delay between collecting radio signals by an interferometer and imaging, the network connections as well as the processing softwares must operate extremely fast. Provid-

[1] http://www.vla.nrao.edu/
[2] http://www.vlba.nrao.edu/
[3] http://21cma.bao.ac.cn
[4] http://www.reionization.org
[5] http://www.skatelescope.org

ing fast and stable connectivity between the instrument and computers, or the Internet, or other local or remote network resources or functions, in order to properly collect and deliver the raw data is essential. On the other hand, various processes, depending on the purpose and quality of observation and on the characteristics of the specific interferometer, must be executed on the raw data before imaging. For instance, averaging or flagging some data initially. Among these systematics and the most crucial one is calibration, the main topic addressed in this thesis.

1.2 Calibration

The raw data collected by a radio interferometer is a mixture of corrupted emissions of radio sources plus some noise. Calibration is the procedure of estimation and correction of the corruptions in data. An efficient calibration procedure must be able to compensate for inaccuracies in the other pre-imaging processes and to perform a complete true data recovery. Therefore, it plays a key role in achieving the scientific goal of design of any radio interferometer. To illustrate this importance, an image of 1.5×1 degree area of the sky at 150 MHz using LOFAR, before and after calibration, is presented in Fig. 1.1. The applied calibration technique is SAGE (Space Alternating Generalized Expectation Maximization) calibration which is extensively introduced in chapter 2. As Fig. 1.1 shows, a significant image-quality improvement is obtained by calibrating the raw data. There are lots of artifacts in the un-calibrated image (image (a) of Fig. 1.1) and sources look blurry. However, in the calibrated image (image (b) of Fig. 1.1), the artifacts are much less and source boundaries look much sharper. Moreover, some new sources have appeared in the calibrated image which were totally invisible in the uncalibrated one, and consequently, were not included in the sky model. This proves that an accurate calibration can correct for errors introduced by the other pre-imaging procedures (source modeling procedure in this particular example) as well. Thus, calibration is essential for converting a “dirty image” into a “clean image”.

1.2.1 Corruptions in radio signals

Systematic corruptions of the radio signals radiated from celestial objects fall into two broad categories, instrumental and non-instrumental.

1. **Instrumental errors**

   - Receiver beam shape: directional voltage pattern of receivers which shows where the receivers are sensitive.
     When radiations from different directions of the sky hit a receiver, depending on their angles, they induce a variable voltage level at the receiver. Receivers are aimed to provide a high sensitivity towards a specific desired observing direction. To change the directionality, one can use dishes which are moved to focus on a specific direction, or can use beam-forming techniques to control the strength of signals coming from different directions. The pattern of this electronic response, known as the beam, must be determined before, or during, calibration.
   - Receiver gain: combined effects of the low noise amplifiers, artificial filters, and Analog to digital convertors.

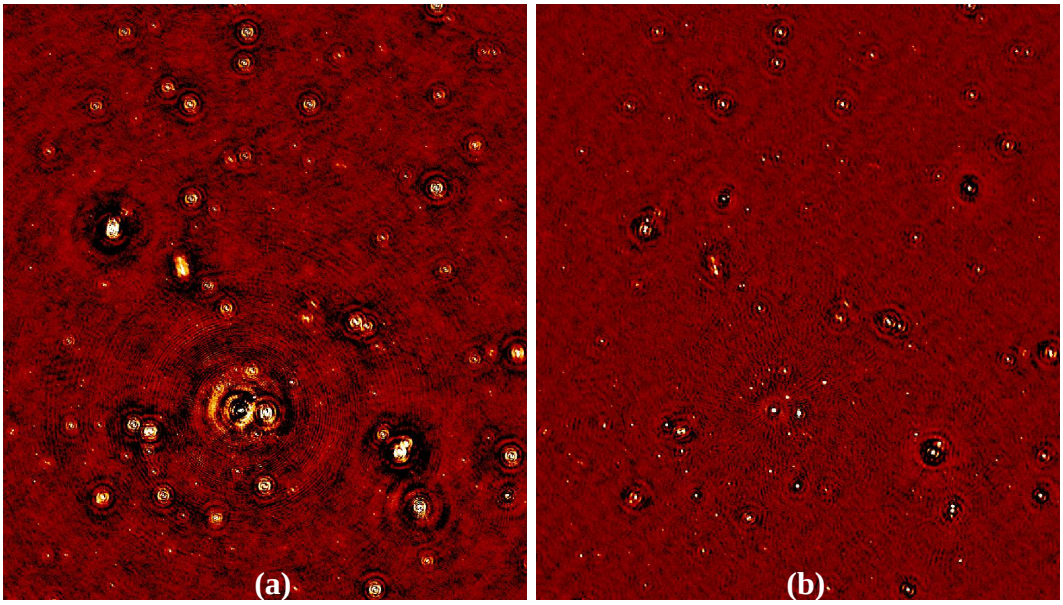

Figure 1.1: An image of 1.5×1 degree area of the sky at 150 MHz using LOFAR, before (a) and after (b) calibration. The applied calibration technique is SAGE calibration which is extensively introduced in chapter 2. A significant image-quality improvement is obtained by calibrating the raw data. There are lots of artifacts in the un-calibrated image and sources look blurry. However, in the calibrated image, the artifacts are much less, source boundaries look much sharper, and some new sources have appeared which were totally invisible before.

Receiver gain is introduced due to different losses (inefficiencies), delays, and leakages in the system. Standing wave patterns due to mismatches in different components of the system also contribute to this gain.

2. **Non-instrumental errors**

   - Atmospheric effects.
     As signals pass through the Earth's atmosphere, especially the ionosphere, they get affected from several sources of errors and correcting these errors is a significant challenge. The errors are mainly ionospheric phase fluctuations causing signal delays and decorrelations, Faraday Rotation which is the polarization rotation imposed over the course of propagation of signal from its origin to the receiver, and tropospheric corruptions (for instance when variations in the level of water vapor in troposphere leads to phase changes propagated radio signals).
   - Radio Frequency Interferences (RFI).
     RFI is caused by man-made corruptions, introduced by radio transmitters such as TV, radar, wireless communications, and satellites. Also natural causes such as lightning and solar flares cause RFI. It ranges from weak corruptions in data to a total loss of data. Although RFI can be mitigated in data up to a very good level via several RFI flagging techniques (Fridman & Baan, 2001; Offringa et al., 2010a,b), its remaining effects in data are considered to contribute to receiver noise.

These systematic sources of interference must be recognised and studied so that steps can be taken to minimize their effect. There are also other random errors affecting signals which are referred to as noise. To summarize, radiated signals from radio sources first get corrupted by the atmosphere and then by the receivers beam patterns. After that, the corrupted signals get cross-correlated in a correlator and the outcome which includes also some noise is transfered to computers to be processed. To a greater extent, some other corruptions introduced by the computer itself can also affect the transfered data. For example, when calibrating or imaging using a specific source model while the model has errors itself. All these sources of corruptions are illustrated by Fig. 1.2 which shows a basic radio interferometer including only two receivers.

1.2.2 External calibration and Self-calibration

There are two major calibration approaches for removal of the mentioned errors in incoming signals: (i) external calibration and, (ii) self-calibration (Pearson & Readhead, 1984). Note that the "external calibration" is referred to as the "internal calibration" by Pearson & Readhead (1984).

The classical calibration method, named external (primary) calibration, is performed using pre-knowledge of properties of some bright reference sources, referred to as calibrators. Based on the error characteristics that are obtained for a calibrator, it corrects for the sources around the calibrator. "Fringe rate mapping" (Moran et al., 1973; Reid et al., 1980), as well as "phase mapping" (Walker et al., 1978) are two examples of external calibration methods. Ideally, the calibrators should be point sources and isolated from the other sources in the sky, because then one is able to properly measure the errors in their signals. There are several disadvantages in the usage of external calibration. The performance of the technique is directly affected by the accuracy with which the calibrators are known. Moreover, choosing isolated bright reference sources in a wide field

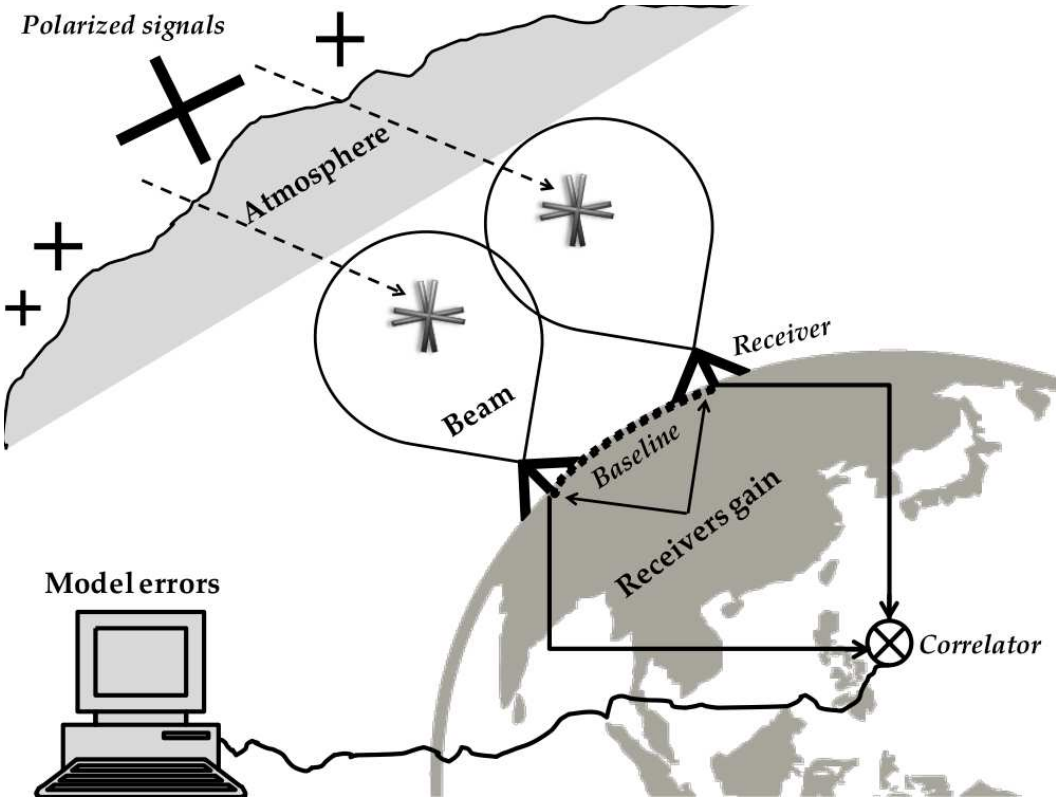

Figure 1.2: A basic radio interferometer including only two receivers which receive signals from far away radio sources. The radiated signals from sources are corrupted by the atmosphere as well as by the receivers beam patterns. The corrupted signals plus the receiver's thermal noise get cross-correlated in a correlator and then they are transfered to computers to be processed.

of view is almost impractical, and even when it is possible, external calibration gives information only around the direction of the calibrators. With the resolution requirements increasing, external calibration was not good enough, and hence, it was replaced by self-calibration.

Self-calibration overcomes the main limitation of the external calibration method, i.e., calibrating only the area close to the calibrators, by using every source itself for its calibration. It also does not need access to exact characteristic of some source. Given a rough estimate of the true sky and a proper instrumental model, self-calibration utilizes the observed data for estimating both the unknown instrumental and sky parameters. The technique's quality is increased by iterating between the sky and the instrument. Thus, its accuracy is also not limited by the pre-knowledge of some specific sources. These advantages are enough reasons to make self-calibration the method of choice in comparison with the external calibration, as it is in this thesis. Some examples of the self-calibration techniques are the method of Redhead and Wilkinson (Baldwin & Warner, 1976, 1978), CLEAN (Högbom, 1974), calibration via Maximum Entropy method (Sanroma & Estalella, 1984), and Redundancy method (Noordam & de Bruyn, 1982) (a detailed introduction of self-calibration techniques is presented in (Pearson & Readhead, 1984)).

1.2.3 Data model

The basic need for an efficient self-calibration run on the raw data is to have reasonable sky and instrumental models. Sky models can be provided by optical or radio catalogs. There are also various software, such as Duchamp (Whiting, 2012), and BuildSky (Yatawatta et al., 2013), for producing sky models from the initial image obtained from the raw data. Thus, having a proper mathematical measurement equation is the main concern.

In order to model the correspondence between the observed and true skies, we use the general measurement equation introduced by Hamaker (2006). The equation is obtained by formulating the corruptive effects in celestial radio signals that were introduced in section 1.2.1 as follows:

$$\mathbf{y} = \mathbf{s}(\boldsymbol{\theta}) + \mathbf{n}. \tag{1.1}$$

In (1.1), $\mathbf{y}$ is the observed data, $\mathbf{s}$ is a non-linear function representing the corruptions, $\boldsymbol{\theta}$ is the unknown sky and instrumental parameters that needs to be estimated, and $\mathbf{n}$ is the noise. From (1.1) it is clear that calibration is a non-linear optimization problem, and for solving it, array signal processing techniques are utilized. After calibration, the data is corrected for systematic errors and the Fourier transform of the data is taken to make images. However, due to incomplete sampling of the Fourier plane and due to the curvature of the sky, simple Fourier transform will not produce good images and signal processing is also used to get better images. We use CASA (http://casa.nrao.edu) software for all imaging tasks in this thesis.

1.3 Array signal processing for radio interferometry

Array signal processing is signal processing of the outputs of an array of receivers. Radio interferometry forms an interesting application area for array signal processing techniques. The measurement equation presented by (1.1) is a non-linear signal processing data model. Consequently, array signal processing can make a considerable contribution in solving for problems such as self-calibration (using weighted least squares algorithm(Wijnholds & van der Veen, 2009) or Maximum Likelihood estimation algorithms(Boonstra & van der Veen, 2003; Kazemi et al.,

2011; Kazemi et al., 2013c; Kazemi & Yatawatta, 2013)), interference removal (using spatial filtering (Fridman & Baan, 2001; Leshem & van der Veen, 2000)), and image formation (using inverse Fourier techniques (Levanda & Leshem, 2010; Leshem & van der Veen, 2000)).

Beam forming is also a signal processing technique that is used for observing radio signals from specific regions of the sky. Radio dishes mechanically turn to observe different parts of sky. However, phased array receivers, such as the ones used in LOFAR and SKA, have no moving parts. Therefore, for such antennas, beams are electronically steered to observe specific regions of sky.

Data from these antennas are transported to correlators, where they will be synchronized, cross-correlated, and divided to various frequency channels, again using signal processing techniques. At the same stage, signal processing filtering schemes also can be used to pre-process the data in order to remove interfering radio frequency signals that would contaminate the data. On the other hand, as was mentioned in section 1.1.2, the most important challenge in the current radio interferometry is developing software to: (i) produce the best quality images (ii) using the fastest computational speeds. Such processing software have computational requirements far beyond the capabilities of the general purpose computer software which have traditionally been used in radio astronomy signal processing. Thus, there is an increasingly need for developing new signal processing libraries which could speed up various tasks of those softwares.

A common task in signal processing is estimation of parameters of a probability distribution function. For instance, statistical estimation of the mean of a signal in the presence of noise. Such parameter estimation problems become more complicated when there is no direct access to the underlying data distribution, or some data are missing. For example, consider the case in which the outcome is a result of an accumulation of simpler un-observed outcomes. There may also be data dropouts in such a way that even the number of underlying outcomes is unknown. The EM (Expectation Maximization) algorithm (Dempster et al., 1977) is ideally suited to problems of this sort. The algorithm is capable of producing ML (Maximum Likelihood) estimation of parameters when there is a many-to-one mapping from underlying distributions to the general observed distribution.

1.3.1 The EM algorithm

EM (Expectation Maximization) algorithm estimates ML (Maximum Likelihood) of parameters when some variables are un-observed by assuming the existence of and values for some underlying hidden variables. There are two main advantages in using the EM algorithm. The first is obtained when the data have missing values, due to problems with (or limitations of) the observational procedure. In such cases, the EM algorithm can converge by re-producing the missing values via those hidden variables. The second advantage is when optimizing the likelihood function is analytically intractable. The EM algorithm simplifies the likelihood function using the hidden variables and iteratively converges to an ML estimation.

The EM algorithm consists of two major steps:

1. **E-step (Expectation step)**: Compute the expected value of the hidden variables using the current estimate of the parameters and the observed data.

2. **M-step (Maximization step)**: Use the data from the E-step as if it were actually observed data to determine an ML estimate of the parameters.

These two steps are iterated until convergence. The concept is illustrated in Fig. 1.3.

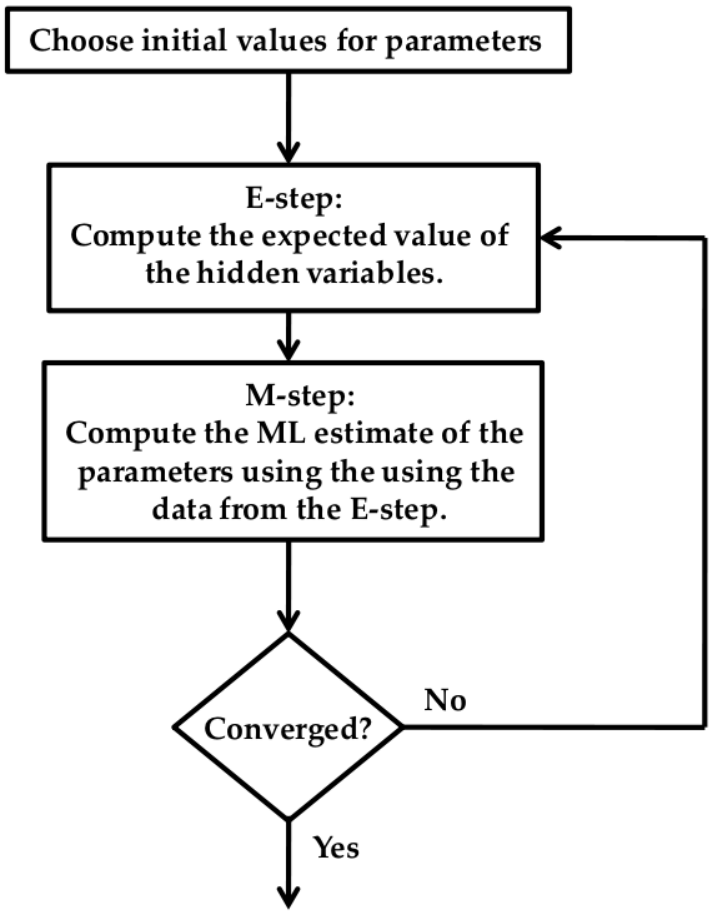

Figure 1.3: An overview of the EM algorithm. After initialization of parameters, it iterates between estimating hidden values and ML of parameter until convergence.

1.3.2 History

The EM algorithm was invented by Arthur Dempster (Dempster et al., 1977) who generalized the method for the first time, sketched its convergence analysis for a wide class of problems, and named it as the "EM algorithm". However, before Dempster et al. (1977), the algorithm was employed by several other researchers. For instance, Dempster et al. (1977) found the earliest usage of the EM algorithm in McKendrick (1925). To go even further in time, the EM algorithm and many other popular statistical methods are in fact originated from Fisher (1925). However, (Dempster et al., 1977) gave the algorithm the "EM" title for the first time and demonstrated its general application for the cases in which some data is missing (in the presence of hidden variables). After Dempster et al. (1977), an enormous and increasing amount of articles employing the EM algorithm were annually published.

1.3.3 Convergence

Since EM is an iterative algorithm, the question of its convergence needs to be addressed: Does the EM algorithm converge to a solution? The answer is yes. It is proved that the EM algorithm guarantees a stable convergence to an ML estimate. Dempster et al. (1977) has presented an analytical proof of the convergence of the algorithm for the first time. However, the proof was incomplete in the sense that it does not prove that the solutions that EM converges to are in fact ML estimates. Later on, Xu & Jordan (1995); Boyles (1983) presented a detailed discussion of the convergence of the EM algorithm to ML estimations of parameters. The proof can be generally stated as: at every iteration of the EM algorithm, parameters are updated such that the likelihood function does not decrease. That is, at every iteration, the estimated parameters provide an increase in the likelihood function until a local maximum is obtained, where the likelihood function can not increase anymore, but will not be decreased as well.

There are two major points in convergence of the EM algorithm that must be taken into account:

1. There is no guarantee that the EM algorithm converges to a global maximum. For a likelihood function with multiple maxima, convergence will be towards a local maximum which depends on the initial parameter estimates (starting point).

2. Based on mathematical and empirical examinations, the convergence rate of the EM algorithm is usually slower than the quadratic convergence typically obtained by Newton-type optimization methods (Redner & Walker, 1984). However, near the maximum likelihood, convergence rate depends on the eigenvalues of the Hessian matrix of the update maximization function, so that a rapid convergence can be obtained (Dempster et al., 1977).

Even considering the above points, there are many advantages in using the EM algorithm instead of Newton-type methods. For instance, using EM, there is no chance of diverging away from the maximum, and a stable convergence to an ML estimate is guaranteed (Moon, 1996).

1.3.4 Speeding up the EM algorithm

EM algorithm gets its popularity due to its easy implementation and stable convergence. However, since its convergence rate can be slower than the quadratic convergence in some applications,

various attempts have been made at speeding up the algorithm, either by simplifying the computations, or by increasing the rate of convergence Roche (2003). Those EM variants include:

- **Aitken's acceleration of EM**
  Dempster et al. (1977) proposed the combination of the EM algorithm with the Newton-Raphson method for speeding up the standard EM iterations. This causes important implementational issues. Besides, Aitken's acceleration of EM does not guarantee a convergence since the monotonicity property of the standard EM algorithm is lost.

- **CEM**
  CEM (Classification EM) algorithm, proposed by Celeux & Govaert (1992), estimates a hidden variable, from which the missing values are generated, when it estimates the ML of parameters at every iteration. This provides the CEM algorithm with several advantages compared to the standard EM algorithm. For example, being easier to implement and typically faster to converge. However, since CEM maximize the likelihood function using a complete data instead of the initial incomplete-data, again the monotonicity property of EM is lost. Hence, the convergence is not guaranteed anymore and more careful monitoring is needed.

- **AEM**
  Jamshidian & Jennrich (1993) introduced AEM (Accelerated EM) algorithm which is a conjugate gradient approach which trades off between EM and its Aitken's acceleration. The method has the advantage of line maximizations, which makes the monotonicity property of EM safe. However, its weak point is that it needs more numerically complex implementations.

- **ECME**
  Meng & Rubin (1993) introduced ECM (Expectation Conditional Maximization) method to deal with cases in which the standard EM maximization step (M-step) is intractable. In ECM, the maximization problem is replaced with a number of lower dimensional maximization problems that all must be solved sequentially at every iteration. That makes computations of the maximum likelihood much simpeler and retains the stable convergence properties of the standard EM algorithm (the monotone convergence of the likelihood values is kept). However, the ECM algorithm has the disadvantage of converging more slowly compared to the standard EM algorithm. Efforts for speeding up the ECM algorithm were resulted in two other generalizations of the EM algorithm: ECME, and SAGE.

  Liu & Rubin (1994) recognized that in some applications of the ECM algorithm, running the standard likelihood maximization of the EM algorithm (M-step) as a posterior operator on the ECM maximizations can provides a faster convergence. Therefore, Liu & Rubin (1994) introduced the ECME (Expectation Conditional Maximization) algorithm whose maximization step is *either* a standard EM maximization *or* a ECM maximization. In the case of having mixture models, ECME benefits from a faster convergence rate compared to the standard EM algorithm.

- **SAGE**
  Fessler & Hero (1993) developed the SAGE (Space Alternating Generalized Expectation

Maximization) algorithm without knowing the ECM or ECME algorithms. As it is explained, ECM algorithm starts with the standard EM algorithm and then, for its maximizations, it breaks the problem to several smaller problems. In contrast, the SAGE algorithm initially partitions the parameters and defines for every subset of parameter a smaller ML estimation problem, and then it runs the standard EM algorithm on each reduced problem (which may still have no analytic solution). It is proved that the algorithm is very efficient for speeding up the standard EM algorithm since the amount of data augmentation needed for the smaller problems can be much less than that needed for the original big problem. This faster speed of convergence was specially shown by applications of the algorithm to the Poisson imaging model.

- **AECM**
  Meng & Dyk (1997) introduced AECM (Alternating ECM) algorithm as a combination of the ECM and SAGE algorithms. The method achieves efficient computations having the data augmentation flexibility of the ECM algorithm as well as the model reduction properties of the SAGE algorithm at the same time.

- **PX-EM**
  Liu et al. (1998) suggested the PX-EM (Sparse EM) algorithm for speeding up the standard EM method. The main idea of the algorithm is to track the hidden variable in a subspace of the original search space (observed values). EM variants such as the CEM algorithm all could be utilized in this scheme. PX-EM procedures typically have strong computational advantages. However, they are prone to estimation bias because they estimate ML on a reduced search space which may not contain the maximum likelihood solution at all.

- **CEMM**
  Celeux et al. (1999) introduced the CEMM (Component-wise EM for Mixtures) algorithm as an extension of the SAGE technique to be applied to constrained likelihood maximization problems. Such problems arise typically in maximization of a mixture model, when the sum of mixing proportions is constrained. The general idea is that CEMM uses a Lagrangian dualization method to recast the initial constrained ML estimation problem into an unconstrained maximization problem by defining a suitable penalized log-likelihood function. It has been proved that under mild regularity conditions, the algorithm converges to a stationary point of the likelihood.

- **Incremental EM**
  The OS (Ordered Subsets) algorithm (Hudson & Larkin, 1994) accelerates the convergence rate of ML estimations. This method decomposes the likelihood function to several sub-surrogate functions and updates the parameters by using the gradient of one, or some, of the sub-surrogate functions as an approximation to the likelihood function's gradient. At the initial iterations, when the parameters are far from the maximum likelihood point, these approximations can be efficient substitutions for the gradient of the likelihood function, and they can significantly accelerate the computations. However, OS methods usually do not converge but rather get stuck at a sub-optimal limit cycle.

  Incremental optimization transfer method (Ahn, 2004) was developed with the goal of achieving convergence for the OS method. The difference between OS method and the incremental optimization transfer method is that OS uses only a partial gradient at every

iteration whereas incremental optimization transfer uses the whole gradient which is incrementally updated. The success key of the incremental transfer algorithm is that at the maximization steps, it uses all the most recent sub-surrogate functions while updating parameter with respect to only one sub-surrogate function. The algorithm is a general framework for developing many different optimization algorithms by using different application-dependent surrogate functions. Incremental EM (Neal & Hinton, 1999) is a special case of the incremental optimization transfer algorithms which uses EM surrogate function at its iterations. The convergence arte of the method is faster than the standard EM algorithm, while is still slower than those non-convergent OS-EM type algorithms.

1.4 Applying EM variants to calibration problem

From a signal processing point of view, calibration is the process of ML estimation of the sky and instrumental unknown parameters using a non linear optimization technique such as the LM (Levenberg Marquardt) algorithm (Levenberg, 1944; Marquardt, 1963). An in depth overview of existing calibration techniques are given in Boonstra & van der Veen (2003); van der Veen et al. (2004). Utilizing such techniques, the sensitivity limit that can be achieved using present radio interferometers is already reached. For instance, this is shown for LOFAR, which can be considered as a pathfinder for the next generation interferometric arrays, by van der Tol et al. (2007). However, despite such instrumental limitations, there is still space for improving the computational cost, or the speed of convergence, of calibration techniques. That lead us toward the use of EM variants for speeding up the calibration procedures. The EM algorithm benefits from the essential property of increasing the likelihood at every iteration. Therefore, those EM variants which have fast speed of convergence could be the best candidates to be applied to the calibration problem.

The standard EM algorithm is used for calibration by Kazemi et al. (2011) (chapter 2). Although it guarantees a stable convergence, it suffers a slow rate of convergence. Utilizing Aitken's acceleration of EM, CEM, AEM, or PX-EM for the calibration ML estimation is not proposed since the methods are not always convergent (the monotonicity property of EM is lost). AEM is not an option either due to its complicated implementation. the ECME algorithm as well as the SAGE algorithm are applied to the calibration problem by Kazemi et al. (2011) (chapter 2) and Kazemi & Yatawatta (2013) (chapter 6), respectively, and it has been shown that both the methods result better convergence rate compared to standard calibration techniques. OS acceleration of the SAGE algorithm, proposed by Kazemi et al. (2013c) (chapter 3), also significantly improves the speed of convergence of calibration at initial iterations of ML estimation.

1.5 This thesis

The subject of this thesis is introducing the application of some well-known signal processing techniques to self-calibration of radio interferometers, in order to:

- increase the speed of convergence of the calibration's procedure,
- minimize self-calibration bias,
- optimize the directions in the sky that must be solved for,

- minimize the effects of outliers in data,
- and minimize loss of fluxes of un-modeled sources.

The result is calibration that is faster by orders of magnitude than before. There is a great interest in application of such methods to calibration for a large-unknown parameter space (the number of the unknowns is proportional to the number of reference sources in the sky, as well as the number of receivers in the instrument). The dissertation combines contributions to the literature: Kazemi et al. (2011); Kazemi & Yatawatta (2012); Yatawatta et al. (2012); Kazemi et al. (2012, 2011, 2013b,a,c); Kazemi & Yatawatta (2013).

1.5.1 Outline and summary of the thesis

In chapter 2, application of SAGE algorithm (Fessler & Hero, 1994) into calibration problem is presented. The introduced SAGE calibration method (Kazemi et al., 2011) has the advantage of iterating over sources in the sky and solving for every source individually. Because of that, its execution time can be significantly faster than the methods that solve for all the unknowns simultaneously at every iteration, such as LS (Least Squares) calibration. Results illustrate that more accurate solutions in a much shorter time are obtained by SAGE calibration in comparison with LS calibration.

In chapter 3, application of the OS (Ordered-Subsets) algorithm (Hudson & Larkin, 1994; Erdogan & Fessler, 1999) for speeding up the convergence at initial iterations of calibration techniques is shown. OS type calibrations (Kazemi et al., 2013c) use partitions of data, rather than the whole observed data, to solve for unknowns. The calibrations benefit from very fast computations and preserve almost the same quality as (never higher than) the one obtained by the non-OS calibrations. Promising performance of OS calibrations is shown in simulations.

In chapter 4, clustered calibration (Kazemi et al., 2011, 2013b) technique, which is calibrating for groups of sources simultaneously, is introduced. The goal is upgrading weak signals of faint sources via signals of other near-by sources in order to increase the information level, and consequently, the accuracy of solutions. For this purpose, sources are grouped into clusters and calibration is performed to solve for a single solution per cluster. As a direct result, clustered calibration achieves a novel speed of convergence because (i) it solves less number of directions than the number of sources in the sky, and (ii) it has less number of iterations compared to the unclustered calibrations due to the fact that it uses information of the upgraded signals to calculate solutions.

In chapter 5, a fuzzy clustered calibration is introduced. Applying fuzzy clustering to calibration in order to define clusters with soft boundaries, where every individual source can be contributed to more than one cluster, is more accurate and efficient than dedicating every source to exactly one cluster as in chapter 4. As a result, in fuzzy clustered calibration, every source signal is considered to be corrupted by a linear combination of the sky errors of all the clusters. This is where in non-fuzzy clustered calibrations, the solution of every source is only the one obtained for the centroid of the cluster that the source belongs to. Therefore, fuzzy clustered calibration is provided with a faster speed of convergence compared to non-fuzzy clustered calibrations.

In chapter 6, the use of Student's t distribution in radio interferometric calibration is proposed. Compared with traditional calibration that has an underlying Gaussian noise model, robust calibration (Yatawatta et al., 2012; Kazemi & Yatawatta, 2013) using Student's t distribution can

handle situations where there are model errors or outliers in the data. Moreover, by automatically selecting the number of degrees of freedom during calibration, it also has the flexibility of choosing the appropriate distribution even when no outliers are present and the noise is perfectly Gaussian. Results show the robustness of the calibration method, especially in preserving the flux of weaker sources that are not included in the sky model.

Chapter 2

Radio Interferometric Calibration Using The SAGE Algorithm

"Radio Interferometric Calibration Using The SAGE Algorithm"
Kazemi S., et al., 2011, MNRAS, 414, 1656

ABSTRACT

The aim of the new generation of radio synthesis arrays such as LOFAR and SKA is to achieve much higher sensitivity, resolution and frequency coverage than what is available now, especially at low frequencies. To accomplish this goal, the accuracy of the calibration techniques used is of considerable importance. Moreover, since these telescopes produce huge amounts of data, speed of convergence of calibration is a major bottleneck. The errors in calibration are due to system noise (sky and instrumental) as well as the estimation errors introduced by the calibration technique itself, which we call solver noise. We define solver noise as the distance between the optimal solution (the true value of the unknowns, uncorrupted by the system noise) and the solution obtained by calibration. We present the Space Alternating Generalized Expectation Maximization (SAGE) calibration technique, which is a modification of the Expectation Maximization algorithm, and compare its performance with the traditional Least Squares calibration based on the level of solver noise introduced by each technique. For this purpose, we develop statistical methods that use the calibrated solutions to estimate the level of solver noise. The SAGE calibration algorithm yields very promising results both in terms of accuracy and speed of convergence. The comparison approaches we adopt introduce a new framework for assessing the performance of different calibration schemes.

2.1 Introduction

Early radio-astronomy predominantly used single-dishes for observations. With the resolution requirements increasing, the single dish approach became impractical. This paved the path for using radio-interferometric techniques with multiple antennas linked together as an array that operates as a large effective single-dish (Thompson et al., 2001).

The sensitivity of an interferometer is greatly increased, compared to a single-dish telescope, due to the larger combined collecting area. The currently planned or built radio interferometers, such as the Square Kilometre Array (SKA)[1], the Murchison Widefield Array (MWA)[2], the Precision Array to Probe Epoch of Reionization (PAPER)[3], the 21-cm Array (21CMA)[4], the Hydrogen Epoch of Reionization Array (HERA)[5], the Long Wavelength Array (LWA)[6] and the LOw Frequency ARray (LOFAR)[7], consist of a large number of elements and include short, intermediate and many of them longer antenna spacings. For an introduction to radio interferometry we refer the reader to Thompson et al. (2001).

In the interferometric visibilities there always exist errors introduced by the sky, the atmosphere (e.g. troposphere and ionosphere), the instrument (e.g. beam-shape, frequency response, receiver gains etc.) and by Radio Frequency Interference (RFI). The process of estimating and reducing the errors in these measurements is called "calibration" and is an essential step before imaging the visibilities.

The classical calibration method, named external (or primary) calibration, is based on observing a celestial radio source with known properties. This approach is strongly dependent on the accuracy with which the source properties are known. The external calibration is improved by using self-calibration (Pearson & Readhead, 1984) which utilizes the observed data for estimating both the unknown instrumental and the sky parameters. The quality of calibration and the imaging is significantly increased by iterating between the sky and the instrument model. The redundant calibration is also independent of the sky model. It calibrates for both the sky and the instrument, using redundant information in the measured data. However, its performance is limited to arrays with a regular arrangement in their antennas layout.

Calibration is an optimization process that is non-linear by nature. It is in essence a Maximum Likelihood (ML) estimation of the unknown parameters by applying non-linear optimization techniques. Traditional calibration is estimating the ML solution by the non-linear Least Squares (LS) method via various gradient-based techniques such as the Levenberg-Marquardt (LM) algorithm (Levenberg, 1944; Marquardt, 1963). This approach was improved by the Expectation Maximization (EM) algorithm (Feder & Weinstein, 1988) and later on by the Space Alternating Generalized Expectation Maximization (SAGE) technique which was introduced by Fessler & Hero (1994) and was applied to interferometer calibration by Yatawatta et al. (2009). The analysis and application of the aforementioned schemes for the calibration of radio interferometers can be found in Yatawatta et al. (2009).

To reach the scientific goals of the new generation of radio arrays, calibration algorithms must have the highest accuracy possible. Furthermore, the number of measured visibilities that has

[1] http://www.skatelescope.org
[2] http://www.mwatelescope.org
[3] http://astro.berkeley.edu/~dbacker/eor
[4] http://21cma.bao.ac.cn
[5] http://www.reionization.org
[6] http://lwa.unm.edu
[7] http://www.lofar.org

to be calibrated is unprecedented. The speed of convergence of the calibration processes must therefore be the fastest with the minimum possible computational cost. Based on these facts, the best calibration method is referred to as the one which minimizes the "distance" between the true values of unknown parameters and the values obtained by calibration and minimizes computational time.

We should take into account that the measured data of an interferometer is always corrupted by different sources of noise such as the thermal noise, which is an additive Gaussian random process, and confusion noise (Condon, 1974), which affects the coherency matrix (see next section and e.g. Born & Wolf (1999)). For a detailed discussion on the sources of noise the reader is referred to the Chapter 6 of Wijnholds (2010). When the calibration process of the measured data is done, the "distance" between the true value of the unknown parameters and their calibrated solutions depends on the initial noise and the errors originating from the calibration process itself (e.g. converging to a local minimum), which is called "solver noise". In other words, because the calibrated solutions are not optimal, there always exists some solver noise between these solutions and the true values of the unknown parameters affected by the initial noise. The lower the solver noise, the higher the accuracy of the calibrated results. Thus, in order to increase the calibration efficiency, we need to choose the calibration scheme which has the minimum solver noise as well as the lowest computational cost. To achieve this, we should be able to compare these two factors between various calibration techniques. We introduce a general framework for detecting the level of solver noise in calibration algorithms based only on their solutions.

In this chapter, we present the SAGE calibration method and emphasize its superiority, compared to the traditional LS calibration, in terms of accuracy and speed of convergence. Mathematical derivations of the algorithms are presented in the appendices. We also investigate the applicability of two well-known measures, the Kullback-Leibler Divergence (KLD) (Kullback, 1997) and the Likelihood Ratio Test (LRT) (Graves, 1978), in revealing the level of solver noise in calibrated solutions. Illustrative examples of both real and simulated observations, show the superior performance of the SAGE calibration compared to the LS one. They also indicate that the LRT approach is very promising at detecting the level of solver noise in the obtained calibrated solutions, while the KLD approach is not always conclusive.

The following notations are used in this chapter: Bold, lowercase letters refer to column vectors, e.g., $\mathbf{y}$. Upper case bold letters refer to matrices, e.g., $\mathbf{C}$. All parameters are complex numbers, unless stated otherwise. The inverse, transpose, Hermitian transpose, and conjugation of a matrix are presented by $(.)^{-1}$, $(.)^T$, $(.)^H$, and $(.)^*$, respectively. The statistical expectation operator is referred to as $E\{.\}$. The matrix Kronecker product and the proper (strict) subset are denoted by $\otimes$ and $\subsetneq$, respectively. The diagonal matrix consisting of only the diagonal entries of a square matrix is given by $\mathrm{diag}(.)$. $\mathbf{I}$ is the identity matrix and $\varnothing$ is the empty set. The Kronecker delta function is presented by δ_{ij}. $\mathbb{R}$ and $\mathbb{C}$ are the sets of Real and Complex numbers, respectively. The Frobenius norm is shown by $||.||$. Estimated parameters are denoted by a hat, $\widehat{(.)}$. All logarithmic calculations are to the base e.

2.2 The measurement equation

The first stage in the (self-)calibration process is to provide an efficient measurement equation which relates the visibilities with the unknown sky and the instrument parameters. In this section, we use the measurement equation presented by Hamaker et al. (1996). For assessing the equation

from the array signal processing point of view, the reader is referred to (Leshem & van der Veen, 2000; Boonstra & van der Veen, 2003; van der Tol et al., 2007).

We assume that we have a radio interferometer consisting of N receiver antennas. Each antenna consists of two orthogonal dual-polarization feeds, which receive the incident polarized waves from astrophysical sources in the sky. We also assume that the radio frequency sky consists of K discrete, uncorrelated sources. The sources are far enough from the array that their radiations can assumed to be plane waves.

Let us consider $\mathbf{e}_i = [e_{Xi}\ e_{Yi}]^T$ represents the electric field vector of the i-th source. This field causes an induced voltage $\tilde{\mathbf{v}}_{pi} = [v_{Xpi}\ v_{Ypi}]^T$ at antenna p for every $p \in \{1, 2, \ldots, N\}$ due to:

$$\tilde{\mathbf{v}}_{pi} = \mathbf{J}_{pi}\mathbf{e}_i. \tag{2.1}$$

In Eq. (2.1), the 2×2 Jones matrix $\mathbf{J}_{pi}$ describes the complex interaction between the fields, the antenna beam-shape and ionosphere, as well as the remaining signal path. The total signal at the antenna p, $\mathbf{v}_p$, is a linear superposition of K such signals as in (2.1). At the end, the receiver noise $\nu = [\nu_X\ \nu_Y]^T$ also is added to this signal.

Before correlating the voltages of the interferometer antennas, each voltage is corrected for a geometric delay depending on the location of its receiver antenna on the earth. Thereafter, the p-th antenna voltage gets correlated to the other $N-1$ array antenna voltages in the array correlator. The correlated voltages, referred to as *visibilities* (Hamaker et al., 1996) of the baseline pq corresponding to the p-th and the q-th antennas, $\mathrm{E}\{\mathbf{v}_p \otimes \mathbf{v}_q^H\}$, can be given as

$$\mathbf{V}_{pq} = \sum_{i=1}^{K} \mathbf{J}_{pi}(\boldsymbol{\theta})\mathbf{C}_i\mathbf{J}_{qi}^H(\boldsymbol{\theta}) + \mathbf{N}_{pq}, \quad p, q \in \{1, 2, \ldots, N\}. \tag{2.2}$$

In Eq. (2.2), the Jones matrices (Hamaker et al., 1996), $\mathbf{J}_{pi}(\boldsymbol{\theta})$ and $\mathbf{J}_{qi}(\boldsymbol{\theta})$ describe the electromagnetic interaction of the source i at antennas p and q, respectively (Born & Wolf, 1999). In particular, the instrumental properties (the beam shape, low-noise amplifier gain, system frequency response, etc.) as well as the propagation properties (tropospheric and ionospheric distortions, etc.) are represented by the Jones matrix formalism. They can be considered as the direction-dependent gains of the corresponding antennas for the i-th source. The unknown parameter vector $\boldsymbol{\theta} \in \mathbb{C}^P$ contains the parameters of both the instrument and the sky model. $\mathbf{N}_{pq}$ is the 2×2 noise matrix of the baseline pq. The *coherency* matrix (Born & Wolf, 1999; Hamaker et al., 1996) is defined as

$$\mathbf{C}_i = \mathrm{E}\{\mathbf{e}_i \otimes \mathbf{e}_i^H\}, \tag{2.3}$$

which provides us information about the polarization state of the radiation of the i-th source (a detailed formula is presented in 4.3). We assume that an initial estimate of the coherency matrix $\mathbf{C}_i$ is known based on some prior information, about the source or sky properties, obtained by previous observations.

Calibration is essentially a step to estimate the elements of the unknown parameter vector $\boldsymbol{\theta}$, i.e., P complex values or $2P$ real values. The parameter vector $\boldsymbol{\theta}$ is a random variable, that varies as a function of time and frequency, by nature. We assume without loss of generality that we are calibrating on a small enough time and frequency interval during which the variation of $\boldsymbol{\theta}$ is negligible. We then split the integration time to several sub-intervals and apply the calibration process to all of them separately.

Finally, the vectorized form of Eq. (2.2) can also be written as

$$\mathbf{v}_{pq} \equiv \text{vec}(\mathbf{V}_{pq}) = \sum_{i=1}^{K} \mathbf{J}_{qi}^{*}(\boldsymbol{\theta}) \otimes \mathbf{J}_{pi}(\boldsymbol{\theta})\text{vec}(\mathbf{C}_i) + \mathbf{n}_{pq}, \tag{2.4}$$

where $\mathbf{n}_{pq} = \text{vec}(\mathbf{N}_{pq})$. Ignoring the auto-correlations for $p = q$, and stacking up all cross correlations as $\mathbf{y} = [\mathbf{v}_{12}^T\ \mathbf{v}_{13}^T\ \ldots\ \mathbf{v}_{(N-1)N}^T]^T$, and all noise vectors as $\mathbf{n} = [\mathbf{n}_{12}^T\ \mathbf{n}_{13}^T\ \ldots\ \mathbf{n}_{(N-1)N}^T]^T$, we obtain the general form of the measurement equation as

$$\mathbf{y} = \sum_{i=1}^{K} \mathbf{s}_i(\boldsymbol{\theta}) + \mathbf{n}. \tag{2.5}$$

In Eq. (2.5), $\mathbf{y}, \mathbf{n} \in \mathbb{C}^M$,where M is at most $2N(N-1)$ providing all the cross-correlations. The dimension of the parameter vector $\boldsymbol{\theta}$, P, is a multiple of KN. Thus, for a large enough N and a small enough K, there are enough constraints for estimating $\boldsymbol{\theta}$. However, when the number of sources in the sky is uncertain, the optimal K could be selected using Aikaike's Information Criterion (AIC, Akaike (1973)) as presented in Yatawatta et al. (2009). The nonlinear function $\mathbf{s}_i(\boldsymbol{\theta})$, defined for $i \in \{1, 2, \ldots, K\}$ as

$$\mathbf{s}_i(\boldsymbol{\theta}) \equiv \begin{bmatrix} \mathbf{J}_{2i}^{*}(\boldsymbol{\theta}) \otimes \mathbf{J}_{1i}(\boldsymbol{\theta})\text{vec}(\mathbf{C}_i) \\ \mathbf{J}_{3i}^{*}(\boldsymbol{\theta}) \otimes \mathbf{J}_{1i}(\boldsymbol{\theta})\text{vec}(\mathbf{C}_i) \\ \vdots \\ \mathbf{J}_{Ni}^{*}(\boldsymbol{\theta}) \otimes \mathbf{J}_{(N-1)i}(\boldsymbol{\theta})\text{vec}(\mathbf{C}_i) \end{bmatrix},$$

corresponds to the contribution of the i-th source in the observation. The noise $\mathbf{n}$ is assumed to have a multivariate Gaussian distribution with zero mean and $M \times M$ covariance matrix $\mathbf{\Pi}$, i.e., $\mathbf{n} \sim \mathcal{N}(0, \mathbf{\Pi})$ (Yatawatta et al., 2009). Having the measurement equation in hand, one can apply different calibration techniques for estimating the ML of the unknowns.

2.3 THE LS, EM, AND THE SAGE CALIBRATION ALGORITHMS

In this section, we briefly discuss the Least Squares (LS, Normal) calibration via the Levenberg-Marquardt (LM) algorithm. We also discuss the new robust calibration techniques, the Expectation Maximization (EM) and in particular the Space Alternating Generalized Expectation Maximization (SAGE) calibration algorithms.

2.3.1 The LS calibration via LM algorithm

LS calibration considers the additive noise $\mathcal{N}$ to be a white Gaussian noise. Because the measurement equation shown in (2.5) has the general form of a non-linear regression model (Gallant, 1975; Bates & Watts, 2007), the likelihood of the unknown parameter $\boldsymbol{\theta}$ is maximized when the sum of squared residuals is minimized. Thus, the ML estimation of $\boldsymbol{\theta}$ will be equal to the below least squared error estimation

$$\widehat{\boldsymbol{\theta}} = \arg\min_{\boldsymbol{\theta}} ||\mathbf{y} - \textstyle\sum_{i=1}^{K} \mathbf{s}_i(\boldsymbol{\theta})||^2. \tag{2.6}$$

It is equivalent to minimize the distance between the observed visibilities in $\mathbf{y}$, and the predicted interferometer response as a superposition of K non-linear functions $\mathbf{s}_i(\boldsymbol{\theta})$ for $i \in \{1, 2, \ldots, K\}$. However, solving (2.6) suffers the same set of problems faced by any non-linear optimization problem, such as convergence to a local minimum, having a slow speed of convergence and significant computational cost.

There are various gradient-based optimization algorithms for estimating $\widehat{\boldsymbol{\theta}}$ at (2.6). The iterative LM algorithm is one of the most robust gradient-based optimization techniques in the sense that most of the time, given suitable initial suggestion $\boldsymbol{\theta}^0$, it converges to a global optimum. Considering $\phi(\boldsymbol{\theta}) = \mathbf{y} - \sum_{i=1}^{K} \mathbf{s}_i(\boldsymbol{\theta})$ as the cost function, the estimation of $\boldsymbol{\theta}$ at the $k+1$-th iteration of the algorithm will be obtained by

$$\boldsymbol{\theta}^{k+1} = \boldsymbol{\theta}^k - (\nabla_{\boldsymbol{\theta}} \nabla_{\boldsymbol{\theta}}^T \phi(\boldsymbol{\theta}) + \lambda \mathbf{H})^{-1} \nabla_{\boldsymbol{\theta}} \phi(\boldsymbol{\theta})|_{\boldsymbol{\theta}^k}. \tag{2.7}$$

In (2.7), $\nabla_{\boldsymbol{\theta}}$ is the gradient with respect to $\boldsymbol{\theta}$, and λ is the damping factor which should be adjusted at each iteration (Lampton, 1997). The matrix $\mathbf{H} = \text{diag}(\nabla_{\boldsymbol{\theta}} \nabla_{\boldsymbol{\theta}}^T \phi(\boldsymbol{\theta}))$ is the diagonal of the Hessian matrix.

The EM algorithm, and in particular the SAGE algorithm, improve the accuracy and computational cost compared with the LS calibration. They have the well-known advantage of ensuring that the likelihood gets increased at each iteration step. Since they break the ML estimation problem into smaller problems, the computational cost will be decreased by an order of magnitude and the rate of convergence is substantially increased. Furthermore, the convergence rate still can be significantly benefited from choosing a suitable starting point.

2.3.2 The EM calibration algorithm

In order to apply the EM algorithm (Feder & Weinstein, 1988) in calibration, we first need to extract a complete data space $\mathbf{x}$ from the observed data $\mathbf{y}$. Similar to Yatawatta et al. (2009), we consider the complete data space as $\mathbf{x} = [\mathbf{x}_1^T \; \mathbf{x}_2^T \ldots \mathbf{x}_K^T]^T$ in which $\mathbf{x}_i$ has the definition

$$\mathbf{x}_i \equiv \mathbf{s}_i(\boldsymbol{\theta}_i) + \mathbf{n}_i, \quad for\ i \in \{1, 2, \ldots K\}. \tag{2.8}$$

In fact, (2.8) assumes that the contribution of the i-th source in the observation depends only on a subset of parameters, $\boldsymbol{\theta}_i$. So, we partition the unknowns over the parameter vector $\boldsymbol{\theta}$ corresponding to all the K sources in the sky as $\boldsymbol{\theta} = [\boldsymbol{\theta}_1^T \; \boldsymbol{\theta}_2^T \ldots \boldsymbol{\theta}_K^T]^T$. This partitioning is justifiable as each source is at a unique direction on the sky, and for each antenna, the signal path of all sources is the same. This is the case for our initial assumption where the sources are separated sufficiently. Also, the total noise is arbitrary decomposed into K components, $\mathbf{n}_i$ for $i \in \{1, 2, \ldots, K\}$, such that

$$\mathbf{n} = \sum_{i=1}^{K} \mathbf{n}_i. \tag{2.9}$$

As the most convenient assumption, we let the noise components $\mathbf{n}_i$s to follow statistically independent zero mean Gaussian distributions with the covariance matrix

$$\mathrm{E}\{\mathbf{n}_i \mathbf{n}_j^H\} = \beta_i \delta_{ij} \mathbf{\Pi}, \tag{2.10}$$

where

$$\beta_i \in [0, 1], \;\; \text{for } i \in \{1, 2, \ldots, K\}, \;\; \sum_{i=1}^{K} \beta_i = 1. \tag{2.11}$$

In principle, we can associate weaker sources with higher noise, hence higher β_is, and vice-versa. Combining (2.5) and (2.8), the observed data $\mathbf{y}$ will be derived from

$$\mathbf{y} = \sum_{i=1}^{K} \mathbf{x}_i. \tag{2.12}$$

Therefore, for the given complete data space $\mathbf{x}$ we have

$$\mathbf{y} = [\mathbf{I}\,\mathbf{I}\ldots\mathbf{I}]\mathbf{x} = \mathbf{G}\mathbf{x}, \tag{2.13}$$

where $\mathbf{G}$ is a block matrix containing the identity matrix $\mathbf{I}$ for K times.
Having the definitions of complete and observed data in hand, the EM algorithm can be used to estimate the ML of the parameter vector $\boldsymbol{\theta}$. Applying the EM method for the new form of the measurement equation, (2.13), the below Expectation (E) and Maximization (M) steps are developed at the $k+1$-th iteration for $i \in \{1, 2, \ldots, K\}$.

E Step: Calculating the conditional mean $\widehat{\mathbf{x}}_i^k = \mathrm{E}\{\mathbf{x}_i|\mathbf{y}, \boldsymbol{\theta}^k\}$. Considering the fact that $\mathbf{x}$ and $\mathbf{y}$ are jointly Gaussian we get

$$\widehat{\mathbf{x}}_i^k = \mathbf{s}_i(\boldsymbol{\theta}_i^k) + \beta_i(\mathbf{y} - \sum_{l=1}^{K} \mathbf{s}_l(\boldsymbol{\theta}_l^k)). \tag{2.14}$$

M Step: Finding $\boldsymbol{\theta}_i^{k+1}$ such that minimizes $||[\widehat{\mathbf{x}}_i^k - \mathbf{s}_i(\boldsymbol{\theta}_i)]^H(\beta_i\mathbf{\Pi})^{-\frac{1}{2}}||^2$ with respect to $\boldsymbol{\theta}_i$. This is also a non-linear optimization problem where the LM technique can be applied. The result is given by:

$$\boldsymbol{\theta}_i^{k+1} = \boldsymbol{\theta}_i^k - (\nabla_{\boldsymbol{\theta}_i}\nabla_{\boldsymbol{\theta}_i}^T\phi_i(\boldsymbol{\theta}_i) + \lambda\mathbf{H}_i)^{-1}\nabla_{\boldsymbol{\theta}_i}\phi_i(\boldsymbol{\theta}_i)|_{\boldsymbol{\theta}_i^k}, \tag{2.15}$$

where the cost function $\phi_i(\boldsymbol{\theta}_i) = [\widehat{\mathbf{x}}_i^k - \mathbf{s}_i(\boldsymbol{\theta}_i)]^H(\beta_i\mathbf{\Pi})^{-\frac{1}{2}}$ and $\mathbf{H}_i = \mathrm{diag}(\nabla_{\boldsymbol{\theta}_i}\nabla_{\boldsymbol{\theta}_i}^T\phi_i(\boldsymbol{\theta}_i))$.

We repeat the above two steps starting from iteration $k = 1$ until convergence or an upper limit which has been reached. Since at each iteration, i goes from 1 to K, the solutions of each source will be updated. In Appendix A.1, we derive the EM algorithm for the problem in details and the results given above.

2.3.3 The SAGE calibration algorithm

The SAGE algorithm (Fessler & Hero, 1994) performs better than the EM algorithm and has a higher speed of convergence and solution accuracy. The major difference between these two approaches is in the way of assigning the noise to the complete data space.

Similar to applying the classical EM algorithm, the first step in the SAGE algorithm is to find a complete data space relating the observations to the unknown parameters. For this purpose, consider the set of all indices related to all the K sources as

$$P = \{1, 2, \ldots, K\}. \tag{2.16}$$

Then, define index sets W_i such that

$$\varnothing \neq W_i \subsetneq P, \tag{2.17}$$

where for all $a, b \in W_i$, we have $a \neq b$, and the sources corresponding to the indexes a and b, source a and source b, have a small angular distance (they are near to each other in the sky) and subsequently they share some elements of the parameter vector $\boldsymbol{\theta}$. We have

$$W_i \cap W_j = \varnothing, \quad \text{for } i \neq j. \tag{2.18}$$

Let us assume that we have m such index sets. Thus,

$$m \leq K, \quad P = \bigcup_{i=1}^{m} W_i. \tag{2.19}$$

For each $i \in \{1, 2, \ldots, m\}$, we define a new parameter vector $\boldsymbol{\theta}_{W_i}$ consisting of all the elements in the parameter vector $\boldsymbol{\theta}$, which are affected by the sources with indexes in W_i. In other words, we provide the possibility to have elements in these new parameter vectors which are shared by more than one source.

Now, we make a new partitioning over the parameter vector $\boldsymbol{\theta}$ as

$$\boldsymbol{\theta} = [\boldsymbol{\theta}_{W_1}^T \; \boldsymbol{\theta}_{W_2}^T \; \ldots \; \boldsymbol{\theta}_{W_m}^T]^T. \tag{2.20}$$

Similar to Fessler & Hero (1994), we define the hidden data space $\mathbf{x}_{W_i}$ as

$$\mathbf{x}_{W_i} = \sum_{l \in W_i} \mathbf{s}_l(\boldsymbol{\theta}_{W_i}) + \mathbf{n}, \tag{2.21}$$

selecting the index set $W_i \in \{W_1, W_2, \ldots, W_m\}$ which preferably consists of the indices of the brightest sources. Note that in (2.21) all the noise has been associated to the sources with indices in W_i. This is the main difference between the SAGE and the classical EM algorithm. Using (2.21), the measurement equation can be written as

$$\mathbf{y} = \mathbf{x}_{W_i} + \sum_{\substack{j=1 \\ j \neq i}}^{m} \sum_{l \in W_j} \mathbf{s}_l(\boldsymbol{\theta}_{W_j}). \tag{2.22}$$

By applying the EM algorithm to this new form of the measurement equation, we arrive at the following steps for the $k+1$-th iteration of the SAGE approach:

SAGE E Step: Computing the conditional mean $\widehat{\mathbf{x}}_{W_i}^k = \mathrm{E}\{\mathbf{x}_{W_i} | \mathbf{y}, \boldsymbol{\theta}^k\}$. Since $\mathbf{x}_{W_i}$ and $\mathbf{y}$ are also jointly Gaussian, we get

$$\begin{aligned} \widehat{\mathbf{x}}_{W_i}^k &= \sum_{l \in W_i} \mathbf{s}_l(\boldsymbol{\theta}_{W_i}^k) + (\mathbf{y} - \sum_{j=1}^{m} \sum_{l \in W_j} \mathbf{s}_l(\boldsymbol{\theta}_{W_j}^k)) \\ &= \mathbf{y} - \sum_{\substack{j=1 \\ j \neq i}}^{m} \sum_{l \in W_j} \mathbf{s}_l(\boldsymbol{\theta}_{W_j}^k). \end{aligned} \tag{2.23}$$

SAGE M Step: Finding $\boldsymbol{\theta}_{W_i}^{k+1}$ which is minimizing $||[\widehat{\mathbf{x}}_{W_i}^k - \sum_{l \in W_i} \mathbf{s}_l(\boldsymbol{\theta}_{W_i})]^H (\boldsymbol{\Pi})^{-\frac{1}{2}}||^2$ with respect to $\boldsymbol{\theta}_{W_i}$. The result is similar to (2.15) where $\phi_{W_i}(\boldsymbol{\theta}_{W_i}) = [\widehat{\mathbf{x}}_{W_i}^k - \sum_{l \in W_i} \mathbf{s}_l(\boldsymbol{\theta}_{W_i})]^H (\boldsymbol{\Pi})^{-\frac{1}{2}}$. As before, we iterate from $k = 1$ to an upper limit. At each iteration, we change the index set W_i

within $\{W_1, W_2, \ldots, W_m\}$ to update all or some sources.

A special case of the SAGE algorithm was presented by Yatawatta et al. (2009) if we consider $W_i = \{i\}$ for all $i \in \{1, 2, \ldots, K\}$. In fact, we apply the same partitioning over the unknown parameter $\boldsymbol{\theta}$ which is used for the classical EM algorithm, $\boldsymbol{\theta} = [\boldsymbol{\theta}_1^T \, \boldsymbol{\theta}_2^T \ldots \boldsymbol{\theta}_K^T]^T$. By choosing the index i, where the source i is preferably the brightest source in the sky, the hidden data space will be defined by

$$\mathbf{x}_i = \mathbf{s}_i(\boldsymbol{\theta}_i) + \mathbf{n}. \tag{2.24}$$

(2.24) gives us the definition of the observed data as

$$\mathbf{y} = \mathbf{x}_i + \sum_{\substack{l=1 \\ l \neq i}}^{K} \mathbf{s}_l(\boldsymbol{\theta}_l), \tag{2.25}$$

and subsequently, applying the EM on the measurement equation, the $k+1$-th iteration of the SAGE technique will be as below:

SAGE E Step: Conditional mean $\widehat{\mathbf{x}}_i^k = \mathrm{E}\{\mathbf{x}_i | \mathbf{y}, \boldsymbol{\theta}^k\}$ is derived from

$$\widehat{\mathbf{x}}_i^k = \mathbf{s}_i(\boldsymbol{\theta}_i^k) + (\mathbf{y} - \sum_{l=1}^{K} \mathbf{s}_l(\boldsymbol{\theta}_l^k)) = \mathbf{y} - \sum_{\substack{l=1 \\ l \neq i}}^{K} \mathbf{s}_l(\boldsymbol{\theta}_l^k). \tag{2.26}$$

SAGE M Step: $\boldsymbol{\theta}_i^{k+1}$ is given by minimizing $||[\widehat{\mathbf{x}}_i^k - \mathbf{s}_i(\boldsymbol{\theta}_i)]^H (\boldsymbol{\Pi})^{-\frac{1}{2}}||^2$.

In Appendix A.2, we present the complete calculation process of applying the SAGE algorithm to the calibration problem.

2.3.4 Computational Cost

At each iteration of the LS calibration scheme via the LM algorithm, the non-linear system presented by (2.7) should be solved which is of order (KN). Therefore, ignoring the cost of calculations for the inverse part in this equation, the computational cost will be $\mathcal{O}((KN)^2)$. Furthermore, for radio synthesis arrays such LOFAR and SKA, computing the matrix inverse in (2.7) is very costly since the number of measured data is becoming very large. While, at each iteration of the EM algorithm, we should solve (2.15) K times and subsequently the computational cost of the EM calibration algorithm will be $K\mathcal{O}(N^2)$, which is still much cheaper compared with the LS calibration approach. Thus, the EM as well as the SAGE calibration techniques are superior to the LS one in terms of computational cost.

Note that the LM optimization technique is employed for all the LS, EM, and the SAGE calibration algorithms. Thus, its corresponding inversion computation is shared in all the methods. However, in the EM and SAGE algorithms the size of the matrix that is inverted is smaller compared to that of the LS algorithm because of the partitioning procedure of the parameters. Given the fact that the computational complexity of the matrix inversion scales a the number of its elements to the third power, it is evident that inverting few smaller matrices as in the EM and SAGE cases is faster than inverting a single large matrix, which is the case for the LS algorithm.

2.4 NOISE IN SOLUTIONS

To compare the accuracy of the SAGE calibration scheme to the LS one, we statistically analyze the solver noise. The lower the solver noise in a calibration method, the smaller the errors in calibrated solutions provided by the calibration algorithm itself. Consequently, the accuracy of the method is higher.

In order to do a proper statistical analysis of the calibration algorithm's solver noise, we make the assumption that their solutions are linear combinations of a deterministic trend and noise. This noise can have many origins. In the ideal case, it is introduced by the primary noise sources (thermal noise at the receiver, the sky noise, radio interference, etc.) and by variations of the instrumental and propagation properties. However, in reality the solver noise, which we are most concerned about and is introduced by the calibration method itself, is also added to those sources.

The goal in this section is to quantify the level of the solver noise for the different calibration algorithms, based on the evaluation of the statistical interaction between their solutions.

2.4.1 Statistical similarity

In order to compare the level of solver noise for the different calibration methods, we assume that the true values of the solutions from different directions at the same antenna are statistically uncorrelated. Therefore, any correlation between the calibrated solutions for different directions is caused by the corresponding calibration technique itself. In reality, there are also correlations that originate from the system noise in the solutions, but this can be ignored when we compare the solutions of a fixed measured data obtained by different calibration methods. Therefore, a high solver noise in a calibration scheme causes strongly correlated solutions for any number of directions at one given antenna (or maybe even more). To detect the statistical similarity between the gain solutions we proceed as follows:

Once we estimate the parameter vector $\boldsymbol{\theta}$, we obtain the Jones matrices $\mathbf{J}_{qs}(\boldsymbol{\theta})$ for different antennas $q \in \{1, 2, \ldots, N\}$ and different directions $s \in \{1, 2, \ldots, K\}$. Let us consider the matrices to be diagonal as

$$\mathbf{J}_{qs} = \left[\begin{array}{cc} J_{11,q} & 0 \\ 0 & J_{22,q} \end{array} \right]_s, \tag{2.27}$$

where $J_{11,q}$ and $J_{22,q}$ are complex values. We treat each gain solution from the direction s of antenna q as a random vector $\boldsymbol{\theta}_{qs}$ defined by

$$\boldsymbol{\theta}_{qs} = [\mathfrak{Re}(J_{11,q})\ \mathfrak{Im}(J_{11,q})\ \mathfrak{Re}(J_{22,q})\ \mathfrak{Im}(J_{22,q})]_s^T. \tag{2.28}$$

Now, we can investigate the statistical similarity between the gain solutions utilizing Kullback-Leibler Divergence (KLD) and Likelihood-Ratio Test (LRT). In general, both KLD and LRT compare the efficiency of fitting two different statistical models to a fixed set of measurements. Utilizing these methods on the random vectors defined by (2.28), we obtain their statistical similarity in two different interpretations. The higher these similarities, the higher the interaction between the solutions, as well as the solver noise.

2.4.2 Kullback-Leibler Divergence (KLD)

An efficient way to quantify the statistical similarity between the solutions is to use KLD.

The relative entropy, defined as the KLD, for each couple of Probability Density Functions (PDFs) f and g of solutions $\boldsymbol{\theta}_{qk}$ and $\boldsymbol{\theta}_{ql}$, respectively, is defined as

$$\mathrm{KLD}(f,g) \equiv \sum_{\boldsymbol{\theta}_{qk}} f(\boldsymbol{\theta}_{qk}) \log \frac{f(\boldsymbol{\theta}_{qk})}{g(\boldsymbol{\theta}_{qk})}, \tag{2.29}$$

where the solutions are corresponding to the given antenna q at the two directions k and l.
The KLD is a measure of information "divergence" between two different PDFs for the same random variable. Larger values of $\mathrm{KLD}(f,g)$ are interpreted as less interaction between the solutions, and subsequently, as less solver noise. We use a Monte-Carlo method to evaluate (2.29).

Density estimation

To calculate the value of KLD we need to estimate the PDFs of the solutions.

We define the PDF of the random vector $\boldsymbol{\theta}_{qs}$, $f(\boldsymbol{\theta}_{qs};\boldsymbol{\beta})$, as a mixture of L isotropic (scalar variance) Gaussian PDFs. The assumption of mixture modeling is based on the fact that the solutions are affected by parameters that belong to different underlying statistical populations and due to the Central Limit Theorem it is reasonable to assume that the distributions of those populations converge to Gaussian distributions. Therefore, it can be written as

$$f(\boldsymbol{\theta}_{qs},\boldsymbol{\beta}) = \sum_{l=1}^{L} p_l g(\boldsymbol{\theta}_{qs};\mathbf{m}_l,\sigma_l), \tag{2.30}$$

where $g(\boldsymbol{\theta}_{qs};\mathbf{m}_l,\sigma_l)$ is the PDF of a four dimensional Gaussian distribution with mean $\mathbf{m}_l$ and variance $\sigma_l^2\mathbf{I}$ given by

$$g(\boldsymbol{\theta}_{qs};\mathbf{m}_l,\sigma_l) = \frac{1}{(\sqrt{2\pi}\sigma_l)^4} exp\bigg(-\frac{1}{2}\bigg(\frac{\|\boldsymbol{\theta}_{qs}-\mathbf{m}_l\|}{\sigma_l}\bigg)^2\bigg), \tag{2.31}$$

and $\boldsymbol{\beta}$ is the vector of the mixture model unknown parameters

$$\boldsymbol{\beta} = [p_1, \mathbf{m}_1^T, \sigma_1, ..., p_L, \mathbf{m}_L^T, \sigma_L]^T, \tag{2.32}$$

which are estimated by the EM algorithm (Bilmes, 1998).

Akaike's Information Criterion for model order selection

To find the optimum number of L (the order of Gaussian mixture model in (2.30)) we use Aikake's Information Criterion (AIC, Akaike 1973).

According to the definition of AIC, we select L such that it gives us the minimum value of $\mathrm{AIC}(L)$ which is defined as

$$\mathrm{AIC}(L) = -2\mathrm{L}(\widehat{\boldsymbol{\beta}}) + 2k, \tag{2.33}$$

where $\mathrm{L}(.)$ is the log-likelihood function of $\boldsymbol{\theta}$, $\widehat{\boldsymbol{\beta}}$ is the maximum likelihood estimate of $\boldsymbol{\beta}$, and k is the number of parameters in the model presented by (2.30).

2.4.3 Likelihood-Ratio Test (LRT)

Another standard approach to investigate the statistical interaction between the solutions is the Likelihood-Ratio Test (LRT). Using this test, we can compare two models, which both can be fitted to our solutions.
Let us define for each antenna q, where $q \in \{1, 2, ..., N\}$, and each pair of directions like k and l, where $k, l \in \{1, 2, ..., K\}$, a new random vector $\mathbf{z}_{qkl}$ as

$$\mathbf{z}_{qkl} = [\boldsymbol{\theta}_{qk}^T \, \boldsymbol{\theta}_{ql}^T]^T. \tag{2.34}$$

In fact, we are concatenating the solutions of the same antenna for two different directions together. Assume that $\mathbf{z}_{qkl}$ is following a multivariate Gaussian distribution with mean

$$\mathbf{m} = [\bar{\mathbf{m}}(\boldsymbol{\theta}_{qk})^T \, \bar{\mathbf{m}}(\boldsymbol{\theta}_{ql})^T]^T, \tag{2.35}$$

and variance

$$\Sigma_{\mathbf{0}} = \begin{bmatrix} \mathbf{s}^2(\boldsymbol{\theta}_{qk}) & 0 \\ 0 & \mathbf{s}^2(\boldsymbol{\theta}_{ql}) \end{bmatrix}, \tag{2.36}$$

where $\bar{\mathbf{m}}$ and $\mathbf{s}^2$ are the sample mean and sample variance of the solutions respectively. The structure of the variance matrix $\Sigma_{\mathbf{0}}$ tells us that the statistical correlation between the components of the random vector $\mathbf{z}_{qkl}$, or between the solutions $\boldsymbol{\theta}_{qk}$ and $\boldsymbol{\theta}_{ql}$, is zero. This is exactly the desirable case in which the solver noise vanishes. Thus, we can consider this model as our null H_0 model defined by

$$H_0 : \ \mathbf{z}_{qkl} \sim \mathcal{N}(\mathbf{m}, \Sigma_0). \tag{2.37}$$

To investigate the validity of the null model compared with the case in which there exist some correlation between the solutions due to the presence of solver noise, we define the alternative H_1 model as

$$H_1 : \ \mathbf{z}_{qkl} \sim \mathcal{N}(\mathbf{m}, \Sigma_1), \tag{2.38}$$

where the variance matrix Σ_1 is given by

$$\Sigma_1 = \begin{bmatrix} \mathbf{s}^2(\boldsymbol{\theta}_{qk}) & \mathbf{Q}(\boldsymbol{\theta}_{qk}, \boldsymbol{\theta}_{ql}) \\ \mathbf{Q}(\boldsymbol{\theta}_{qk}, \boldsymbol{\theta}_{ql})^T & \mathbf{s}^2(\boldsymbol{\theta}_{ql}) \end{bmatrix}, \tag{2.39}$$

and the 4×4 matrix $\mathbf{Q}(\boldsymbol{\theta}_{qk}, \boldsymbol{\theta}_{ql})$ denotes the sample covariance of the solutions.
Using the above models, the Likelihood-Ratio is defined as

$$\Lambda = -2\ln\left(\frac{\text{Likelihood for null model}}{\text{Likelihood for alternative model}}\right), \tag{2.40}$$

which has a χ^2 distribution with 16 (number of elements of matrix $\mathbf{Q}$) degrees of freedom. As Λ becomes smaller, the null model, in which the statistical correlation as well as the statistical similarity between the solutions is zero, becomes more acceptable compared to the alternative one. Therefore, the smallest the Λ, the less the solver noise and vice-versa.

Note that the test result is reliable only when a large number of sample solutions is in hand. In this case, because of the Central Limit Theorem, the distribution of solutions tends to be a multivariate LS distribution, which is assumed initially by the test.

2.5 ILLUSTRATIVE EXAMPLES

2.5.1 Simulated observation

First we use a simulated observation to compare the efficiency of the SAGE calibration algorithm with the LS algorithm. Utilizing simulations instead of real observations has the advantage of having the true underlying gains available, which is a luxury not available with real data. Therefore, assessing the convergence of the calibration techniques as well as comparing the accuracy between different calibrated solutions is much more objective.

We consider a linear, East-West radio synthesis array that has 14 dipoles with dual polarization. We put three bright sources in our sky model named A, B, and C with intensities 2950, 2900, and 2700 Jy, and three other weak sources named D, E, and F with intensities 4, 3.5, and 3 Jy, respectively. The simulated single channel image at 355 MHz is shown in Fig. 2.1. As we can see in Fig. 2.1, the weak sources are not visible in the image. We also consider that there is no beam pattern, therefore the whole sky is being observed with uniform sensitivity.

As it is shown in (2.2), in the measured visibilities, the coherency of the sources are multiplied by the Jones matrices (gain errors). We consider the matrices to be diagonal. It means that the signal received at each dipole is not affected by the other one which is an ideal case. We produce gain errors in the norm and phase of the Jones matrices diagonal terms which are 1 and 0 initially. We generate the norm and the phase of the gains as multiplications of random numbers with different linear combinations of sin and cos functions, whose gradients increase with time. We also add another random term increasing as a function of time, just to the phase errors, to provide the phases with positive and negative slopes. The simulated result is presented by Fig. 2.2.

Finally, we apply the SAGE and the LS calibration to solve only for the gains of the visible strong sources A, B, and C. The residuals of the SAGE and LS calibration using nine iterations are shown in Fig. 2.3 and Fig. 2.4, respectively. As we can see in Fig. 2.3 and Fig. 2.4, The strong sources are completely removed and the three weak sources are visible in the residuals of the both algorithms which mean both are converging to real solutions. But, the weak sources intensities in the residuals of the SAGE calibration are closer to the absolute intensities in our sky model which shows the superiority of the SAGE calibration in terms of accuracy. This fact is shown more clearly by table 2.5.1 where the real intensities of the weak sources are compared with the calibrated ones.

Table 5.1

Source	D	E	F
Real intensity(Jy)	4	3.5	3
SAGE calibration	3.8399	3.6695	2.3085
LS calibration	2.8327	2.6329	1.6081

Note that as this is a single channel simulated observation without any additive noise, the difference between the two method's residuals is slight. However, the importance of applying the SAGE instead of LS calibration is evident since the computational cost of the SAGE is much smaller, as it is discussed in section 2.3.4. Fig. 2.5 shows the performance of the algorithms in terms of accuracy and speed of convergence. As we can see in Figure 2.5, the SAGE algorithm's speed of convergence is much higher than that of the standard LS calibration.

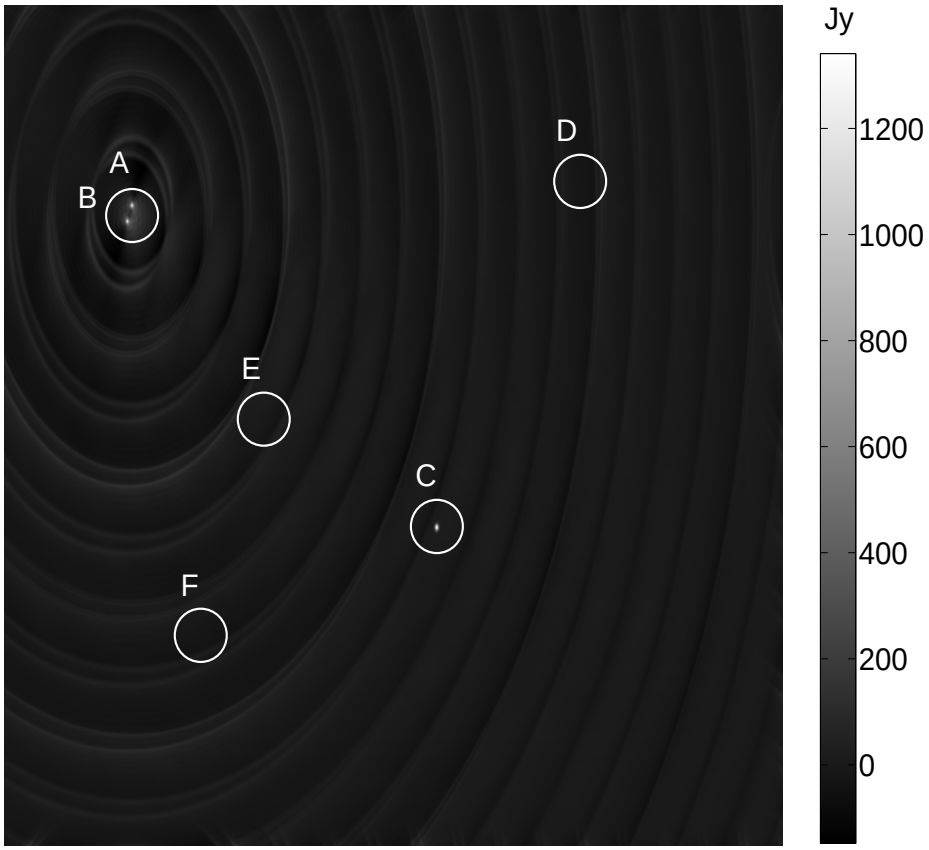

Figure 2.1: *Single channel simulated observation of three bright sources, A, B, and C, and three weak sources, D, E, and F. The intensity of the bright sources are 2950, 2900, and 2700 Jy and of the weak sources are 4, 3.5, and 3 Jy, respectively. The image size is 8 by 8 degrees at 355 MHz. There are no gain errors and noise in the simulation.*

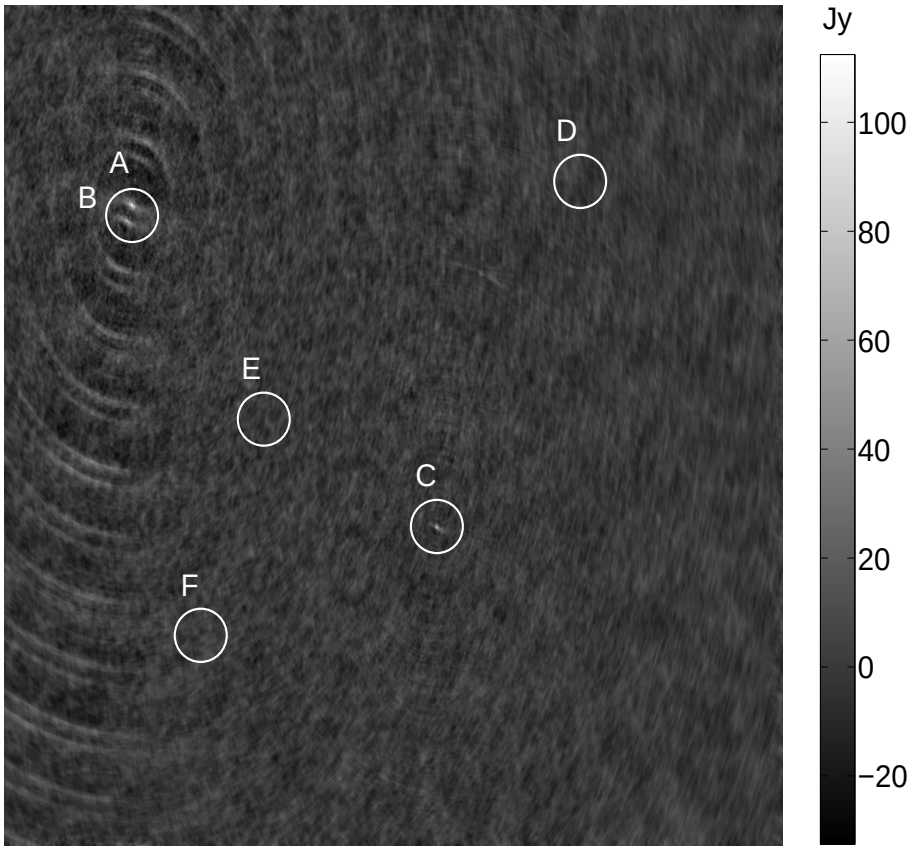

Figure 2.2: *Simulated observation with added gain errors. The errors are complex numbers having norms and phases as multiplications of random numbers with various linear combinations of sin and cos functions. The gradients of the errors increase as a function of time and the phases are in different negative and positive slopes.*

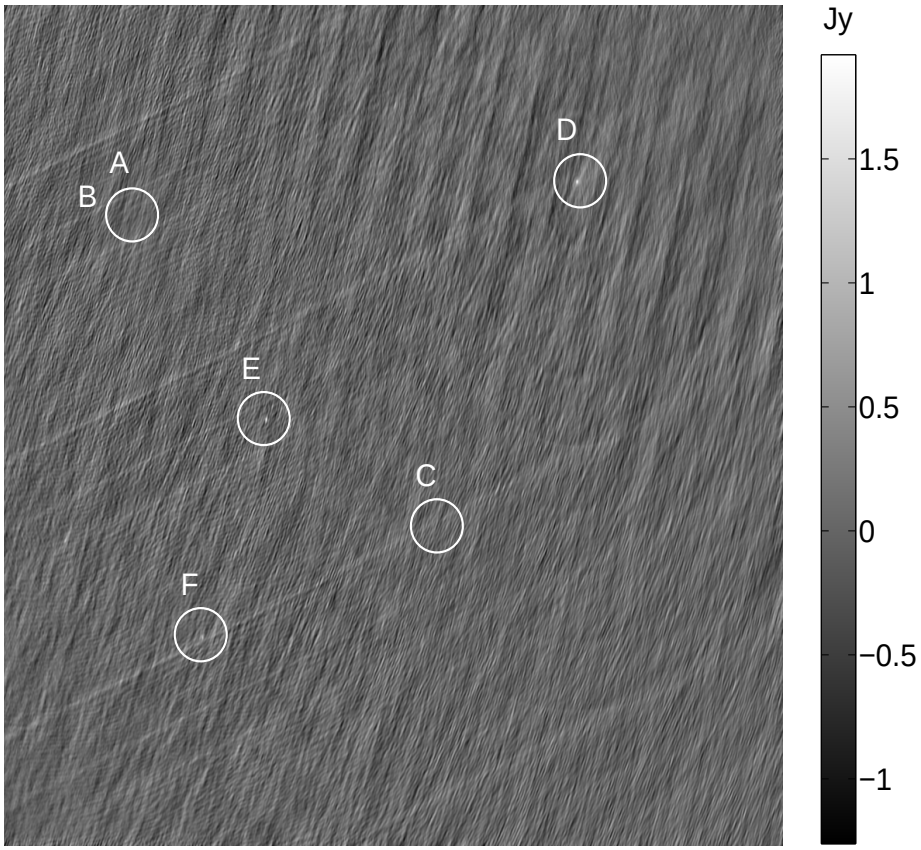

Figure 2.3: *Residual image of the SAGE calibration using nine iterations. The image is only calibrated for the bright sources A, B, and C, which are perfectly removed. The weak sources D, E, and F appear in the residuals, including source F which is the weakest source in the simulation.*

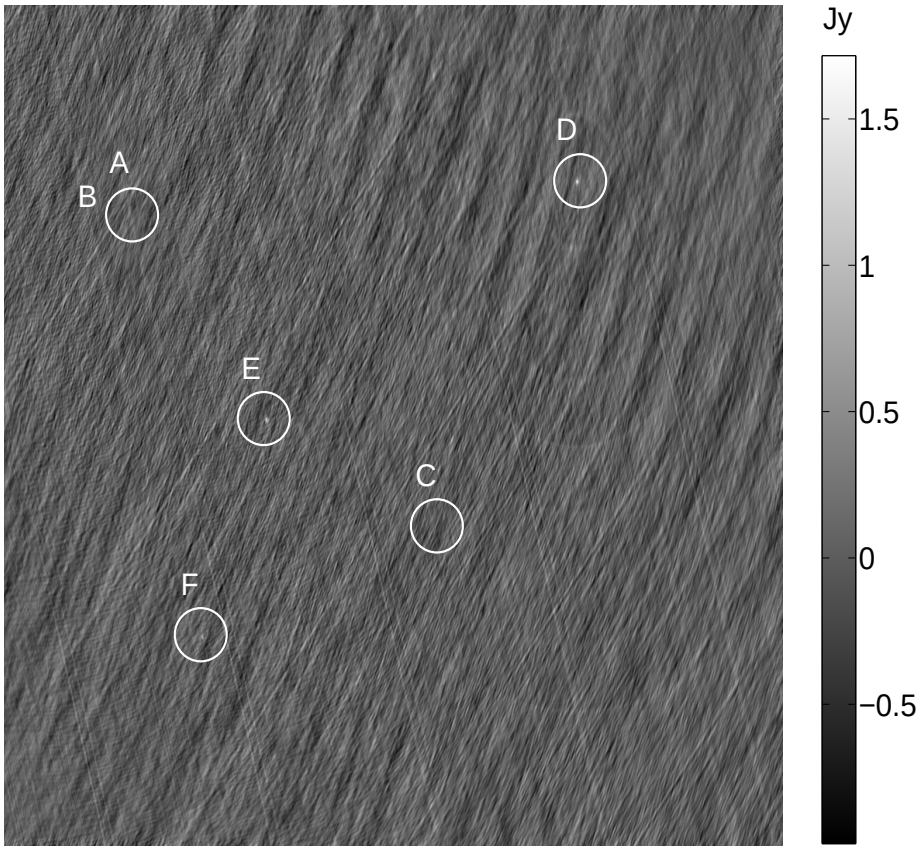

Figure 2.4: *Residual image of the LS calibration using nine iterations. The calibration is processed only for the strong sources A, B, and C, that are completely removed in the residuals. The two weak sources D, and E appear in the image, but the weakest source F is hardly visible.*

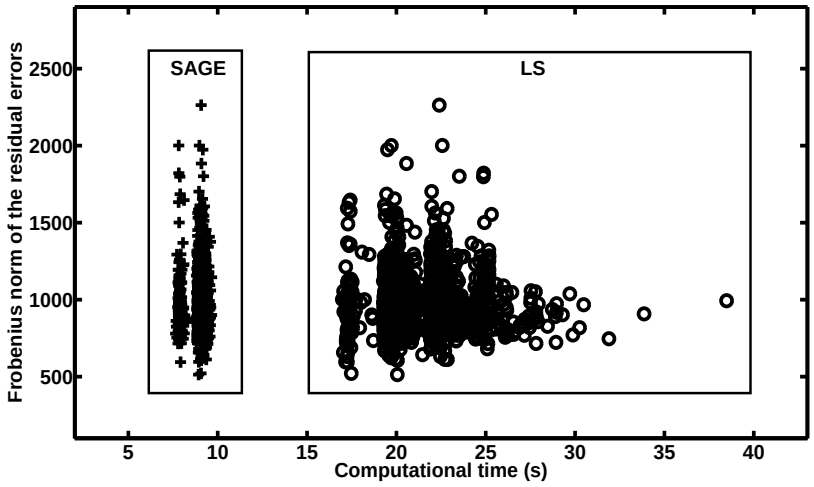

Figure 2.5: *Comparison between the performance of the SAGE and the LS calibrations (nine iterations) in order of the accuracy of solutions and the speed of convergence. Different points correspond to different snapshots made from the simulation. The speed of the SAGE calibration technique is higher than the LS calibration, while the norm of their residual errors are almost the same*

In order to investigate the efficiency of the LRT and KLD approaches in revealing the statistical similarity of gain solutions, we applied both methods, using 2.29 and 2.40, to the SAGE and the LS calibration solutions and compared their results with the LRT and KLD of the true Jones parameters (simulated gains). The comparison is shown by Fig. 2.6 and Fig. 2.7. Fig. 2.6 exhibits an outstanding performance of the LRT approach in which the direction dependent gain's lowest statistical similarity belongs to the real Jones values, that is almost zero. For SAGE calibration's solutions this similarity becomes higher, and in LS results it reaches to its highest level. This result demonstrates the superior accuracy of the SAGE calibration's solutions regardless of the residual images. But, the KLD results in Fig. 2.7 show the same level of statistical correlation in the calibrations' solutions and in the True Jones parameters. This is due to the fact that these results are calculated by Gaussian mixture models, which are fitted to the gains. This characteristic of the KLD approach (using fitted PDFs for gains distributions rather than the true PDFs) decreases the methods sensitivity in revealing the level of statistical similarity between different directions' gains, especially in our case where the simulated gains' correlations are low. However, we anticipate better performance of KLD method in real observations in which the higher gain errors plus additive noise cause higher solver noise.

2.5.2 Real observations

To illustrate the applicability of the KLD and LRT approaches in detecting solver noise in real observations calibrated solutions, we use the data from the example in Yatawatta et al. (2009). Yatawatta et al. (2009) presents the calibration results using real data obtained during a 24 hours long LOFAR test core station (CS1) observation, via SAGE and LS calibration techniques. The

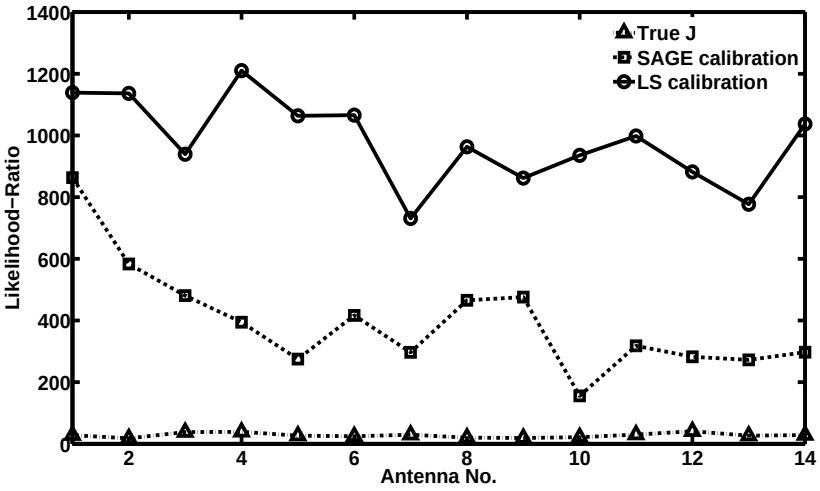

Figure 2.6: *Averaged Likelihood-Ratio of direction dependent gains (True values and calibrated ones) for all two source combinations between the bright sources A, B, and C*

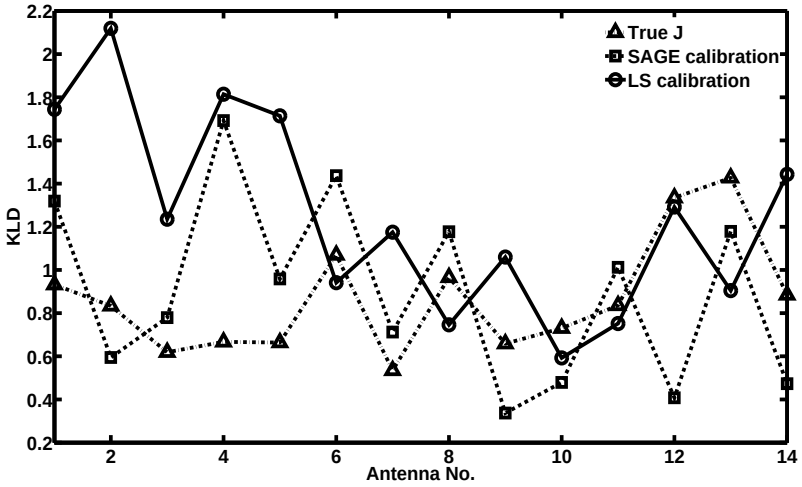

Figure 2.7: *Averaged KLD of direction dependent gains (True values and calibrated ones) for all two source combinations between the bright sources A, B, and C*

one channel images around 3C 461 (Cassiopeia A, CasA) and 3C 401 (Cygnus A, CygA) at 50 MHz after applying these calibration methods using twelve iterations are shown in Fig. 2.8. The result at Fig. 2.8 clearly verifies the superiority of the SAGE calibration scheme as it was mentioned in Yatawatta et al. (2009) as well. We calculate the KLD using (2.29) as well as Likelihood-Ratio using (2.40) for the calibrated solutions of these two sources obtained by the mentioned calibration techniques. In the KLD approach, we fit a Gaussian mixture model, which its components have full rank covariance matrices, to the solutions. The KLD and LRT results are shown in Fig 2.9 and Fig 2.10, respectively. As we can see in Fig 2.9, the KLD of the solutions derived by the LS calibration is always lower than that of the SAGE calibration. It is also shown in Fig 2.10 that the LRT of the LS calibration's solutions is always higher than the SAGE calibration's. Therefore, the solver noise in the LS calibration results is measurably higher than in the solutions obtained by the SAGE calibration. This means that the accuracy of the SAGE calibration is always higher than that of the LS calibration, which is visible in Fig. 2.8 as well as the aforementioned images in Yatawatta et al. (2009).

2.6 Summary

Since the new generation of radio synthesis arrays are producing a large amount of data with high sensitivity, it is of great interest to devise new calibration techniques in order to increase the accuracy of solutions with the highest possible speed of convergence.

In this chapter, we presented the superior performance of the SAGE calibration scheme compared with the traditional LS calibration method. The superiority is in the sense that SAGE calibration has the highest accuracy, the fastest speed of convergence, and the cheapest computational cost. Since both the algorithms are estimating the ML of unknowns in different ways, it is possible that in some special cases, such as having a very low initial noise in the measured visibilities, we don't have a specific difference between the accuracy of their solutions. While, even in this case, the SAGE calibration's faster speed of convergence and cheaper computational cost justify its application instead of the LS calibration. We compare the accuracy and the rate of convergence of the SAGE and the LS calibration in a simulated observation example. More accurate results in a much shorter time are obtained by the SAGE algorithm compared with the LS. The challenge in improving the performance of the SAGE calibration technique is to find the best way of partitioning over the unknown parameter space. This can highly affect both the accuracy and speed of convergence of the calibration process.

On the other hand, there always exists some estimation errors in the calibrated solutions. These errors are originated from the system noise (sky and instrumental) in the measurements, plus "solver noise" which is referred to errors produced by the calibration algorithm itself. The more accurate the calibrated solutions are, the less the amount of solver noise is. Based on this fact, the best calibration method is the one which provides us with the minimum solver noise. KLD and LRT are utilized to reveal the level of solver noise in the solutions of different calibration schemes. We showed in illustrative examples that the LRT algorithm produces a very promising result. The KLD method is rather inconclusive according to the initial assumption for the PDFs fitted to the solutions. We assumed that the distribution of the solutions is a mixture of Gaussian distributions. However, in reality, the solutions may follow a different distribution and subsequently the KLD result may not have the same efficiency as the LRT's. Therefore, initially we should find the proper distribution which is appropriate for the solutions in order to calculate the KLD.

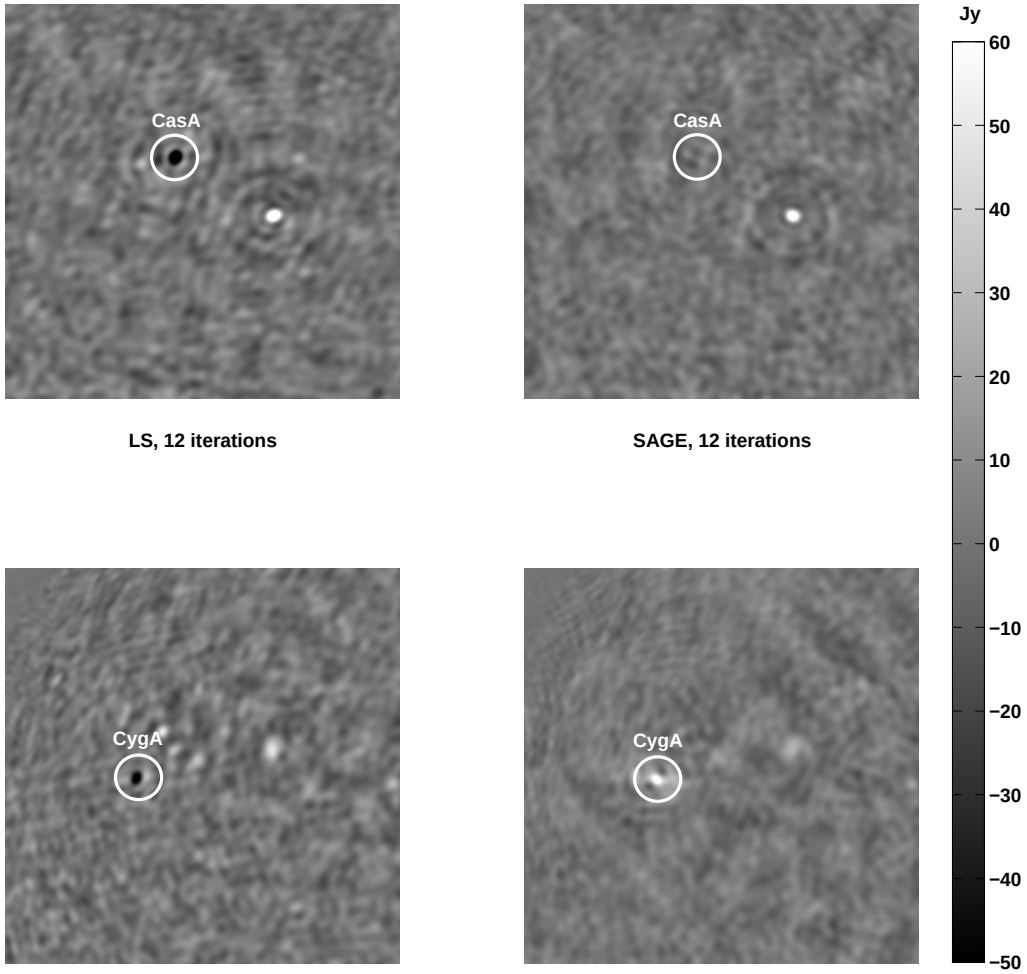

Figure 2.8: *Residual images around CasA (top row) and CygA (bottom row) obtained by the LS calibration (left column) and the SAGE calibration (right column) using twelve iterations. CasA is over-subtracted in the residual of the LS calibration result, due to the inaccuracy in the estimation of the relevant direction-dependent gain, while in the SAGE calibration result it is removed almost perfectly. On the other hand, Both the SAGE and the LS calibrations present some problems around CygA since at some point of the integration time it goes very close to the horizon. Even in that case, the subtraction residual for the SAGE algorithm is 10 percent lower than for the LS method.*

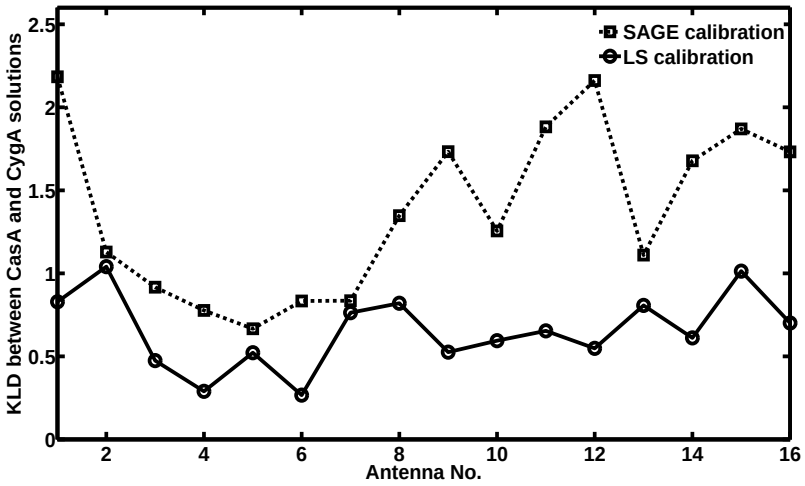

Figure 2.9: *KLD of the gain solutions for CasA and CygA. The KLD of the solutions derived by the LS calibration is always lower than that of the SAGE calibration. Therefore, the solver noise in the LS calibration results is higher than in the solutions the SAGE calibration's solutions.*

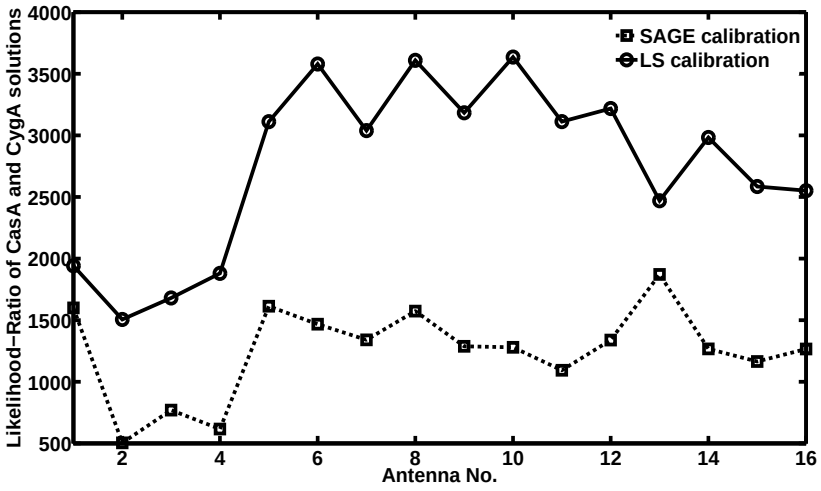

Figure 2.10: *Likelihood-Ratio of the gain solutions for CasA and CygA. The LRT of the LS calibration's solutions is always higher than the SAGE calibration's. Thus, the solver noise in the LS calibration results is higher than in the solutions obtained by the SAGE calibration.*

The main direction of future work should be to investigate the application of the proposed calibration technique to real data obtained by LOFAR. Since LOFAR is observing the whole sky, the number of radio sources in the sky model will be very large. Subsequently, for applying the SAGE calibration, partitioning over the unknowns by manually checking the characteristics of all the sources will not be efficient. Therefore, the first challenge in utilizing the SAGE calibration to real data would be automating the partitioning over the unknowns for any given problem. Furthermore, we saw in the chapter that all the mentioned calibration algorithms involve essentially the solution of a non-linear optimization problem. Applying suitable regularization techniques using proper smoothing functions to improve the accuracy of the solutions is an issue that must be investigated further in the near future. Add to that, that all the calibration schemes have the possibility of converging to a local optimum. Utilizing probabilistic techniques such as Simulated Annealing (SA) (Kirkpatrick et al., 1983) to assure that we are converging to a global optimum has the problem of decreasing the speed of convergence. Providing extra constraints for the mentioned calibration schemes which can guarantee the convergence to the real solutions could be one of the challenging areas of research in the future. Moreover, we have shown that the solver noise criterion could be used for revealing the level of accuracy in the calibrated solutions. Investigating possible systematic effects on the solver noise as well as the level of their influence are amongst the main issues for the future work.

Chapter 3

Radio Interferometric Calibration via Ordered-Subsets Algorithms: OS-LS and OS-SAGE calibrations

"Radio Interferometric Calibration via Ordered-Subsets Algorithms: OS-LS and OS-SAGE calibrations"
Kazemi S., Yatawatta S., Zaroubi S., 2013, MNRAS, 434, 3130

ABSTRACT
The main objective of this work is to accelerate the Maximum-Likelihood (ML) estimation procedure in radio interferometric calibration. We introduce the OS-LS and the OS-SAGE radio interferometric calibration methods, as a combination of the Ordered-Subsets (OS) method with the Least-Squares (LS) and Space Alternating Generalized Expectation maximization (SAGE) calibration techniques, respectively. The OS algorithm speeds up the ML estimation and achieves nearly the same level of accuracy of solutions as the one obtained by the non-OS methods. We apply the OS-LS and OS-SAGE calibration methods to simulated observations and show that these methods have a much higher convergence rate relative to the conventional LS and SAGE techniques. Moreover, the obtained results show that the OS-SAGE calibration technique has a superior performance compared to the OS-LS calibration method in the sense of achieving more accurate results while having significantly less computational cost.

3.1 Introduction

Radio interferometry is the technique of combining and correlating signals from two or more separate antennas to observe the target astronomical object with a resolution determined not by

the size of a single antenna but by the area covered with all the incorporated antennas. Therefore, a much better angular resolution can be achieved using radio interferometers with multiple antennas instead of single dishes (Thompson et al., 2001; Burke & Graham-Smith, 2009).

The main objective of designing the new generation of radio interferometers, such as the Square Kilometre Array (SKA)[1], the Murchison Widefield Array (MWA)[2], the Precision Array to Probe Epoch of Reionization (PAPER)[3], the 21-cm Array (21CMA)[4], the Hydrogen Epoch of Reionization Array (HERA)[5], the Long Wavelength Array (LWA)[6] and the LOw Frequency ARray (LOFAR)[7], with the ability to collect enormous amounts of data, is improving the sensitivity, resolution and frequency coverage of observations. Therefore, to deliver their scientific goals, there is a need for processing a large amount of data and for upgrading the accuracy as well as the processing time of the existing calibration techniques.

Propagation medium and the receivers' effect in radio interferometric data are initially unknown and have to be calibrated and corrected before imaging. Self-calibration (Pearson & Readhead, 1984) estimates the Maximum-Likelihood (ML) estimate of the unknowns utilizing only the measurements, and due to its high accuracy, it has become the method of choice, as in this chapter, for calibrating the new generation of radio synthesis arrays.

In the presence of additive Gaussian noise, calibration is performed as a non-linear Least-Squares (LS) optimization that calculates the ML estimation using iterative gradient based methods such as Levenberg-Marquardt (LM) method (Marquardt, 1963; Levenberg, 1944). However, the LS calibration suffers from a very low convergence rate because the parameters must be updated simultaneously on a complete data space. Solving for a large number of unknowns, the Jacobian computation corresponding to the applied gradient based method is considerably costly. This makes the LS calibration impractical for calibration of giant radio telescopes like SKA with thousands of receivers.

The convergence rate and computational efficiency of calibration is significantly improved by the recently proposed Space Alternating Generalized Expectation maximization (SAGE) calibration technique (Yatawatta et al. (2009); Kazemi et al. (2011), chapter 2). SAGE method (Fessler & Hero, 1994) is a specific version of the Expectation Maximization (EM) algorithm (Feder & Weinstein, 1988) which converges even faster than the conventional EM (Fessler & Hero, 1993). The SAGE algorithm partitions the data space to smaller "hidden" data spaces and at every iteration, it alternates between updating parameters on some or all of them. Obtaining the ML estimate for the parameters of these small data spaces, which carry less information compared to the complete data space, provides SAGE algorithm with a superior accuracy as well as lower computational cost compared to the LS technique. Nevertheless, there is still a need for improving the speed of calibration process especially for radio synthesis arrays such as LOFAR and SKA.

In this chapter, we utilize the Ordered-subsets (OS) algorithm for accelerating the speed of calibration. The well known OS algorithm accelerates the convergence rate of iterative ML estimations and has been widely used in medical imaging (Hudson & Larkin, 1994; Erdogan & Fessler, 1999). This method decomposes the objective (likelihood) function to several sub-objective functions and updates the parameters by using the gradient of one, or some, of the sub-objective func-

[1] http://www.skatelescope.org
[2] http://www.mwatelescope.org
[3] http://astro.berkeley.edu/~dbacker/eor
[4] http://21cma.bao.ac.cn
[5] http://www.reionization.org
[6] http://lwa.unm.edu
[7] http://www.lofar.org

tions as an approximation to the original objective function's gradient. At the initial iterations, when the parameters are far from the optimum point, these approximations are quite reasonable since the gradient is only an approximation at those stages. Thus, they can be efficient substitutions for the gradient of the original cost function and considerably accelerate the computations of the OS algorithm. However, it must be taken into account that the highest accuracy that OS methods can achieve is the same as the one which could be obtained by the conventional (non-OS) techniques. Close to the optimal solution, OS methods generally do not converge but rather become stuck at a sub-optimal limit cycle of as many points as there are sub-objective functions. Therefore, if OS method becomes globally convergent (Ahn, 2004; Hudson & Larkin, 1994), it maintains exactly the same accuracy of the convergent non-OS methods.

This chapter is organized as follows: In sections 3.2 and 3.3, we present the general data model of radio interferometric calibration and the classical LS and SAGE calibration techniques. In section 3.4, we introduce the OS-LS and OS-SAGE calibration techniques in order to cut down the processing time of the conventional LS and SAGE calibration methods. The computational advantages of applying the OS type calibrations instead of the conventional methods are also shown. For the ML estimations, the LM method is applied. At the end of section 3.4, we show an application of OS calibration to accelerate computations when calibrating for an individual data sample. The technique is based on partitioning data over baselines and hence could also be useful in speeding up the calibration procedure of radio telescopes with a large number of receivers. In section 3.5, we give results based on simulations to demonstrate the superior convergence rate of the OS calibration schemes compared to the non-OS ones. Finally, we draw our conclusions in section 3.6.

The following notations are used in this chapter: Bold, lowercase letters refer to column vectors, e.g., $\mathbf{y}$. Upper case bold letters refer to matrices, e.g., $\mathbf{C}$. The transpose, Hermitian transpose, and conjugation of a matrix are presented by $(.)^T$, $(.)^H$, and $(.)^*$, respectively. The matrix Kronecker product is denoted by $\otimes$. $\mathbb{R}$ is the set of Real numbers. $\mathrm{E}\{\}$ denotes the statistical expectation operator. The real and imaginary parts of complex quantities are shown by $\mathfrak{Re}$ and $\mathfrak{Im}$, respectively.

3.2 Calibration Data Model

In this section, the general measurement equation of a polarimetric radio interferometer is presented. For some introduction to radio polarimetry and calibration the reader is referred to Hamaker et al. (1996) and Hamaker (2006).

Consider a radio interferometer with N antennas which observes K uncorrelated sources. The induced voltage at antenna p, $\tilde{\mathbf{v}}_{pl}$, due to radiation of the l-th source, $\mathbf{e}_l$, is given by $\tilde{\mathbf{v}}_{pl} = \tilde{\mathbf{J}}_{pl}\mathbf{e}_l$ where $\tilde{\mathbf{J}}_{pl}$ is the complex 2×2 Jones matrix (Hamaker et al., 1996) corresponding to the sky and instrumental corruptions of the signal.
The total signal obtained at antenna p, $\mathbf{v}_p$, is a linear superposition of K such signals plus the antenna's thermal noise. After correcting for geometric delays and the instrumental effects, the p-th antenna voltage is correlated with the other $N-1$ antennas voltages. The correlated voltages $\mathrm{E}\{\mathbf{v}_p\mathbf{v}_q^H\}$, referred to as *visibility* (Hamaker et al., 1996) of baseline $p-q$ is given by

$$\mathbf{V}_{pq} = \mathrm{E}\{\mathbf{v}_p\mathbf{v}_q^H\} = \mathbf{G}_p\left(\sum_{l=1}^{K}\mathbf{J}_{pl}\mathbf{C}_l\mathbf{J}_{ql}^H\right)\mathbf{G}_q^H + \mathbf{N}_{pq}, \tag{3.1}$$

where $\mathbf{N}_{pq}$ is the baseline's additive noise and $\mathbf{C}_l = \mathrm{E}\{\mathbf{e}_l\mathbf{e}_l^H\}$ is the l-th source *coherency* matrix (Born & Wolf, 1999; Hamaker et al., 1996). The errors common to all directions (mainly the receiver delay and amplitude errors) are given by $\mathbf{G}_p$ and $\mathbf{G}_q$. We assume that an initial calibration, at a finer time and frequency resolution, is performed to estimate $\mathbf{G}_p$-s (direction independent effects). Then, the corrected data is obtained as

$$\widetilde{\mathbf{V}}_{pq} = \mathbf{G}_p^{-1}\mathbf{V}_{pq}\mathbf{G}_q^{-H}, \tag{3.2}$$

where $\widetilde{\mathbf{V}}_{pq}$ are the visibilites after correction for effects common to all directions. The remaining errors are unique to a given direction, but residual errors in $\mathbf{G}_p$-s are also absorbed into these errors, which are denoted by $\mathbf{J}_{pl}$ in the usual notation. The vectorized form of corrected visibilities are given by

$$\mathbf{v}_{pq} \equiv \mathrm{vec}(\widetilde{\mathbf{V}}_{pq}) = \sum_{l=1}^{K} \mathbf{s}_{pql} + \mathbf{n}_{pq}, \tag{3.3}$$

where $\mathbf{s}_{pql} = \mathbf{J}_{ql}^* \otimes \mathbf{J}_{pl}\mathrm{vec}(\mathbf{C}_l)$ and $\mathbf{n}_{pq} = \mathrm{vec}(\mathbf{G}_p^{-1}\mathbf{N}_{pq}\mathbf{G}_q^{-H})$. The unknowns of the calibration problem are the real and imaginary parts of the Jones matrices complex elements

$$\boldsymbol{\theta} = [\mathrm{vec}(\mathfrak{Re}\{\mathbf{J}_{11}\})^T\ \mathrm{vec}(\mathfrak{Im}\{\mathbf{J}_{11}\})^T\ \mathrm{vec}(\mathfrak{Re}\{\mathbf{J}_{12}\})^T \ldots]^T,$$

and therefore, $\boldsymbol{\theta} \in \mathbb{R}^{8KN\times 1}$.

Consider a dataset of τ time and frequency samples that form a small enough time and frequency interval over which $\boldsymbol{\theta}$ is invariant. Stacking up the real and imaginary parts of the instrument's visibilities and noise vectors in $\mathbf{y} = [\mathfrak{Re}\{\mathbf{v}_{12}^T\}\ \mathfrak{Im}\{\mathbf{v}_{12}^T\}\ \mathfrak{Re}\{\mathbf{v}_{13}^T\}\ \ldots]^T$ and $\mathbf{n} = [\mathfrak{Re}\{\mathbf{n}_{12}^T\}\ \mathfrak{Im}\{\mathbf{n}_{12}^T\}\ \mathfrak{Re}\{\mathbf{n}_{13}^T\}\ \ldots]^T$, respectively, the general measurement equation becomes

$$\mathbf{y} = \sum_{l=1}^{K} \mathbf{s}_l(\boldsymbol{\theta}) + \mathbf{n}. \tag{3.4}$$

In (3.4), $\mathbf{s}_l(\boldsymbol{\theta}) = [\mathfrak{Re}\{\mathbf{s}_{12l}^T\}\ \mathfrak{Im}\{\mathbf{s}_{12l}^T\}\ \mathfrak{Re}\{\mathbf{s}_{13l}^T\}\ \ldots]^T$. $\mathbf{y}$, $\mathbf{n}$, and $\mathbf{s}_l$ are vectors of size $4\tau N(N-1)$, and the noise vector $\mathbf{n}$ is assumed to be white Gaussian. Calibration is the ML estimation of the unknown parameter vector $\boldsymbol{\theta}$ from (3.4). Note that calibration methods could also be applied to the uncorrected visibilities of (3.1) to estimate $\mathbf{G}_p$ and $\mathbf{G}_q$ errors as well. Moreover, having a large enough N and small enough K, there will be enough constrains to solve for the $8KN$ unknown parameters of $\boldsymbol{\theta}$ using the $4\tau N(N-1)$ measurements of $\mathbf{y}$.

3.3 The LS and SAGE Calibration Methods

In this section, both the LS and SAGE calibration algorithms are briefly outlined. The OS scheme is applied to both methods.

3.3.1 LS calibration

Since the noise vector $\mathbf{n}$ in the calibration data model (3.4) is assumed to be white Gaussian, LS calibration method estimates the ML estimate of $\boldsymbol{\theta} \in \mathbb{R}^{8KN\times 1}$ by minimizing the sum of squared errors:

$$\widehat{\boldsymbol{\theta}} = \arg\min_{\boldsymbol{\theta}} ||\mathbf{y} - \textstyle\sum_{l=1}^{K} \mathbf{s}_l(\boldsymbol{\theta})||^2. \tag{3.5}$$

Gradient-based optimization techniques are used for solving (3.5). Among those, the LM method (Marquardt, 1963; Levenberg, 1944) is one of the most robust in the sense that it mostly converges to a global optimum. Defining the cost function $\phi(\boldsymbol{\theta}) = \mathbf{y} - \sum_{l=1}^{K} \mathbf{s}_l(\boldsymbol{\theta})$, where $\phi(\boldsymbol{\theta}) \in \mathbb{R}^{4\tau N(N-1)\times 1}$, and initializing the starting point $\widehat{\boldsymbol{\theta}}^1$, the LS calibration method via LM algorithm is outlined as follows:

for every iteration $k = 1, 2, \ldots$ until an upper limit or convergence of $\widehat{\boldsymbol{\theta}}^k$,

Calculate $\widehat{\boldsymbol{\theta}}^{k+1} \in \mathbb{R}^{8KN\times 1}$ using LM algorithm as

$$\widehat{\boldsymbol{\theta}}^{k+1} = \widehat{\boldsymbol{\theta}}^{k} - (\nabla_{\boldsymbol{\theta}}^T \nabla_{\boldsymbol{\theta}} + \lambda \mathbf{H})^{-1} \nabla_{\boldsymbol{\theta}}^T \phi(\boldsymbol{\theta})|_{\widehat{\boldsymbol{\theta}}^k}. \tag{3.6}$$

endfor

In (3.6), $\nabla_{\boldsymbol{\theta}} = \frac{\partial}{\partial \boldsymbol{\theta}} \phi(\boldsymbol{\theta})$, λ is the damping factor (Lampton, 1997), and $\mathbf{H} = \text{diag}(\nabla_{\boldsymbol{\theta}}^T \nabla_{\boldsymbol{\theta}})$ is the diagonal of the Hessian matrix. The sizes of the Jacobian $\nabla_{\boldsymbol{\theta}}$ and the linear system solved in (3.6) are $4\tau N(N-1) \times 8KN$ and $8KN$, respectively. Consequently, the cost of computing $\nabla_{\boldsymbol{\theta}}^T \nabla_{\boldsymbol{\theta}}$ is $\mathcal{O}((8KN)^2 \times 4\tau N(N-1))$. Therefore, since at every iteration all the $8KN$ parameters of $\boldsymbol{\theta}$ are simultaneously updated, LS calibration has a very low speed of convergence. Furthermore, estimating a large number of unknowns, the Jacobian computation also becomes considerably costly.

3.3.2 SAGE calibration

In the case of solving for multiple sources in the sky, the SAGE calibration algorithm (Kazemi et al. (2011); Yatawatta et al. (2009), chapter 2) has a significantly improved computational cost and convergence rate compared to the LS calibration. The key point is that, in general, the SAGE algorithm (Fessler & Hero, 1994) partitions the complete data space to smaller "hidden" data spaces and estimates parameters in them rather than in the complete data space. Applying the SAGE algorithm to the calibration problem, the contribution of every l-th source in the observation is assumed to depend only on a subset of parameters, $\boldsymbol{\theta}_l \in \mathbb{R}^{8N\times 1}$. Therefore, the parameter vector $\boldsymbol{\theta} \in \mathbb{R}^{8KN\times 1}$ could be partitioned for different directions (sources) in the sky as

$$\boldsymbol{\theta} = [\boldsymbol{\theta}_1^T \; \boldsymbol{\theta}_2^T \ldots \boldsymbol{\theta}_K^T]^T.$$

This partitioning is justifiable when the sources are sufficiently separated from each other. Initializing a starting parameter vector $\widehat{\boldsymbol{\theta}}^1$, where $\widehat{\boldsymbol{\theta}}^k$ denotes the estimate of $\boldsymbol{\theta}$ obtained at the k-th iteration, SAGE calibration algorithm is executed as follows:

for every iteration $k = 1, 2, \ldots$ until an upper limit for k or convergence of $\widehat{\boldsymbol{\theta}}^k$:

for all or some $l \in \{1, 2, \ldots, K\}$, update the l-th source parameters $\boldsymbol{\theta}_l \in \mathbb{R}^{8N\times 1}$:

1. Define the hidden data space as

$$\mathbf{x}_l = \mathbf{s}_l(\boldsymbol{\theta}_l) + \mathbf{n} \in \mathbb{R}^{4\tau N(N-1)\times 1}. \tag{3.7}$$

Thus, the observed data $\mathbf{y} \in \mathbb{R}^{4\tau N(N-1)\times 1}$ is given by

$$\mathbf{y} = \mathbf{x}_l + \sum_{\substack{z=1 \\ z\neq l}}^{K} \mathbf{s}_z(\boldsymbol{\theta}_z). \tag{3.8}$$

2. *SAGE E Step*: Calculate the conditional mean $\widehat{\mathbf{x}}_l^k = \mathrm{E}\{\mathbf{x}_l|\mathbf{y}, \widehat{\boldsymbol{\theta}}^k\}$ as

$$\widehat{\mathbf{x}}_l^k = \mathbf{s}_l(\widehat{\boldsymbol{\theta}}_l^k) + (\mathbf{y} - \sum_{z=1}^{K} \mathbf{s}_z(\widehat{\boldsymbol{\theta}}_z^k)) = \mathbf{y} - \sum_{\substack{z=1 \\ z\neq l}}^{K} \mathbf{s}_z(\widehat{\boldsymbol{\theta}}_z^k).$$

3. *SAGE M Step*: Estimate

$$\widehat{\boldsymbol{\theta}}_l^{k+1} = \arg\min_{\boldsymbol{\theta}_l} |||[\widehat{\mathbf{x}}_l^k - \mathbf{s}_l(\boldsymbol{\theta}_l)]|||^2,$$

by the LM method as

$$\widehat{\boldsymbol{\theta}}_l^{k+1} = \widehat{\boldsymbol{\theta}}_l^k - (\nabla_{\boldsymbol{\theta}_l}^T \nabla_{\boldsymbol{\theta}_l} + \lambda \mathbf{H})^{-1} \nabla_{\boldsymbol{\theta}_l}^T \phi(\boldsymbol{\theta}_l)|_{\widehat{\boldsymbol{\theta}}_l^k}, \tag{3.9}$$

where $\phi(\boldsymbol{\theta}_l) = [\widehat{\mathbf{x}}_l^k - \mathbf{s}_l(\boldsymbol{\theta}_l)] \in \mathbb{R}^{4\tau N(N-1)\times 1}$.

endfor

endfor

Based on the above, at every k-th iteration, SAGE method alternates between updating parameters of some or all the sources, $l \in \{1, 2, \ldots, K\}$. Calculating the ML estimate of $\boldsymbol{\theta}_l \in \mathbb{R}^{8N\times 1}$ in (3.9), instead of the ML estimate of all parameters $\boldsymbol{\theta} \in \mathbb{R}^{8KN\times 1}$ as in (3.6), it has been proved that the SAGE algorithm benefits from an accelerated convergence rate (Fessler & Hero, 1994) compared to the LS method. The sizes of the Jacobian $\nabla_{\boldsymbol{\theta}_l}$ and the linear system solved in (3.9) are $4\tau N(N-1) \times 8N$ and $8N$, respectively. In addition, the cost of computing $\nabla_{\boldsymbol{\theta}_l}^T \nabla_{\boldsymbol{\theta}_l}$ is $\mathcal{O}((8N)^2 \times 4\tau N(N-1))$. Thus, applying LM algorithm for estimating $\boldsymbol{\theta}_l$ from (3.9), the computational expense of the SAGE calibration is much cheaper compared to the LS calibration.

Note that in the SAGE calibration, instead of partitioning the parameters of the individual sources, one could also make partitions including more than a single source sharing common parameters (Kazemi et al. (2013b), chapter 4). This is more efficient when some sources have a small angular separation from each other in the sky and hence share some parameters.

3.4 The OS-LS and OS-SAGE Calibration Methods

In this section, OS-LS (Liu L. & B., 2005) and OS-SAGE (Hongqing et al., 2004) calibration algorithms, combinations of Ordered-Subsets (OS) algorithm with LS and SAGE calibration methods, are introduced to speed up the conventional LS and SAGE calibration procedures.

Ordered-Subsets (OS) algorithm is applied to those optimization problems with a cost function that can be expressed as a sum of several other cost functions for accelerating the convergence rate. The solutions obtained by the OS method attain almost the same accuracy as those obtained by the non-OS optimization methods in a fraction of the time (Hudson & Larkin, 1994). The key idea is to consider the Jacobian of one, or some, sub-cost functions as an approximate gradient of the original cost function. These approximations are quite reasonable when one is far from the optimal point, and provide OS method with a very fast convergence rate. However, at later iterations and when the parameters are close to the global optimum, the approximations restrict the

OS method to a sub-optimal limit cycle (the optima of the individual sub-observations which are processed in OS iterations). Therefore, the OS method does not converge globally (Ahn, 2004).

Denote the visibility vectors of the τ time and frequency samples that have the fixed gain errors $\boldsymbol{\theta} \in \mathbb{R}^{8KN\times 1}$ by $\mathbf{y}_1, \mathbf{y}_2, \ldots, \mathbf{y}_\tau$, where $\mathbf{y}_t \in \mathbb{R}^{4N(N-1)\times 1}$, for $t \in \{1, 2, \ldots, \tau\}$. Since the noise vectors of the samples are statistically independent from each other, calibration problem could be restated as

$$\widehat{\boldsymbol{\theta}} = \arg\max_{\boldsymbol{\theta}} \prod_{t=1}^{\tau} f_t(\mathbf{y}_t;\boldsymbol{\theta}) = \arg\max_{\boldsymbol{\theta}} \sum_{t=1}^{\tau} \mathcal{L}_t(\boldsymbol{\theta}|\mathbf{y_t}), \tag{3.10}$$

where f_t and $\mathcal{L}_t$ are the probability density and the log-likelihood functions for the visibility vector $\mathbf{y}_t$, respectively. The OS algorithm is applied for accelerating the maximization of this sum of log-likelihood functions. Supposing that the following Jacobian equivalence conditions hold

$$\nabla_{\boldsymbol{\theta}}\mathcal{L}_1 \cong \nabla_{\boldsymbol{\theta}}\mathcal{L}_2 \cong \ldots \cong \nabla_{\boldsymbol{\theta}}\mathcal{L}_\tau, \tag{3.11}$$

then the OS method sequentially updates the parameters $\boldsymbol{\theta}$ for one or some visibility vectors $\mathbf{y}_t$ (sub-observations). The solution of every sub-observation is used as the starting point of the next sub-observation. Since each sub-cost function $\mathcal{L}_t$ involves a subset of data, $\mathbf{y}_t$, which is independent from the others, the method is named "ordered subsets". Sub-observations might be ordered for updating by some scheme that gives preferences to the data items, or, as in this work, in random. An introduction to the OS algorithm is presented by Ahn (2004). In the following, the OS-LS and OS-SAGE methods are outlined. Note that the size of sub-observations $\mathbf{y}_t$-s must be grater than or equal to the number of unknown parameters in $\boldsymbol{\theta}$.

3.4.1 OS-LS calibration

In the presented OS-LS calibration, the LM method is selected as the gradient-based ML estimation algorithm of the LS calibration. Starting with an initial suggestion $\widehat{\boldsymbol{\theta}}^1 \in \mathbb{R}^{8KN\times 1}$, OS-LS is executed as:

for every iteration $k = 1, 2, \ldots$ until an upper limit or convergence of $\widehat{\boldsymbol{\theta}}^k$, run m *OS iterations*:

for some or all sub-observation $\{\mathbf{y}_t | t = 1, \ldots, m \leq \tau\}$:

Select $\boldsymbol{\theta}^k = \widehat{\boldsymbol{\theta}}^t$, and calculate

$$\boldsymbol{\theta}^{k+1} = \boldsymbol{\theta}^k - (\nabla_{\boldsymbol{\theta}}^T \nabla_{\boldsymbol{\theta}} + \lambda \mathbf{H})^{-1} \nabla_{\boldsymbol{\theta}}^T \phi(\boldsymbol{\theta})|_{\boldsymbol{\theta}^k}, \tag{3.12}$$

where $\phi(\boldsymbol{\theta}) = [\mathbf{y}_t - \sum_{l=1}^{K} \mathbf{s}_l(\boldsymbol{\theta})] \in \mathbb{R}^{4N(N-1)\times 1}$.

Select $\widehat{\boldsymbol{\theta}}^{(t \bmod m)+1} = \boldsymbol{\theta}^{k+1}$ for the next sub-observation.

endfor

endfor

As given above, at every LM iteration, parameters are sequentially updated for some or all sub-observations. The sizes of the Jacobian $\nabla_{\boldsymbol{\theta}}$ and the linear system solved in (3.12) are $4N(N -$

$1) \times 8KN$ and $8KN$, respectively. Moreover, the cost of computing $\nabla_{\boldsymbol{\theta}}^T \nabla_{\boldsymbol{\theta}}$ is $\mathcal{O}((8KN)^2 \times 4N(N-1))$. When (3.11) holds, the Jacobian is calculated only for one, or a few, number of sub-observations per iteration and hence, the OS-LS method's convergence rate is considerably increased compared to the LS method.

3.4.2 OS-SAGE calibration

In this section, the OS-SAGE calibration method is introduced. A similar OS-SAGE technique is used for positron emission tomography (PET) by Hongqing et al. (2004).

Initializing $\widehat{\boldsymbol{\theta}}^1 \in \mathbb{R}^{8N\times 1}$, OS-SAGE is outlined as follows:

for every $k = 1, 2, \ldots$ until an upper limit for k or convergence of $\widehat{\boldsymbol{\theta}}^k$, execute m *OS iterations*:

for some or all sub-observations $\{\mathbf{y}_t | t = 1, \ldots, m \leq \tau\}$:

Select $\boldsymbol{\theta}^k = \widehat{\boldsymbol{\theta}}^t$.

for all or some $l \in \{1, 2, \ldots, K\}$, update the l-th source parameters $\boldsymbol{\theta}_l \in \mathbb{R}^{8N\times 1}$:

1. Define
$$\mathbf{y}_t = \mathbf{x}_l + \sum_{\substack{z=1 \\ z\neq l}}^{K} \mathbf{s}_z(\boldsymbol{\theta}_z), \quad \mathbf{x}_l = \mathbf{s}_l(\boldsymbol{\theta}_l) + \mathbf{n}.$$

2. *SAGE E Step*: Calculate $\widehat{\mathbf{x}}_l^k = \mathrm{E}\{\mathbf{x}_l | \mathbf{y}_t, \boldsymbol{\theta}^k\}$ as
$$\widehat{\mathbf{x}}_l^k = \mathbf{y}_t - \sum_{\substack{z=1 \\ z\neq l}}^{K} \mathbf{s}_z(\boldsymbol{\theta}_z^k), \ \mathbf{y}_t \in \mathbb{R}^{4N(N-1)\times 1}.$$

3. *SAGE M Step*: Similar to (3.9), estimate
$$\boldsymbol{\theta}_l^{k+1} = \arg\min_{\boldsymbol{\theta}_l} |||[\widehat{\mathbf{x}}_l^k - \mathbf{s}_l(\boldsymbol{\theta}_l)]|||^2,$$
using the LM method, by
$$\boldsymbol{\theta}_l^{k+1} = \boldsymbol{\theta}_l^k - (\nabla_{\boldsymbol{\theta}_l}^T \nabla_{\boldsymbol{\theta}_l} + \lambda \mathbf{H})^{-1} \nabla_{\boldsymbol{\theta}_l}^T \phi(\boldsymbol{\theta}_l)|_{\boldsymbol{\theta}_l^k} \tag{3.13}$$

endfor

Select $\widehat{\boldsymbol{\theta}}^{(t \bmod m)+1} = \boldsymbol{\theta}^{k+1}$ for the next sub-observation.

endfor

endfor

OS method reduces the data size from $4\tau N(N-1)$ to $4N(N-1)$, since it calculates the partial gradients for sub-observations $\mathbf{y}_t \in \mathbb{R}^{4N(N-1)\times 1}$, $t \in \{1, 2, \ldots, \tau\}$, instead of the whole observed data $\mathbf{y} \in \mathbb{R}^{4\tau N(N-1)\times 1}$. Thus, the size of the Jacobian $\nabla_{\boldsymbol{\theta}_l}$, where $\phi(\boldsymbol{\theta}_l) = [\widehat{\mathbf{x}}_l^k - \mathbf{s}_l(\boldsymbol{\theta}_l)] \in \mathbb{R}^{4N(N-1)\times 1}$, calculated by LM method for every OS iteration of the OS-SAGE

calibration at (3.13), is $4N(N-1) \times 8N$. The size of the linear system solved in (3.13) is $8N$ and the cost of computing $\nabla_{\boldsymbol{\theta}_l}^T \nabla_{\boldsymbol{\theta}_l}$ is $\mathcal{O}((8N)^2 \times 4N(N-1))$. When $m \ll \tau$, the OS-SAGE method converges much faster than the conventional SAGE algorithm for which the Jacobian size is $4\tau N(N-1) \times 8N$. On the other hand, for every t-th OS iteration, the updated result of the $(t-1)$-th sub-observation is used as the starting point. Every OS-SAGE iteration includes m number of SAGE iterations. Therefore, at initial iterations when (3.11) holds, OS-SAGE algorithm increases the likelihood function as equivalent to SAGE method with m iterations. Thus, the convergence of OS-SAGE compared with SAGE is accelerated.

3.4.3 Partitioning the baselines

So far, we have divided the data into sub-observations only based on their integration time and frequency. However, there are cases in which we need to calibrate for a single time and frequency interval. For instance, consider calibrating only for the i-th time and frequency interval when $1 \leq i \leq \tau$. To apply OS calibration to such a case, one can define sub-observations by partitioning the data vector $\mathbf{y}_i$ over the instrument's baselines as,

$$\mathbf{y}_i = [\mathbf{y}_{i1}^T \; \mathbf{y}_{i2}^T \; \dots \mathbf{y}_{iB}^T]^T, \quad B \ll \frac{N(N-1)}{2}.$$

Then, similar to (3.11), the calibration problem becomes

$$\widehat{\boldsymbol{\theta}} = \arg\max_{\boldsymbol{\theta}} \sum_{b=1}^{B} \mathcal{L}_b(\boldsymbol{\theta}|\mathbf{y}_{ib}), \tag{3.14}$$

for which OS methods presented by sections 3.4.1 and 3.4.2 are applicable, and where *OS iterations* are executed over $\{\mathbf{y}_{ib}|b = 1, \dots, m \leq B\}$. Utilizing such an OS calibration could also be beneficial in cutting down the computational expense of calibration of interferometers with a large number of receivers. The only points that should be taken into account are:

- Every partition of data (sub-observation) $\mathbf{y}_{ib}$, for $b \in \{1, 2, \dots, B\}$, must have visibilities from different baselines such that the baselines cover all the receivers of the instrument (or all the parameters).
- The number of visibilities of every sub-observation must be equal to, or larger than, the number of calibration unknowns,

$$||\mathbf{y}_{ib}||_1 \geq 8KN. \tag{3.15}$$

3.4.4 Discussion

To wrap up all the discussed calibration algorithms, we present a general overview in Fig. 3.1. Fig. 3.1 illustrates LS, SAGE, OS-LS, and OS-SAGE calibrations algorithms.

Note that:

- As it is discussed at the beginning of this section 3.4, the OS algorithms do not necessarily converge. Nevertheless, there exist two major approaches in dealing with the convergence

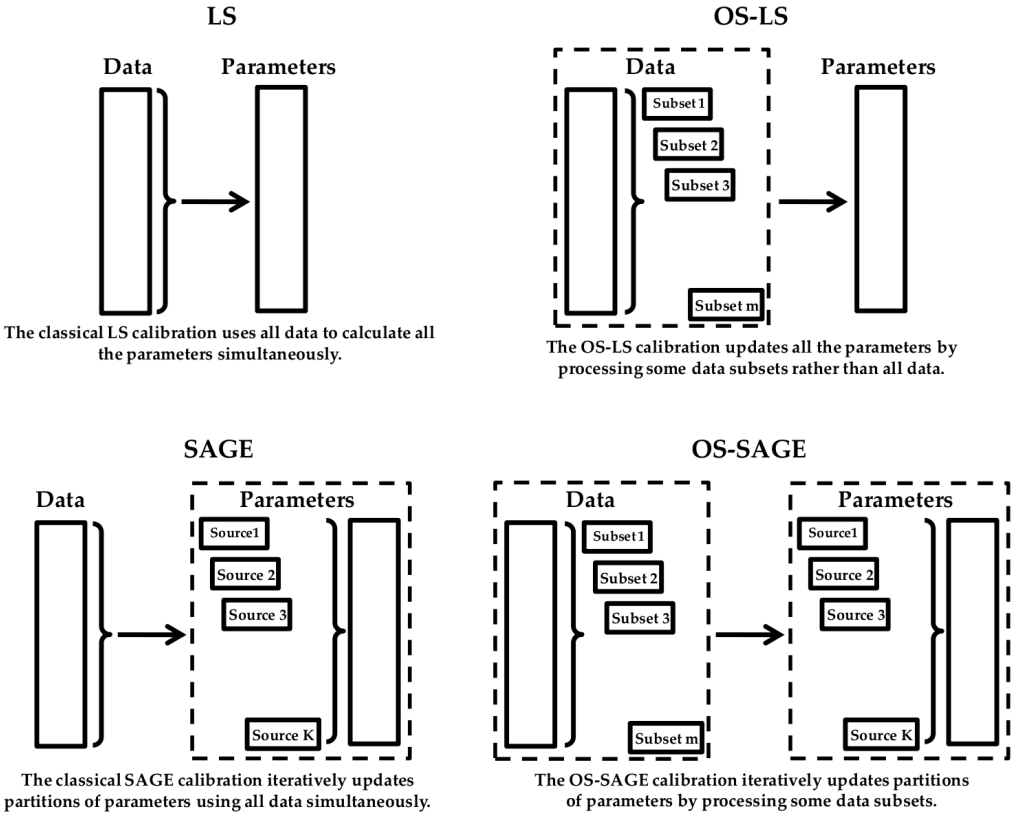

Figure 3.1: Diagrams illustrating LS, SAGE, OS-LS, and OS-SAGE calibrations algorithms.

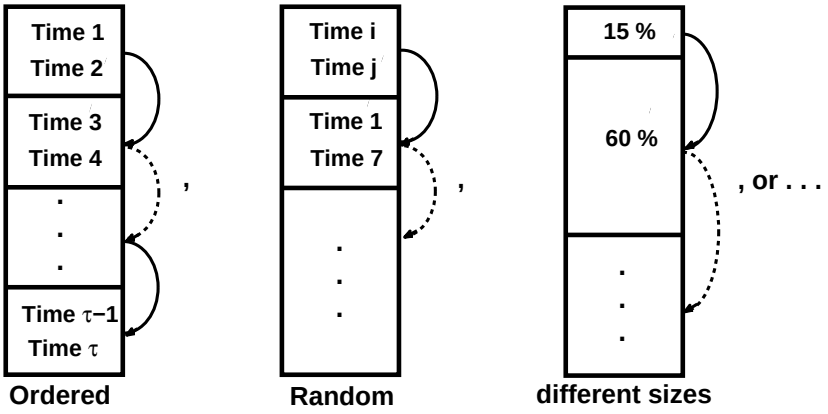

Figure 3.2: Instead of running the OS method on every individual sub-observation, one could also apply the method to combinations of two or more sub-observations to improve the Signal to Noise Ratio (SNR). Examples of having incrementally ordered datasets of size two, randomly chosen datasets of the same size, and randomly chosen datasets from different sizes, are shown from left to right, respectively.

problem of the OS method: (i) using relaxation parameters (stepsizes) (Ahn, 2004). Calculating suitable relaxation parameters per every iteration is considerably costly. That makes the approach of progressively decreasing the number of sub-observations in OS method to be preferable. (ii) Reducing the number of subsets with increasing iterations until the complete dataset estimate is reconstructed (Hudson & Larkin, 1994). In the OS method, one can incrementally combine some sub-observations together until there are no individual sub-observations remaining. Therefore, at the final iteration, the OS method is in fact changed to the non-OS technique which is used for the ML approximations, solving for the complete dataset. This approach guarantees global convergence as long as the non-OS ML estimation techniques (LS, SAGE, etc.) converge. However, it must be taken into account that the highest accuracy achievable by the proposed scheme is equal to any non-OS optimization methods. Modifying OS calibration in order to achieve an accuracy superior to the ones obtained by non-OS calibrations is addressed in future work.

- When the Signal to Noise Ration (SNR) is poor, shifting to non-OS calibrations after running a few number of OS iterations is recommended.. Moreover, instead of running the OS method on every individual time and frequency sub-observation $\mathbf{y}_t$, for $t \in \{1, 2, \ldots, \tau\}$, one could also apply the method to combinations of two or more sub-observations to improve the SNR. Fig. 3.2 shows examples of having incrementally ordered datasets of size two, randomly chosen datasets of the same size, and randomly chosen datasets from different sizes, from left to right, respectively. The datasets could be arranged in different orders depending on the characteristics of specific observations. Similarly, subsets of frequency ordered sub-observations could be introduced.

- In the calibration data model presented by (3.4), we consider a very general form of the Jones matrices $\mathbf{J}$, as complex 2×2 matrices, and then search for the real and imaginary

parts of their elements which are collected in $\boldsymbol{\theta}$. However, one can use a more detailed presentation of the Jones matrices in the data model, for instance, when the elements of the Jones matrices are functions of time ζ and frequency ξ,

$$\mathbf{J} = \begin{bmatrix} \eta_1(\zeta,\xi) & \eta_2(\zeta,\xi) \\ \eta_3(\zeta,\xi) & \eta_4(\zeta,\xi) \end{bmatrix}. \tag{3.16}$$

Then, calibration is estimation of these functions, denoted by η in (3.16). But, this leads again to estimation of some constant parameters which define the functions. Therefore, OS calibration is also useful for such a case as well and its partitioning of data to time and frequency sub-observations would not cause any degradation of the accuracy of calibration.

3.5 Results

In this section, simulated data are used to compare the performance of LS and SAGE calibrations with OS-LS and OS-SAGE ones. Note that n in this section denotes the number of iterations of the conventional LS and SAGE methods. The implementation of the calibration algorithms are done using MATLAB software. The unit of color bars of all the images are in Jansky (Jy).

3.5.1 Simulations

A 12 hour observation of Westerbork Synthesis Radio Telescope (WSRT), including 14 receivers observing a sky with 50 sources, is simulated. Three sources are very bright with intensities 160, 107, and 108 Jy, and forty seven other sources are faint with intensities below 15 Jy. The source positions are following a uniform distribution. The Jones matrices are generated as multiplications of different linear combinations of sin and cos functions. Their gradients vary slowly (coherence time about three minutes) as a function of time such that on a few seconds time intervals the variation could be negligible. We keep the SNR $= 80$. The simulated single channel image at 355 MHz is shown in Fig. 3.3 in which the background faint sources are almost invisible.

We partition the simulated data to ten seconds time intervals, $\tau = 10$, including sub-observations obtained from ten individual seconds, for which the gain errors are assumed to be the same. Then, we calibrate the data partitions only for the three brightest sources via the LS and SAGE calibration methods. The residual images, obtained after $n = 9$ iterations, are presented in Fig. 3.4. As Fig. 3.4 shows, among those three subtracted bright sources, the central one is the best removed (slightly underestimated) by both SAGE and the LS calibration methods. The unsolved forty seven faint sources are also visible in both residual images. But, the two other bright sources are not subtracted perfectly (overestimated in the left and right sides and underestimated in the central parts). This problematic pattern is expected to be improved by increasing the number of iterations. There is no significant difference between the residual images produced by the LS and SAGE methods in Fig. 3.4. However, as it is shown in Table 3.1, the noise level in the residual image of the SAGE calibration is lower than the one of the LS method. Therefore, SAGE calibration reveals a superior performance compared to the LS calibration since it achieves more accurate results with a considerably less computational complexity (Kazemi et al. (2011), chapter 2).

The data is also calibrated by the OS-LS and OS-SAGE methods using $n = 9$ iterations. OS iterations are executed for $m = 1, 2$ number of sub-observations which are randomly chosen. The residual images after subtracting the three brightest sources are presented in Fig. 3.5. As Fig.

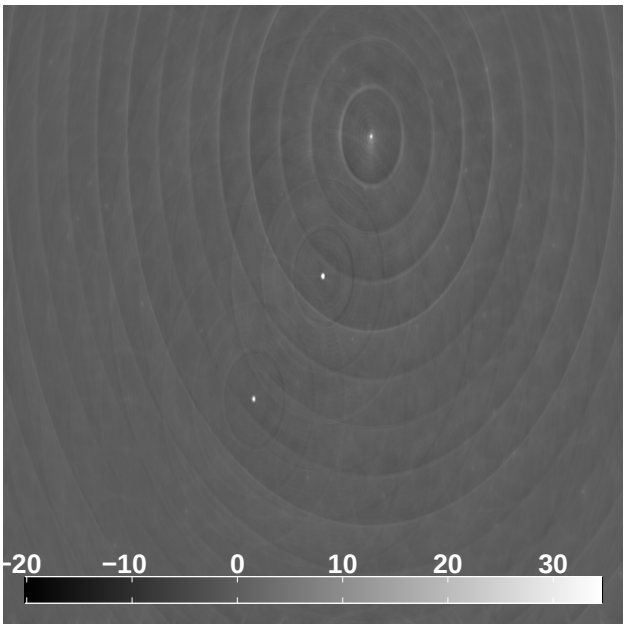

Figure 3.3: An 8×8 degrees WSRT 12 hour simulated observation of three bright sources, with intensities 160, 107, and 108 Jy, and forty seven faint sources, with intensities below 15 Jy. The frequency is 355 MHz and the SNR is eighty.

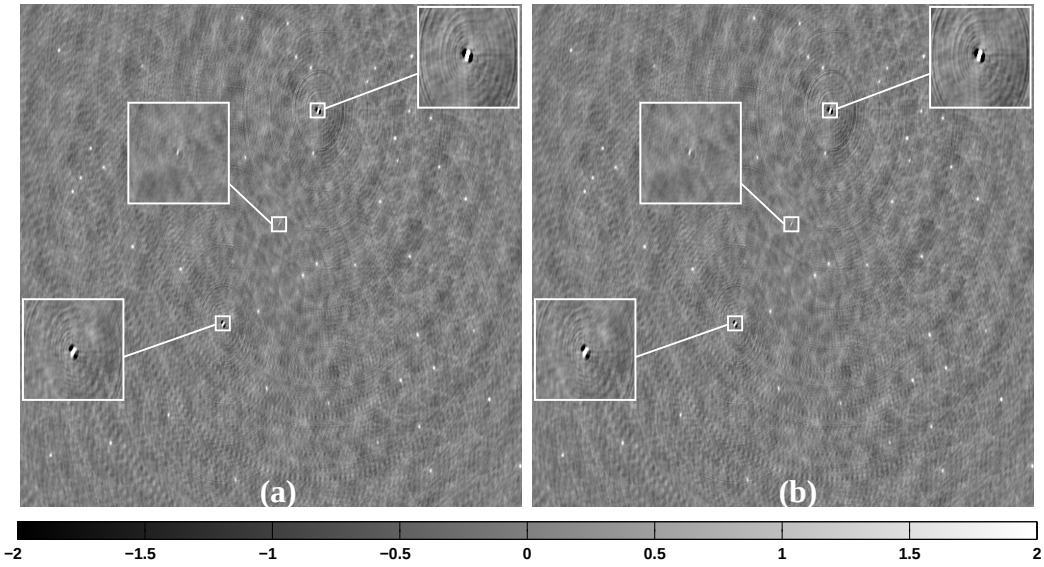

Figure 3.4: The residual images of the LS (a) and the SAGE (b) calibrations, solving only for the three brightest sources with $n = 9$ iterations. Calibrations are executed on every $\tau = 10$ sub-observations simultaneously. From the three subtracted sources, the central one is the best removed (slightly underestimated) by both the SAGE and the LS calibrations. The unsolved forty seven faint sources are also visible in both (a) and (b). However, the two other bright sources are not subtracted perfectly which is expected to be improved by increasing the number of iterations. The residual noise of the SAGE algorithm is lower than of the LS method (Table 3.1). This reveals the superior performance of the SAGE calibration compared to the LS calibration.

Table 1

m= number of OS iterations	LS		SAGE	
LS or SAGE iterations $n = 9$	Time [minutes]	Noise [mJy]	Time [minutes]	Noise [mJy]
OS, $m = 1$	41.3	234.2	9.7	226.1
OS, $m = 2$	75.5	232.9	20.4	225.7
Conventional methods	103.9	180.1	86.3	179.2

Table 3.1: Execution times of calibration (minutes) and the standard deviation of the residual noise (mJy). The OS calibrations perform much faster than the conventional LS and SAGE calibrations. The lowest execution time of the OS results are obtained for $m = 1$. On the other hand, the most accurate results are obtained for $m = 2$ number of OS iterations. Moreover, SAGE type calibrations is always preferred to the LS ones, having a higher accuracy and less computational complexity.

3.5 shows, the central source becomes problematic in the results of the OS calibrations and it was much better removed by the conventional LS and SAGE calibrations in Fig. 3.4. Except for this source, the OS calibrations have a similar quality in the residual images to the conventional LS and SAGE calibrations. The two other subtracted sources are not perfectly removed and the other forty seven faint sources are visible in the images, similar to Fig. 3.4. The residual images obtained for m=1 and m=2 OS iterations look almost the same. There is no significant improvement in the residual noise level when using $m = 2$ OS iterations instead of $m = 1$, as it is evident in Table 3.1. In this case, the OS calibration with m=1 OS iteration is preferable in comparison with m=2 since it carries a lower computational cost.

The calibrations execution times, in minutes, and the residual noise levels, in milliJansky (mJy), are presented in Table 3.1. Table 3.1 shows that the OS calibrations have a much faster processing speed compared to the conventional LS and SAGE calibrations. Among OS calibrations, the ones with a smaller number of OS iterations always have faster execution, as it is the case comparing the processing times for $m = 1$ to $m = 2$. The fastest execution speed of the calibration method belongs to the OS calibrations with $m = 1$ OS iteration. On the other hand, the OS calibrations including a large number of OS iterations usually produce more accurate solutions since they use a higher level of information in their computations. As the results of Table 3.1 demonstrate, the accuracy obtained by $m = 2$ number of OS iterations is slightly higher than the one achieved by $m = 1$. However, the use of $m = 1$ number of OS iterations is still preferred compared to $m = 2$ since it has a considerably lower processing time. Note that the use of the SAGE type calibration methods are always preferred compared to the LS ones, providing more accurate results in a lower processing time.

Fig. 3.6 illustrates the residual noise level achieved by the calibration procedures versus the number of iterations of the LS and SAGE methods, when it varies between one to nine, $n \in \{1, \ldots, 9\}$. The number of OS iterations are denoted by m. In the plots of Fig. 3.6, the residual noise levels of the OS calibrations are higher than the ones of the non-OS calibrations. However, it must be taken into account that these results are obtained by using a comparably less computational cost compared to the classical LS and SAGE calibrations. By increasing n, the result of SAGE calibrations are always better than the one of LS calibrations. Moreover, the accuracy of OS calibration using $m = 2$ OS iterations are also always superior to the results obtained

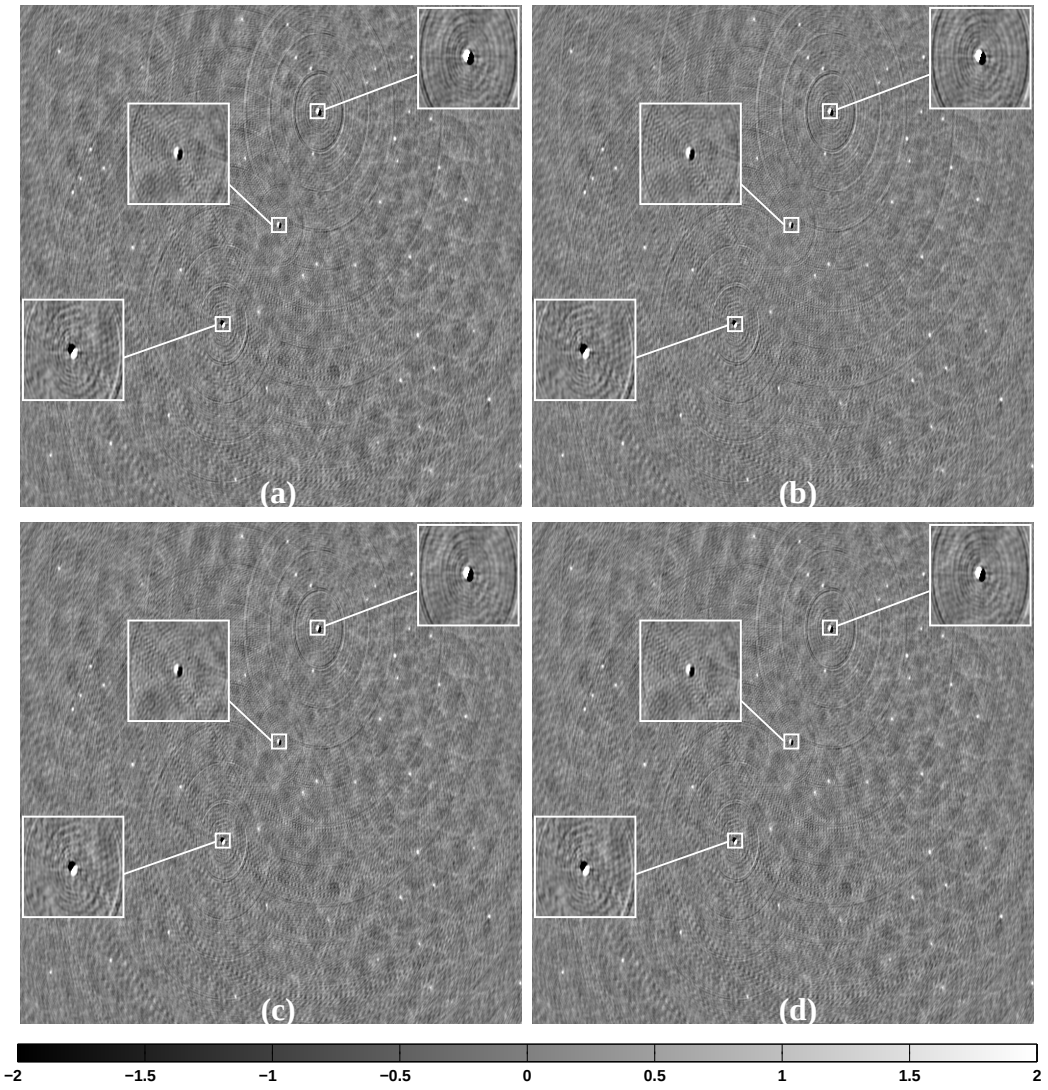

Figure 3.5: The residual images of the OS-LS calibration for m=1 (a) and m=2 (c), and the OS-SAGE calibration for m=1 (b) and m=2 (d) OS iterations. Calibrations are executed for the three brightest sources using $n = 9$ iterations. The central source is problematic in the residuals of the OS calibrations and was much better removed in the results of the conventional LS and SAGE calibrations presented in Fig. 3.4. Except for this source, the residual images obtained by the OS calibrations maintain the quality of the ones produced by the conventional LS and SAGE calibrations in Fig. 3.4. There is no visible difference between the results of m=1 and m=2 OS iterations in the images. That makes the OS calibration with m=1 OS iteration preferable in comparison with m=2 since it carries a lower computational cost.

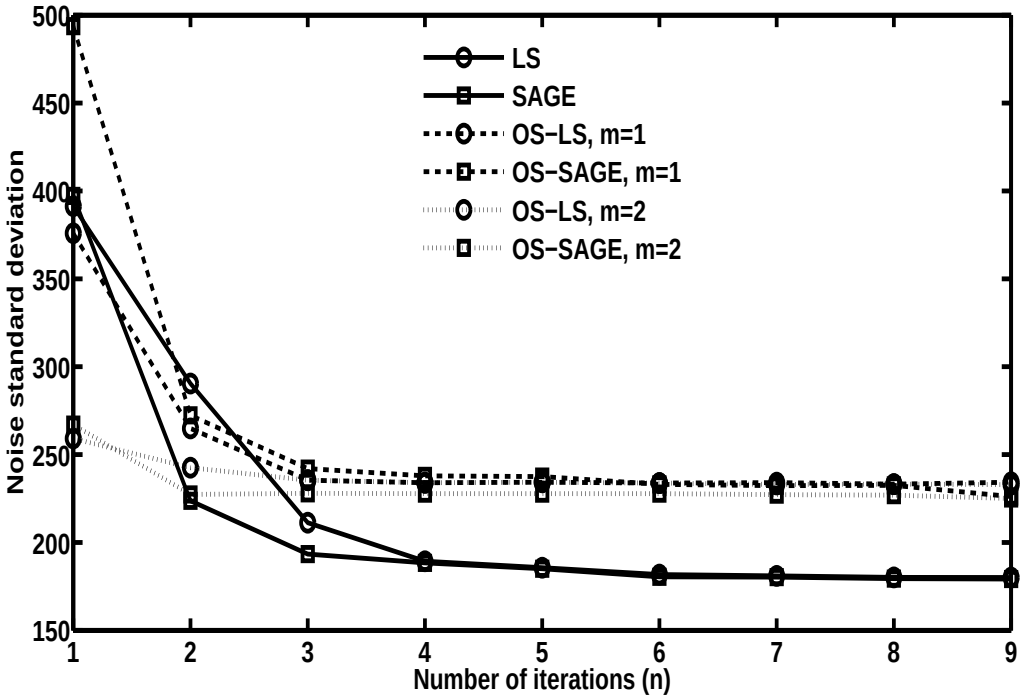

Figure 3.6: The residual noise standard deviations of the calibration methods in (mJy) versus their number of iterations which varies between one to nine, $n \in \{1, \ldots, 9\}$. The number of OS iterations are denoted by m. In the plots of Fig. 3.6, the residual noise levels of the OS calibrations are higher than the ones obtained by the non-OS calibrations. However, it must be taken into account that these results are generated spending a comparably less computational cost compared to the classical LS and SAGE calibrations. By increasing n, the result of SAGE calibrations are always better than of LS calibrations. Moreover, the accuracy of OS calibrations which use $m = 2$ OS iterations are superior to the one obtained by $m = 1$.

by $m = 1$.

As we have seen so far in this simulation, among the OS calibrations, the ones with a smaller number of OS iterations (smaller m) have a lower execution time. On the other hand, the OS calibrations including a large number of OS iterations usually produce more accurate solutions since they use a higher level of information in their computations of the Jacobian. However, the use of a small number of OS iterations is still preferable since it is considerably faster and applying a high enough number of calibration iterations, we would achieve the same accuracy as with large m.

In this section, we also demonstrate the applicability of the OS calibration in calibrating for a single time and frequency data sample, as it is discussed in section 3.4.3, where the data must be partitioned over the instrument's baselines. There are various ways of such a partitioning of visibilities among which we use the most efficient one for this specific simulation.

1. The first question is "*what is the maximum number of partitions of data over the baselines*

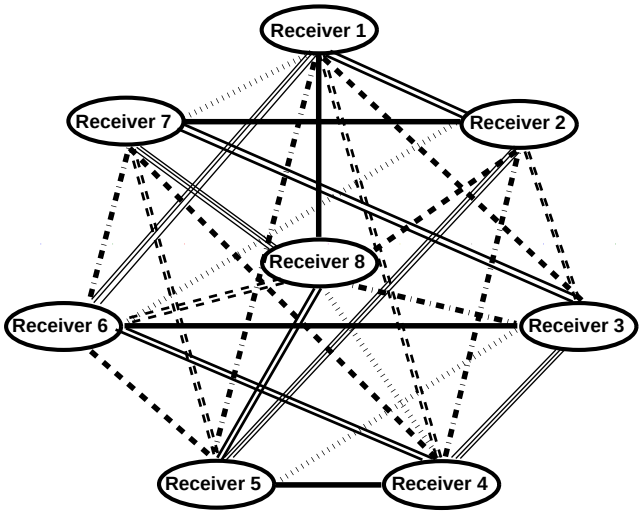

Figure 3.7: A complete graph of order eight, colored by $8-1=7$ number of colors. Every color covers all the nodes and $\frac{8}{2}=4$ number of edges.

that we can define such that the baselines of every single partition cover all the receivers of the interferometer?". The reason of searching the maximum is to get the highest level of information at every calibration's sub-observation later on. To answer this question, we use some well-known definitions of graph theory (Diestel, 2012) .
Consider the interferometer as a complete graph of order N [8] where the receivers and the baselines are the nodes and edges of the graph, respectively. Therefore, since in this simulation N is even, the answer to our question is the chromatic index of this graph which is qual to $N-1$. This means we can color the $\frac{N(N-1)}{2}$ edges of the graph by $N-1$ colors where every color is covering all the N nodes and $\frac{N}{2}$ number of edges. For instance, Fig. 3.7 shows a complete graph of order eight, colored by $8-1=7$ colors, where every color covers all the nodes by $\frac{8}{2}=4$ number of edges. We partition the visibilities based on the color of their corresponding baselines in the graph. Thus, at every partition, we have $\frac{N}{2}$ number of visibility matrices.

2. The second question is "*how many partitions should be collected at every OS calibration's sub-observation to ensure that (3.4) is not an under-determined system?*''. Every partition has $\frac{N}{2}$ of baselines and we are trying to estimate KN Jones matrices. Therefore, we must have at least x partitions at every OS calibration's sub-dataset where

$$x\frac{N}{2} > KN. \tag{3.17}$$

Thus,

$$x \geq 2K+1. \tag{3.18}$$

[8] A complete graph of order N has N nodes and every pair of nodes are connected to each other by a unique edge.

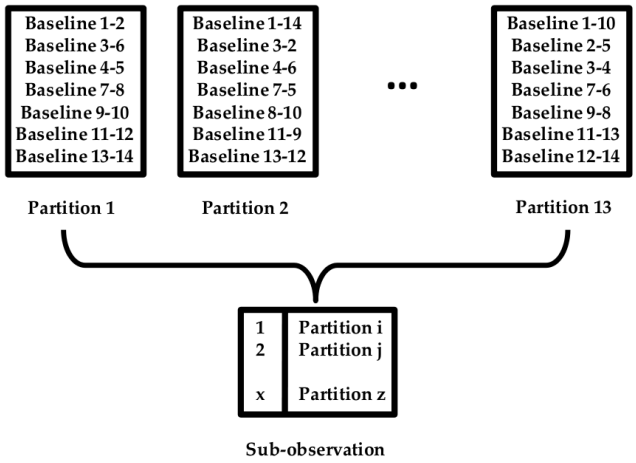

Figure 3.8: There are $N = 14$ number of receivers in WSRT and hence $N - 1 = 13$ number of partitions over its baselines, each including $\frac{N}{2} = 7$ number of visibilities and covering all the receivers. Every OS sub-observation consists of $x \leq 7$ number of such partitions. Thus, at every sub-observation we have $x \times \frac{N}{2}$ number of visibility matrices.

We have $N = 14$ number of receivers in WSRT. Thus, $\frac{N(N-1)}{2} = 91$ number of baselines, providing 2×2 visibility matrices, at every time and frequency sample. According to (i) we can make thirteen partitions of baselines so that every partition includes $\frac{N}{2} = 7$ number of visibilities covering all the receivers. Since we calibrate for $K = 3$ bright sources A, B, and C, using (ii), $x \geq 7$. This means at every OS sub-observation we must collect at least seven number of those partitions. Thus, at every sub-observation we have $x \times \frac{N}{2} = 49$ number of visibility matrices and that is enough for estimating $KN = 42$ number of Jones matrices. Indeed better accuracy of OS calibration is expected to be obtained by increasing x till $x \leq N - 1$. This approach of defining sub-observations of the OS calibration is demonstrated in Fig. 3.8. As this figure shows, there are no overlaps between the baselines of the thirteen different partitions. Therefore, the maximum information level, achievable by using $x \times \frac{N}{2} = 49$ number of visibilities, is provided for every sub-observation of the OS calibration.

OS-SAGE calibration is executed, using $m = 2$ number of time samples at every iteration (two number of OS iterations), for $x = 7$ and $x = 10$. The residual images are shown in Fig. 3.9. We can see that by increasing the number of visibilities in the sub-observations from forty nine ($x = 7$) to seventy ($x = 10$), the calibration accuracy is highly improved. We also can see that the two images of Fig. 3.9 have a higher residual noise and artifacts compared to the result obtained for $x = N - 1 = 13$, which is presented by Fig. 3.5 as image (d). This shows that better accuracy of the OS calibration is achieved when the number of visibilities in every sub-observation is large. However, the calibration's processing times for $x = 7$ and $x = 10$ are 73.5 and 92.8 minutes, respectively, while for $x = 13$ it is 108.8 minutes (Table 1). Remember that the whole point of partitioning the baselines was to cut down the computations. We also can benefit from this approach to speed up the initial calibration iterations for the telescope with a large number of baselines such as SKA.

As a final remark, for partiting baselines of a telescope with an odd number of receivers N, an

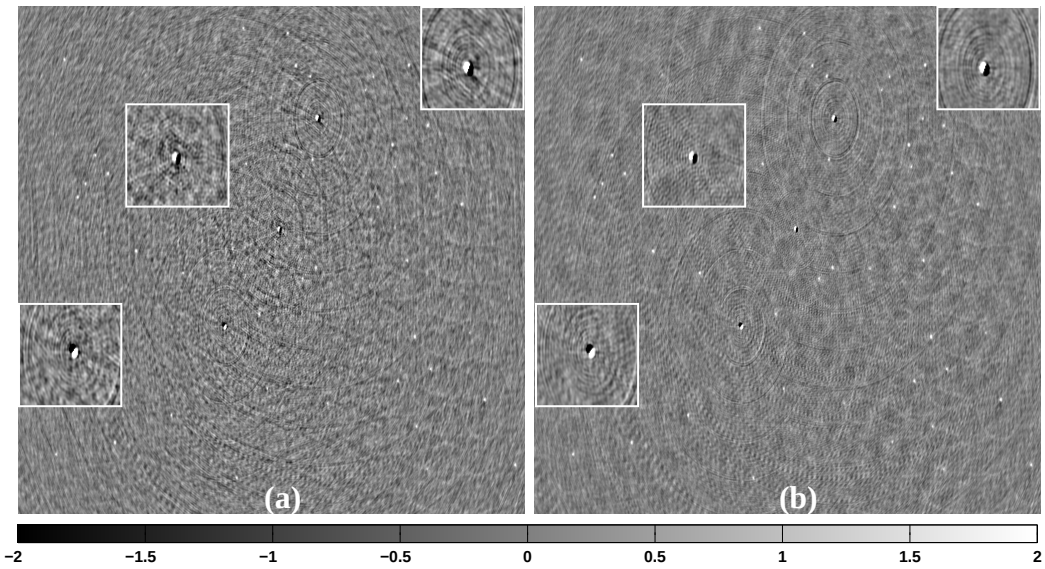

Figure 3.9: The residual images obtained by the OS-SAGE calibration, using $m = 2$ number of sub-observations at every iteration, for $x = 7$ (a) and $x = 10$ (b). By increasing the number of visibilities in the sub-observations from forty nine ($x = 7$) to seventy ($x = 10$), the calibration accuracy is highly improved. Plus, the two images have a higher residual noise and artifacts compared to the result obtained for $x = N - 1 = 13$, which is presented by Fig. 3.5 as image (d). This shows that better accuracy of the OS calibration is achieved when there exist a larger number of visibilities in every sub-observation. However, the calibration's processing time for $x = 7$ and $x = 10$ is 73.5 and 92.8 minutes, respectively, which is faster than the one for $x = 13$ that was 108.8 minutes (Table 1).

alternative would be: (i) first partitioning baselines for $N-1$ number of receivers, as it is already explained in this section, and (ii) assigning the remained baselines to these $N-1$ partitions.

3.5.2 Averaging of visibilities

The OS calibration method divides the data into sub-observations and alternates. The use of fewer data samples in each iteration is the principle cause of the speedup. So far, we have used segments of data consisting of multiple integrations in time and have considered the individual integrations as the sub-observations. This is reasonable for the use of OS calibrations. However, for the non-OS type calibrations all of these integrations are explicitly considered to be equivalent. Therefore, one could ask if it is easier to average the data before calibration to decrease the computational cost.
To answer this question, consider the case of calibrating data for a point source far away from the phase center of an observation. Based on (3.3), the visibilities of baseline $p-q$ at every sub-observation are formulated as

$$\mathbf{v}_{pq} = \mathbf{J}_q^* \otimes \mathbf{J}_p \text{vec}(\mathbf{C}) + \mathbf{n}_{pq}, \tag{3.19}$$

where,

$$\mathbf{C} = e^{\frac{-2\pi j\xi}{c}(ul+vm+w(\sqrt{1-l^2-m^2}-1))} \begin{bmatrix} \frac{I}{2} & 0 \\ 0 & \frac{I}{2} \end{bmatrix}. \tag{3.20}$$

In (3.20), $j^2 = -1$, ξ is the frequency of the observation, c is the speed of light, (l,m) are the source direction components corresponding to the observation phase center, (u,v,w) are the geometric components of baseline $p-q$, and I is the intensity of the source.
Since the source is far away from the phase center, (l,m) in (3.20) are large. Therefore, even very small variation of the baselines (u,v,w) on different sub-observations cause huge differences in the phase terms of (3.20). Subsequently, averaging the visibilities of (3.19) causes de-correlation (losing amplitude) and smearing effects in the calibration residuals.

To illustrate this, we simulate a 12 hour observation of WSRT from a very bright source with 130 Jy intensity is simulated. The source is about four degrees away from the phase center. In the center of the field we also put twenty three faint sources with intensities below 9 Jy. The Jones matrices for the faint sources are considered as identity matrices. For the bright source, they are multiplications of different linear combinations of sin and cos functions which are invariant on twenty five seconds time intervals. That provides time samples of size $\tau = 25$ including sub-observations, from every individual second, for which the gain errors are exactly the same. White Gaussian noise is also added to the simulated data.

It is expected that traditional calibration after averaging data performs as equivalent as the OS calibration which iterates on the individual sub-observations. The reason is that the simulated corruptions in the signals on twenty five seconds time intervals are invariant. However, the results, illustrated by Fig 3.11, is completely the opposite.

Fig. 3.11 shows the residual images obtained by the LS and the OS-LS calibration, utilizing $m = 2$ number of OS iterations and $n = 9$ number of LS iterations. The processing time in min is shown at the bottom right corner of every image. In image (a) of Fig. 3.11, LS calibration is applied on averaged data obtained from $\tau = 25$ time samples. In this image, the bright source is highly underestimated (almost not subtracted at all) and there exist elongated radial features. This is due to the de-correlation by averaging the visibilities. However, in image (b) of Fig. 3.11,

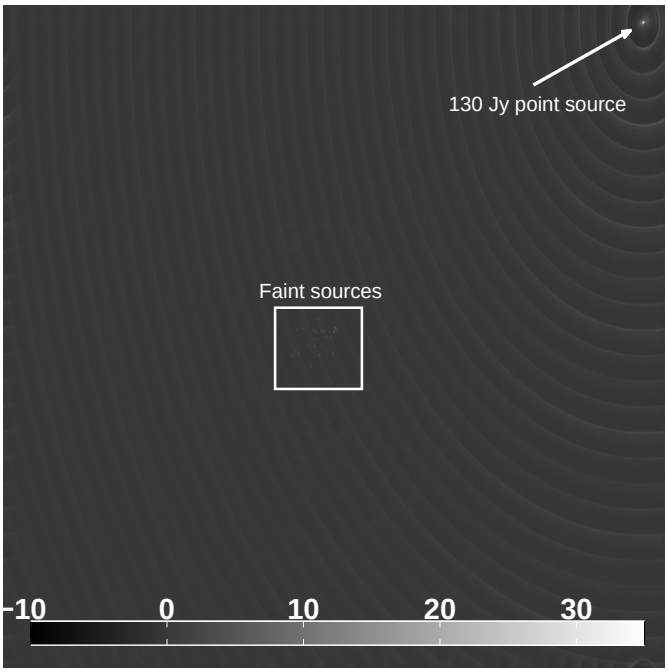

Figure 3.10: A 12 hour simulation of WSRT with a bright, 130 Jy source. The source is about four degrees away from the phase center. There also exist twenty three other faint sources with intensities below 9 Jy in the center of the field. White Gaussian noise is also added to the simulated data.

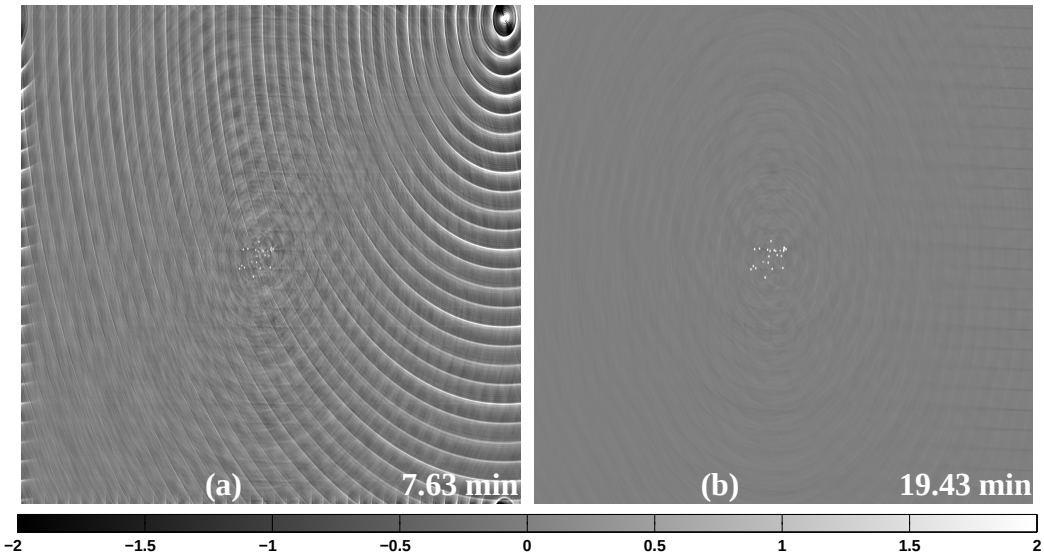

Figure 3.11: The residual images obtained by the LS and the OS-LS calibrations, utilizing $m = 2$ number of OS iterations and $n = 9$ number of LS iterations. The processing time is shown at the bottom right corner of every image. LS calibration on averaged visibilities (a), and OS-LS (b) calibration are applied. In (a), the bright source is highly underestimated (almost not subtracted at all) and there exist severe smearing effects. This is due to the de-correlation by averaging the visibilities. However, in (b), for which OS-LS calibrations is applied on individual integrations, the bright source is perfectly subtracted and the other fainter sources are completely visible. That makes OS-LS calibration the method of choice, despite its longer execution time.

for which OS-LS calibration is applied on individual integrations, the bright source is perfectly subtracted and the other fainter sources are completely visible. This proves that we can not simply apply calibration on averaged visibilities to cut down the computations and reveals the need of using the OS calibration. We have also executed LS calibration on non-averaged data sets of $\tau = 25$ time samples. The resulted residual image has been exactly the same as image (b) of Fig. 3.11, which is generated by OS-LS calibration. The reason is that the Jones matrices on every twenty five seconds calibrated data are invariant. Therefore, the solution which is obtained by OS calibrations, using few integrations (sub-observations) within twenty five seconds, is the same as the one obtained by non-OS calibrations using all the data. However, in reality, Jones matrices vary with time. In such a case, the result of the non-OS calibrations is always better than, or equivalent to, the one of OS calibrations. It is because finding a global solution which fits all data is generally more efficient than solving only for a part of dataset. The execution time of the LS calibration was 78.15 min, which is indeed longer than the one of OS-LS calibration (19.43 min).

3.6 Conclusions

This chapter introduces OS-LS and OS-SAGE radio interferometric calibration, as combinations of the OS method with LS and SAGE calibration techniques. We show that the OS calibration provide a significant improvement in the execution speed compared to the conventional (non-OS) calibration algorithms. The key idea is to partition the observed data into groups of sub-observations for which the gain errors are considered to be fixed. OS type calibrations solve for every group by iteratively updating the solutions for that group's sub-observations in an ordered sequence. The calibrations benefit from very fast computations and preserve almost the same quality as the one obtained by the non-OS calibrations. But, we must take in to account that their accuracy never becomes higher than the one of the non-OS calibration. Simulations show that OS calibration methods have considerable computational improvements compared to the conventional non-OS calibration methods. They also indicate that the OS-SAGE calibration provides a better quality results in a shorter time compared to the OS-LS calibration, as it is the case for the conventional SAGE and LS calibrations. In Future work, we address a novel accuracy of calibration obtained via a hybrid of non-OS and OS calibration techniques which has a computational cost almost as cheap as the one of OS calibrations.

Chapter 4

Clustered Calibration: An Improvement to Radio Interferometric Direction Dependent Self-Calibration

"Clustered calibration: an improvement to radio interferometric direction-dependent self-calibration"
Kazemi S., Yatawatta S., Zaroubi S., 2013, MNRAS, 430, 1457

ABSTRACT

The new generation of radio synthesis arrays, such as LOFAR and SKA, have been designed to surpass existing arrays in terms of sensitivity, angular resolution and frequency coverage. This evolution has led to the development of advanced calibration techniques that ensure the delivery of accurate results at the lowest possible computational cost. However, the performance of such calibration techniques is still limited by the compact, bright sources in the sky, used as calibrators. It is important to have a bright enough source that is well distinguished from the background noise level in order to achieve satisfactory results in calibration. We present ”clustered calibration” as a modification to traditional radio interferometric calibration, in order to accommodate faint sources that are almost below the background noise level into the calibration process. The main idea is to employ the information of the bright sources' measured signals as an aid to calibrate fainter sources that are nearby the bright sources. In the case where we do not have bright enough sources, a source cluster could act as a bright source that can be distinguished from background noise. We construct a number of source clusters assuming that the signals of the sources belonging to a single cluster are corrupted by almost the same errors, and each cluster is calibrated as a single source, using the combined coherencies of its sources simultaneously. This upgrades the power of an individual faint source by the effective power of its cluster. We give performance analysis of clustered calibration to show the superiority of this approach compared to the traditional unclustered calibration. We also provide analytical criteria to choose the optimum number of clusters for a given observation in an efficient manner.

4.1 Introduction

With the intention of increased sensitivity and resolution, especially at low frequencies, a new set of radio interferometers such as the LOw Frequency ARray (LOFAR)[1], the Murchison Wide-field Array (MWA) [2] and the Square Kilometre Array (SKA)[3] are being devised and some are already becoming operational. These arrays form a large effective aperture by the combination of a large number of antennas using aperture synthesis (Thompson et al., 2001). In order to achieve the full potential of such an interferometer, it is essential that the observed data is properly calibrated before any imaging is done. Calibration of radio interferometers refers to the estimation and reduction of errors introduced by the atmosphere and also by the receiver hardware, before imaging. We also consider the removal of bright sources from the observed data part of calibration, that enable imaging the weak background sources. For low frequency observations with a wide field of view, calibration needs to be done along multiple directions in the sky. Proper calibration across the full field of view is required to achieve the interferometer's desired precision and sensitivity giving us high dynamic range images.

Early radio astronomy used external (classical) calibration which estimates the instrumental unknown parameters using a radio source with known properties. This method has a relatively low computational cost and a fast execution time, but it generates results strongly affected by

[1] http://www.lofar.org
[2] http://www.mwatelescope.org
[3] http://www.skatelescope.org

the accuracy with which the source properties are known. In addition, existence of an isolated bright source, which is the most important requirement of external calibration, in a very wide field of view is almost impractical, and even when it does, external calibration would only give information along the direction of the calibrator. The external calibration was then improved by self-calibration (Pearson & Readhead, 1984). Self-calibration has the advantage of estimating both the source and instrumental unknowns, without the need of having a pre-knowledge of the sky, only utilizing the instrument's observed data. Moreover, it can achieve a superior precision by iterating between the sky and the instrumental parameters.

The accuracy of any calibration scheme, regardless of the used technique, is determined by the level of Signal to Noise Ratio (SNR). This limits the feasibility of any calibration scheme to only bright sources that have a high enough SNR to be distinguished from the background noise (Bernardi et al., 2011; Liu et al., 2009; Pindor et al., 2010). Note that interferometric images are produced using the data observed during the total observation (integration) time. However, calibration is done at shorter time intervals of that total duration. This increases the noise level of the data for which calibration is executed compared to the one in the images. In other words, there are some faint sources that appear well above the noise in the images while they are well below the noise level during calibration. It has been a great challenge to calibrate such faint sources having a very low SNR. In this chapter we present clustered self-calibration, introduced in Kazemi et al. (2011), and emphasize its better performance compared to un-clustered calibration below the calibration noise level. Existing un-clustered calibration approaches (Intema et al., 2009; Smirnov, 2011) can only handle a handful of directions where strong enough sources are present and we improve this, in particular for subtraction of thousands of sources over hundres of directions in the sky, as in the case for LOFAR.

The implementation of clustered calibration is performed by clustering the sources in the sky, assuming that all the sources in a single cluster have the same corruptions, and calibrating each cluster as a single source. At the end, the obtained calibration solutions for every source cluster is assigned to all the sources in that cluster. This procedure improves the information used by calibration by incorporating the total of signals observed at each cluster instead of each individual source's signal. Therefore, when SNR is very low, it provides a considerably better result compared to un-clustered calibration. Moreover, calibrating for a set of source clusters instead of for all the individual sources in the sky reduces the number of directions along which calibration has to be performed, thus considerably cutting down the computational cost. However, there is one drawback in clustered calibration: The corruptions of each individual source in one given cluster will almost surely be slightly different from the corruptions estimated for the whole cluster by calibration. We call this additional error as "clustering error" and in order to get the best performance in clustered calibration, we should find the right balance between the improvement in SNR as opposed to degradation by clustering error.

Clustering methods have gained a lot of popularity in dealing with large data sets (Kaufman & Rousseeuw, 1990). There are various clustering approaches that could be applied to calibration based on their specific characteristics. An overview of different clustering methods is given in Xu & Wunsch (2008). Clustering of radio sources should take into account (i) their physical distance from each other and (ii) their individual intensity. The smaller the angular separations of sources are, the higher the likelihood that they share the same corruptions in their radiated signals is. Moreover, in order to get the best accuracy in the calibration results, there should be a balance between effective intensities of different clusters. Thus, in the clustering procedure, every source should be weighted suitably according to its brightness intensity.

The brightness distribution of radio source in the sky is a power law and the spatial distribution is Possion. Therefore, clustering the sources via probabilistic clustering approaches is computationally complex. Hierarchical clustering (Johnson, 1967) is a well-known clustering approach with a straight forward implementation suitable for our case. But, its computational cost grows exponentially with the size of its target data set which can be a disadvantage when the number of sources is huge. Weighted K-means clustering (Kerdprasop et al., 2005; MacQueen, 1967) is also one of the most used of clustering schemes applicable in clustered calibration. The advantage of this clustering technique is its low computational cost, which is proportional to the number of clusters and the size of the target data set. Nonetheless, we emphasize that the computational time taken by any of the aforementioned clustering algorithms is negligible compared with the computational time taken by the actual calibration. Therefore, we pursue all clustering approaches in this chapter. However, the use of Fuzzy C-means clustering (Bezdek, 1981) in clustered calibration requires major changes in the calibration data model and will be explored in future work.

This chapter is organized as follows: First, in section 4.2 we present the general data model used in clustered calibration. In section 4.3, we present modified weighted K-means and divisive hierarchical clustering for clustering sources in the sky. Next, in section 4.4, we focus on analyzing the performance of clustered calibration, with an a priori clustered sky model, and compare the results with un-clustered calibration. In clustered calibration, there is contention between the improvement of SNR by clustering sources and the errors introduced by the clustering of sources itself. Thus, we relate the clustered calibration's performance to the effective Signal to Interference plus Noise Ratio (SINR) obtained for each cluster. For this purpose, we use statistical estimation theory and the Cramer-Rao Lower Bounds (CRLB) (Kay, 1993). In section 4.5, we derive criteria for finding the optimum number of clusters for a given sky. We use the SINR analysis and adopt Akaike's Information Criterion (AIC) (Akaike, 1973) and the Likelihood Ratio Test (LRT) (Graves, 1978) to estimate the optimum number of clusters. We present simulation results in section 4.6 to show the superiority of clustered calibration to un-clustered calibration and the performance of the presented criteria in detecting the optimum number of clusters. Finally, we draw our conclusions in section 4.7. Through this chapter, calibration is executed by the Space Alternating Generalized Expectation maximization (SAGE) (Fessler & Hero (1994); Yatawatta et al. (2009); Kazemi et al. (2011), chapter 2) algorithm. Moreover, in our simulations, radio sources are considered to be uniformly distributed in the sky and their flux intensities follow Raleigh distribution, which is the worst case scenario. In real sky models, there usually exist only a few (two or three) number of bright sources which dominate the emission. In the presence of these sources and the background noise, it is impractical to solve for the other faint sources in the field of view individually. Therefore, obtaining a better calibration performance via the clustered calibration approach, compared to the un-clustered one, is guaranteed. Therefore, in section 4.6 we illustrate this using simulations in which the brightness distribution of sources is a power law with a very steep slope. On top of that, Kazemi et al. (2013b); Yatawatta et al. (2013) (chapter 4) also present the superior performance of the clustered calibration on real observations of LOFAR.

The following notations are used in this chapter: Bold, lowercase letters refer to column vectors, e.g., $\mathbf{y}$. Upper case bold letters refer to matrices, e.g., $\mathbf{C}$. All parameters are complex numbers, unless stated otherwise. The inverse, transpose, Hermitian transpose, and conjugation of a matrix are presented by $(.)^{-1}$, $(.)^T$, $(.)^H$, and $(.)^*$, respectively. The statistical expectation operator is referred to as $E\{.\}$. The matrix Kronecker product and the proper (strict) subset are denoted by $\otimes$ and $\subsetneq$, respectively. $\mathbf{I}_n$ is the $n \times n$ identity matrix and $\varnothing$ is the empty set. The Kronecker delta function is presented by δ_{ij}. $\mathbb{R}$ and $\mathbb{C}$ are the sets of Real and Complex numbers, respectively. The

Frobenius norm is shown by $||.||$. Estimated parameters are denoted by a hat, $\widehat{(.)}$. All logarithmic calculations are to the base e. The multivariate Gaussian and Complex Gaussian distributions are denoted by $\mathcal{N}$ and $\mathcal{CN}$, respectively.

4.2 Clustered Self-calibration Data Model

In this section, we present the measurement equation of a polarimetric clustered calibration in detail (Hamaker et al., 1996; Hamaker, 2006). Suppose we have a radio interferometer consisting of N polarimetric antennas where each antenna is composed of two orthogonal feeds that observe K compact sources in the sky. Every i-th source signal, $i \in \{1, 2, \ldots, K\}$, causes an induced voltage of $\widetilde{\mathbf{v}}_{pi} = [v_{Xpi}\ v_{Ypi}]^T$ at X and Y dipoles of every p-th antenna, $p \in \{1, 2, \ldots, N\}$. In practice,

$$\widetilde{\mathbf{v}}_{pi} = \mathbf{J}_{pi}\mathbf{e}_i, \tag{4.1}$$

where $\mathbf{e}_i = [e_{Xi}\, e_{Yi}]^T$ is the source's electric field vector and $\mathbf{J}_{pi}$ represents the 2×2 Jones matrix (Hamaker et al., 1996) corresponding to the direction-dependent gain corruptions in the radiated signal. These corruptions are originated from the instrumental (the beam shape, system frequency response, etc.) and the propagation (tropospheric and ionospheric distortions, etc.) properties which later on, in this section, will be explained in more detail.

The signal $\mathbf{v}_p$ obtained at every antenna p is a linear superposition of the K sources corrupted signals, $\widetilde{\mathbf{v}}_{pi}$ where $i \in \{1, 2, \ldots, K\}$, plus the antenna's thermal noise. The multitude of ignored fainter sources also contributes to this additive noise.

The voltages collected at the instrument antennas get corrected for geometric delays, based on the location of their antennas, and some instrumental effects, like the antenna clock phases and electronic gains. Then, they are correlated in the array's correlator to generate visibilities (Hamaker et al., 1996). The visibility matrix of the baseline $p-q$, $\mathrm{E}\{\mathbf{v}_p \otimes \mathbf{v}_q^H\}$, is given by

$$\mathbf{V}_{pq} = \mathbf{G}_p \left(\sum_{i=1}^{K} \mathbf{J}_{pi}(\boldsymbol{\theta}) \mathbf{C}_{i\{pq\}} \mathbf{J}_{qi}^H(\boldsymbol{\theta}) \right) \mathbf{G}_q^H + \mathbf{N}_{pq}. \tag{4.2}$$

In (4.2), $\boldsymbol{\theta} \in \mathbb{C}^P$, $P = 4KN$, is the unknown instrumental and sky parameter vector, $\mathbf{N}_{pq}$ is the additive 2×2 noise matrix of the baseline $p-q$, and $\mathbf{C}_{i\{pq\}}$ is the i-th source coherency matrix $\mathbf{C}_i = \mathrm{E}\{\mathbf{e}_i \otimes \mathbf{e}_i^H\}$ (Born & Wolf, 1999; Hamaker et al., 1996). If the i-th source radiation intensity is I_i, then $\mathbf{C}_i = \frac{I_i}{2}\mathbf{I}_2$. Considering this source to have equatorial coordinate, (Right Ascension α, Declination δ), equal to (α_i, δ_i), and the geometric components of baseline $p-q$ to be (u, v, w), then

$$\mathbf{C}_{i\{pq\}} = e^{-2\pi j(ul+vm+w(\sqrt{1-l^2-m^2}-1))}\mathbf{C}_i, \tag{4.3}$$

where $j^2 = -1$ and,

$$\begin{aligned} l &= sin(\alpha_i - \alpha_0)cos(\delta_i), \\ m &= cos(\delta_0)sin(\delta_i) - cos(\alpha_i - \alpha_0)cos(\delta_i)sin(\delta_0), \end{aligned}$$

are the source direction components corresponding to the observation phase reference of (α_0, δ_0) (Thompson et al., 2001). The errors common to all directions, such as the receiver delay and amplitude errors, are given by $\mathbf{G}_p$ and $\mathbf{G}_q$. Initial calibration at a finer time and frequency resolution

is performed to estimate and correct for $\mathbf{G}_p$-s and the corrected visibilities are obtained as

$$\widetilde{\mathbf{V}}_{pq} = \mathbf{G}_p^{-1}\mathbf{V}_{pq}\mathbf{G}_q^{-H}. \tag{4.4}$$

The remaining errors are unique to a given direction, but residual errors in $\mathbf{G}_p$-s are also absorbed into these errors, which are denoted by $\mathbf{J}_{pi}$ in the usual notation.

Vectorizing (4.4), the final visibility vector of the baseline $p-q$ is given by

$$\mathbf{v}_{pq} = \sum_{i=1}^{K} \mathbf{J}_{qi}^{*}(\boldsymbol{\theta}) \otimes \mathbf{J}_{pi}(\boldsymbol{\theta})\text{vec}(\mathbf{C}_{i\{pq\}}) + \mathbf{n}_{pq}. \tag{4.5}$$

Stacking up all the cross correlations (measured visibilities) and noise vectors in $\mathbf{y}$ and $\mathbf{n}$, respectively, the un-clustered self-calibration measurement equation is given by

$$\mathbf{y} = \sum_{i=1}^{K} \mathbf{s}_i(\boldsymbol{\theta}) + \mathbf{n}. \tag{4.6}$$

In (4.6), $\mathbf{y}, \mathbf{n} \in \mathbb{C}^M$, $M = 2N(N-1)$, the noise vector is considered to have a zero mean Gaussian distribution with covariance $\mathbf{\Pi}$, $\mathbf{n} \sim \mathcal{N}(0, \mathbf{\Pi}_{M\times M})$, and the nonlinear function $\mathbf{s}_i(\boldsymbol{\theta})$ is defined as

$$\mathbf{s}_i(\boldsymbol{\theta}) \equiv \begin{bmatrix} \mathbf{J}_{2i}^{*}(\boldsymbol{\theta}) \otimes \mathbf{J}_{1i}(\boldsymbol{\theta})\text{vec}(\mathbf{C}_{i\{12\}}) \\ \mathbf{J}_{3i}^{*}(\boldsymbol{\theta}) \otimes \mathbf{J}_{1i}(\boldsymbol{\theta})\text{vec}(\mathbf{C}_{i\{13\}}) \\ \vdots \\ \mathbf{J}_{Ni}^{*}(\boldsymbol{\theta}) \otimes \mathbf{J}_{(N-1)i}(\boldsymbol{\theta})\text{vec}(\mathbf{C}_{i\{(N-1)N\}}) \end{bmatrix}. \tag{4.7}$$

Calibration is essentially the Maximum Likelihood (ML) estimation of the unknown parameters $\boldsymbol{\theta}$ (P complex values or $2P$ real values), or of the Jones matrices $\mathbf{J}(\boldsymbol{\theta})$, from (4.6) and removal of the K sources. Note that calibration methods could also be applied to the uncorrected visibilities of (4.4) to estimate $\mathbf{G}_p$ and $\mathbf{G}_q$ errors as well.

The Jones matrix $\mathbf{J}_{pi}$, for every i-th direction and at every p-th antenna, is given as

$$\mathbf{J}_{pi} \equiv \mathbf{E}_{pi}\mathbf{Z}_{pi}\mathbf{F}_{pi}. \tag{4.8}$$

In (4.8), $\mathbf{E}_{pi}$, $\mathbf{Z}_{pi}$, and $\mathbf{F}_{pi}$ are the antenna's voltage pattern, ionospheric phase fluctuation, and Faraday Rotation Jones matrices, respectively. In practice, the $\mathbf{E}$, $\mathbf{Z}$, and $\mathbf{F}$ Jones matrices obtained for nearby directions and for a given antenna are almost the same. Thus, for every antenna p, if the i-th and j-th sources have a small angular separation from each other, we may consider

$$\mathbf{J}_{pi} \cong \mathbf{J}_{pj}. \tag{4.9}$$

This is the underlying assumption for clustered calibration.

Clustered calibration first assigns source clusters, L_i for $i \in \{1, 2, \ldots, Q\}$ where $Q \ll K$, on which the sky variation is considered to be uniform. Then, it assumes there exists a unique $\widetilde{\mathbf{J}}_{pi}$ which is shared by all the sources of the i-th cluster L_i, $i \in \{1, 2, \ldots, Q\}$, at receiver p, $p \in \{1, 2, \ldots, N\}$. Based on that, the visibility at every baseline $p-q$, given by (4.2), is reformulated as

$$\mathbf{V}_{pq} = \sum_{i=1}^{Q} \widetilde{\mathbf{J}}_{pi}(\widetilde{\boldsymbol{\theta}})\{\sum_{l\in L_i} \mathbf{C}_{l\{pq\}}\}\widetilde{\mathbf{J}}_{qi}^{H}(\widetilde{\boldsymbol{\theta}}) + \widetilde{\mathbf{N}}_{pq}. \tag{4.10}$$

In (4.10), $\widetilde{\mathbf{N}}_{pq}$ is the clustered calibration's effective noise at baseline $p-q$ which will be explicitly discussed at section 4.4. Note that clustered calibration estimates the new unknown parameter $\widetilde{\boldsymbol{\theta}} \in \mathbb{C}^{\widetilde{P}}$ where $\widetilde{P} = 4QN$. Denoting the effective signal of every i-th cluster at baseline $p-q$ by

$$\widetilde{\mathbf{C}}_{i\{pq\}} \equiv \sum_{l \in L_i} \mathbf{C}_{l\{pq\}}, \tag{4.11}$$

the clustered calibration visibility vector at this baseline (vectorized form of (4.10)) is

$$\mathbf{v}_{pq} = \sum_{i=1}^{Q} \widetilde{\mathbf{J}}^{*}_{qi}(\widetilde{\boldsymbol{\theta}}) \otimes \widetilde{\mathbf{J}}_{pi}(\widetilde{\boldsymbol{\theta}}) \text{vec}(\widetilde{\mathbf{C}}_{i\{pq\}}) + \widetilde{\mathbf{n}}_{pq}. \tag{4.12}$$

Finally, stacking up the visibilities of all the instrument's baselines in vector $\mathbf{y}$, clustered calibration's general measurement equation is resulted as

$$\mathbf{y} = \sum_{i=1}^{Q} \widetilde{\mathbf{s}}_i(\widetilde{\boldsymbol{\theta}}) + \widetilde{\mathbf{n}}. \tag{4.13}$$

In (4.13) $\widetilde{\mathbf{s}}_i$ is defined similar to $\mathbf{s}_i$ in (4.7) where $\mathbf{J}$ and $\mathbf{C}$ are replaced by $\widetilde{\mathbf{J}}$ and $\widetilde{\mathbf{C}}$, respectively.

Because of the similarity between the clustered and the un-clustered calibration's measurement equations presented by (4.13) and (4.6), respectively, they could utilize the same calibration techniques. Thus, the only difference between these two types of calibration is that clustered calibration solves for clusters of sources instead of for the individual ones. That upgrades the signals which should be calibrated for from (4.3) to (4.11).

4.3 Clustering Algorithms

Clustering is grouping a set of data so that the members of the same group (cluster) have some similarities (Kaufman & Rousseeuw, 1990). This similarity is defined based on the application of the clustering method.

We need to define clustering schemes in which two radio sources merge to a single cluster based on the similarity in their direction dependent gain errors (see 4.8). Radiations of sources that are close enough to each other in the sky are assumed to be affected by almost the same corruptions (see 4.9). Based on that, we aim to design source clusters with small angular diameters. On the other hand, every cluster's intensity is the sum of the intensities of its members (see (4.11)). In order to keep a balance between different clusters' intensities, we intend to apply weighted clustering techniques in which the sources are weighted proportional to their intensities.

Suppose that the K sources, $x_1, x_2, \ldots, x_K$ have $(\alpha_1, \delta_1), (\alpha_2, \delta_2), \ldots, (\alpha_K, \delta_K)$ equatorial coordinates, respectively. The aim is to provide Q clusters so that the objective function $f = \sum_{q=1}^{Q} D(L_q)$ is minimized. $D(L_q)$ is the angular diameter of cluster L_q, for $q \in \{1, 2, \ldots, Q\}$, defined as

$$D(L_q) \equiv \max \{d(x_i, x_j) | x_i, x_j \in L_q\}, \tag{4.14}$$

and $d(.,.)$ is the angular separation between any two points on the celestial sphere. Having two radio sources a and b with equatorial coordinates (α_a, δ_a) and (α_b, δ_b), respectively, the angular

separation $d(a,b)$, in radians, is obtained by

$$\tan^{-1}\frac{\sqrt{\cos^2\delta_b\sin^2\Delta\alpha+[\cos\delta_a\sin\delta_b-\sin\delta_a\cos\delta_b\cos\Delta\alpha]^2}}{\sin\delta_a\sin\delta_b+\cos\delta_a\cos\delta_b\cos\Delta\alpha}, \tag{4.15}$$

where $\Delta\alpha=\alpha_b-\alpha_a$.
For defining the centroids, we associate a weight to every source x_i, as

$$w_i=w(x_i)\equiv\frac{I_i}{I^*},\quad \text{for } i\in\{1,2,\ldots,K\}, \tag{4.16}$$

where I_i is the source's intensity and $I^*=\min\{I_1,I_2,\ldots,I_K\}$. Applying the weights to the clustering procedure, the centroids of the clusters lean mostly towards the brightest sources. That causes a tendency in faint sources to gather with brighter sources close to them into one cluster. Thus, their weak signals are promoted being added up with some brighter sources' signals. Moreover, very strong sources will be isolated such that their signals are calibrated individually, without being affected by the other faint sources.

We cluster radio sources using weighted K-means (Kerdprasop et al., 2005) and divisive hierarchical clustering (Johnson, 1967) algorithms. Since the source clustering for calibration is performed offline, its computational complexity is negligible compared with the calibration procedure itself.

4.3.1 Weighted K-means clustering

Step 1. Select the Q brightest sources, $x_{1^*},x_{2^*},\ldots,x_{Q^*}$, and initialize the centroids of Q clusters by their locations as

$$c_q\equiv[\alpha_{q^*},\delta_{q^*}],\quad \text{for } q\in\{1,2,\ldots,Q\},\ q^*\in\{1^*,2^*,\ldots,Q^*\}. \tag{4.17}$$

Step 2. Assign each source to the cluster with the closest centroid, defining the membership function

$$m_{L_q}(x_i)=\begin{cases}1, & \text{if } d(x_i,c_q)=\min\{d(x_i,c_j)|j=1,\ldots,Q\}\\ 0, & \text{Otherwise}\end{cases}$$

Step 3. Update the centroids by

$$c_q=\frac{\sum_{i=1}^{K}m_{L_q}(x_i)\,w_ix_i}{\sum_{i=1}^{K}m_{L_q}(x_i)\,w_i},\quad \text{for } q\in\{1,2,\ldots,Q\}. \tag{4.18}$$

Repeat steps 2 and 3 until there are no reassignments of sources to clusters.

4.3.2 Divisive hierarchical clustering algorithm

Step 1. Initialize the cluster counter Q' to 1, assign all the K sources to a single cluster L_1 and $\varnothing$ to a set of null clusters A.
Step 2. Choose cluster L_{q^*}, for $q^*\in\{1,2,\ldots,Q'\}-A$, with the largest angular diameter

$$D(L_{q^*})=\max\{D(L_q)|q\in\{1,2,\ldots,Q'\}-A\}. \tag{4.19}$$

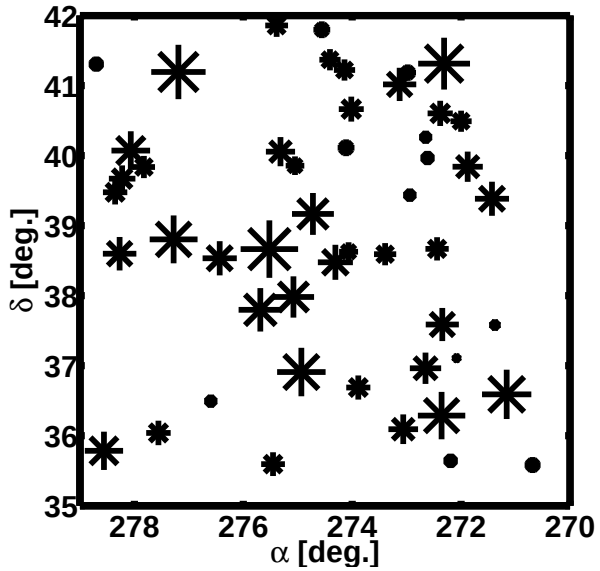

Figure 4.1: A simulated 8 by 8 degrees sky of fifty point sources with intensities below 3 Jy. The source positions and their brightness are following uniform and Rayleigh distributions, respectively. The marker sizes are proportional to sources intensities.

Step 3. Apply the presented weighted K-means clustering technique to split L_{q^*} into two clusters, L'_{q^*} and L''_{q^*}.

Step 4. If $D(L'_{q^*}) + D(L''_{q^*}) < D(L_{q^*})$, then set $Q' = Q' + 1$, $L_{q^*} \equiv L'_{q^*}$, $L_{Q'} \equiv L''_{q^*}$, and $A = \varnothing$, otherwise set $A = A \cup \{q^*\}$.
Repeat steps 2, 3, and 4 until $Q' = Q$.

4.3.3 Clustering methods comparison

Hierarchical clustering method tends to design clusters with almost the same angular diameters, whereas, the K-means clustering method tends to keep the same level of intensity at all its clusters. In practice, since hierarchical clustering method makes less errors in dedicating the same solutions to sources in small clusters, it performs better than Weighted K-means Clustering in a clustered calibration procedure. But, when the number of source clusters is very large ($Q \geq 100$), its prohibitive computational costs makes the fast K-means clustering method preferable.

Example 1: Weighted K-means and hierarchical clustering

We simulate an 8 by 8 degrees sky with fifty point sources with intensities below 3 Jansky (Jy). The source positions and their brightness follow uniform and Rayleigh distributions, respectively. The result is shown by Fig. 4.1 in which the symbol sizes are proportional to intensities of sources. Weighted K-means and divisive hierarchical clustering methods are applied to cluster the fifty sources into ten source clusters. The results are presented in Fig. 4.2 and Fig. 4.3, respectively.

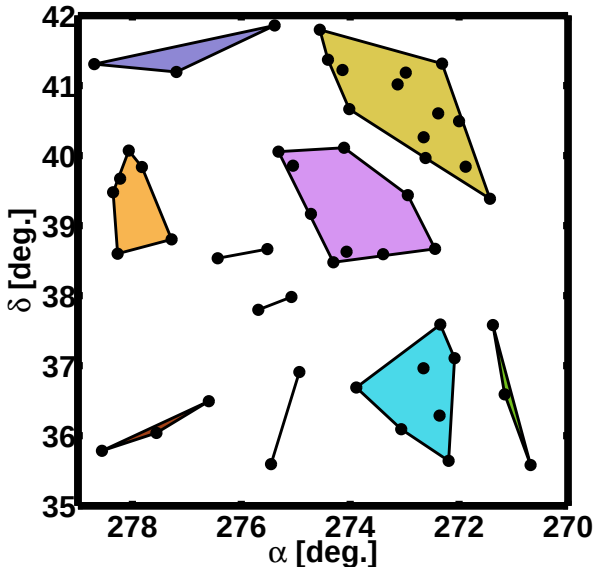

Figure 4.2: Fifty point sources are clustered into ten source clusters by Weighted K-means clustering technique. There is not a good balance between different clusters angular diameters.

Fig. 4.2 shows that the Weighted K-means clustering could design source clusters with considerably large angular diameters. Assigning the same calibration solutions to the sources of these large clusters could cause significant errors. However, as Fig. 4.3 shows, this is not the case for the hierarchical clustering and it constructs clusters with almost the same angular diameters.

Since the number of sources in this simulation is not that large ($K = 50$), the difference between execution time of the two clustering methods is not significant. Hence in such a case, the use of hierarchical clustering method, rather than the Weighted K-means, is advised. However, this is not the case when we have a large number of sources, and subsequently a large number of source clusters, in the sky. To demonstrate this, we use the two clustering techniques for clustering thousand of sources ($K = 1000$) into Q source clusters, $Q \in \{3, 4, \ldots, 100\}$. The methods' computational times versus the number of clusters are plotted in Fig. 4.4. As Fig. 4.4 shows, for large Qs, the computational cost of Weighted K-means is much cheaper than the one of the hierarchical clustering. That can make the Weighted K-means clustering method more suitable than the hierarchical clustering for such a case.

4.4 Performance Analysis

In this section, we explain the reasons for clustered calibration's better performance, compared to un-clustered calibration, at a low SNR (Kazemi & Yatawatta, 2012). This superiority is in the sense of achieving an unprecedented precision in solutions with a considerably low computational complexity, given the optimum clustering scheme. In the next section, we present different criteria for finding the optimum number of clusters at which the clustered calibration performs the best.

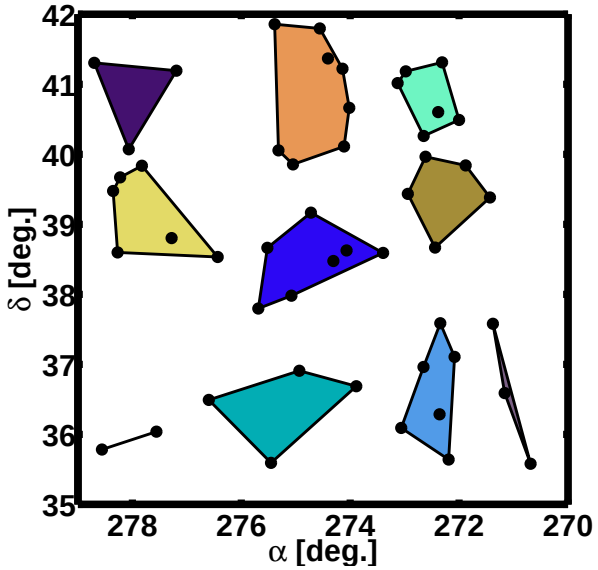

Figure 4.3: Fifty point sources are clustered into ten source clusters via hierarchical clustering method. Different clusters have almost the same angular diameters.

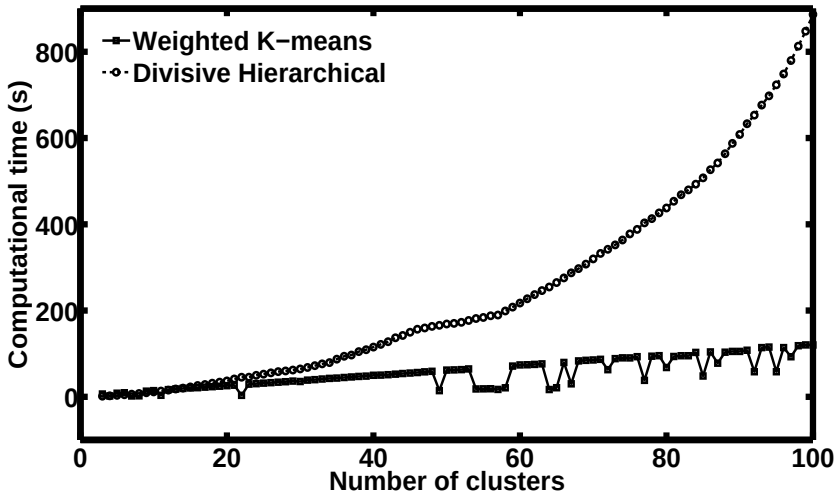

Figure 4.4: Weighted K-means and divisive hierarchical clustering methods computational costs. For small number of source clusters, there is no difference between execution times of the two clustering methods. But, when the number of source clusters is large, the computational cost of Weighted K-means becomes much cheaper than the one of the hierarchical clustering.

4.4.1 Cramer-Rao Lower Bounds

The most fundamental assumption in clustered calibration is that the sources at the same cluster have exactly the same corruptions in their radiated signals. This assumption is of course incorrect, nonetheless, it provides us with a stronger signal, the sum of the signals in the whole cluster. We present an analytic comparison of clustered and un-clustered calibration where we use the Cramer-Rao Lower Bound (CRLB) (Kay, 1993) as a tool to measure the performance of the calibration.

Estimations of CRLB for two sources at a single cluster

For simplicity, first consider observing two point sources at a single baseline, for example at baseline $p-q$. Based on (4.2), the visibilities are given by

$$\mathbf{V}_{pq} = \mathbf{J}_{p1}\mathbf{C}_{1\{pq\}}\mathbf{J}_{q1}^{H} + \mathbf{J}_{p2}\mathbf{C}_{2\{pq\}}\mathbf{J}_{q2}^{H} + \mathbf{N}_{pq}, \tag{4.20}$$

in the un-clustered calibration strategy. Vectorizing $\mathbf{V}_{pq}$, the visibility vector is

$$\mathbf{y} = \mathbf{J}_{q1}^{*} \otimes \mathbf{J}_{p1}\text{vec}(\mathbf{C}_{1\{pq\}}) + \mathbf{J}_{q2}^{*} \otimes \mathbf{J}_{p2}\text{vec}(\mathbf{C}_{2\{pq\}}) + \mathbf{n}_{pq}.$$

Assuming $\mathbf{n}_{pq} \sim \mathcal{CN}(\mathbf{0}, \sigma^2\mathbf{I}_4)$, we have

$$\mathbf{y} \sim \mathcal{CN}(\mathbf{s}(\boldsymbol{\theta}), \sigma^2\mathbf{I}_4), \tag{4.21}$$

where

$$\mathbf{s}(\boldsymbol{\theta}) \equiv \sum_{i=1,2} \mathbf{J}_{qi}^{*}(\boldsymbol{\theta}) \otimes \mathbf{J}_{pi}(\boldsymbol{\theta})\text{vec}(\mathbf{C}_{i\{pq\}}). \tag{4.22}$$

Using (4.21), the log-likelihood function of the visibility vector $\mathbf{y}$ is given by

$$\mathcal{L}(\boldsymbol{\theta}|\mathbf{y}) = -4\ln\{\frac{\pi}{\sigma^2}\} - \sigma^{-2}(\mathbf{y}-\mathbf{s}(\boldsymbol{\theta}))^{H}(\mathbf{y}-\mathbf{s}(\boldsymbol{\theta})). \tag{4.23}$$

CRLB is a tight lower bound on the error variance of any unbiased parameter estimators (Kay, 1993). Based on its definition, if the log-likelihood function of the random vector $\mathbf{y}$, $\mathcal{L}(\boldsymbol{\theta}|\mathbf{y})$, satisfies the "regularity" condition

$$\text{E}_{\mathbf{y}}\left[\frac{\partial}{\partial\boldsymbol{\theta}}\mathcal{L}(\boldsymbol{\theta}|\mathbf{y})\right] = 0, \quad \text{for all } \boldsymbol{\theta}, \tag{4.24}$$

then for any unbiased estimator of $\boldsymbol{\theta}$, $\widehat{\boldsymbol{\theta}}$,

$$\text{var}(\widehat{\boldsymbol{\theta}}_i) \geq [\mathcal{I}^{-1}(\boldsymbol{\theta})]_{ii}, \quad \text{for } i \in \{1,\ldots,M\}, \tag{4.25}$$

where $\mathcal{I}(\boldsymbol{\theta})$ is the Fisher information matrix defined as

$$\mathcal{I}(\boldsymbol{\theta}) = -\text{E}_{\mathbf{y}}\left[\frac{\partial^2\mathcal{L}(\boldsymbol{\theta}|\mathbf{y})}{\partial\boldsymbol{\theta}\partial\boldsymbol{\theta}^{T}}\right]. \tag{4.26}$$

In other words, the variance of any unbiased estimator of the unknown parameter vector $\boldsymbol{\theta}$ is bounded from below by the diagonal elements of $[\mathcal{I}(\boldsymbol{\theta})]^{-1}$.

Using (4.23) and (4.26), the Fisher information matrix of the visibility vector $\mathbf{y}$ is obtained as

$$\mathcal{I}(\boldsymbol{\theta}) = 2\sigma^{-2}\,\mathfrak{Re}(J_{\mathbf{s}}^H J_{\mathbf{s}}), \tag{4.27}$$

where $J_{\mathbf{s}}$ is the Jacobian matrix of $\mathbf{s}$ with respect to $\boldsymbol{\theta}$

$$J_{\mathbf{s}}(\boldsymbol{\theta}) = \sum_{i=1}^{2} \frac{\partial}{\partial \boldsymbol{\theta}} \{\mathbf{J}_{qi}^* \otimes \mathbf{J}_{pi}\}[\mathbf{I}_4 \otimes \mathrm{vec}(\mathbf{C}_{i\{pq\}})]. \tag{4.28}$$

Thus, variations of any unbiased estimator of parameter vector $\boldsymbol{\theta}$, lets say $\widehat{\boldsymbol{\theta}}$, is bounded from below by the CRLB as

$$\mathrm{Var}(\widehat{\boldsymbol{\theta}}) \geq [2\sigma^{-2}\,\mathfrak{Re}(J_{\mathbf{s}}^H J_{\mathbf{s}})]^{-1}. \tag{4.29}$$

Lets try to bound the error variations of the clustered calibration parameters assuming that the two sources construct a single cluster, called cluster number 1. We reform (4.20) as

$$\mathbf{V}_{pq} = \widetilde{\mathbf{J}}_{p1}(\mathbf{C}_{1\{pq\}} + \mathbf{C}_{2\{pq\}})\widetilde{\mathbf{J}}_{q1}^H + \boldsymbol{\Gamma}_{1\{pq\}} + \boldsymbol{\Gamma}_{2\{pq\}} + \mathbf{N}_{pq}, \tag{4.30}$$

where $\boldsymbol{\Gamma}_{i\{pq\}}$, referred to as the "clustering error" matrices, are given by

$$\boldsymbol{\Gamma}_{i\{pq\}} = \mathbf{J}_{pi}\mathbf{C}_{i\{pq\}}\mathbf{J}_{qi}^H - \widetilde{\mathbf{J}}_{p1}\mathbf{C}_{i\{pq\}}\widetilde{\mathbf{J}}_{q1}^H, \tag{4.31}$$

and $\widetilde{\mathbf{J}}_{p1}(\widetilde{\boldsymbol{\theta}})$ is the clustered calibration solution at receiver p.
(4.30) implies that what is considered as the noise matrix $\widetilde{\mathbf{N}}_{pq}$ in the clustered calibration data model, (4.10), is in fact

$$\widetilde{\mathbf{N}}_{pq} \equiv \boldsymbol{\Gamma}_{1\{pq\}} + \boldsymbol{\Gamma}_{2\{pq\}} + \mathbf{N}_{pq}. \tag{4.32}$$

Vectorizing (4.30), the clustered calibration visibility vector is obtained by

$$\mathbf{y} = \widetilde{\mathbf{J}}_{q1}^* \otimes \widetilde{\mathbf{J}}_{p1}\mathrm{vec}(\mathbf{C}_{1\{pq\}} + \mathbf{C}_{2\{pq\}}) + \widetilde{\mathbf{n}}_{pq}, \tag{4.33}$$

where $\widetilde{\mathbf{n}}_{pq} = \mathrm{vec}(\widetilde{\mathbf{N}}_{pq})$.

We point out that depending on the observation as well as the positions of the two sources on the sky, the clustering error $\boldsymbol{\Gamma}_{i\{pq\}}$ will have different properties. However, in order to study the performance of the clustered calibration in a statistical sense, and to simplify our analysis, we make the following assumptions.

1. Consider statistical expectation over different observations and over different sky realizations where the sources are randomly distributed on the sky. In that case, almost surely $\mathrm{E}\{\widetilde{\mathbf{J}}\} \to \mathrm{E}\{\mathbf{J}\}$ and consequently

   $$\mathrm{E}\{\boldsymbol{\Gamma}_{i\{pq\}}\} \to \mathbf{0}. \tag{4.34}$$

   In other words, we assume the clustering error to have zero mean over many observations of different parts of the sky.

2. We assume that the closer the sources are together in the sky, the smaller the errors introduced by clustering would be. Therefore, given a set of sources, the clustering error will reduce as the number of clusters increase. In fact this error introduced by clustering vanishes when the number of clusters is equal to the number of sources (each cluster contains only one source). Therefore, given a set of sources, the variance of $\boldsymbol{\Gamma}_{i\{pq\}}$ will decrease as the number of clusters increase.

Using (4.34), and bearing in mind that $\mathrm{E}\{\mathbf{N}_{pq}\} = \mathbf{0}$, we can consider $\widetilde{\mathbf{n}}_{pq} \sim \mathcal{CN}(\mathbf{0}, \widetilde{\sigma}^2\mathbf{I}_4)$ where $\mathrm{E}\{\widetilde{\mathbf{n}}_{pq}\widetilde{\mathbf{n}}_{pq}^H\} = \widetilde{\sigma}^2\mathbf{I}_4$. Therefore,

$$\mathbf{y} \sim \mathcal{CN}(\widetilde{\mathbf{s}}, \widetilde{\sigma}^2\mathbf{I}_4),$$
$$\widetilde{\mathbf{s}} \equiv \widetilde{\mathbf{J}}_{q1}^* \otimes \widetilde{\mathbf{J}}_{p1}\mathrm{vec}(\mathbf{C}_{1\{pq\}} + \mathbf{C}_{2\{pq\}}),$$

and similar to (4.29), we have

$$\mathrm{Var}(\widehat{\widetilde{\boldsymbol{\theta}}}) \geq [2\widetilde{\sigma}^{-2}\,\mathfrak{Re}(J_{\widetilde{\mathbf{s}}}^H J_{\widetilde{\mathbf{s}}})]^{-1}. \tag{4.35}$$

We use numerical simulations to compare the un-clustered and clustered calibrations performances via their CRLBs which are given by (4.29) and (4.35), respectively.

Example 2: CRLB for two sources and one cluster

We simulate a twelve hour observation of two point sources with intensities $I_1 = 11.25$ and $I_2 = 2.01$ Jy at sky coordinates (l, m) equal to $(-0.014, -0.005)$ and $(-0.011, -0.010)$ radians, respectively. We use the uv-coverage of Westerbork Radio Synthesis Telescope (WSRT) with 14 receivers in this simulation.
We consider the $\mathbf{J}$ Jones matrices in (4.20) to be diagonal. Their amplitude and phase elements follow $\mathcal{U}(0.75, 0.95)$ and $\mathcal{U}(0.003, 0.004)$ distributions, respectively. The background noise is $\mathbf{N} \sim \mathcal{CN}(\mathbf{0}, 10\mathbf{I})$. Jones matrices of the clustered calibration, $\widetilde{\mathbf{J}}_{p1}$ for $p = 1, 2$, are obtained as $\mathbf{J}_{p1} + \mathcal{U}(0.02, 0.40)e^{j\mathcal{U}(0.5,2)}$. For 20 realizations of $\widetilde{\mathbf{J}}$ matrices, we calculated CRLB of the un-clustered and clustered calibrations using (4.29) and (4.35), respectively. The results are presented in Fig. 4.5. As shown in this figure, for small enough errors matrices $\boldsymbol{\Gamma}$ of (4.31), the clustered calibration's CRLB stands below the un-clustered calibration's CRLB. On the other hand, with increasing power of error matrices, or the power of effective noise $\widetilde{\mathbf{N}}$, the un-clustered calibration's CRLB becomes lower than the clustered calibration's CRLB.

Analysis of CRLB

Generally, if source 1 is considerably brighter than source 2, $||\mathbf{C}_{1\{pq\}}|| \gg ||\mathbf{C}_{2\{pq\}}||$, and if the weak source power is much lower than the noise level, $||\mathbf{C}_{2\{pq\}}|| \ll ||\mathbf{N}_{pq}||$, then clustered calibration's performance is better than un-clustered calibration. Note that the worst performance of both calibrations is at the faintest source and we are more concerned to compare the CRLBs for this source.

The CRLBs obtained for the un-clustered and clustered calibrations in (4.29) and (4.35), respectively, are both almost equal to the inverse of the Signal to Interference plus Noise Ratio (SINR), SINR^{-1}. In un-clustered calibration, the effective signal for the faintest source is $\mathbf{C}_{2\{pq\}}$ where the noise is $\mathbf{N}_{pq}$. Therefore, SINR for this source is

$$\mathrm{SINR}_2 = \frac{||\mathbf{C}_{2\{pq\}}||^2}{||\mathbf{N}_{pq}||^2}. \tag{4.36}$$

But, in clustered calibration, the effective signal and noise are $\widetilde{\mathbf{C}}_{\{pq\}} \equiv \mathbf{C}_{1\{pq\}} + \mathbf{C}_{2\{pq\}}$ and $\widetilde{\mathbf{N}}_{pq}$, respectively. Thus, SINR for the cluster is

$$\mathrm{SINR}_c = \frac{||\widetilde{\mathbf{C}}_{\{pq\}}||^2}{||\widetilde{\mathbf{N}}_{pq}||^2}. \tag{4.37}$$

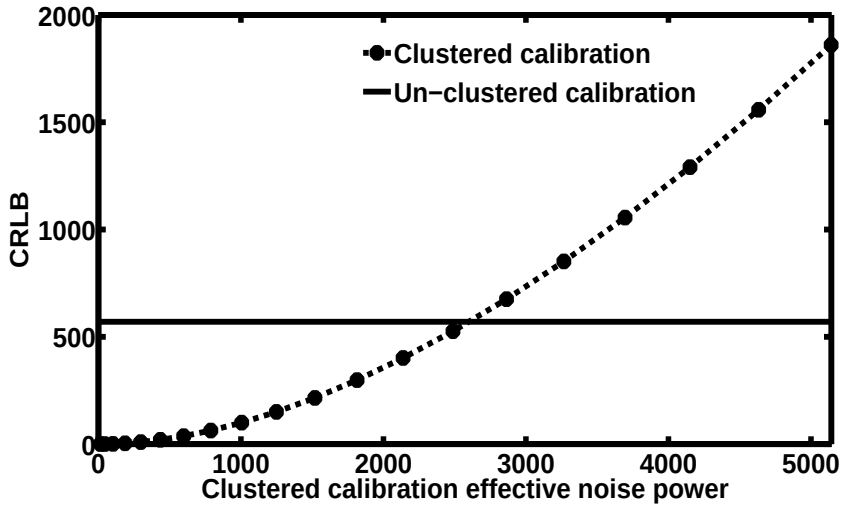

Figure 4.5: Clustered and un-clustered calibrations CRLB. When the effective noise power of the clustered calibration, $||\widetilde{\mathbf{N}}||^2$, is small enough, then its CRLB is lower than of the un-clustered calibration's and it reveals a superior performance.

Clustered calibration has an improved performance when

$$\text{SINR}_c \gg \text{SINR}_2. \tag{4.38}$$

Consider the two possible extremes in a clustered calibration procedure:

1. Clustering many sources in a large field of view to a very small number of clusters. In this case, the angular diameter of a cluster is probably too large for the assumption of uniform corruptions to apply. Subsequently, dedicating a single solution to all the sources of every cluster by clustered calibration introduces clustering error matrices $\mathbf{\Gamma}$ with a large variance (see (4.31)). Having high interference power, the clustered calibration effective noise $\widetilde{\mathbf{N}}$ of (4.32) becomes very large. Therefore, clustered calibration SINR will be very low and it does not produce high quality results.

2. Clustering sources in a small field of view to a very large number of clusters. In this case, the variance of $\mathbf{\Gamma}$ matrices are almost zero while the signal powers of source clusters are almost as low as of the individual sources. Therefore, the SINR of clustered calibration is almost equal to the un-clustered calibration SINR and the calibration performance is expected to be almost the same as well.
   Thus, the best efficiency of clustered calibration is obtained at the smallest number of clusters for which (4.38) is satisfied. We use the SINR of (4.38) as an efficient criterion for detecting the optimum number of clusters.

Generalization to many sources and many clusters

For the visibility vector $\mathbf{y}$ of un-clustered calibration's general data model, presented by (4.6), we have

$$\mathbf{y} \sim \mathcal{CN}(\sum_{i=1}^{K} \mathbf{s}_i(\boldsymbol{\theta}), \boldsymbol{\Pi}). \tag{4.39}$$

Therefore, the CRLB of un-clustered calibration is

$$\text{var}(\boldsymbol{\theta}) \geq \left[2\,\mathfrak{Re}\left\{ (\sum_{i=1}^{K} J_{\mathbf{s}_i}(\boldsymbol{\theta}))^H \boldsymbol{\Pi}^{-1} (\sum_{i=1}^{K} J_{\mathbf{s}_i}(\boldsymbol{\theta})) \right\} \right]^{-1},$$

where $J_{\mathbf{s}_i}$ is the Jacobian matrix of $\mathbf{s}_i$ with respect to $\boldsymbol{\theta}$.

Computing the exact CRLB is more complicated when we have clustered calibration. In the clustered calibration measurement equation, given by (4.13), we have

$$\widetilde{\mathbf{n}} \equiv \sum_{i=1}^{K} \boldsymbol{\Gamma}_i + \mathbf{n}, \tag{4.40}$$

where $\mathbf{n}$ is the un-clustered calibration's noise vector,

$$\boldsymbol{\Gamma}_i = [\text{vec}(\boldsymbol{\Gamma}_{i\{12\}})^T \ldots \text{vec}(\boldsymbol{\Gamma}_{i\{(N-1)N\}})^T]^T, \tag{4.41}$$

and $\boldsymbol{\Gamma}_{i\{pq\}}$ is given by (4.31). Due to the existence of the nuisance parameters $\boldsymbol{\Gamma}_i$ in the clustered calibration data model, calculation of its conventional CRLB is impractical. This leads us to the use of Cramer-Rao like bounds devised in the presence of the nuisance parameters (Gini & Reggiannini, 2000). We apply the Modified CRLB (MCRLB) (Gini et al., 1998) to the performance of clustered calibration.

The MCRLB for estimating the errors of $\widehat{\tilde{\boldsymbol{\theta}}}$ in the presence of the nuisance parameters $\boldsymbol{\Gamma}$ (clustering error) is defined as

$$\text{var}(\widehat{\tilde{\boldsymbol{\theta}}}) \geq \left[\text{E}_{\mathbf{y},\boldsymbol{\Gamma}} \left\{ -\text{E}_{\mathbf{y}|\boldsymbol{\Gamma}} \left\{ \frac{\partial}{\partial \tilde{\boldsymbol{\theta}}} \frac{\partial}{\partial \tilde{\boldsymbol{\theta}}^T} \ln\{P(\mathbf{y}|\boldsymbol{\Gamma}; \tilde{\boldsymbol{\theta}})\} \right\} \right\} \right]^{-1}, \tag{4.42}$$

where $P(\mathbf{y}|\boldsymbol{\Gamma}; \tilde{\boldsymbol{\theta}})$ is the Probability Density Function (PDF) of the visibility vector $\mathbf{y}$ assuming that the $\boldsymbol{\Gamma}$ matrices of (4.41) are a priori known. Since $\mathbf{n} \sim \mathcal{CN}(\mathbf{0}, \boldsymbol{\Pi})$, from (4.13) we have

$$\mathbf{y}|\boldsymbol{\Gamma} \sim \mathcal{CN}([\sum_{i=1}^{Q} \tilde{\mathbf{s}}_i + \sum_{i=1}^{K} \boldsymbol{\Gamma}_i], \boldsymbol{\Pi}), \tag{4.43}$$

and therefore in (4.42), $-\text{E}_{\mathbf{y}|\boldsymbol{\Gamma}} \left[\frac{\partial}{\partial \tilde{\boldsymbol{\theta}}} \frac{\partial}{\partial \tilde{\boldsymbol{\theta}}^T} \ln\{P(\mathbf{y}|\boldsymbol{\Gamma}; \tilde{\boldsymbol{\theta}})\} \right]$, which is called the modified Fisher information, is equal to

$$2\mathfrak{Re}\{[\sum_{i=1}^{Q} J_{\tilde{\mathbf{s}}_i}(\tilde{\boldsymbol{\theta}}) + \sum_{i=1}^{K} J_{\boldsymbol{\Gamma}_i}(\tilde{\boldsymbol{\theta}})]^H \boldsymbol{\Pi}^{-1} [\sum_{i=1}^{Q} J_{\tilde{\mathbf{s}}_i}(\tilde{\boldsymbol{\theta}}) + \sum_{i=1}^{K} J_{\boldsymbol{\Gamma}_i}(\tilde{\boldsymbol{\theta}})]\}.$$

Note that $\mathrm{E}_{\mathbf{y},\mathbf{\Gamma}}$ in (4.42) could be estimated by Monte-Carlo method.

As a rule of thumb, reducing the heavy computational cost of MCRLB, one can interpret the SINR test of (4.38) as follows: If in average the effective SINR of clustered calibration, SINR_c, gets higher than the effective SINR of un-clustered calibration obtained for the weakest observed signal, SINR_w,

$$\mathrm{E}\{\mathrm{SINR}_c\} \gg \mathrm{E}\{\mathrm{SINR}_w\}, \tag{4.44}$$

then clustered calibration can achieve a better results. In (4.44), the expectation is taken with respect to the thermal noise $\mathbf{N}$, error matrices $\mathbf{\Gamma}$, and all the baselines.

Example 3: MCRLB and SINR estimations

We simulate WSRT including $N = 14$ receivers which observe fifty sources with intensities below 15 Jy. The source positions and their brightness follow uniform and Rayleigh distributions, respectively. The background noise is $\mathbf{N} \sim \mathcal{CN}(\mathbf{0}, 15\mathbf{I}_M)$, where $M = 2N(N-1) = 364$. We cluster sources using divisive hierarchical clustering, into Q number of clusters where $Q \in \{3, 4, \ldots, 50\}$. Clustered calibration's Jones matrices, $\widetilde{\mathbf{J}}$, are generated as $\mathcal{U}(0.9, 1.1)e^{j\mathcal{U}(0,0.2)}$. Since for smaller number of clusters, we expect larger interference (errors) in clustered calibration's solutions, for every Q, we consider $\sum_{i=1}^{50} \mathbf{\Gamma}_i \sim \mathcal{CN}(\mathbf{0}, \frac{150}{Q}\mathbf{I}_M)$. The choice of the complex Gaussian distribution for the error matrices $\mathbf{\Gamma}$ is due to the central limit theorem and the assumptions made in section 4.4.1.

We proceed to calculate the clustered calibration's MCRLB, given by (4.42), and $\mathrm{E}\{\mathrm{SINR}_c\}$, utilizing the Monte-Carlo method. Jacobian matrices for MCRLB are calculated numerically and in computation of $\mathrm{E}\{\mathrm{SINR}_c\}$, signal power of every cluster is obtained only using the cluster's brightest and faintest sources. The estimated results of MCRLB and $\mathrm{E}\{\mathrm{SINR}_c\}$ are presented by Fig. 4.6 and Fig. 4.7, respectively. As we can see in Fig. 4.6, for very small Q, where the effect of interference is large, MCRLB is high. By increasing the number of clusters, MCRLB decreases and reaches its minimum where the best performance of the clustered calibration is expected. After that, due to the dominant effect of the background noise, MCRLB starts to increase until it reaches the CRLB of un-clustered calibration. The same result is derived from $\mathrm{E}\{\mathrm{SINR}_c\}$ plot of Fig. 4.7. As Fig. 4.7 shows, $\mathrm{E}\{\mathrm{SINR}_c\}$ is low for very small Q, when the interference (i.e., the error due to clustering) is large. By increasing the number of clusters, $\mathrm{E}\{\mathrm{SINR}_c\}$ increases and gets its highest peak for which the clustered calibration performs the best. After that, it decreases and converges to the $\mathrm{E}\{\mathrm{SINR}\}$ of un-clustered calibration.

4.4.2 Computational cost

In the measurement equation of un-clustered calibration, presented in (4.6), we have $M = 2N(N-1)$ constraints given by the visibility vector $\mathbf{y}$, and need to solve for $P = 4KN$ unknown parameters $\boldsymbol{\theta}$. If $P > M$, then (4.6) will be an under-determined non-linear system. This clarifies the need of having a small enough N (number of antennas) and a large enough K (number of sources) for estimating $\boldsymbol{\theta}$. However, clustered calibration, (4.13), has the advantage of decreasing the number of directions, K, relative to the number of source clusters, $Q \ll K$. This considerably cuts down the number of unknown parameters P that needs to be calibrated, thus reducing the computational cost of calibration.

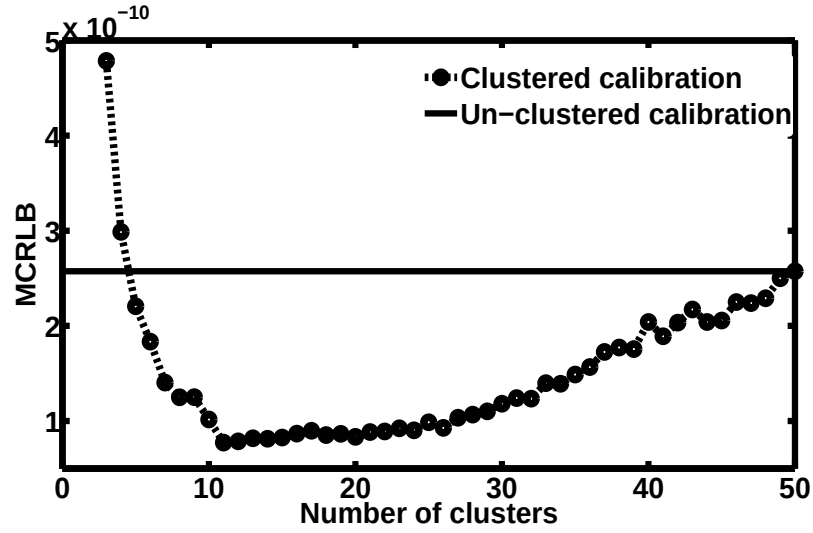

Figure 4.6: Clustered calibration's MCRLB. For very small Q, where the effect of interference is large, MCRLB is high. By increasing the number of clusters, MCRLB decreases and reaches its minimum where the best performance of the clustered calibration is expected. After that, due to the dominant effect of the background noise, MCRLB starts to increase until it reaches the un-clustered calibration CRLB.

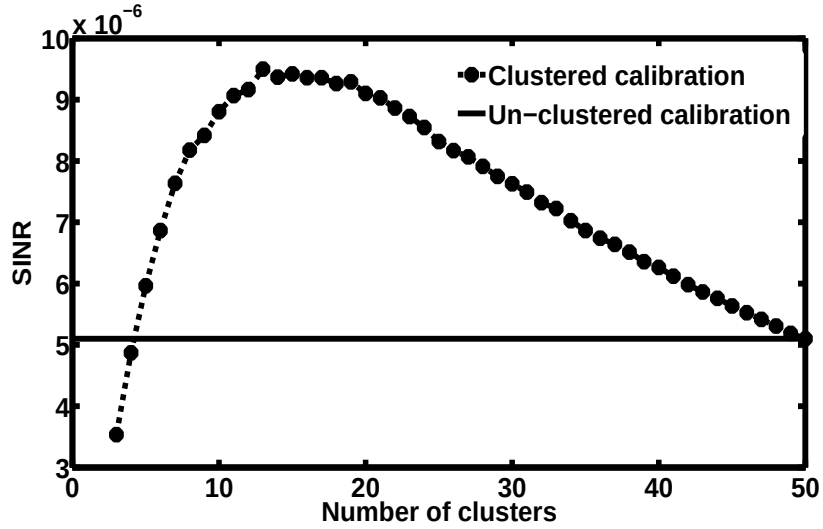

Figure 4.7: Clustered calibration's SINR. SINR is low for small Q, when the interference is large. By increasing the number of clusters the SINR increases and gets its highest level for which the best performance of the calibration is expected. After that, it decreases due to the dominant effect of the background noise, and converges to the un-clustered calibration SINR.

4.5 Selection Of Number Of Clusters

Consider a clustered calibration procedure with a predefined clustering scheme. There is no guarantee that the calibration results for Q number of clusters, where $Q \in \{1, 2, \ldots, K\}$ is randomly chosen, is the most accurate. Thus, we seek the optimum number of clusters at which the clustered calibration performs the best. In this section, we describe the use of: (i) Akaike's Information Criterion (AIC) (Akaike, 1973), as well as (ii) Likelihood-Ratio Test (LRT) (Graves, 1978), in finding this optimum Q for a given observation. Some other alternative criteria could also be found in Wax & Kailath (1985). Note that for different clustering schemes the optimum Q is not necessarily the same.

4.5.1 Akaike's Information Criterion (AIC)

We utilize Akaike's Information Criterion (AIC) to find the optimum Q for clustered calibration. Consider having $\widetilde{\mathbf{n}} \sim \mathcal{CN}(\mathbf{0}, \widetilde{\sigma}^2\mathbf{I}_M)$ in the general data model of clustered calibration, (4.13). Then, the log-likelihood of the visibility vector $\mathbf{y}$ is given by

$$\begin{aligned} \mathcal{L}(\widetilde{\boldsymbol{\theta}}|\mathbf{y}) &= -M\log\pi - M\log\widetilde{\sigma}^2 \\ &- \frac{1}{\widetilde{\sigma}^2}(\mathbf{y} - \sum_{i=1}^{Q}\widetilde{\mathbf{s}}_i(\widetilde{\boldsymbol{\theta}}))^H(\mathbf{y} - \sum_{i=1}^{Q}\widetilde{\mathbf{s}}_i(\widetilde{\boldsymbol{\theta}})). \end{aligned} \tag{4.45}$$

The maximum likelihood estimation of the noise variance $\widetilde{\sigma}^2$ is

$$\widehat{\widetilde{\sigma}^2} = \frac{1}{M}(\mathbf{y} - \sum_{i=1}^{Q}\widetilde{\mathbf{s}}_i(\widetilde{\boldsymbol{\theta}}))^H(\mathbf{y} - \sum_{i=1}^{Q}\widetilde{\mathbf{s}}_i(\widetilde{\boldsymbol{\theta}})). \tag{4.46}$$

Substituting (4.46) in (4.45), we arrive at the maximum likelihood estimation of $\widetilde{\boldsymbol{\theta}}$,

$$\begin{aligned} \mathcal{L}(\widehat{\widetilde{\boldsymbol{\theta}}}|\mathbf{y}) &= -M\log\pi - M \\ &- M\log\{\frac{1}{M}(\mathbf{y} - \sum_{i=1}^{Q}\widetilde{\mathbf{s}}_i(\widetilde{\boldsymbol{\theta}}))^H(\mathbf{y} - \sum_{i=1}^{Q}\widetilde{\mathbf{s}}_i(\widetilde{\boldsymbol{\theta}}))\}. \end{aligned} \tag{4.47}$$

Using (4.47), the AIC is given by

$$\mathrm{AIC}(Q) = -2\mathcal{L}(\widehat{\widetilde{\boldsymbol{\theta}}}|\mathbf{y}) + 2(2\widetilde{P}). \tag{4.48}$$

The optimum Q is selected as the one that minimizes $\mathrm{AIC}(Q)$.

4.5.2 Likelihood-Ratio Test (LRT)

Errors in clustered calibration originate from the system (sky and instrumental) noise, "clustering errors" introduced in section 4.4.1, and "solver noise" which is referred to as errors produced by the calibration algorithm itself. We assume that the true Jones matrices along different directions (clusters) at the same antenna are statistically uncorrelated. Therefore, if such correlations exist,

they are caused by the aforementioned errors. Consequently, the more accurate the clustered calibration solutions are, the smaller their statistical similarities would be. Based on this general statement, the best number of clusters in a clustered calibration procedure is the one which provides us with the minimum correlations in the calibrated solutions. Note that for a fixed measurement, the correlation due to the system noise is fixed. Therefore, differences in the statistical similarities of solutions obtained by different clustering schemes are only due to "clustering errors" and "solver noise".

To investigate the statistical interaction between the gain solutions we apply the Likelihood-Ratio Test (LRT).
Consider the clustered calibration solution $\widetilde{\mathbf{J}}_{pi}(\widetilde{\boldsymbol{\theta}})$ for directions i, $i \in \{1, 2, \ldots, Q\}$, at antennas p, where $p \in \{1, 2, \ldots, N\}$,

$$\widetilde{\mathbf{J}}_{pi} = \left[\begin{array}{cc} \widetilde{J}_{11,p} & \widetilde{J}_{12,p} \\ \widetilde{J}_{21,p} & \widetilde{J}_{22,p} \end{array} \right]_i . \tag{4.49}$$

Then, the parameter vector $\widetilde{\boldsymbol{\theta}}_{pi}$ (corresponding to the i-th direction and p-th antenna) is obtained by

$$\widetilde{\boldsymbol{\theta}}_{pi} = [\mathfrak{Re}(\widetilde{J}_{11,p})\ \mathfrak{Im}(\widetilde{J}_{11,p})\ \ldots\ \mathfrak{Re}(\widetilde{J}_{22,p})\ \mathfrak{Im}(\widetilde{J}_{22,p})]_i^T. \tag{4.50}$$

Let us define for each antenna p and each pair of directions k and l, where k and l are belong to $\{1, 2, ..., Q\}$, a vector $\mathbf{z}_{pkl}$ as

$$\mathbf{z}_{pkl} = [\widetilde{\boldsymbol{\theta}}_{pk}^T\ \widetilde{\boldsymbol{\theta}}_{pl}^T]^T. \tag{4.51}$$

In fact, we are concatenating the solutions of the same antenna for two different directions (clusters) together.

We define the null H_0 model as

$$H_0 :\ \mathbf{z}_{pkl} \sim \mathcal{N}(\mathbf{m}, \Sigma_0). \tag{4.52}$$

where

$$\mathbf{m} = [\bar{\mathbf{m}}(\widetilde{\boldsymbol{\theta}}_{pk})^T\ \bar{\mathbf{m}}(\widetilde{\boldsymbol{\theta}}_{pl})^T]^T, \tag{4.53}$$

and

$$\Sigma_{\mathbf{0}} = \left[\begin{array}{cc} s^2(\widetilde{\boldsymbol{\theta}}_{pk}) & 0 \\ 0 & s^2(\widetilde{\boldsymbol{\theta}}_{pl}) \end{array} \right]. \tag{4.54}$$

In (4.53) and (4.54), $\bar{\mathbf{m}}$ and s^2 are denoting sample mean and sample variance, respectively. Note that having a large number of samples in hand, the assumption of having a Gaussian distribution for solutions is justified according to the Central Limit theorem. The structure of the variance matrix $\Sigma_{\mathbf{0}}$ tells us that the statistical correlation between the components of the random vector $\mathbf{z}_{qkl}$, or between the solutions $\widetilde{\boldsymbol{\theta}}_{pk}$ and $\widetilde{\boldsymbol{\theta}}_{pl}$, is zero. This is the ideal case in which there are no estimation errors.

To investigate the validity of the null model compared with the case in which there exists some correlation between the solutions, we define the alternative H_1 model as

$$H_1 :\ \mathbf{z}_{pkl} \sim \mathcal{N}(\mathbf{m}, \Sigma_1), \tag{4.55}$$

where the variance matrix Σ_1 is given by

$$\Sigma_1 = \left[\begin{array}{cc} s^2(\widetilde{\boldsymbol{\theta}}_{pk}) & \mathrm{Cov}(\widetilde{\boldsymbol{\theta}}_{pk}, \widetilde{\boldsymbol{\theta}}_{pl}) \\ \mathrm{Cov}(\widetilde{\boldsymbol{\theta}}_{pk}, \widetilde{\boldsymbol{\theta}}_{pl})^T & s^2(\widetilde{\boldsymbol{\theta}}_{pl}) \end{array} \right]. \tag{4.56}$$

$\text{Cov}(\widetilde{\boldsymbol{\theta}}_{pk}, \widetilde{\boldsymbol{\theta}}_{pl})$ in (4.56) is the 8×8 sample covariance matrix.
Using the above models, the Likelihood-Ratio is defined as

$$\Lambda = -2\ln\left(\frac{\text{Likelihood for null model}}{\text{Likelihood for alternative model}}\right), \tag{4.57}$$

which has a χ^2 distribution with 64 degrees of freedom. As Λ becomes smaller, the null model, in which the statistical correlation between the solutions is zero, becomes more acceptable rather than the alternative model. Therefore, the smaller the Λ is, the less the clustered calibration's errors are, and vice-versa.

4.6 Simulation studies

We use simulations to compare the performance of un-clustered and clustered calibration. Working with simulations has the advantage of having the true solutions available, which is not the case in real observations. That makes the comparison much more objective. Nevertheless, the better performance of the clustered calibration in comparison with the un-clustered ones in calibrating for real observations of LOFAR is also shown by Kazemi et al. (2011); Yatawatta et al. (2013).

We simulate an East-West radio synthesis array including 14 antennas (similar to WSRT) and an 8 by 8 degrees sky with fifty sources with low intensities, below 3 Jy. The source positions and their brightness follow uniform and Rayleigh distributions, respectively. The single channel simulated observation at 355 MHz is shown in Fig. 4.8.

We proceed to add gain errors, multiplying source coherencies by the Jones matrices, as it is shown in (4.2), to our simulation. The amplitude and phase of the Jones matrices' elements are generated using linear combination of *sine* and *cosine* functions. We aim at simulating a sky with almost uniform variations on small angular scales. In other words, we provide very similar Jones matrices for sources with small angular separations. To accomplish this goal, for every antenna, we first choose a single direction as a reference and simulate its Jones matrix as it is explained before. Then, for the remaining forty nine sources, at that antenna, the Jones matrices (amplitude and phase terms) are that initial Jones matrix multiplied by the inverse of their corresponding angular distances from that reference direction. The result of adding such gain errors to our simulation is shown in Fig. 4.9.

4.6.1 Performance comparison of the Clustered and un-clustered calibrations at SNR=2

We add the thermal noise $\mathbf{n} \sim \mathcal{CN}(\mathbf{0}, \sigma^2\mathbf{I})$ with $\sigma^2 = 28$, as it is shown in (4.6), to our simulation. The result has a $SNR = 2$ and is presented in Fig. 4.10. We have chosen to present the case of $SNR = 2$ since for this particular simulated observation both the divisive hierarchical and the weighted K-means clustered calibrations achieve their best performances at the same number of clusters, which will be shown later in this section.

We apply un-clustered and clustered calibration on the simulation to compare their efficiencies. The fifty sources are grouped into $Q \in \{3, 4, \ldots, 49\}$ number of clusters, using the proposed divisive hierarchical and weighted K-means clustering algorithms. Self-calibration is implemented via Space Alternating Generalized Expectation Maximization (SAGE) algorithm (Fessler

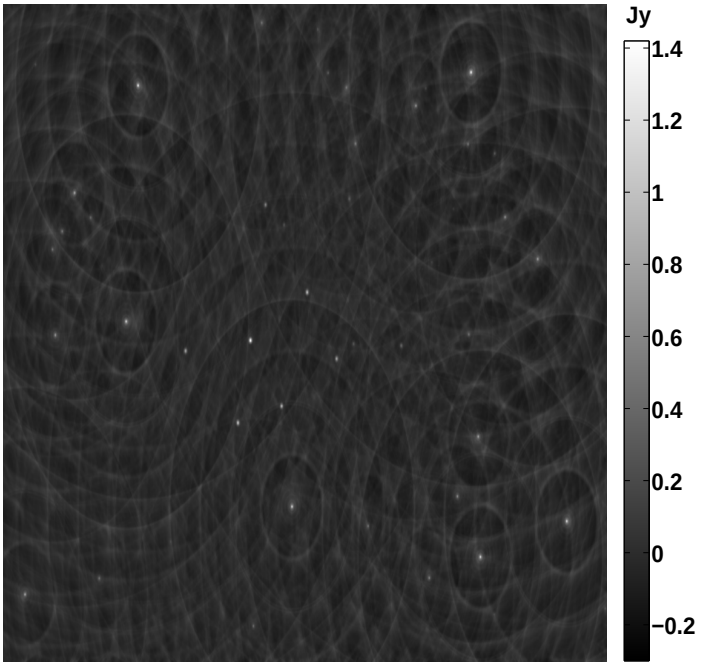

Figure 4.8: Single channel simulated observation of fifty sources, with intensities below 3 Jy. The source positions and their brightness are following uniform and Rayleigh distributions, respectively. The image size is 8 by 8 degrees at 355 MHz. There are no gain errors and noise in the simulation.

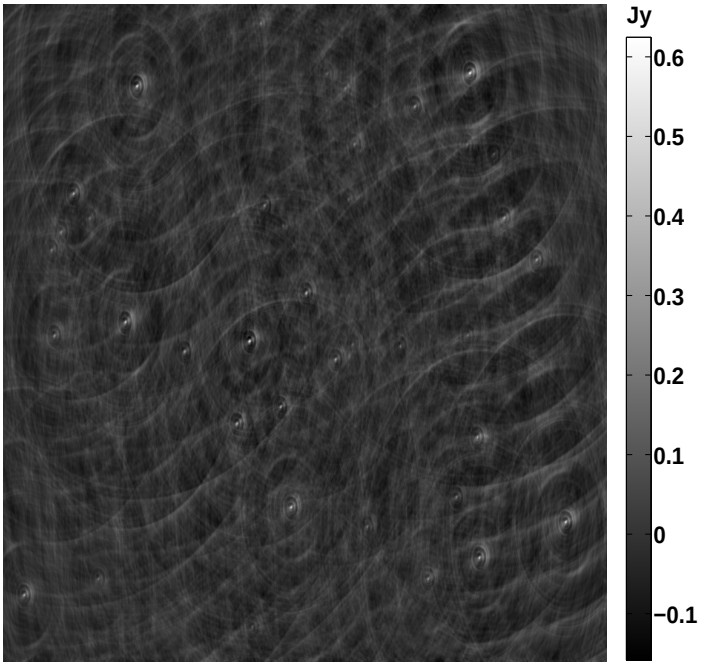

Figure 4.9: Simulated image with added gain errors. The errors, the complex 2×2 Jones matrices, are generated as linear combinations of *sin* and *cos* functions. The variation of the sky is almost uniform on small angular scales.

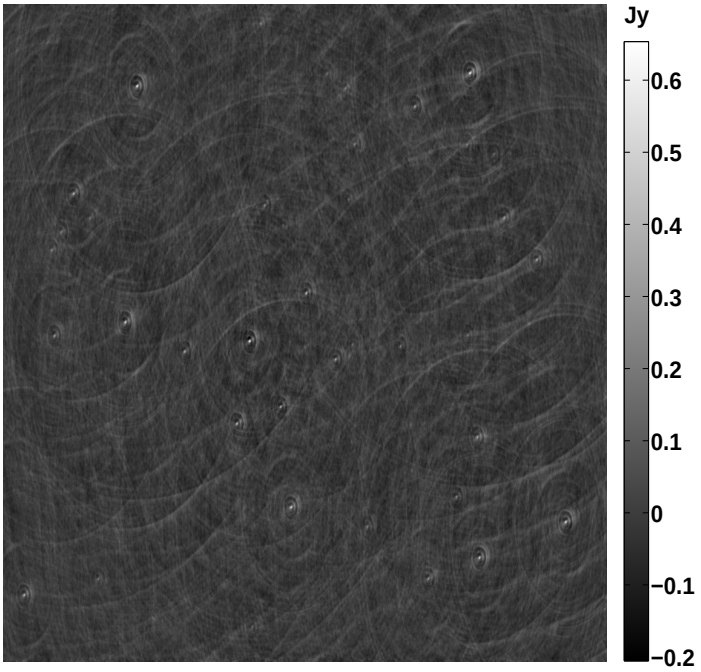

Figure 4.10: Simulated image of signals, corrupted by gain errors and added by the thermal noise, as in (4.6). The simulated noise vector $\mathbf{n}$ has zero mean complex Gaussian distribution and the resulted SNR is equal to 2.

& Hero (1994); Yatawatta et al. (2009); Kazemi et al. (2011), chapter 2) with nine iterations. Plots of the averaged Frobenius distance between the simulated (true) Jones matrices and the obtained solutions is shown in Fig. 4.11. As we can see in Fig. 4.11, for both clustering schemes, increasing the number of clusters decreases this distance and the minimum is reached at thirty three clusters ($Q = 33$). Beyond this number of clusters, it increases until the fifty individual sources become individual clusters. This shows that the best performance of both the divisive hierarchical and the weighted K-means clustered calibrations is at thirty three clusters and is superior to that of the un-clustered calibration.
The Frobenius distance curves in Fig. 4.11, the MCRLB curve in Fig. 4.6, and the SINR curve in Fig. 4.7 illustrate that clustered calibration with an extremely low number of clusters does not necessarily perform better than the un-clustered calibration. The reason is that when there are only a small number of clusters, the interference, or the so-called "clustering errors" introduced in section 4.4.1, is relatively large. Therefore, the effect of this interference dominates the clustering of signals. On the other hand, we reach the theoretical performance limit approximately after twenty five number of clusters and therefore increasing the number beyond this point gives highly variable results, mainly because we are limited by the number of constraints as opposed to the number of parameters that we need to solve for. But, this is not the case for the plots in Fig. 4.6 and Fig. 4.7. The reason is that the MCRLB results of Fig. 4.6 as well as the SINR results of Fig. 4.7 are obtained by Monte-Carlo method with iterations over fifty different sky and noise realizations. However, Fig. 4.11 is limited to the presented specific simulation with only one sky and one noise realization.

The residual images of the un-clustered calibration as well as the divisive hierarchical and weighted K-means clustered calibrations for $Q = 33$ are shown by Fig. 4.21 and Fig. 4.13, respectively. As it is shown by Fig. 4.21, in the result of un-clustered calibration, the sources are almost not subtracted at all and there is a significant residual error remaining. The residuals have asymmetric Gaussian distribution with variance $\sigma^2 = 82.29$ which is much larger than the simulated (true) noise variance $\sigma^2 = 10.85$. On the other hand, the sources have been perfectly subtracted in the case of clustered calibration, Fig. 4.13, and the residuals converge into the simulated background noise distribution. The residuals of the divisive hierarchical and Weighted K-means clustered calibrations follow symmetric zero mean Gaussian distributions with $\sigma^2 = 20.17$ and $\sigma^2 = 18.76$, respectively. These variances are closer to the simulated one $\sigma^2 = 10.85$ and this indicates the promising performance of clustered calibration. As we can see, hierarchical clustered calibration provides a slightly better result compared to the K-means one. This is due to the fact that hierarchical clustering constructs clusters of smaller angular diameters and thus it assigns the same calibration solutions to the sources with smaller angular separations.

We also calculate the Root Mean Squared Error of Prediction (RMSEP) to assess the performance of clustered and un-clustered calibrations' non-linear regressions. The results of log(RMSEP), presented by Fig. 4.14, also justify that the best efficiencies of the hierarchical and K-means clustered calibrations are obtained at thirty three number of clusters. But, note that there is a difference between the behavior of log(RMSEP) plot of Fig. 4.14 and the plots of MCRLB, SINR, and Frobenius distance between the simulated Jones matrices and solutions in Fig. 4.6, Fig. 4.7, and Fig. 4.11, respectively. In Fig. 4.14, log(RMSEP) of clustered calibration is less than that of un-clustered calibration, even for extremely low number of clusters. This means that even with those low number of clusters, clustered calibration performs better than the un-clustered calibration. This is somewhat in disagreement with the scenarios shown in Fig. 4.6, Fig. 4.7, and Fig. 4.11. For a better understanding of the reason behind this contrast, first lets see how the residual

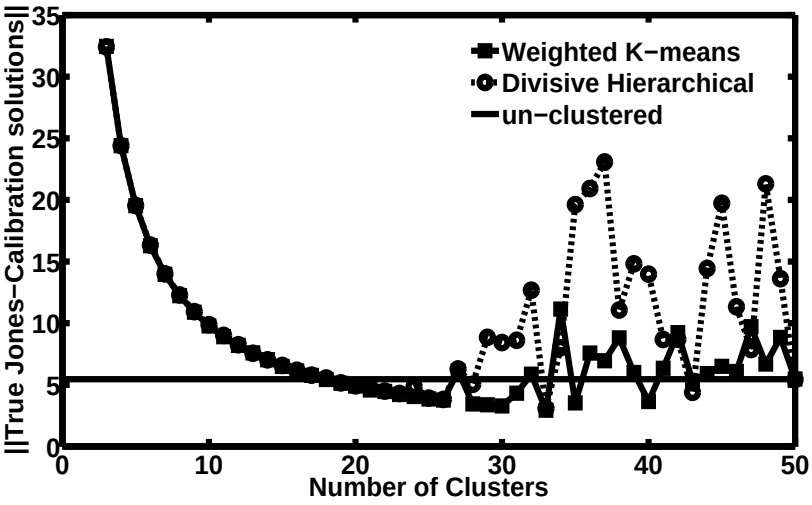

Figure 4.11: The averaged Frobenius distance between the simulated (true) Jones matrices and the solutions of clustered and un-clustered calibrations. The two curves represent clustered calibration via divisive hierarchical and weighted K-means clustering algorithms. By increasing the number of clusters, for both clustering methods, this distance is decreased and gets its minimum at thirty three clusters. After that, it is increased till the fifty individual sources. That shows that the best performance of the clustered calibration is at thirty three clusters.

errors are originated.
Based on (4.13) and (4.40), in the clustered calibration strategy, we have

$$\mathbf{y} = \sum_{i=1}^{Q} \widetilde{\mathbf{s}}_i(\widetilde{\boldsymbol{\theta}}) + \sum_{i=1}^{K} \boldsymbol{\Gamma}_i + \mathbf{n}, \tag{4.58}$$

After executing a calibration for the above data model, there is a distance between the target parameters $\widetilde{\boldsymbol{\theta}}$ and the estimated solutions $\widehat{\widetilde{\boldsymbol{\theta}}}$. This is the so-called "solver noise", mentioned in section 4.5.2. Thus, the residuals are given as

$$\mathbf{y} - \sum_{i=1}^{Q} \widetilde{\mathbf{s}}_i(\widehat{\widetilde{\boldsymbol{\theta}}}) = \sum_{i=1}^{Q} \{\widetilde{\mathbf{s}}_i(\widetilde{\boldsymbol{\theta}}) - \widetilde{\mathbf{s}}_i(\widehat{\widetilde{\boldsymbol{\theta}}})\} + \sum_{i=1}^{K} \boldsymbol{\Gamma}_i + \mathbf{n}. \tag{4.59}$$

From (4.59), we immediately see that the background noise $\mathbf{n}$ is fixed and the "clustering errors" are calculated for all the sources as $\sum_{i=1}^{K} \boldsymbol{\Gamma}_i$. However, since we solve only for Q directions and not for all the K sources individually, the "solver noise" part, $\sum_{i=1}^{Q} \{\widetilde{\mathbf{s}}_i(\widetilde{\boldsymbol{\theta}}) - \widetilde{\mathbf{s}}_i(\widehat{\widetilde{\boldsymbol{\theta}}})\}$, is also calculated only for Q clusters and not for all the K sources. It is clear that for a very small Q, this term could be much less than for $Q \simeq K$. Therefore, in Fig. 4.11, the result of RMSEP at a very low number of clusters is still less than the ones at $Q = K$. When Q is not at the two extremes of being very small or very large (almost equal to the number of individual sources), then the result of RMSEP is promising. Moreover, applying more accurate calibration methods or increasing the

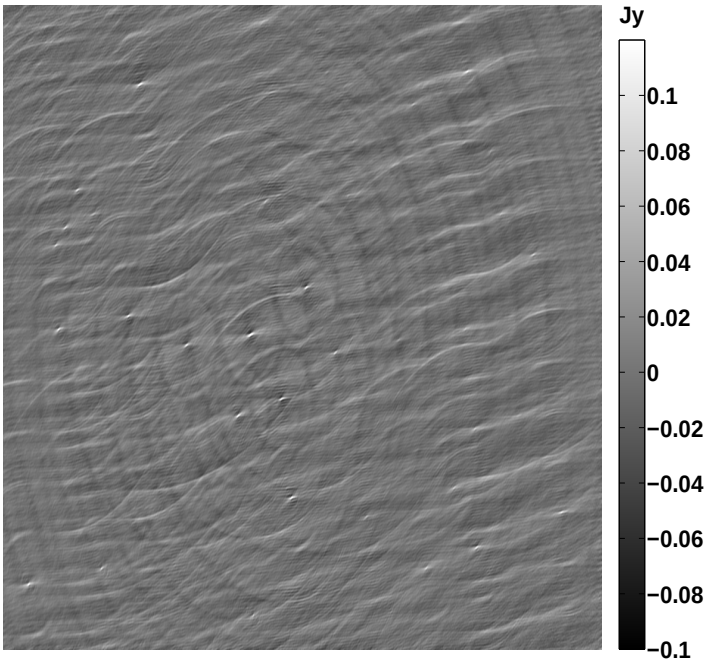

Figure 4.12: Residual image of the un-clustered SAGE calibration for fifty sources. The sources are almost not subtracted at all and there are significant residual errors around them. The residuals have asymmetric Gaussian distribution with variance $\sigma^2 = 82.29$ which is much larger than the true noise variance $\sigma^2 = 10.85$.

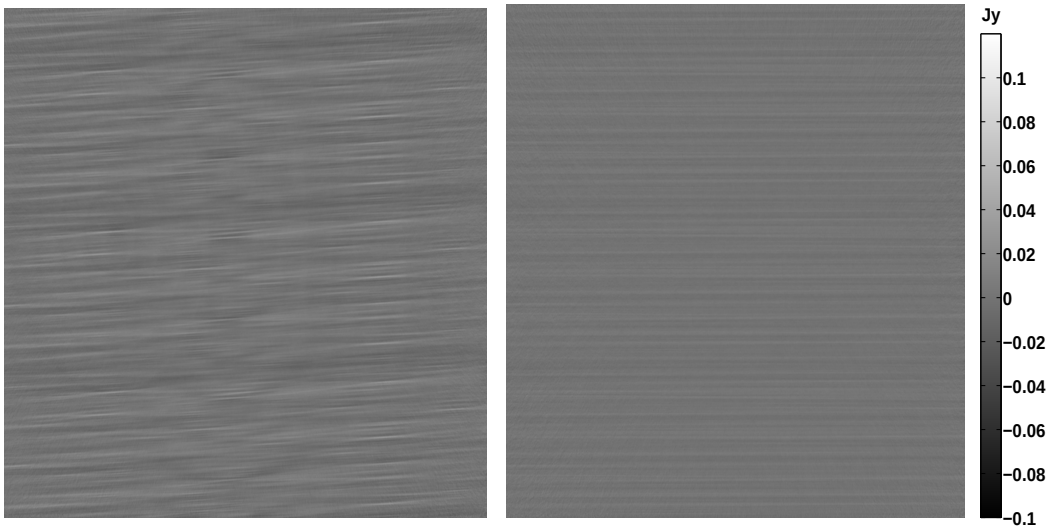

Figure 4.13: The residual images of the clustered calibration using hierarchical (right) and Weighted K-means (left) clustering methods with thirty three source clusters. Calibration is implemented by SAGE algorithm. The sources are subtracted perfectly and the residuals converge the simulated background noise distribution. The hierarchical clustering and Weighted K-means residuals follow symmetric zero mean Gaussian distributions with $\sigma^2 = 20.17$ and $\sigma^2 = 18.76$, respectively, where the simulated noise distribution is, $\mathcal{CN}(\mathbf{0}, 10.85\mathbf{I})$.

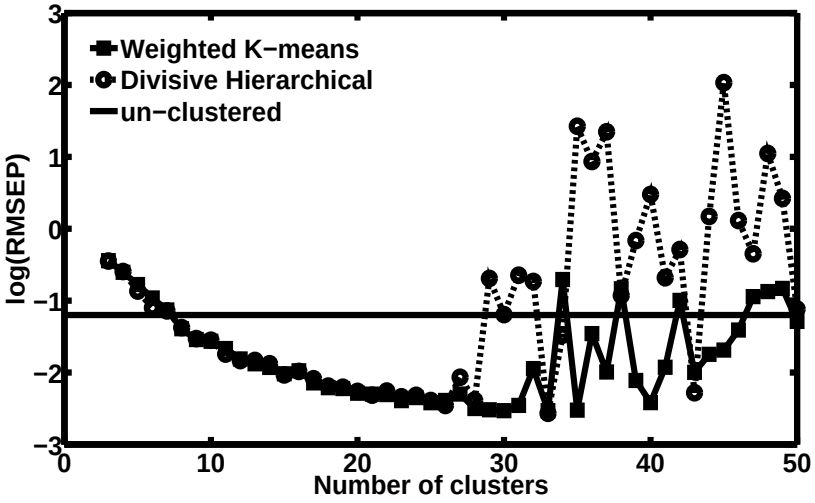

Figure 4.14: The RMSEP for clustered and un-clustered calibrations. The results are obtained using a base ten logarithmic scale. The two curves are corresponding to clustered calibration via divisive hierarchical and weighted K-means clustering algorithms. By increasing the number of clusters, the results are decreased and the minimum result is obtained at thirty three clusters. After that, the results are increased till the fifty individual sources. That shows the superior performance of the clustered calibration compared to the un-clustered one. The best performance of the clustered calibration for both of the applied clustering methods is at thirty three number of clusters.

number of iterations, the "solver noise" will decrease and subsequently, we expect the RMSEP curve to have the same behavior as the curves of Fig. 4.7 and Fig. 4.14.

4.6.2 Optimum number of clusters for SNR=2

We utilize AIC and LRT to select the optimum number of clusters for which clustered calibration achieves its best performance. The methods are applied to our simulation for the case of SNR=2. The AIC and Likelihood-Ratio results are shown by Fig. 4.15 and Fig. 4.16, respectively. They both agree on $Q = 33$ as the optimum number of clusters for the divisive hierarchical and Weighted K-means clustered calibrations. Likelihood-Ratio plot of Fig. 4.16 has almost the same behavior as the plot of Frobenius distance between the simulated Jones matrices and the obtained solutions presented by Fig. 4.11. The reason is that the results of the both plots are obtained using the solutions themselves as the input data. However, since AIC results are computed using the residual errors as inputs, which is also the case for obtaining the RMSEP curves of Fig. 4.14, AIC curves of Fig. 4.15 are slightly steeper than the Frobenius distance between the simulated Jones matrices and solutions and the Likelihood-Ratio curves of Fig. 4.11 and Fig. 4.16, respectively.

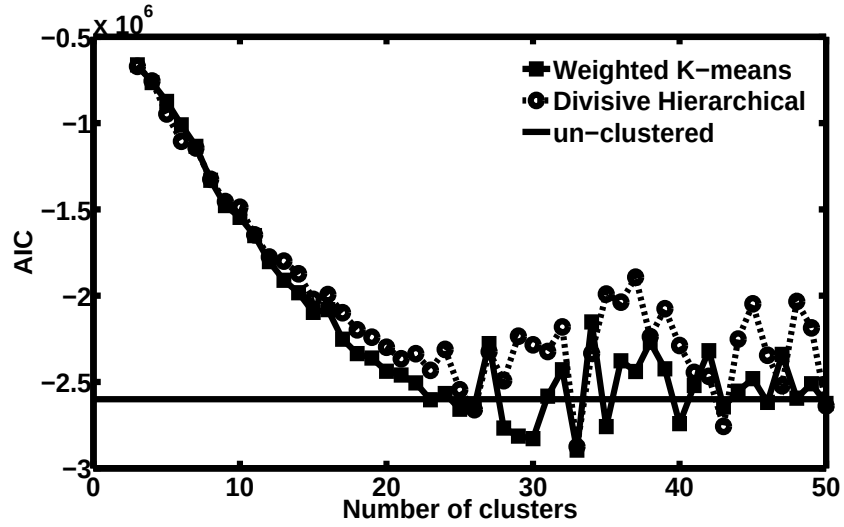

Figure 4.15: AIC plot for clustered and un-clustered calibrations. Both the weighted K-means and divisive hierarchical clustered calibrations get their minimum AIC at thirty three clusters. This illustrates that their best performances are obtained at this number of clusters. Also, their AIC results at thirty three clusters is lower than the un-clustered calibration's AIC, which shows their better performances compared to the un-clustered calibration.

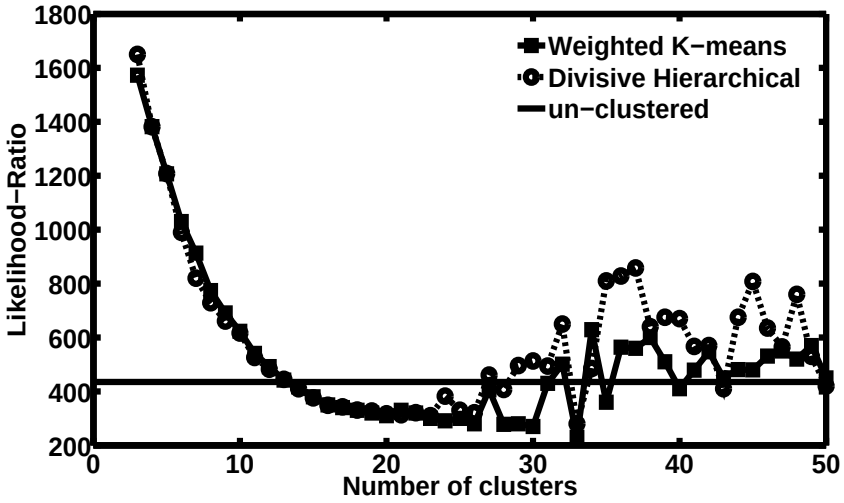

Figure 4.16: Likelihood-ratio of the gain solutions obtained by clustered and un-clustered calibrations. In the both cases of weighted K-means and divisive hierarchical clustered calibrations, the minimum Likelihood-ratio values belong to thirty three number of clusters. These minimums are also lower than the un-clustered calibration's Likelihood-ratio result. Therefore, clustered calibration via both the clustering methods performs better than the un-clustered calibration and it achieves the best accuracy in its solutions at thirty three clusters.

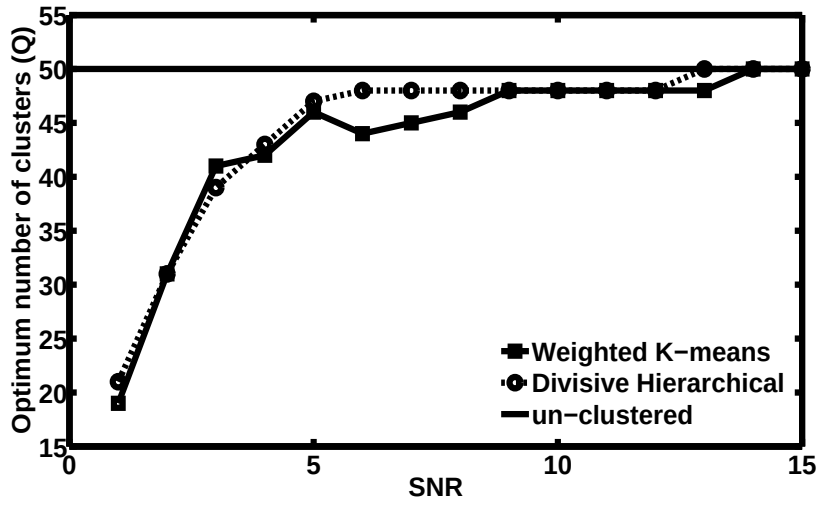

Figure 4.17: The optimum number of clusters, on which the best performance of clustered calibration is obtained, at different SNRs. For low SNRs, the efficiency of the clustered calibration is superior to the un-clustered calibration. As the SNR gets higher, clustered calibrations achieve their best solutions utilizing a higher number of clusters. Finally, when the SNR is high enough, the performance of un-clustered calibration becomes better than the clustered one.

4.6.3 Clustered calibration's efficiency at different SNRs

We start changing the noise in our simulation to see how it effects the clustered calibration's efficiency. We simulate the cases for which SNR$\in \{1, 2, \ldots, 15\}$ and apply clustered calibration on them. Since the sky model does not change, the clusters obtained by divisive hierarchical and weighted K-means methods for the case of SNR$= 2$ remain the same. Fig. 4.17 shows the optimum number of clusters, on which the best performances of clustered calibrations are obtained for those different SNRs. As we can see in Fig. 4.17, for low SNRs, the optimum Q is small. By increasing the SNR, the optimum Q is increased till it becomes equal to the number of all the individual sources that we have in the sky, i.e., K. This means that when the SNR is very low, the benefit of improving signals by clustering sources is much higher than the payoff of introducing "clustering errors" in a clustered calibration procedure. Therefore, clustered calibration for $Q \ll K$ has a superior performance compared to the un-clustered calibration. While for a high enough SNR, the situation becomes the opposite. In this case, the un-clustered calibration achieves better results compared to clustered calibration having the disadvantage of introducing "clustering errors".

Emperical estimation of SINR

Having the results of Fig. 4.17 in hands, we could find an empirical model for estimating the optimum number of clusters for various SNRs. Note that by changing the observation and the instrument characteristics, this model will also be changed.

As it is explained in section 4.4.1, the best performance of clustered calibration is obtained

when the SINR is at its highest level. Fig. 4.17 shows the number of clusters on which the maximum SINR was obtained, where the signal (sky) and the noise powers are known a priori. Thus, the only unknown for estimating the SINR is the interference, or the "clustering errors", for which we need to have a prediction model. After estimating the SINR using this model, finding the optimum Q will be straightforward.

Consider the definition of "clustering errors" given by (4.31). It is logical that for every source, the difference between its true Jones matrix and the clustered calibration solution, $||\mathbf{J} - \widetilde{\mathbf{J}}||$, is a function of the angular distance between the source and the centroid of the cluster that it belongs to. Based on this and using (4.31) and (4.34), for the interference of the i-th cluster at baseline $p - q$ we assume that

$$\sum_{l \in L_i} \mathbf{\Gamma}_{l\{pq\}} \sim \mathcal{CN}(\mathbf{0}, \eta||\widetilde{\mathbf{C}}_{i\{pq\}}||^2\{D(L_i)\}^{\nu}\mathbf{I}_2), \tag{4.60}$$

where η and ν are unknowns. (4.60), in fact, considers an interference power (variance) of $\eta||\widetilde{\mathbf{C}}_{i\{pq\}}||^2\{D(L_i)\}^{\nu}$ for every i-th cluster, $i \in \{1, 2, \ldots, Q\}$, at baseline $p - q$. Assuming the interferences of different clusters to be statistically independent from each other, and bearing in mind that the baseline's additive noise $\mathbf{N}_{pq}$ has also a complex Gaussian distribution independent from those interferences', then the noise plus interference power for the i-th cluster at baseline $p - q$ is obtained by

$$\eta||\widetilde{\mathbf{C}}_{i\{pq\}}||^2\{D(L_i)\}^{\nu} + ||\mathbf{N}_{pq}||^2. \tag{4.61}$$

Fitting suitable η and ν to (4.61), the SINR for the i-th cluster at baseline $p - q$ is equal to the cluster's signal power, $||\widetilde{\mathbf{C}}_{i\{pq\}}||^2$, divided by the result of (4.61). Subsequently, estimation of $\mathrm{E}\{\mathrm{SINR}_c\}$ will be straight forward where the expectation is calculated with respect to all the source clusters and all the baselines. Note that simulation provides us with the true noise power, $||\mathbf{N}_{pq}||^2$. In the case of having a real observation, this power could be estimated by (4.46).
Fig. 4.18 shows the number of clusters on which divisive hierarchical and weighted K-means clustered calibrations achieve their maximum estimated $\mathrm{E}\{\mathrm{SINR}_c\}$. The results are calculated for SNR$\in \{1, 2, \ldots, 15\}$. For the hierarchical clustering $\eta = 1550$ and $\nu = 0.3$, and for the K-means clustering $\eta = 2500$ and $\nu = 0.003$. As we can see, for both the clustering methods, these maximum $\mathrm{E}\{\mathrm{SINR}_c\}$s are mostly obtained at the true optimum number of clusters for which clustered calibration performed the best. Introducing more refined models compared to (4.60) could even improve the current result.

4.6.4 Different sky models

So far, we have limited our studies to sky models in which the brightness and position of the radio sources follow Rayleigh and uniform distributions, respectively. These characteristics provide us with a smooth and uniform variation of flux intensities in our simulated skies. In such a case, the effects of the background noise on the faintest and the strongest signals are almost the same. Therefore, if clustered calibration performs better than the un-clustered calibration that would be only based on upgrading the signals against the noise. Although, in nature, we mostly deal with the sky models in which the distribution of the flux intensities is a power law, with a steep slope, and the spatial distribution is Possion. Hence, there exist a few number of very bright sources, whose signals are considerably stronger than the others, and they are sparse in the field of view. The corruptions of the background noise plus the interferences of the strong signals of those few

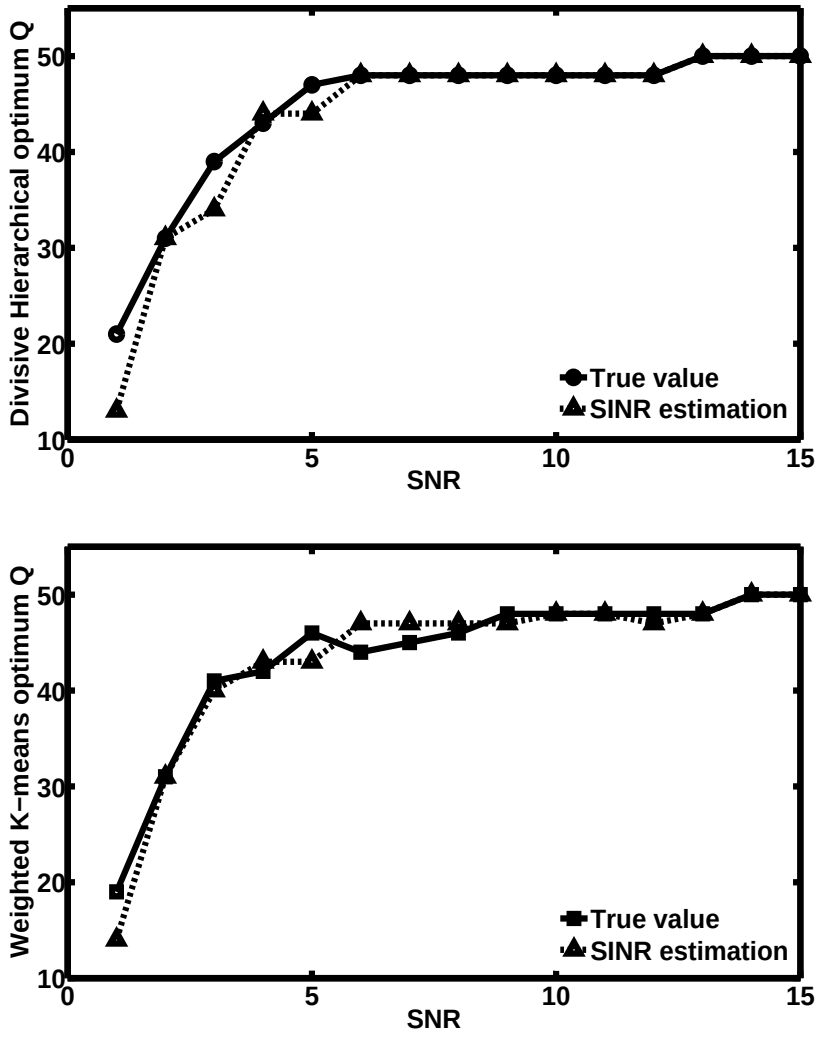

Figure 4.18: Optimum number of clusters at which the divisive hierarchical (top) and Weighted K-means (bottom) clustered calibrations perform the best. For both of the clustering methods, the results obtained by SINR estimations mostly match the true optimum number of clusters.

bright sources make the calibration of the other faint point sources impractical. Thus, there is the need for utilizing the clustered calibration which applies the solutions of the bright sources to their closed by fainter ones or solves for upgraded signals obtained by adding up a group of faint signals together. This has been shown by Kazemi et al. (2011); Yatawatta et al. (2013), when comparing the efficiency of the clustered and un-clustered calibrations on LOFAR real observations. In this section, using simulations, we also reveal the superiority of clustered calibration compared to the un-clustered calibration for such sky models.

We simulate a sky of 52 radio point sources which are obtained by modified Jelić et al. (2008) foreground model. The brightness distribution of the point sources follows the source count function obtained at 151 MHz (Willott et al., 2001), while the angular clustering of the sources are characterized by a typical two-point correlation function,

$$\rho(d) = Ad^{-0.8}. \tag{4.62}$$

In (4.62), ρ is the two point correlation function, d is the angular separation, and A is the normalisation amplitude of ρ. The flux cut off is 0.1 Jy.
We convolve the signals with gain errors which are linear combinations of *sin* and *cos* functions, as in the previous simulation of this section. At the end, a zero mean Gaussian thermal noise with a variance of 3 mJy is added to the simulated data. The result is shown by Fig. 4.19. In Fig. 4.19, all the bright sources are gather in the right side of the image, rather than being uniformly distributed in the field of view, and the rest of the sources are so faint that are almost invisible.

We apply the clustered and un-clustered calibrations on $Q \in \{3, 4, \dots 51\}$ number of clusters and $K = 52$ number of individual sources, respectively. The clustering method used is the divisive hierarchical and the calibrations are executed via SAGE algorithm with nine number of iterations. The residual noise variances obtained are demonstrated in Fig. 4.20. As Fig. 4.20 shows, the level of the residual noise obtained by the clustered calibration for $Q \in \{15, 16, \dots 45\}$ number of clusters is always below the result of the un-clustered calibration. This proves the better performance of the clustered calibration. The best result of the clustered calibration, with the minimum noise level, is achieved for $Q = 27$ number of clustered.

The residual images of the clustered calibration with $Q = 27$ number of source clusters, and the un-clustered calibration for $K = 52$ individual sources are shown by Fig. 4.21. In the right side of the residual image of the un-clustered calibration there exist artificial strips caused by over and under estimating the brightest sources of the field of view. That shows the problematic performance of the un-clustered calibration. However, clustered calibration has generated much less artificial effects after subtracting these sources. On top of that, the zoomed in window in the left side of the images of Fig. 4.21 show that the faint sources are not removed by the un-clustered calibration at all, while being almost perfectly subtracted by the clustered calibration. Moreover, the residual noise of the clustered calibration follows a symmetric zero mean Gaussian distributions with a variation of 4.2 mJy, while the one from the un-clustered calibration has an asymmetric Gaussian distribution with mean and variance equal to -1.2 and 5.3 mJy, respectively. Taking to account that the simulated noise distribution is a zero mean Gaussian distribution with a variance of 3 mJy, the superior performance of the clustered calibration compared to the un-clustered one is evident.

As the final conclusion of this simulation, calibrating below the noise level, clustered calibration always performs better than the un-clustered calibration. This is regardless of the sky model and is only based on the fact that solving for individual sources with very poor signals is impractical. Nevertheless, when some sources are very close to each other, the sky corruption on their

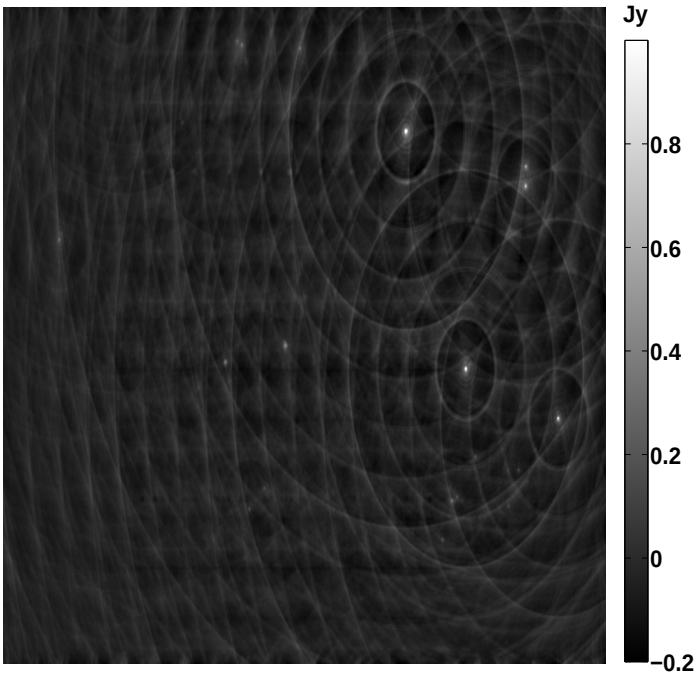

Figure 4.19: Thirty channel simulated observation of fifty two sources which are obtained by modified Jelić et al. (2008) foreground model. The convolved gain errors are generated as linear combinations of *sin* and *cos* functions. The image size is 8 by 8 degrees and the additive thermal noise is a zero mean Gaussian noise with a variance of 3 mJy.

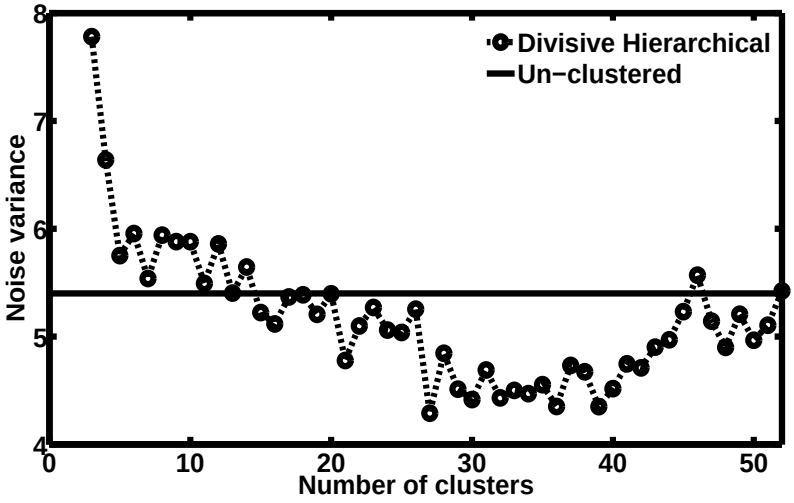

Figure 4.20: The noise variances of the residual images, obtained by clustered and un-clustered calibrations, in mJy. The level of the residual noise obtained by the clustered calibration for $Q \in \{15, 16, \ldots 45\}$ number of clusters stands below the result of the un-clustered calibration. That reveals the superior performance of the clustered calibration in comparison with the un-clustered one. The best result of the clustered calibration which achieves the minimum noise level is at $Q = 27$ number of clustered.

signals would be exactly the same and there is no point in solving for every of them individually.

4.7 Conclusions

In this chapter, we demonstrate the superior performance of "clustered calibration" compared to un-clustered calibration especially in calibrating sources that are below the calibration noise level. The superiority is in the sense of having more accurate results by the enhancement of SNR as well as by the improvement of computational efficiency by reducing the number of directions along which calibration has to be performed.

In a "clustered calibration" procedure, sky sources are grouped into some clusters and every cluster is calibrated as a single source. That replaces the coherencies of individual sources by the total coherency of the cluster. Clustered calibration is applied to these new coherencies that carry a higher level of information compared with the individual ones. Thus, for the calibration of sources below the noise level it has a considerably better performance compared to un-clustered calibration. An analytical proof of this superiority, for an arbitrary sky model, is presented using MCRLB and SINR analysis.

KLD and LRT are utilized to detect the optimum number of clusters, for which the clustered calibration accomplishes its best performance. A model for estimating SINR of clustered calibration is also presented by which we could find the optimum number of clusters at low computational cost.

Divisive hierarchical as well as Weighted K-means clustering methods are used to exploit the spatial proximity of the sources. Simulation studies reveal clustered calibration's improved

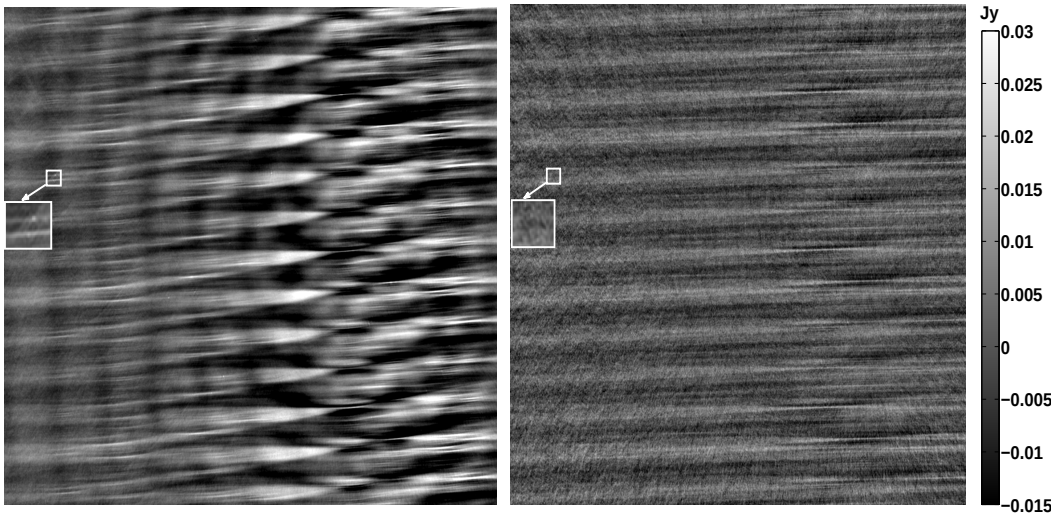

Figure 4.21: The residual images of the clustered calibration for $Q = 27$ number of clusters (right) and the un-clustered calibration for $K = 52$ (left). Calibration is implemented by SAGE algorithm with nine number of iterations and the clustering method applied is divisive hierarchical. In the right side of the residual image of the un-clustered calibration we see strips of over and under estimations due to problematic performance of the clustered calibration in subtracting the brightest sources. The zoomed in window in the left side of the image also shows that the faint sources are not removed at all. However, clustered calibration could remove all the faint sources almost perfectly and has generated much less artificial effects after subtracting for the brightest sources in the right side of the field of view. Moreover, the residual noise of the clustered calibration follows a symmetric zero mean Gaussian distributions with a variation of 4.2 mJy, while the one from the un-clustered calibration has an asymmetric Gaussian distribution with mean and variance equal to -1.2 and 5.3 mJy, respectively. Taking to account that the simulated noise distribution is a zero mean Gaussian distribution with a variance of 3 mJy, the better performance of the clustered calibration compared to the un-clustered one is evident.

performance at a low SNR, utilizing these clustering algorithms. Both the clustering methods are hard clustering techniques which divide data to distinct clusters. However, we expect more accurate results using fuzzy (soft) clustering, which constructs overlapping clusters with uncertain boundaries. Application and performance of this type of clustering for clustered calibration will be explored in future work.

Chapter 5

Application of fuzzy clustering in radio interferometric calibration

submitted to MNRAS

ABSTRACT

Calibration of radio interferometric telescopes is an essential step in order to reach the full potential of their data in terms of precision and sensitivity. Traditional calibration algorithms use bright point sources in the observed field as a collection of single source calibrators. Recently, we have proposed the clustered calibration technique which groups the sources into well defined clusters. Assuming all the sources in a single cluster to be corrupted by the same errors, clustered calibration calibrates every cluster as a single source, where it uses all the source coherencies of that cluster simultaneously. This improves the accuracy of calibration as well as the computational cost. In our previous clustered calibration method we used a hard clustering technique to assign every source to exactly one cluster. However, in reality, the intensities of different sources affect each other. Therefore, defining clusters with soft boundaries, which means assigning every source to different clusters with different degrees of membership, is more accurate and efficient. In this chapter, we introduce a new method that applied fuzzy (soft) clustering in order to perform the calibration. In this method, which we call fuzzy-clustered calibration, the solution of every source is a linear combination of errors along different directions. This is obviously is more accurate and hence offers an improvement on hard clustered calibration in which the solution of every source is obtained only in the direction of its cluster's centroid. We apply the new fuzzy-clustered calibration on simulations and show that it performs better compared to the hard clustering one.

5.1 Introduction

Calibration of radio synthesis arrays refers to the estimation and reduction of errors introduced by the sky and the instrument in the measured data, before imaging. It is the most crucial task in order to achieve the interferometer's desired precision and sensitivity.

Very large radio interferometers such as the Square Kilometre Array (SKA)[1], the Murchison Widefield Array (MWA) (Lonsdale et al., 2009), the Precision Array to Probe Epoch of Reionization (PAPER) (Parsons et al., 2010), and the LOw Frequency ARray (LOFAR) (van Haarlem et al., 2013), produce a huge amount of data which need to be very accurately calibrated in the shortest time possible. Therefore, the two main calibration challenges are increasing the accuracy of solutions, and decreasing the computations. Advanced calibration techniques have been proposed (e.g. Kazemi et al. (2012)) which meet the two challenges up to a very high level. However, it has always been a great challenge to calibrate data with a low Signal to Noise Ratio (SNR). Performance of calibration techniques (Bernardi et al., 2011; Liu et al., 2009; Pindor et al., 2010) is in fact limited to sources that have a high enough SNR (SNR) to be distinguished from the background noise.

The recently introduced clustered calibration technique (Kazemi et al. (2013b), chapter 4) has shown a better performance in source calibration below the noise level. The calibration groups sources into well defined clusters, and improves the information used for calculating solutions by incorporating the total of signals observed at every cluster. Every cluster is calibrated as a single source with an intensity equal to the sum of the intensities of its sources. Thus, in the case of calibrating the signals of faint sources, it provides a considerably better result compared to un-clustered calibration. Moreover, calibrating for a fewer number of source clusters than the number of individual sources in the sky, the computations of clustered calibration is considerably cheaper than the un-clustered one. Nevertheless, we would like to note that when the SNR is very high, applying clustered calibration could be a disadvantage. In such a case, it is better to use the signal of every individual (bright) source to calibrate the data as this will give more accurate results across the observational field.

The clustered calibration introduced by Kazemi et al. (2013b) (chapter 4) performs calibration on source clusters with hard boundaries. This means every source belongs to exactly one cluster. Consequently, the solution of every source is the one obtained in the direction of the centroid of the cluster that the source belongs to. However, in reality, calibration corrections vary continuously across the field of view, a fact that is captured much better with fuzzy (soft) clustering rather than hard clustering. The radiated signal of sources can be mixed with each other, and affect the areas of various clusters, and not only one cluster. Therefore, it is not accurate to consider sources in clusters with hard boundaries, and limit their signals to the area of their corresponding clusters. In order to increase the accuracy of clustered calibration, in this chapter, we apply fuzzy clustering ideas and implement them in the clustered calibration procedure. Note that, since in clustered calibration the source clustering is performed offline, using fuzzy clustering rather than any other hard clustering techniques does not cost any extra execution time.

The role of fuzzy clustering (Bezdek, 1981) becomes quite prominent among clustering techniques (Xu & Wunsch, 2008) due to its ability for quantifying a level of membership of the target data to detected clusters. We perform clustered calibration on fuzzy source clusters, where every source belongs to a number of clusters, simultaneously, according to some pre-defined membership degrees. In other words, in the clustered calibration procedure, we consider the source clus-

[1] http://www.skatelescope.org

ters to have soft boundaries. Such a clustered calibration, named as "soft clustered calibration", provides every source with a solution which is in fact a linear combination of the errors obtained along different directions. Applying fuzzy clustering of sources, we show that soft clustered calibration achieves a considerably higher accuracy level compared to hard clustered calibration.

This chapter is organized as follows: The data model of hard and soft clustered calibrations are presented in sections 5.2 and 5.3, respectively. A weighted fuzzy clustering of sources is proposed in section 5.4. In section 5.5, we demonstrate the superiority of the soft clustered calibration compared to the hard one, using simulations. Finally, we draw our conclusions in section 5.6.

The following notations are used in this chapter: Bold, lower case letters refer to column vectors, e.g., $\mathbf{y}$. Upper case bold letters refer to matrices, e.g., $\mathbf{C}$. All parameters are complex numbers, unless stated otherwise. The transpose and conjugation of a matrix are presented by $(.)^T$ and $(.)^*$, respectively. The matrix Kronecker product is denoted by $\otimes$. The uniform distribution is shown by $\mathcal{U}$.

5.2 Hard Clustered Calibration

In this section, we briefly describe the data model of hard clustered calibration (Kazemi et al. (2013b), chapter 4). For more details on the data model of radio interferometric calibration the reader is referred to Hamaker et al. (1996); Hamaker (2006).

Consider an interferometer with N receivers that observes K radio sources $x_1, \ldots, x_K$. The voltage introduced at the p-th receiver by the radiation of the i-th source, $\mathbf{e}_i$, is given by

$$\widetilde{\mathbf{v}}_{pi} = \mathbf{J}_{pi}\mathbf{e}_i, \tag{5.1}$$

where $\mathbf{J}_{pi}$ is the 2×2 Jones matrix (Hamaker et al., 1996), corresponding to direction-dependent corruptions in the signal. These corruptions are identified as,

$$\mathbf{J}_{pi} \equiv \mathbf{E}_{pi}\mathbf{Z}_{pi}\mathbf{F}_{pi}, \tag{5.2}$$

where $\mathbf{E}_{pi}$, $\mathbf{Z}_{pi}$, and $\mathbf{F}_{pi}$ are error matrices corresponding to the receiver's beam, ionospheric phase fluctuation, and Faraday Rotation for the radiated signal of the i-th source, at receiver p, respectively.

The total signal observed at every receiver p, $\mathbf{v}_p$, is a linear superposition of the corrupted signals $\widetilde{\mathbf{v}}_{pi}$ of the K sources, $i = 1, \ldots, K$, plus the thermal noise of the receiver. Note that the multitude of the ignored fainter sources also contribute to the noise. After correcting for the geometric delays of the receivers, the collected signals at every pair of receivers p and q are correlated with each other to introduce visibilities $\mathbf{V}_{pq} \equiv \mathrm{E}\{\mathbf{v}_p\mathbf{v}_q^H\}$ (Hamaker et al., 1996)

$$\mathbf{V}_{pq} = \mathbf{G}_p \left(\sum_{i=1}^{K} \mathbf{J}_{pi}\mathbf{C}_{i\{pq\}}\mathbf{J}_{qi}^H \right) \mathbf{G}_q^H + \mathbf{N}_{pq}. \tag{5.3}$$

In (5.3), $\mathbf{G}_p$ represents the errors which are common to all directions at receiver p, such as the receiver delay and amplitude errors. $\mathbf{C}_{i\{pq\}}$ and $\mathbf{N}_{pq}$ are also the Fourier transform of the i-th source *coherency* matrix $\mathrm{E}\{\mathbf{e}_i\mathbf{e}_i^H\}$ (Born & Wolf, 1999; Hamaker et al., 1996), and the additive noise of the baseline pq, respectively.

Since the gain $\mathbf{G}$ in (5.3) does not depend on the source directions, initially, the visibilities are corrected for that as,

$$\widetilde{\mathbf{V}}_{pq} = \mathbf{G}_p^{-1}\mathbf{V}_{pq}\mathbf{G}_q^{-H}. \tag{5.4}$$

Stacking up the vectorized visibilities of all the baselines in a vector $\mathbf{y} \equiv [\text{vec}(\widetilde{\mathbf{V}}_{12})^T \dots \text{vec}(\widetilde{\mathbf{V}}_{(N-1)N})^T]^T$, we arrive to the general data model of a traditional (un-clustered) calibration as

$$\mathbf{y} = \sum_{i=1}^{K} \begin{bmatrix} \mathbf{J}_{2i}^* \otimes \mathbf{J}_{1i}\text{vec}(\mathbf{C}_{i\{12\}}) \\ \vdots \\ \mathbf{J}_{Ni}^* \otimes \mathbf{J}_{(N-1)i}\text{vec}(\mathbf{C}_{i\{(N-1)N\}}) \end{bmatrix} + \mathbf{n}. \tag{5.5}$$

In (5.5), $\mathbf{n}$ is the additive noise vector,

$$\mathbf{n} \equiv [\text{vec}(\mathbf{G}_1^{-1}\mathbf{N}_{12}\mathbf{G}_2^{-H})^T \dots \text{vec}(\mathbf{G}_{(N-1)}^{-1}\mathbf{N}_{(N-1)N}\mathbf{G}_N^{-H})^T]^T,$$

which is normally assumed to be Gaussian. Calibration is, in fact, estimation of the $\mathbf{J}$ Jones matrices for all the K source directions in (5.5), and correcting for them before imaging.

Note that according to the definition of Jones matrices in (5.2), at a fixed receiver p,

$$\mathbf{J}_{pi} \approx \mathbf{J}_{pj}, \tag{5.6}$$

for every i-th and j-th sources, x_i and x_j, that have a very small angular separation from each other. This is the general assumption of the clustered calibration technique. Clustered calibration uses (5.6), on one hand, to decrease the number of directions that we need to calibrate for, and on the other hand, to improve the accuracy below the noise level, as follows:

Assume that we group the K sources $x_1, \dots, x_K$ into Q ($Q \ll K$) source clusters L_i, for $i \in \{1, \dots, Q\}$, with small enough angular diameters such that for the sources at the same cluster the sky variation is uniform. Based on (5.6), for every cluster L_i and at every receiver p, there is a unique solution $\widetilde{\mathbf{J}}_{pi}$ which is shared by all the sources of the cluster. Therefore, the un-clustered calibration data model of (5.5) is reformulated as,

$$\mathbf{y} = \sum_{i=1}^{Q} \begin{bmatrix} \widetilde{\mathbf{J}}_{2i}^* \otimes \widetilde{\mathbf{J}}_{1i}\text{vec}(\sum_{l\in L_i} \mathbf{C}_{l\{12\}}) \\ \vdots \\ \widetilde{\mathbf{J}}_{Ni}^* \otimes \widetilde{\mathbf{J}}_{(N-1)i}\text{vec}(\sum_{l\in L_i} \mathbf{C}_{l\{(N-1)N\}}) \end{bmatrix} + \mathbf{n}, \tag{5.7}$$

where (5.7) is the measurement equation of clustered calibration. Therefore, the whole difference between un-clustered and clustered calibrations is that in un-clustered calibration (5.5) we solve for every individual source x_i, $i \in \{1, \dots, K\}$, which has a signal power equal to $\mathbf{C}_i$, while in clustered calibration (5.7), we solve for every source cluster L_i, $i \in \{1, \dots, Q\}$, which has a boosted signal power of $\sum_{l\in L_i} \mathbf{C}_l$. Therefore, below the noise level, clustered calibration has better accuracy compared to un-clustered calibration due to upgrading signal powers (Kazemi et al. (2013b), chapter 4). Moreover, clustered calibration has much lower computational cost relative to un-clustered calibration. This is due to two reasons: i) clustered calibration solves for $Q \ll K$ number of directions, while the un-clustered for K number of directions, ii) clustered calibration would have less number of iterations (higher speed of convergence) compared to the un-clustered one because it uses a higher SNR to calculate solutions.

From now on, we refer to clustered calibration given in (5.7) as "hard" clustered calibration. Because, clustering of sources is a hard clustering scheme. This means every source belongs to one and only one cluster. In the next section, we introduce soft clustered calibration which utilizes fuzzy clustering methods to cluster sources in clustered calibration procedure.

5.3 Soft Clustered Calibration

In hard clustered calibration presented in (5.7), sources are grouped into clusters with hard boundaries. For every cluster, calibration is performed to estimate a unique solution in the direction of its centroid, using the total intensity of every source that belongs to it. Therefore, it is assumed that the brightness of every individual source affects exactly one cluster. However, if a source is very bright, its brightness affects almost all the field of view. Thus, since its intensity is used by hard clustered calibration only in the cluster that it belongs to, and not in any other clusters, the size of the cluster must be very large. That means that we must consider, and solve for, a single solution on a large part of the sky (the area of that large cluster), which harms the accuracy of calibration. The sky can actually vary even on very small scales. On the other hand, even the weak signal of a very faint source can affect more than the limited area of a small single cluster. To deal with these issues in the clustered calibration technique, the most efficient way is to execute the calibration on source clusters with soft boundaries; where a source can belong to more than one cluster. For this purpose, we apply fuzzy clustering techniques (Bezdek, 1981) to assign a source to different clusters via different membership degrees. We name the clustered calibration method via fuzzy clustering of sources as "soft clustered calibration". It is formulated as follows:

Consider a fuzzy clustering of the K sources $x_1, \ldots, x_K$ into Q clusters $L_1, \ldots, L_Q$. Also assume that u_{il} is the degrees of membership that the source x_l belongs to the cluster L_i,

$$\sum_{i=1}^{Q} u_{il} = 1, \quad \text{for } l = 1, \ldots, K, \tag{5.8}$$

$$0 \leq u_{il} \leq 1, \quad \text{for } i = 1, \ldots, Q, \text{ and } l = 1, \ldots, K. \tag{5.9}$$

The model used to determine the exact values of u_{il} will be explained in section 5.4. We introduce the soft clustered calibration data model as,

$$\mathbf{y} = \sum_{i=1}^{Q} \begin{bmatrix} \widetilde{\mathbf{J}}^*_{2i} \otimes \widetilde{\mathbf{J}}_{1i} \text{vec}(\sum_{l=1}^{K} u_{il} \mathbf{C}_{l\{12\}}) \\ \vdots \\ \widetilde{\mathbf{J}}^*_{Ni} \otimes \widetilde{\mathbf{J}}_{(N-1)i} \text{vec}(\sum_{l=1}^{K} u_{il} \mathbf{C}_{l\{(N-1)N\}}) \end{bmatrix} + \mathbf{n}. \tag{5.10}$$

Thus, both hard (5.7) and soft (5.10) clustered calibrations estimate Jones matrices of Q directions (Q clusters' centroids). The only difference between them is that, for a given cluster L_i, the hard clustered calibration solves for a brightness intensity equal to the total of all the intensities of sources in L_i, $\sum_{x_l \in L_i} \mathbf{C}_l$, while the soft clustered calibration solves for the brightness contribution of every source of the sky model in L_i, $\sum_{l=1}^{K} u_{il} \mathbf{C}_l$. Table 1 shows this difference from another point of view. Table 1 presents the contribution of a given source x_l in visibilities of a given baseline $p-q$ for the un-clustered, hard clustered, and soft clustered calibration data models (5.5), (5.7), and (5.10), respectively. As we can see in Table 1, for un-clustered and hard clustered calibrations, the signal of the source x_l is considered to be corrupted by the Jones matrices of a single direction, which is the direction of the sources x_l, and of the cluster L_i, respectively. However, in soft clustered calibration, the corruptions are assumed to be a linear combination of the Jones matrices of all the Q clusters. This is more practical than the two alternative cases, because the errors mostly vary smoothly as a function of angular position of sources. Therefore, among the three methods, for calibrating below the noise level, a better performance in the sense of the speed of convergence is expected from soft clustered calibration. The reasons for such a claim are:

Table 1

calibration method	contribution of the source x_l in visibilities of the baseline $p-q$
un-clustered	$[\mathbf{J}_{ql}^{*} \otimes \mathbf{J}_{pl}]\text{vec}\mathbf{C}_{l\{pq\}}$
Hard clustered, $x_l \in L_i$	$[\widetilde{\mathbf{J}}_{qi}^{*} \otimes \widetilde{\mathbf{J}}_{pi}]\text{vec}\mathbf{C}_{l\{pq\}}$
Soft clustered	$[\sum_{i=1}^{Q} u_{il}\widetilde{\mathbf{J}}_{qi}^{*} \otimes \widetilde{\mathbf{J}}_{pi}]\text{vec}\mathbf{C}_{l\{pq\}}$

Table 5.1: This table presents the contribution of a given source x_l in the visibilities of a given baseline $p-q$ for the un-clustered, hard clustered, and soft clustered calibration data models (5.5), (5.7), and (5.10), respectively. As we can see, for un-clustered and hard clustered calibrations, the signal of the source x_l is considered to be corrupted by the Jones matrices of a single direction, which is the direction of the sources x_l, and of the cluster L_i, respectively. However, in soft clustered calibration, the corruptions are assumed to be a linear combination of the Jones matrices of all the Q clusters.

(i) it calibrates for a few number of source clusters with strong signal powers rather than a large number of individual sources with weak signals, (ii) it can preserve the effect of every source in the whole field of view using the fuzzy membership degrees.

5.4 Weighted Fuzzy Clustering of radio sources

In this section, we design the optimum Q fuzzy clusters for the K sources in our sky model such that the centroids of the clusters are inclined towards the strongest signals. The reason of such a design is to get the most out of the high information carried by the signals of the brightest sources for providing the highest accuracy of calibration. Thus, we search for a fuzzy clustering of radio sources which takes into account their angular positions in the sky, as well as their intensities. For this purpose, we utilized the weighted fuzzy clustering scheme presented by Wan et al. (2008), and we defined the weights based on source intensities. This led to minimizing the objective function,

$$f = \sum_{i=1}^{Q}\sum_{l=1}^{K} w_l (u_{il})^m (d_{il})^2. \tag{5.11}$$

where w_l is the weight associated to the source x_l as

$$w_l \equiv \frac{\text{Intensity of } x_l}{\text{Minimum intensity of all the sources}}, \tag{5.12}$$

component $m > 1$, and d_{il} is the angular separation between the source and the centroid of the cluster L_i. The angular separation between two equatorial coordinates (α_a, δ_a) and (α_b, δ_b), in radians, is obtained by

$$\tan^{-1}\frac{\sqrt{\cos^2\delta_b \sin^2\Delta\alpha + [\cos\delta_a \sin\delta_b - \sin\delta_a \cos\delta_b \cos\Delta\alpha]^2}}{\sin\delta_a \sin\delta_b + \cos\delta_a \cos\delta_b \cos\Delta\alpha},$$

where $\Delta\alpha = \alpha_b - \alpha_a$.

Based on Wan et al. (2008), the membership degrees and the centroid of every i-th cluster, denoted as c_i, can be iteratively updated as,

$$u_{il} = \frac{1}{\sum_{j=1}^{K} (\frac{d_{il}}{d_{jl}})^{2/(m-1)}},$$
$$c_i = \frac{\sum_{l=1}^{K} w_l (u_i l)^m x_l}{\sum_{l=1}^{K} w_l (u_{il})^m},$$

until the objective function f in (5.11) is minimized, or is below a certain value. Note that the component m defines the level of fuzziness of the clustering. When $m \simeq 1$, the membership degrees become either one or zero. That means, fuzzy clustering becomes hard clustering in which every source belongs to only one cluster. By increasing m, the membership degrees converge to the uniform distribution. In such a case, every source belong to all the clusters with equal membership degrees and the centroid of the clusters become the same. Thus, the sky corruption will be considered to be uniform for all the field of view. To understand this better, we present an illustrative example as follows:

We apply fuzzy clustering using different ms to cluster seven sources into two clusters. The source positions have a $\mathcal{U}(0, \pi)$ distribution and the brightness intensities are chosen between one and five Jansky (Jy). The plots of the obtained membership degrees for $m = 1.01,\ 3,\ 6,$ and 10 as well as relative intensities of the sources are shown by Fig. 5.1. As we see in Fig. 5.1, when $m = 1.01$, the fuzzy clustering becomes hard clustering and the memberships are either zero or one. In this case, the regions below the plots of the membership degrees are disjoint which means the clusters have hard boundaries. For $m = 3$, the plots of the membership degrees become more smooth and the regions below the plots overlap. That shows that the membership degrees are no more just zero and one. However, still we see that for some sources the membership degrees are significantly higher than the others. Thus, their distribution is not uniform yet. As we increase m to 6, the plots become even more smooth and the overlap of the region below them increases. Finally, in the case of $m = 10$, the membership plots are almost horizontal lines. Hence, Fuzzy clustering shows its extreme case where the membership degrees follow a uniform distribution.

The soft clustered calibration method with the data model of (5.10) can be carried out in two different ways:

(i) First we apply a weighted fuzzy clustering to calculate the membership degrees. Then, we run calibration techniques (Kazemi et al., 2012) on (5.10) to solve for QN Jones matrices $\mathbf{J}_{pi}$, $1 \leq p \leq N,\ 1 \leq i \leq Q$, using the known memberships.

(ii) We use constrained non-linear optimization algorithms (Conn et al., 1997) to simultaneously solve for QN number of Jones matrices $\mathbf{J}_{pi}$, plus for QK number of membership degrees u_{il}, $1 \leq i \leq Q,\ 1 \leq l \leq K$, in (5.10), satisfying the constrains of (5.8), and (5.9).

This chapter follows the first approach, when the weighted fuzzy clustering presented in section 5.4 is initially executed to obtain the membership degrees. Solving for too many number of unknowns, as well as satisfying some additional constrains in approach (ii), could significantly increase the computational expenses. However, unlike approach (i), this approach has the advantage of calculating the optimal membership degrees, which provide us with the best accuracy of the calibration, during the calibration procedure itself. Finding a proper solution for minimizing the computational expenses of approach (ii) is addressed in future work.

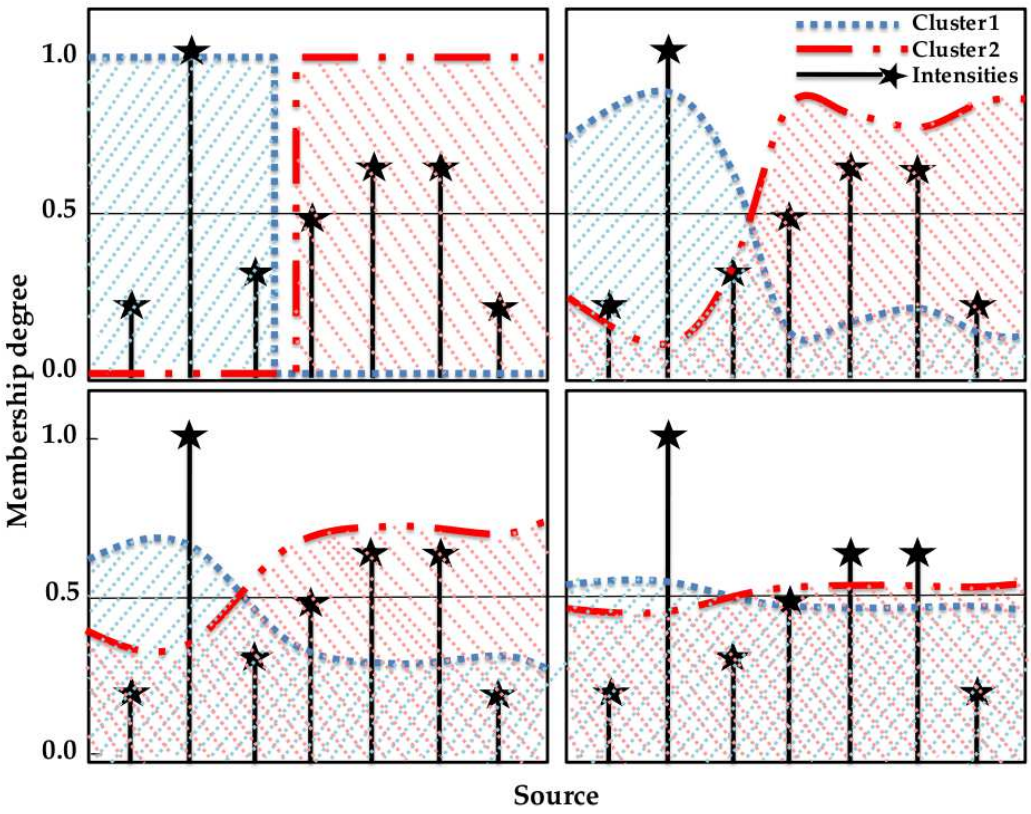

Figure 5.1: Membership degrees obtained by clustering seven point sources into two clusters. The vertical lines in the plot present relative brightness intensities of sources in Jy. The horizontal lines show the membership degrees obtained by soft clustering for four scenarios: $m = 1.01,\ 3,\ 6,$ and 10. When $m = 1.01$, the fuzzy clustering becomes hard clustering and the memberships are either zero or one. In this case, the regions below the plots of the membership degrees are disjoint which means the clusters have hard boundaries. For $m = 3$, the plots of membership degrees become more smooth and the regions below the plots overlap. That shows that the membership degrees are no more just zero and one. However, still we see that for some sources the membership degrees are significantly higher than the others. Thus, their distribution is not uniform yet. As we increase m to 6, the plots become even more smooth and the overlap of the region below them increases. Finally, In the case of $m = 10$, the membership plots are almost horizontal lines. Hence, Fuzzy clustering shows its case extreme where the membership degrees follow a uniform distribution.

5.5 Simulation studies

In this section, we use simulations to test the performance and convergence rate of soft clustered calibration and compare then to that of the hard clustered one. We show that when the brightness distribution of sources in the sky is a power law with a steep slope, which is mostly the case in real nature, the performance of soft clustered calibration compared to hard one is significantly better. For such skies, since there are a few number of very bright sources, whose signals are considerably stronger than the others, and a large number of very faint sources, the intensity of sources could be dramatically mixed by each other. Thus, there is a need for applying soft clustered calibration, rather than hard one, to deal with those effects. A Monte Carlo experiment shows that this correct in an even more general framework.

5.5.1 WSRT Simulation

We simulate a sky of fifty two point sources which are obtained by modified Jelić et al. (2008) foreground model. The brightness distribution of the point sources follows the source count function obtained at 151 MHz (Willott et al., 2001), while the angular clustering of the sources are characterized by a typical two-point correlation function,

$$\rho(d) = Ad^{-0.8}. \tag{5.13}$$

In (5.13), ρ is the two point correlation function, d is the angular separation, and A is the normalisation amplitude of ρ. The flux cut off is 0.1 Jy and the simulated image is shown by Fig. 5.2-(a). We proceed to add gain errors, multiplying source coherencies by the Jones matrices, as it is shown in (5.3), to our simulation. The amplitude and phase of the Jones matrices' elements are generated using linear combinations of *sine* and *cosine* functions, such that their amplitudes and phases have $\mathcal{U}(0.7, 0.9)$ and $\mathcal{U}(0.003, 0.004)$ distributions, respectively. We aim at simulating a sky with almost uniform variations on small angular scales. In other words, we provide very similar Jones matrices for sources with small angular separations. This way our simulation mimics the actual measurement better, hence, justifies the use of clustered calibration. To accomplish this goal, for every antenna, we first choose a single direction as a reference and simulate its Jones matrix as it is explained before. Then, for the remaining fifty one sources, at that antenna, the Jones matrices (amplitude and phase terms) are that initial Jones matrix multiplied by the inverse of their corresponding angular distances from that reference direction. We multiply the signals with these gain errors. At the end, zero mean Gaussian noise with a variance of 3 mJy is added to the simulated data. The result is shown in Fig. 5.2-(b). As we can see, in Fig. 5.2-(b), we have only a small number of sources which are significantly brighter than the others. Moreover, all of them are gathered in the right side of the image, rather than being uniformly distributed in the field of view. Therefore, their brightness intensities highly affect the fainter sources, specially the ones on the right side of the image. This paves the path to illustrate the advantage of using fuzzy clustered calibration for obtaining a higher convergence rate compared to hard clustered calibration.

We apply fuzzy clustered calibration, on 20 s time intervals, using $Q = 7$ clusters, and for $m = 1.05,\ 1.5,\ 2,\ 2.5,\ 3,\ 3.5,\ 4$. The calibration technique used is the SAGE algorithm with nine iterations. In this simulation case, when $m = 1.05$, fuzzy clustering becomes hard clustering. As we can see from the obtained residual noise levels shown in Fig. 5.3, shifting from hard clustered calibration, $m = 1.05$, to soft clustered calibration, the results get better until the minimum noise

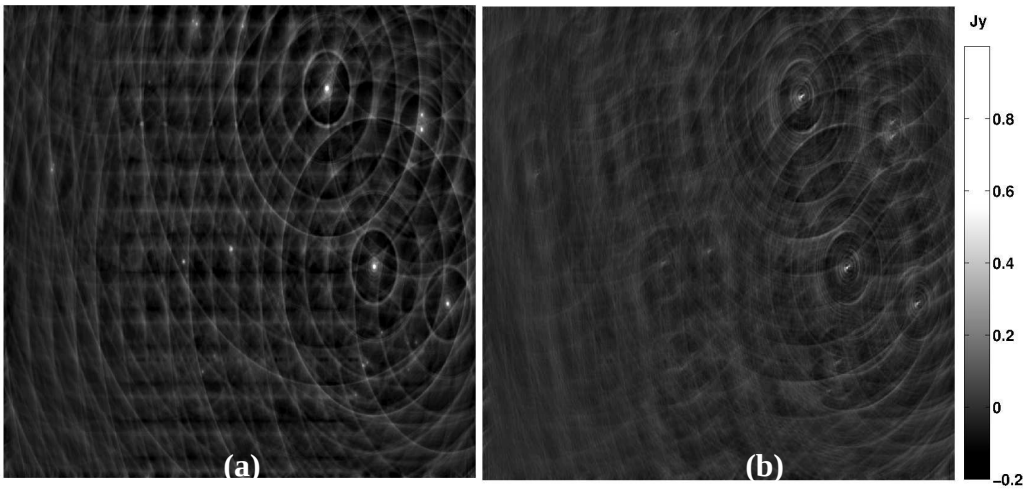

Figure 5.2: Simulated observation of fifty two sources which are obtained by modified Jelić et al. (2008) foreground model (a). The signals are convolved with gain error, as linear combinations of *sin* and *cos* functions, and a zero mean Gaussian noise with a variance of 3 mJy is also added (b). The size of images is 8 by 8 degrees

level is achieved at $m = 2.5$. After that, the noise level gets higher. For $m = 3$, it is still lower than the one of hard clustered calibration. But, for $m = 3.5$ and $m = 4$, it is the oposite and hard clustered calibration performs better than soft one. Thus, the best result of clustered calibration is obtained by fuzzy clustered calibration with $m = 2.5$. Note that we have achieved almost the same level of accuracy by hard clustered calibration for $Q = 27$ number of clusters in Kazemi et al. (2013b) (chapter 4). However, the computational cost of calibrating for twenty seven clusters is much more expensive than for seven clusters. Therefore, the main goal of applying fuzzy clustered calibration, instead of hard one, is to improve the speed of convergence while at the same time achieving a better accuracy.

The residual images obtained for $m = 1.05$, and $m = 2.5$ are shown in Fig. 5.4-(a), and Fig. 5.4-(b), respectively. In Fig. 5.4-(a), there are stripes of over and under estimations, due to problematic performance of hard clustered calibration, which is improved by 27 clusters in Kazemi et al. (2013b) (chapter 4). However, in Fig. 5.4-(b), soft clustered calibration with $m = 2.5$ could perfectly remove all the faint sources. Moreover, it has also generated much less affects after subtracting the brightest sources in the right side of the field of view.

The results of fuzzy clustering of the sources for $m = 1.05,\ 2.5,$ and $m = 4$ are presented in Figs. 5.5-5.6, respectively. The marker sizes are proportional to sources intensities, and the centroids of clusters are denoted by numbered-filled circles. For $m = 1.05$, where fuzzy clustering becomes hard clustering, we used different markers, as in Fig. 5.5, to distinguish between the members of different clusters. In Fig. 5.5, every source belongs to exactly one cluster, and hence, the performance of the clustered calibration utilizing those clusters is not the best possible.

As we have seen in the results of Fig. 5.3, the lowest residual noise level is obtained by fuzzy clusters generated with $m = 2.5$. The centroids of these clusters are shown in Fig. 5.6. Since the

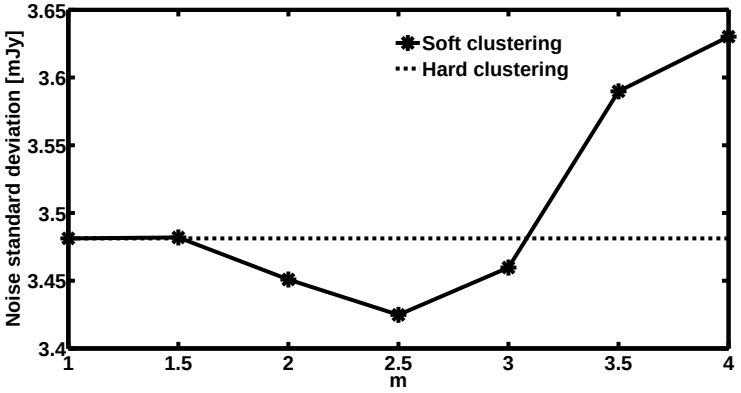

Figure 5.3: The standard deviation of the residual noise (mJy) for soft clustered calibration with $m = 1.05,\ 1.5,\ 2,\ 2.5,\ 3,\ 3.5,\ 4$. When $m = 1.05$, fuzzy clustering is a hard clustering. Shifting from hard clustered calibration, $m = 1.05$, to the soft clustered calibration, the results get better until the minimum noise level which is achieved by $m = 2.5$. After that, the get higher and for $m = 3.5$ and $m = 4$ it is even worse than the hard clustered calibration's performance. Thus, the optimal result is obtained by fuzzy clustered calibration with $m = 2.5$.

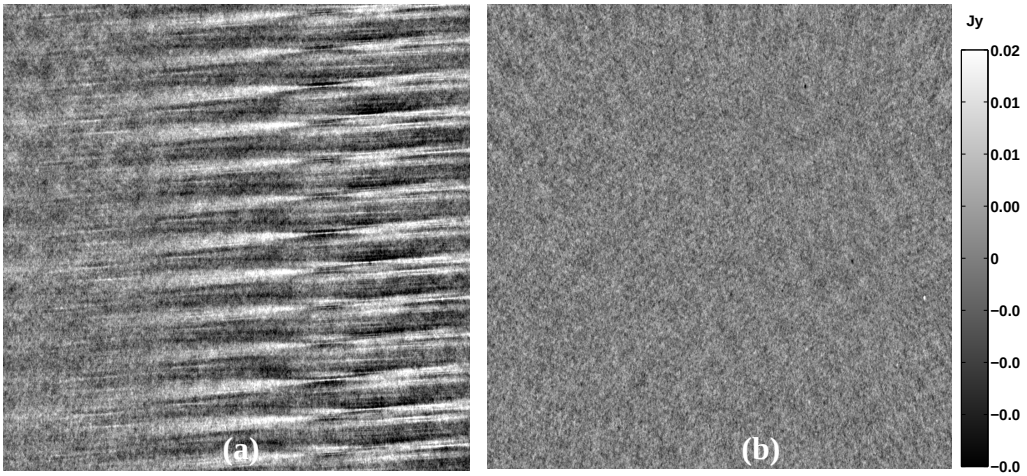

Figure 5.4: The residual images of hard clustered calibration (a) and soft clustered calibration with m=2.5 (b). Calibration is implemented by SAGE algorithm with nine number of iterations and on twenty seconds time intervals. There are strips of over and under estimations due to problematic performance of hard clustered calibration in (a). However, soft clustered calibration with $m = 2.5$ in (b) could perfectly remove all the faint sources. On top of that, it has generated much less artificial effects after subtracting for the brightest sources in the right side of the field of view.

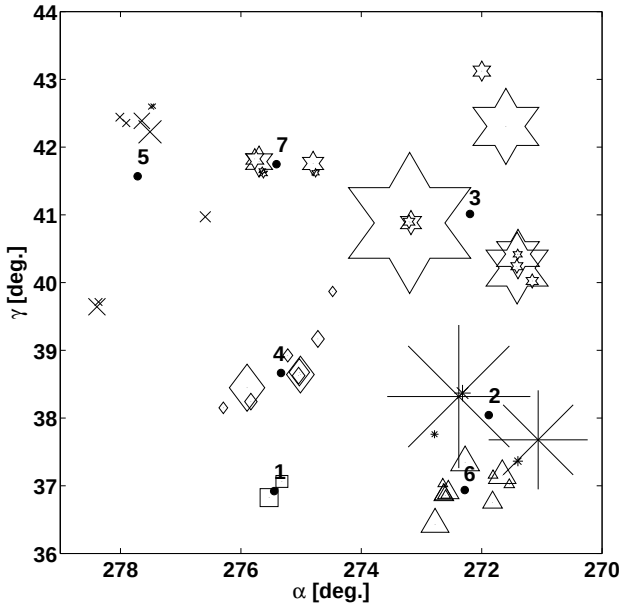

Figure 5.5: Fifty two point sources are clustered into seven source clusters by the weighted fuzzy clustering technique presented in section 5.4. The component $m = 1.05$ is used. Consequently, the membership degrees obtained are only zero and one. Thus, the fuzzy clustering in this limits is in fact the same as the hard clustering. Different markers are used for distinguishing between the members of different clusters. The centroids of clusters are denoted by numbered-filled circles.

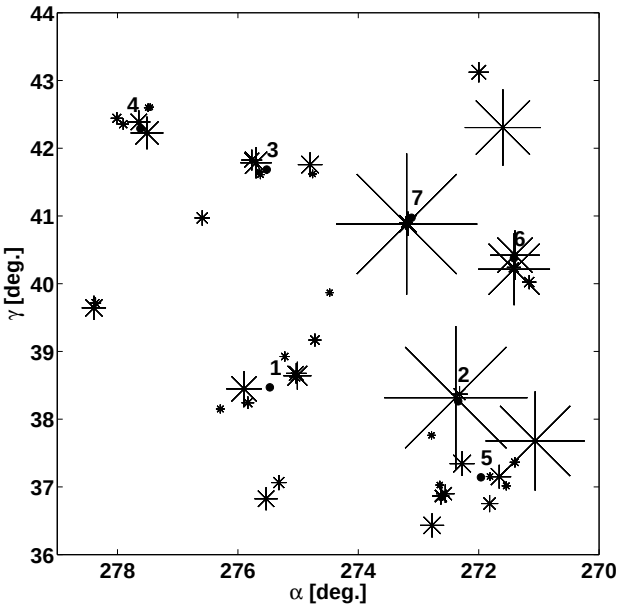

Figure 5.6: Fifty two point sources are clustered into seven source clusters by fuzzy clustering of section 5.4. The component $m = 2.5$ is used by which the best performance of fuzzy clustered calibration is obtained. The marker sizes are proportional to sources intensities. The centroids of the clusters are uniformly scattered in the field of view, and are covering whole the sky.

sources belong to different clusters according to some membership degree, we have plotted all of them using the same marker. In Fig. 5.6, the centroids of the clusters are uniformly scattered in the field of view, and are covering the whole sky. Applying fuzzy clustered calibration, we solve for the directions of these centroids, and at the end, errors are estimated as linear combinations of the obtained solutions. Having proper membership degrees, which are partly shown in Table 5.2, achieving the best accuracy of calibration is guaranteed.

In Table 5.2, membership degrees generated by the weighted fuzzy clustering with $m = 2.5$ are given for fifteen randomly chosen sources. As we can see, most of the sources belong with a degree of membership greater than 50% to one cluster. That means every source belongs with a large membership degrees to the cluster whose centroid is the closet to it, and with a very small ones to the other farther clusters. This is the most reasonable clustering senario. The worst clustering senario is when every source belongs to all clusters with equal membership degrees. That happened for the case of $m = 4$, as it can be seen in Table 5.3. In Table 5.3, the membership degrees generated by fuzzy clustering with $m = 4$ are shown for the fifteen sources. The memberships follow a uniform distribution. This means that the brightness of every source affects all the sky at the same level. This is not realistic for an 8 degrees field of view. That is why the performance of clustered calibration using such fuzzy source clusters is not good. As an immediate result of considering such membership degrees, as presented in Table 5.3, the centroids of clusters are inclined towards the phase center of the observation. This can be seen in Fig. 5.7, where the result of fuzzy clustering of sources for $m = 4$ is plotted. The centroids of the clusters are focused

Table 2

Source Number	Cluster 1	2	3	4	5	6	7
1	0.0702	0.0993	0.0540	0.0598	0.0327	0.5733	0.1106
2	0.0270	0.0307	0.0214	0.0195	0.0144	0.8493	0.0377
3	0.1564	0.2695	0.0547	0.1076	0.0542	0.2419	0.1156
4	0.0073	0.0142	0.7780	0.0231	0.0045	0.0182	0.1547
5	0.0006	0.0012	0.9808	0.0018	0.0004	0.0019	0.0133
6	0.0044	0.0077	0.9023	0.0109	0.0029	0.0128	0.0591
7	0.0003	0.0006	0.0029	0.0009	0.0001	0.0007	0.9946
8	0.0007	0.0016	0.0070	0.0025	0.0004	0.0018	0.9860
9	0.1922	0.3177	0.0470	0.2181	0.0948	0.0590	0.0712
10	0.0361	0.0081	0.0022	0.0042	0.9408	0.0055	0.0031
11	0.0035	0.0007	0.0002	0.0004	0.9945	0.0005	0.0003
12	0.0397	0.0088	0.0024	0.0045	0.9351	0.0060	0.0034
13	0.0045	0.0010	0.0003	0.0005	0.9926	0.0007	0.0004
14	0.0002	0.0011	0.0002	0.9979	0.0001	0.0002	0.0004
15	0.0002	0.0009	0.0002	0.9983	0.0001	0.0001	0.0003

Table 5.2: Membership degrees generated by fuzzy clustering of $K = 52$ sources in to $Q = 7$ clusters, for $m = 2.5$. The largest membership degree of every source is underlined. Most of the sources belong with a membership bigger than $.5$ to one cluster. That means every source more belongs with a large membership degrees to the cluster whose centroid is the closet to it, and with a very small ones to the other farther clusters.

Table 3

Source Number	Cluster 1	2	3	4	5	6	7
1	0.1207	0.1160	0.0958	0.1186	0.1215	0.1263	0.3011
2	0.1312	0.1274	0.1106	0.1302	0.1358	0.1437	0.2212
3	0.1623	0.1518	0.1280	0.1296	0.1148	0.1094	0.2040
4	0.1320	0.1329	0.1208	0.1490	0.1647	0.1696	0.1311
5	0.1308	0.1315	0.1188	0.1475	0.1650	0.1729	0.1335
6	0.1320	0.1324	0.1207	0.1467	0.1622	0.1700	0.1360
7	0.1209	0.1221	0.1035	0.1505	0.1877	0.1963	0.1189
8	0.1217	0.1230	0.1043	0.1520	0.1879	0.1930	0.1181
9	0.1506	0.1517	0.1712	0.1407	0.1305	0.1248	0.1305
10	0.1487	0.1475	0.1549	0.1380	0.1320	0.1298	0.1491
11	0.1487	0.1472	0.1540	0.1377	0.1318	0.1298	0.1508
12	0.1488	0.1475	0.1551	0.1380	0.1319	0.1298	0.1490
13	0.1485	0.1472	0.1539	0.1379	0.1321	0.1302	0.1502
14	0.1513	0.1566	0.1682	0.1520	0.1351	0.1230	0.1137
15	0.1513	0.1566	0.1681	0.1521	0.1351	0.1230	0.1137

Table 5.3: Membership degrees generated by fuzzy clustering with $m = 4$, for the fifteen chosen sources. The largest membership degree of every source is underlined. Each source belongs to all the cluster with equal membership degrees. This means that the brightness of every source affects all the sky at the same level, which is not realistic. Thus, the performance of fuzzy clustered calibration using such membership degrees is not expected to be good.

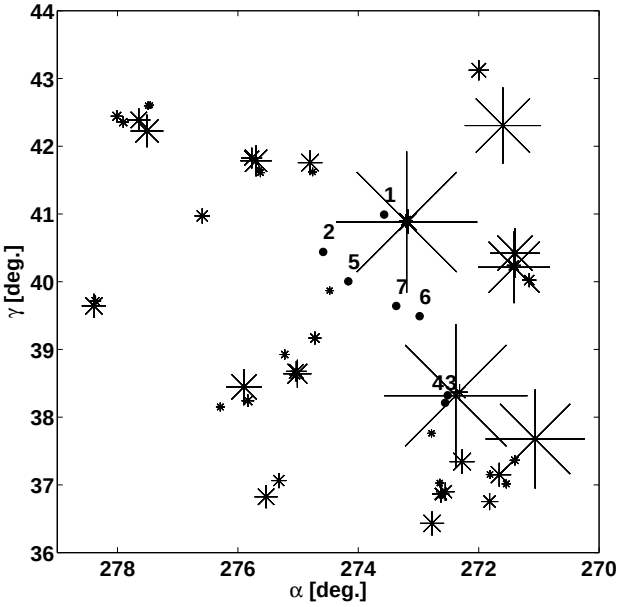

Figure 5.7: The result of fuzzy clustering of sources for $m = 4$. The centroids of the clusters are focused around the strong sources in the field of view. Thus, applying these clusters to clustered calibration, we solve for almost only one direction in the sky, towards the area from wich the strongest signals are emitted. That is the reason of the bad performance of soft clustered calibration in the plot of Fig. 5.3

around the strong sources in the field of view. Thus, clustered calibration via those fuzzy clusters in fact solves for a single direction, towards the strongest sources. That is why the performance of such a calibration is the worst, as it is shown in the plot of Fig. 5.3.

Comparing Fig. 5.8 and Fig. 5.9, we can see the difference between the results of fuzzy clustering for $m = 2.5$ and $m = 4$ from anther point of view. Fig. 5.8 and Fig. 5.9 show the contour plots of membership degrees for six fuzzy clusters (out of the total seven generated clusters) in six sub-plots, for $m = 2.5$ and $m = 4$, respectively. The plots show how the fuzzy membership degrees are scattered in the field of view. In Fig. 5.8, we see that at the centroids of the clusters, which were plotted in Fig. 5.6, contour lines are very close to each other. This shows a steep slope of membership values around the centroids. The contour labels have a maximum between 0.7 and 0.9, occurring at the centroids. Getting far from the centroids, contour lines become far apart, till they make a huge flat area with the minimum of membership degrees, which is 0.1. Thus, sources close to centroids have a large membership degrees (between 0.7 and 0.9), and the ones farther, have very small ones. This is similar to hard clustering. However, in the plots of Fig. 5.9, which are for the case of fuzzy clustering with $m = 4$, contour lines are scattered almost all over the field of view. The reason is because, as it is shown in Fig. 5.7, the centroid of fuzzy cluster generated for $m = 4$ are very close to each other and are focused around the strongest sources in the sky. That is the reason of having too many circles which are far apart from each other at every plot of Fig. 5.9. On top of that, the contour labels in Fig. 5.9 have a maximum between 0.1 and 0.2. This shows every cluster covers a large part of the field of view

with almost uniform membership degrees. This is quite different from hard clustering.

5.5.2 Monte Carlo simulation

As the last part of this section, we present a Monte Carlo simulation to demonstrate the faster speed of convergence of soft clustered calibration compared to that of the hard clustered one, in a more general framework. Ten simulations are made, just as the one produced at the beginning of this section with different errors. For all of them, the standard deviation of the obtained residual noise for soft clustered calibration, with $m = 1.05,\ 1.5,\ 2,\ 2.5,\ 3,\ 3.5,\ 4$, are calculated. Bear in mind that for $m = 1.05$ fuzzy clustering becomes hard clustering. The averaged standard deviation is shown in Fig. 5.10. As we can see in Fig. 5.10, shifting from hard clustered calibration, $m = 1.05$, to soft one, the results get better. The minimum noise level is obtained for soft clustered calibration with $m = 2$. After that, the noise level gets higher, and for $m = 3,\ 3.5,$ and 4, it is even higher than the one of hard clustered calibration. Thus, the best result is obtained by fuzzy clustered calibration with $m = 2$. This means, soft clustered calibration can achieve a higher convergence rate compared to hard clustered calibration. Note that this does not mean that hard clustered calibration can not provide the same level of accuracy in its solutions. It is possible that one obtains the same accuracy as the one obtained via soft clustered calibration with $m = 2$ by hard clustered calibrations with a larger number of clusters, $Q \gg 7$. The superiority of soft clustered calibration compared to hard clustered calibration is only in achieving this accuracy with a less computational cost.

5.6 Conclusions

We have introduced soft clustered calibration for calibrating radio interferometric data towards the sensitivity limit. The method applies fuzzy clustering in order to design source clusters with soft boundaries. Then, it runs directional calibration to solve along the centroids of these clusters. The coherency of every cluster is defined as the sum of coherency of the sources of the cluster, where they are multiplied by the membership degrees with which their corresponding source belongs to that cluster. Using such coherencies in the calibration procedure, the brightness of every individual source can be contributed to more than one cluster. The level of this contribution is defined by some membership degrees. As an immediate result, in soft clustered calibration, every source signal is considered to be corrupted by a linear combination of the sky errors (Jones matrices) of all the clusters. This is where in the hard clustered calibration, which runs calibration on clusters with hard boundaries, the solution of every source is only the one obtained for the centroid of the cluster that the source belongs to. This provides soft clustered calibration with a faster speed of convergence compared to hard one, specially when the brightness distribution of sources yields from uniform to power law distribution. Simulated observations proved our claim.

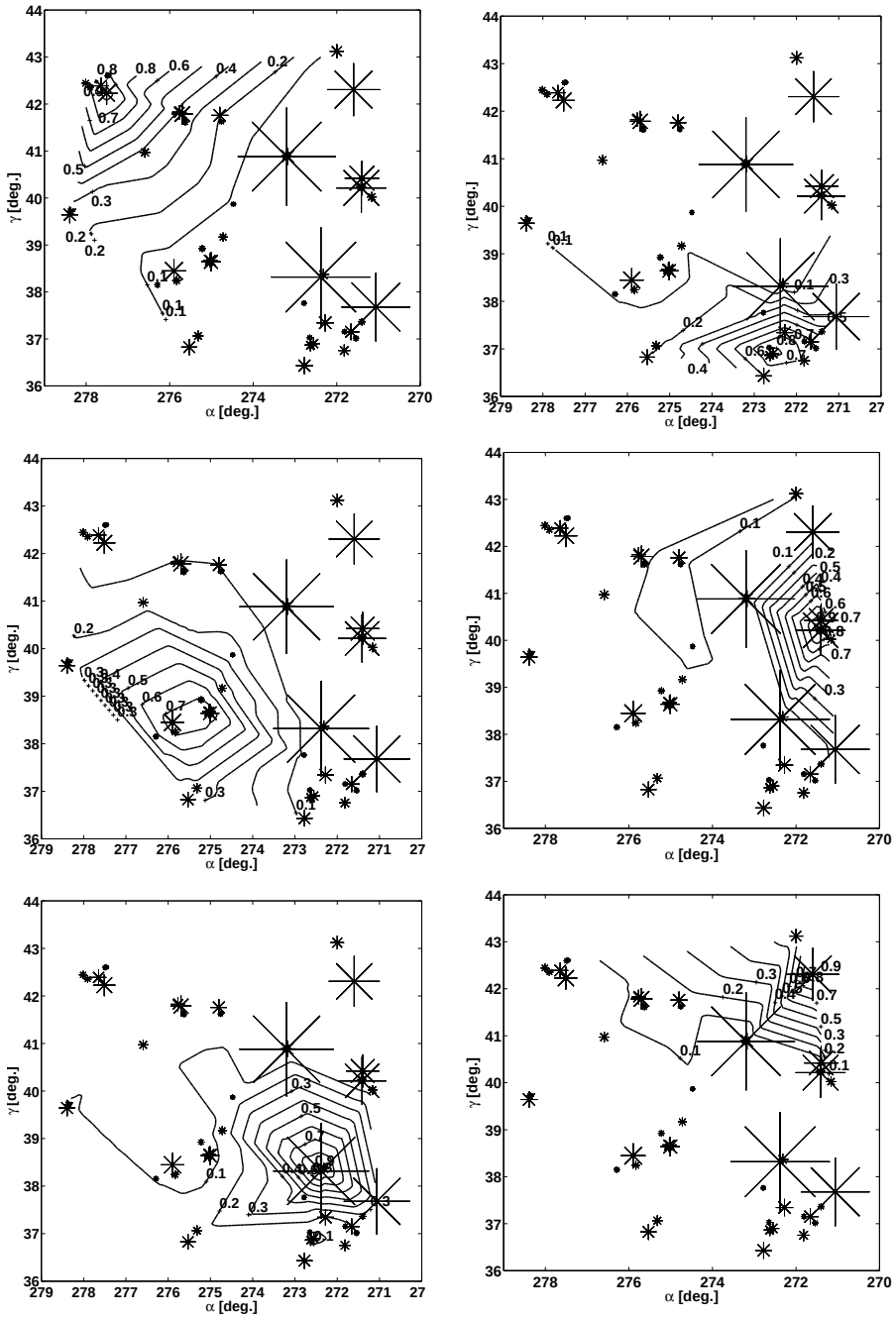

Figure 5.8: The contour plots of membership degrees for six fuzzy clusters (out of the total seven generated fuzzy clusters), when $m = 2.5$. The plots show how the fuzzy membership degrees are scattered in the field of view. There are contour lines close together at the centroids of the clusters, which are plotted in Fig. 5.6. This shows a steep slope of membership values around the centroids. The contour labels have a maximum between 0.7 and 0.9, occurring at the centroids. Getting far from the centroids, contour lines become far apart, till they make a huge flat area with the minimum membership degrees, which is 0.1. Thus, sources close to centroids have a large membership degrees (between 0.7 and 0.9), and the ones farther, have very small ones. This is close to hard clustering.

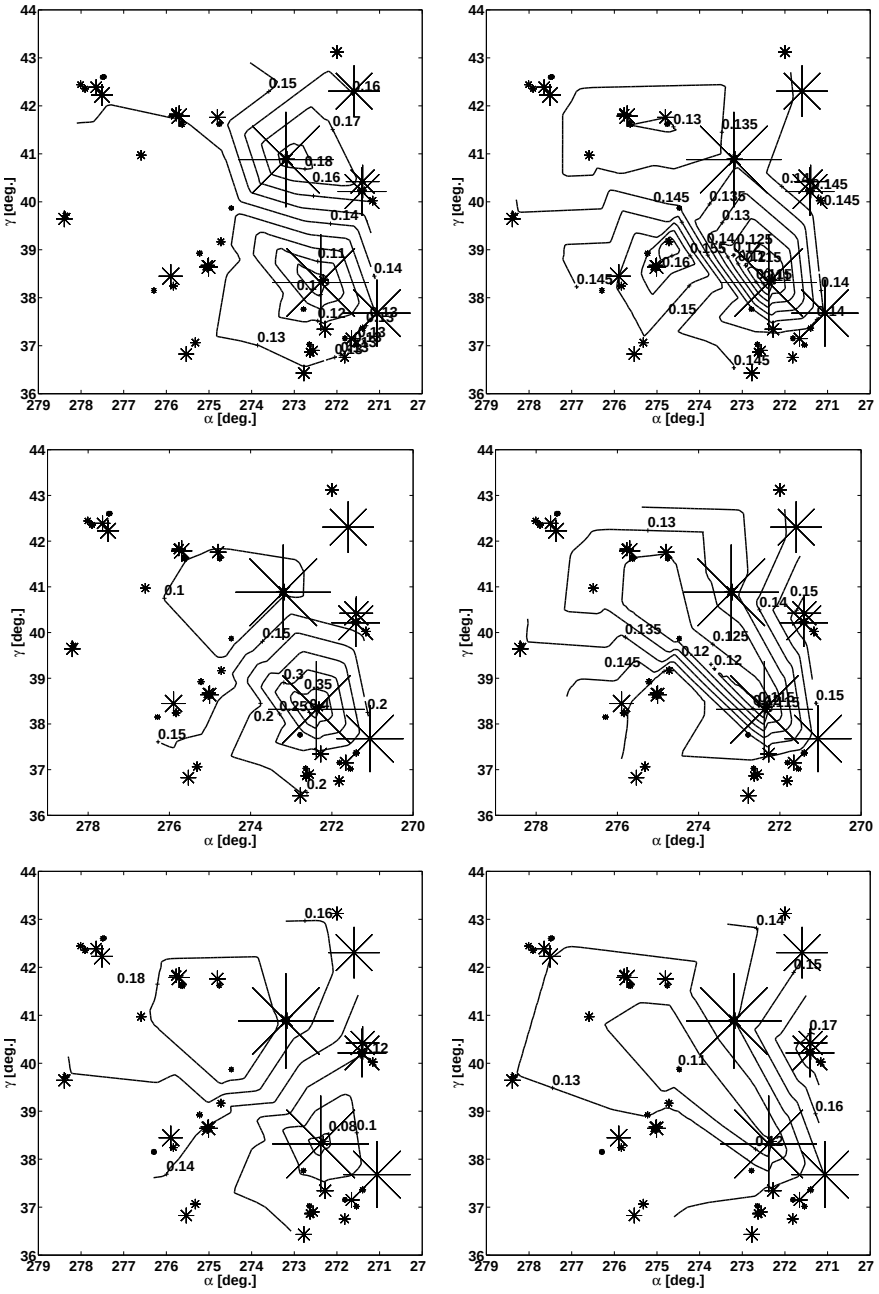

Figure 5.9: The contour plots of membership degrees for six fuzzy clusters (out of the total seven generated fuzzy clusters), when $m = 4$. As it is shown in Fig. 5.7, the centroid of fuzzy cluster generated for $m = 4$ are very close to each other and are focused at the phase center. Consequently, there are contour lines in the above plots are scattered almost all over the field of view. At every plot, there are too many closed circles far apart from each other. On top of that, the contour labels have a maximum between 0.1 and 0.2. This shows every cluster covers a large part of the field of view with almost uniform membership degrees. This is quite far from hard clustering.

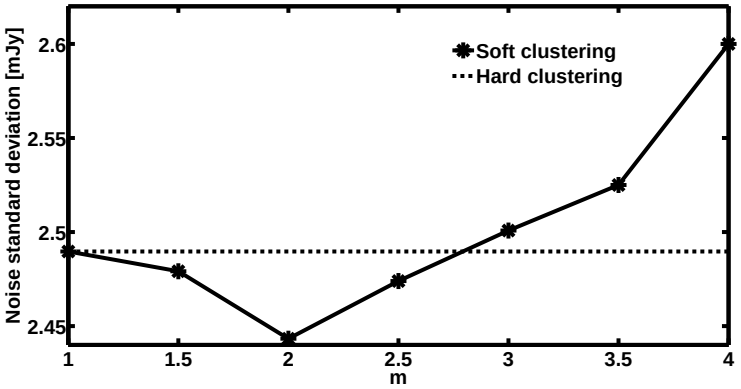

Figure 5.10: The averaged standard deviation of the residual noise of ten simulations, obtained by soft clustered calibration for $m = 1.05,\ 1.5,\ 2,\ 2.5,\ 3,\ 3.5,\ 4$. When $m = 1.05$, fuzzy clustering is in fact hard clustering. Shifting from hard clustered calibration, $m = 1.05$, to soft clustered calibration, the results get better. The minimum noise level is obtained for soft clustered calibration with $m = 2$. After that, the noise level gets higher, and for $m = 3,\ 3.5,$ and 4, it is even higher than the one of hard clustered calibration. Thus, the best result is obtained by fuzzy clustered calibration with $m = 2$. Therefore, applying clustered calibration to cases in which the brightness distribution of sources is a power law, the hard clustered calibration achieves a higher convergence rate compared to hard one.

Chapter 6

Robust Radio Interferometric Calibration Using the t-Distribution

"Robust Radio Interferometric Calibration Using the t-Distribution"
Kazemi S., Yatawatta S., 2013, MNRAS, 435, 597

ABSTRACT
A major stage of radio interferometric data processing is calibration or the estimation of systematic errors in the data and the correction for such errors. A stochastic error (noise) model is assumed, and in most cases, this underlying model is assumed to be Gaussian. However, outliers in the data due to interference or due to errors in the sky model would have adverse effects on processing based on a Gaussian noise model. Most of the shortcomings of calibration such as the loss in flux or coherence, and the appearance of spurious sources, could be attributed to the deviations of the underlying noise model. In this chapter, we propose to improve the robustness of calibration by using a noise model based on Student's t distribution. Student's t noise is a special case of Gaussian noise when the variance is unknown. Unlike Gaussian noise model based calibration, traditional least squares minimization would not directly extend to a case when we have a Student's t noise model. Therefore, we use a variant of the Expectation Maximization (EM) algorithm, called the Expectation-Conditional Maximization Either (ECME) algorithm when we have a Student's t noise model and use the Levenberg-Marquardt algorithm in the maximization step. We give simulation results to show the robustness of the proposed calibration method as opposed to traditional Gaussian noise model based calibration, especially in preserving the flux of weaker sources that are not included in the calibration model.

6.1 Introduction

Radio interferometry gives an enhanced view of the sky, with increased sensitivity and higher resolution. There is a trend towards using phased arrays as the building blocks of radio telescopes (LOFAR [1], SKA [2]) as opposed to traditional dish based interferometers. In order to reach the true potential of such telescopes, calibration is essential. Calibration refers to estimation of systematic errors introduced by the instrument (such as the beam shape and receiver gain) and also by the propagation path (such as the ionosphere), and correction for such errors, before any imaging is done. Conventionally, calibration is done by observing a known celestial object (called the external calibrator), in addition to the part of the sky being observed. This is improved by self-calibration (Cornwell & Wilkinson, 1981), which is essentially using the observed sky itself for the calibration. Therefore, self calibration entails consideration of both the sky as well as the instrument as unknowns. By iteratively refining the sky and the instrument model, the quality of the calibration is improved by orders of magnitude in comparison to using an external calibrator.

From a signal processing perspective, calibration is essentially the Maximum Likelihood (ML) estimation of the instrument and sky parameters. An in depth overview of existing calibration techniques from an estimation perspective can be found in e.g. Boonstra & van der Veen (2003); van der Veen et al. (2004); van der Tol et al. (2007) and Kazemi et al. (2011) (chapter 2). All such calibration techniques are based on a Gaussian noise model and the ML estimate is obtained by minimizing the least squares cost function using a nonlinear optimization technique such as the Levenberg-Marquardt (Levenberg, 1944; Marquardt, 1963) (LM) algorithm. Despite the obvious advantages of self-calibration, there are also some limitations. For instance, Cornwell & Fomalont (1999) give a detailed overview of the practical problems in self-calibration, in particular due to errors in the initial sky model. It is well known that the sources not included in the sky model have lower flux (or loss of coherence) and Martí-Vidal et al. (2010) is a recent study on this topic. Moreover, under certain situations, fake or spurious sources could appear due to calibration as studied by Martí-Vidal & Marcaide (2008).

In this chapter, we propose to improve the robustness of calibration by assuming a Student's t (Gosset, 1908) noise model instead of a Gaussian noise model. One of the earliest attempts in deviating from a Gaussian noise model based calibration can be found in Schwab (1982), where instead of minimizing a least squares cost function, an l_1 norm minimization was considered. Minimizing the l_1 norm is equivalent to having a noise model which has a Laplacian distribution (Aravkin et al., 2012). The motivation for Schwab (1982) to deviate from the Gaussian noise model was the ever present outliers in the radio interferometric data.

In a typical radio interferometric observation, there is a multitude of causes for outliers in the data:

- Radio frequency interference caused by man made radio signals is a persistent cause of outliers in the data. However, data affected by such interference is removed before any calibration is performed by flagging (e.g. Offringa et al. (2010b)). But there might be faint interference still present in the data, even after flagging.
- The initial sky model used in self calibration is almost always different from the true sky that is observed. Such model errors also create outliers in the data. This is especially significant when we observe a part of the sky that has sources with complicated, extended structure.

[1] The Low Frequency Array
[2] The Square Kilometre Array

Moreover, during calibration, only the brightest sources are normally included in the sky model and the weaker sources act together to create outliers.

- During day time observations, the Sun could act as a source of interference, especially during high solar activity. In addition the Galactic plane also affects the signals on short baselines.

- An interferometer made of phased arrays will have sidelobes that change with time and frequency. It is possible that a strong celestial source, far away from the part of the sky being observed, will pass through such a sidelobe. This will also create outliers in the data.

To summarize, model errors of the sky as well as the instrument will create outliers in the data and in some situations calibration based on a Gaussian noise model will fail to perform satisfactorily. In this chapter, we consider the specific problem of the effect of unmodeled sources in the sky during calibration. We consider 'robustness' to be the preservation of the fluxes of the unmodeled sources. Therefore, our prime focus is to minimize the loss of flux or coherence of unmodeled sources and our previous work (Yatawatta et al., 2012) have measured robustness in terms of the quality of calibration.

Robust data modeling using Student's t distribution has been applied in many diverse areas of research and Lange et al. (1989); Bartkowiak (2007) and Aravkin et al. (2012) are few such examples. However, the traditional least squares minimization is not directly applicable when we have a non-Gaussian noise model, and we apply the Expectation Maximization (EM) (Dempster et al., 1977) algorithm to convert calibration into an iteratively re-weighted least squares minimization problem, as proposed by Lange et al. (1989). In fact, we use an extension of the EM algorithm called the Expectation-Conditional Maximization Either (ECME) algorithm (Liu & Rubin, 1995) to convert calibration to a tractable minimization problem. However, we emphasize that we do not force a non-Gaussian noise model onto the data. In the case if there are no outliers and the noise is actually Gaussian, our algorithms would work as traditional calibration would.

The rest of the chapter is organized as follows: In section 6.2, we give an overview of radio interferometric calibration. We consider the effect of unmodeled sources in the sky during calibration in section 6.3. Next, in section 6.4, we discuss the application of Student's t noise model in calibration. We also present the weighted LM routine used in calibration. In section 6.5, we present simulation results to show the superiority of the proposed calibration approach in minimizing the loss in coherence and present conclusions in section 6.6.

Notation: Lower case bold letters refer to column vectors (e.g. $\mathbf{y}$). Upper case bold letters refer to matrices (e.g. $\mathbf{C}$). Unless otherwise stated, all parameters are complex numbers. The matrix inverse, transpose, Hermitian transpose, and conjugation are referred to as $(.)^{-1}$, $(.)^T$, $(.)^H$, $(.)^\star$, respectively. The matrix Kronecker product is given by $\otimes$. The statistical expectation operator is given as $E\{.\}$. The vectorized representation of a matrix is given by $\mathrm{vec}(.)$. The i-th diagonal element of matrix $\mathbf{A}$ is given by $\mathbf{A}_{ii}$. The i-th element of a vector $\mathbf{y}$ is given by $\mathbf{y}_i$. The identity matrix is given by $\mathbf{I}$. Estimated parameters are denoted by a hat, $\widehat{(.)}$. All logarithms are to the base e, unless stated otherwise. The l_2 norm is given by $\|.\|$ and the infinity norm is given by $\|.\|_\infty$. A random variable X that has a distribution $\mathcal{P}$ is denoted by $X \sim \mathcal{P}$.

6.2 Data Model

We give a brief overview of radio interferometry in this section. For more information about radio interferometry, the reader is referred to Thompson et al. (2001), and Hamaker et al. (1996) for the data model in particular. We consider the radio frequency sky to be composed of discrete sources, far away from the earth such that the approaching radiation from each one of them appears to be plane waves. We decompose the contribution from the i-th source into two orthogonal polarizations $\mathbf{u}_i = [u_{xi}\ u_{yi}]^T$. The interferometric array consists of R receiving elements with dual polarized feeds. At the p-th station, this plane wave causes an induced voltage, which is dependent on the beam attenuation as well as the radio frequency receiver chain attenuation. The induced voltages at the x and y polarization feeds, $\tilde{\mathbf{v}}_{pi} = [v_{xpi}\ v_{ypi}]^T$ due to source i are given as

$$\tilde{\mathbf{v}}_{pi} = \mathbf{J}_{pi}\mathbf{u}_i. \tag{6.1}$$

The 2 by 2 Jones matrix $\mathbf{J}_{pi}$ in (6.1) represents the effects of the propagation medium, the beam shape and the receiver. If there are K known sources (that are in the sky model) and K' unknown sources, the total signal will be a superposition of $K + K'$ such signals as in (6.1).

After correlating signals at the p-th receiver and the q-th receiver, with proper signal delay, the correlated signal (named as the *visibilities*), $\mathbf{V}_{pq} = E\{\mathbf{v}_p\mathbf{v}_q^H\}$ is given by

$$\mathbf{V}_{pq} = \sum_{i=1}^{K} \mathbf{J}_{pi}\mathbf{C}_{pqi}\mathbf{J}_{qi}^H + \sum_{i'=1}^{K'} \mathbf{J}_{pi'}\mathbf{C}_{pqi'}\mathbf{J}_{qi'}^H + \mathbf{N}_{pq}. \tag{6.2}$$

In (6.2), $\mathbf{J}_{pi}$ and $\mathbf{J}_{qi}$ are the Jones matrices describing errors along the direction of source i, at station p and q, respectively. The 2 by 2 noise matrix is given as $\mathbf{N}_{pq}$. The contribution from the i-th source on baseline pq is given by the 2 by 2 matrix $\mathbf{C}_{pqi}$. The noise matrix $\mathbf{N}_{pq}$ is assumed to have elements with zero mean, complex Gaussian entries with equal variance in real and imaginary parts. Moreover, in (6.2), we have split the contribution from the sky into two parts: K sources that are known to us and K' sources that are unknown. Generally, the bright sources are always known but there are infinitely many faint sources that are too weak to be detected and too numerous to be included in the sky model. Therefore, almost always K' is much larger than K.

During calibration, we only estimate the Jones matrices $\mathbf{J}_{pi}$ for $p \in [1, R]$ and $i \in [1, K]$, in other words, we estimate the errors along the known bright sources. Due to our ignorance of the K' unknown sources, the effective noise during calibration becomes

$$\mathbf{N}'_{pq} = \sum_{i'=1}^{K'} \mathbf{J}_{pi'}\mathbf{C}_{pqi'}\mathbf{J}_{qi'}^H + \mathbf{N}_{pq} \tag{6.3}$$

and our assumption regarding the noise being complex circular Gaussian breaks down, depending on the properties of the signals of the weak sources. The prime motivation of this chapter is to address this problem of the possible non-Gaussianity of the noise due to an error in the sky model. A similar situation could arise even for calibration along one direction (or direction independent calibration), when $K = 1$, if there is an error in the source model, for instance in the shape of the source.

The vectorized form of (6.2), $\mathbf{v}_{pq} = \mathrm{vec}(\mathbf{V}_{pq})$ can be written as

$$\mathbf{v}_{pq} = \sum_{i=1}^{K} \mathbf{J}^{\star}_{qi} \otimes \mathbf{J}_{pi} \mathrm{vec}(\mathbf{C}_{pqi}) + \sum_{i'=1}^{K'} \mathbf{J}^{\star}_{qi'} \otimes \mathbf{J}_{pi'} \mathrm{vec}(\mathbf{C}_{pqi'}) + \mathbf{n}_{pq} \tag{6.4}$$

where $\mathbf{n}_{pq} = \mathrm{vec}(\mathbf{N}_{pq})$. Depending on the time and frequency interval within which calibration solutions are obtained, we can stack up all cross correlations within that interval as

$$\mathbf{d} = [\mathrm{real}(\mathbf{v}_{12}^T)\ \mathrm{imag}(\mathbf{v}_{12}^T)\ \mathrm{real}(\mathbf{v}_{13}^T) \ldots\ldots \mathrm{imag}(\mathbf{v}_{(R-1)R}^T)]^T \tag{6.5}$$

where $\mathbf{d}$ is a vector of size $N = 4R(R-1)$ of real data points. Thereafter, we can rewrite the data model as

$$\mathbf{d} = \sum_{i=1}^{K} \mathbf{s}_i(\boldsymbol{\theta}) + \sum_{i'=1}^{K'} \mathbf{s}_{i'} + \mathbf{n} \tag{6.6}$$

where $\boldsymbol{\theta}$ is the real parameter vector (size $M \times 1$) that is estimated by calibration. The contribution of the i-th known source on all data points is given by $\mathbf{s}_i(\boldsymbol{\theta})$ (size $N \times 1$) and the unknown contribution from the i'-th unknown source is given by $\mathbf{s}_{i'}$ (size $N \times 1$). The noise vector based on a Gaussian noise model is given by $\mathbf{n}$ (size $N \times 1$). The parameters $\boldsymbol{\theta}$ are the elements of $\mathbf{J}_{pi}$-s, with real and imaginary parts considered separately.

The ML estimate of $\boldsymbol{\theta}$ under a zero mean, white Gaussian noise is obtained by minimizing the least squares cost

$$\widehat{\boldsymbol{\theta}} = \arg\min_{\boldsymbol{\theta}} \|\mathbf{d} - \sum_{i=1}^{K} \mathbf{s}_i(\boldsymbol{\theta})\|^2 \tag{6.7}$$

as done in current calibration approaches (Boonstra & van der Veen, 2003; van der Veen et al., 2004; van der Tol et al., 2007; Kazemi et al., 2011). However, due to the unmodeled sources, the effective noise is actually

$$\mathbf{n}' = \sum_{i'=1}^{K'} \mathbf{s}_{i'} + \mathbf{n} \tag{6.8}$$

even when $\mathbf{n}$ is assumed to be Gaussian. Therefore, traditional calibration based on a least squares cost minimization would not perform optimally. In order to improve this, we have to consider the statistical properties of the effective noise $\mathbf{n}'$ and we shall do that in the section 6.3.

6.3 Effect of unmodeled sources in calibration

In this section we study the effect of unmodeled sources on $\mathbf{N}'_{pq}$ in (6.3) when $\mathbf{N}_{pq}$ has elements with zero mean, complex circular white Gaussian statistics. We only select one element from the 2×2 matrix (say at 1-st row and column) for simplicity. Let us denote the baseline coordinates as u, v, w in wavelengths (we omit the pq subscript for simplicity). We can rewrite (6.3) for just one element as

$$z_{pq} = \sum_{i'=1}^{K'} g_{pqi'} I_{pqi'} \exp\left(-\jmath 2\pi \left(ul_{i'} + vm_{i'} + w(n_{i'} - 1)\right)\right) + n_{pq}. \tag{6.9}$$

In (6.9), $g_{pqi'}$ correspond to the corruptions along the direction i' (contributions from $\mathbf{J}_{pi'}$ and $\mathbf{J}_{qi'}$). The intensity of the i'-th source seen on baseline pq is given by $I_{pqi'}$. The direction cosines of the i'-th source are given by $l_{i'}, m_{i'}, n_{i'}$. The Gaussian noise is given by $n_{pq} \sim \mathcal{CN}(0, \rho^2)$. We assume that $g_{pqi'}$, $I_{pqi'}$, $l_{i'}, m_{i'}, n_{i'}$ and n_{pq} are statistically independent from each other. Moreover, the sources are assumed to be uniformly distributed in a field of view defined by $-\overline{l} \leq l_{i'} \leq \overline{l}$ and $-\overline{m} \leq m_{i'} \leq \overline{m}$ and that $(n_{i'} - 1) \approx 0$, where the center is at zero. The sources outside this area in the sky have almost no contribution to the signal due to the fact that the values of $|g_{pqi'}|$ are very small, mainly due to attenuation by the beam shape.

With the above assumptions, we see that

$$E\{z_{pq}\} = \sum_{i'=1}^{K'} E\{g_{pqi'}\}E\{I_{pqi'}\}\text{sinc}\left(2\pi u\overline{l}\right)\text{sinc}\left(2\pi v\overline{m}\right) + E\{n_{pq}\} \tag{6.10}$$

which is almost zero if $|u| > \frac{1}{2\overline{l}}$ and $|v| > \frac{1}{2\overline{m}}$. Therefore, we make the following assumptions applicable to long baselines:

- The mean of the effective noise is almost equal to the mean of noise, $E\{z_{pq}\} \to E\{n_{pq}\} = 0$.
- The variance of effective noise is greater than the variance of noise, $E\{|z_{pq}|^2\} > E\{|n_{pq}|^2\}$.

Let us briefly consider the implications of (6.10) above. First, the field of view is $2\overline{l} \times 2\overline{m}$ in the sky. Now, consider the longest baseline length or the maximum value of $\sqrt{u^2 + v^2}$ to be $\overline{u}$. Therefore, the image resolution will be about $1/\overline{u}$ and consider the field of view to be of width $2\overline{l} \approx P \times 1/\overline{u}$. In other words, the field of view is P image pixels when the pixel width is $1/\overline{u}$. Now, in order for $E\{z_{pq}\} \approx 0$ in (6.10), we need $|u| > \frac{1}{2\overline{l}}$, or $|u| > \overline{u}/P$ (and a similar expression can be derived for $|v|$). This means that for baselines that are at least $1/P$ times the maximum baseline length, we can assume $E\{z_{pq}\} \approx 0$.

To illustrate the above discussion, we give a numerical example considering the LOFAR high-band array at 150 MHz. The point spread function ($1/\overline{u}$) at this frequency is about $6''$ and the field of view is about 10 degrees in diameter. Therefore, $P \approx 10 \times 3600/6 = 6000$. The longest baselines is about 80 km and for all baselines that are greater than $80/6 = 13$ m, the assumptions made above more or less hold.

To summarize the discussion in this section, we claim that

$$E\{\sum_{i'=1}^{K'} \mathbf{s}_{i'}\} \to \mathbf{0} \tag{6.11}$$

in (6.8) and therefore, $E\{\mathbf{n}'\} \to E\{\mathbf{n}\}$. However, the covariance of $\mathbf{n}'$ is different than the covariance of $\mathbf{n}$ and in general, the effective noise is not necessarily Gaussian anymore.

6.3.1 SAGE algorithm with unmodeled sources

In our previous work Kazemi et al. (2011) (chapter 2), we have presented the Space Alternating Generalized Expectation Maximization (SAGE) (Fessler & Hero, 1994) algorithm as an efficient and accurate method to solve (6.7), when the noise model is Gaussian. However, when there are unmodeled sources, as we have seen in this section, the noise model is not necessarily Gaussian.

The SAGE Expectation step is finding the conditional mean of the k-th signal,

$$\mathbf{x}^k = \mathbf{s}_k(\boldsymbol{\theta}) + \mathbf{n}' = \mathbf{s}_k(\boldsymbol{\theta}) + \sum_{i'=1}^{K'} \mathbf{s}_{i'} + \mathbf{n} \tag{6.12}$$

where $\mathbf{x}^k$ is the hidden data. Using this, we can rewrite the observed data $\mathbf{d}$ as

$$\mathbf{d} = \mathbf{x}^k + \sum_{i=1, i\neq k}^{K} \mathbf{s}_i(\boldsymbol{\theta}). \tag{6.13}$$

The conditional mean of $\mathbf{x}^k$ given $\mathbf{d}$, is given as $\widehat{\mathbf{x}^k}$ where

$$\widehat{\mathbf{x}^k} = \mathbf{s}_k(\boldsymbol{\theta}) + \left(\mathbf{d} - \sum_{i=1, i\neq k}^{K} \mathbf{s}_i(\boldsymbol{\theta}) - \sum_{i'=1}^{K'} \mathbf{s}_{i'} \right) \tag{6.14}$$

where we still assume a Gaussian noise model $\mathbf{n}$. Under assumption $\sum_{i'=1}^{K'} \mathbf{s}_{i'} \rightarrow \mathbf{0}$, the conditional mean simplifies to

$$\widehat{\mathbf{x}^k} \approx \mathbf{s}_k(\boldsymbol{\theta}) + \left(\mathbf{d} - \sum_{i=1, i\neq k}^{K} \mathbf{s}_i(\boldsymbol{\theta}) \right). \tag{6.15}$$

The SAGE Maximization step maximizes the likelihood of the conditional mean $\widehat{\mathbf{x}^k}$ under the noise $\mathbf{n}'$. However, we cannot use a least squares cost function as $\mathbf{n}'$ is not necessarily Gaussian anymore, because of the unmodeled sources. In section 6.4, we explore an alternative noise model based on Student's t distribution (Gosset, 1908) for the maximization of the likelihood.

6.4 Robust Calibration

First, we briefly describe the univariate Student's t distribution Lange et al. (1989); Bartkowiak (2007). Let X be a random variable with a normal distribution $\mathcal{N}(\varepsilon, \sigma^2/\gamma)$ where γ is also a random variable. Then the conditional distribution of X is

$$p(x|\varepsilon, \sigma^2, \gamma) = \frac{1}{(\sigma/\sqrt{\gamma})\sqrt{2\pi}} \exp\left(-\frac{1}{2} \left(\frac{x-\varepsilon}{\sigma/\sqrt{\gamma}} \right)^2 \right). \tag{6.16}$$

We consider γ to have a Gamma distribution, $\gamma \sim \mathrm{Gamma}(\frac{\nu}{2}, \frac{\nu}{2})$, where ν is positive (also called the number of degrees of freedom). The density function of γ can be given as

$$p(\gamma|\nu) = \frac{1}{\Gamma(\frac{\nu}{2})} \left(\frac{\nu}{2} \right)^{\frac{\nu}{2}} \gamma^{\frac{\nu}{2}-1} \exp\left(\frac{-\nu\gamma}{2} \right). \tag{6.17}$$

Then, the marginal distribution of X is

$$p(x; \varepsilon, \sigma^2, \nu) = \frac{\Gamma(\frac{\nu+1}{2})}{(\pi\nu)^{1/2}\Gamma(\frac{\nu}{2})\sigma} \left(1 + \frac{1}{\nu} \left(\frac{x-\varepsilon}{\sigma} \right)^2 \right)^{-\frac{1}{2}(\nu+1)} \tag{6.18}$$

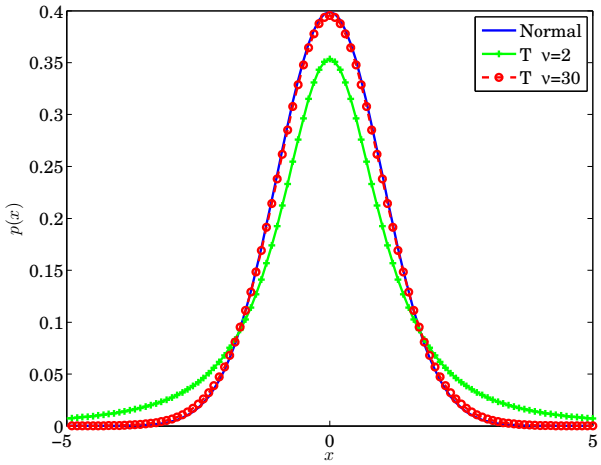

Figure 6.1: Probability density functions for standard normal distribution and Student's t distribution, with $\nu = 2$ and $\nu = 30$. At $\nu = 30$, the Student's distribution is indistinguishable from the normal distribution.

and this is the probability density function which defines the Student's t distribution. In Fig. 6.1, we have shown the probability density functions for Gaussian distribution and Student's t distribution, both with zero mean and unit variance. We see that for low values of the number of degrees of freedom ν, Student's t distribution has a higher tail. The asymptotic limit of Student's t distribution is Gaussian as $\nu \to \infty$, and for $\nu > 30$, the two distributions are indistinguishable, within the resolution of the data points used in Fig. 6.1.

Reverting back to (6.8), we see that the increase in the noise variance due to the unmodeled sources can be considered as the effect of γ in (6.16). Therefore, we consider the noise vector $\mathbf{n}'$ to have independent, identically distributed entries, with the distribution given by (6.18) with $\varepsilon = 0$ and $\sigma = \rho = 1$. In the SAGE iterations outlined in section 6.3.1, at the k-th iteration (6.15), we have $\widehat{\mathbf{x}^k}$ as the data vector and $\mathbf{s}_k(\boldsymbol{\theta})$ as the model that is used to estimate the parameters $\boldsymbol{\theta}$ (or a subset of the parameters). Therefore, the estimation problem is to find the ML estimate of $\boldsymbol{\theta}$ (size $M \times 1$), given the data $\mathbf{y} = \widehat{\mathbf{x}^k}$ (size $N \times 1$) and the model $\mathbf{f}(\boldsymbol{\theta}) = \mathbf{s}_k(\boldsymbol{\theta})$ (size $N \times 1$) with noise $\mathbf{n}'$. Hence, we can rewrite our data model as

$$\mathbf{y} = \mathbf{f}(\boldsymbol{\theta}) + \mathbf{n}' \tag{6.19}$$

where the unknowns are $\boldsymbol{\theta}$ and ν, the number of degrees of freedom of noise $\mathbf{n}'$. Then, the i-th element of the vector $\mathbf{y}$ (denoted by $\mathbf{y}_i$) in (6.6) will have a similar distribution as (6.18) with $\sigma = 1$ and $\mu_i = \mathbf{f}_i(\boldsymbol{\theta})$, where $\mathbf{f}_i(\boldsymbol{\theta})$ is the i-th element of the vector function $\mathbf{f}(\boldsymbol{\theta})$. The likelihood function becomes

$$l(\boldsymbol{\theta}, \nu|\mathbf{y}) = \prod_{i=1}^{N} \frac{\Gamma(\frac{\nu+1}{2})}{(\pi\nu)^{1/2}\Gamma(\frac{\nu}{2})} \left(1 + \frac{(\mathbf{y}_i - \mathbf{f}_i(\boldsymbol{\theta}))^2}{\nu}\right)^{-\frac{1}{2}(\nu+1)} \tag{6.20}$$

and the log-likelihood function is

$$\begin{aligned} & L(\boldsymbol{\theta}, \nu|\mathbf{y}) \\ = \quad & N \log \Gamma(\frac{\nu+1}{2}) - N \log \Gamma(\frac{\nu}{2}) - \frac{N}{2} \log(\pi\nu) \\ - \quad & \frac{(\nu+1)}{2} \sum_{i=1}^{N} \log \left(1 + \frac{(\mathbf{y}_i - \mathbf{f}_i(\boldsymbol{\theta}))^2}{\nu}\right). \end{aligned} \tag{6.21}$$

Note that unlike for the Gaussian case, minimizing a least squares cost function (or maximizing the likelihood) will not give us the ML estimate. In addition, we have an extra parameter, ν, which is the number of degrees of freedom. Hence, we use the Expectation-Conditional Maximization Either algorithm (Liu & Rubin, 1995; Li et al., 2006) to solve this problem. The ECME algorithm is an extension of the EM algorithm for t distribution presented by Lange et al. (1989).

The auxiliary variables are the weights w_i (N values) and a scalar λ. All these are initialized to 1 at the beginning. The Expectation step in the ECME algorithm involves the conditional estimation of hidden variables γ_i (or the weights w_i) as

$$w_i \leftarrow E\{\gamma_i|\mathbf{y}_i, \boldsymbol{\theta}, \nu\} = \lambda \frac{\nu+1}{\nu + (\mathbf{y}_i - \mathbf{f}_i(\boldsymbol{\theta}))^2} \tag{6.22}$$

and the update of the scalar λ

$$\lambda \leftarrow \frac{1}{N} \sum_{i=1}^{N} w_i. \tag{6.23}$$

The Maximization step involves finding the value for ν that is a solution for

$$\begin{aligned} & \Psi(\frac{\nu+1}{2}) - \log\left(\frac{\nu+1}{2}\right) - \Psi(\nu/2) + \log(\nu/2) \\ & + \frac{1}{N} \sum_{i=1}^{N} (\log(w_i) - w_i) + 1 = 0 \end{aligned} \tag{6.24}$$

where $\Psi(x) = \frac{d}{dx} \log(\Gamma(x))$ is the digamma function. Since we know that beyond $\nu > 30$, we almost get a Gaussian distribution, and therefore the search space for finding a solution for (6.24) is kept within $2 \leq \nu \leq 30$ and initial value for ν is chosen to be 2.

Once w_i is known, $\mathbf{y}_i$ has a normal distribution with variance determined by w_i. Therefore, in the Maximization step of the EM algorithm, we minimize the weighted least squares cost function

$$l(\boldsymbol{\theta}|\nu) = \sum_{i=1}^{N} w_i (\mathbf{y}_i - \mathbf{f}_i(\boldsymbol{\theta}))^2. \tag{6.25}$$

With this formulation at hand, we present the LM algorithm for robust calibration in Algorithm 1, similar to the presentations in Lourakis (2004) and Madsen et al. (2004). The additional information needed in Algorithm 1 is the Jacobian of $\mathbf{f}(\boldsymbol{\theta})$, i.e., $\mathbf{J}(\boldsymbol{\theta}) = \frac{\partial \mathbf{f}(\boldsymbol{\theta})}{\partial \boldsymbol{\theta}}$, that can be calculated in closed form using (6.2) and (6.4). The diagonal matrix with the weights $\sqrt{w_i}$ as its diagonal entries is given by $\mathbf{W}$.

Algorithm 1 Robust Levenberg-Marquardt (ECME)

Require: Data $\mathbf{y}$, mapping $\mathbf{f}(\boldsymbol{\theta})$, Jacobian $\mathbf{J}(\boldsymbol{\theta})$, ν, initial value $\boldsymbol{\theta}^0$

$\boldsymbol{\theta} \leftarrow \boldsymbol{\theta}^0$; $w_i \leftarrow 1$; $\lambda \leftarrow 1$
while $l <$ max EM iterations **do**
  $k \leftarrow 0; \eta \leftarrow 2$
  $\mathbf{J}(\boldsymbol{\theta}) \leftarrow \mathbf{W}\mathbf{J}(\boldsymbol{\theta})$
  $\mathbf{A} \leftarrow \mathbf{J}(\boldsymbol{\theta})^T\mathbf{J}(\boldsymbol{\theta}); \mathbf{e} \leftarrow \mathbf{W}(\mathbf{y} - \mathbf{f}(\boldsymbol{\theta})); \mathbf{g} \leftarrow \mathbf{J}(\boldsymbol{\theta})^T\mathbf{e}$
  found $\leftarrow (\|\mathbf{g}\|_\infty < \epsilon_1); \mu \leftarrow \frac{\max \mathbf{A}_{ii}}{3}$
  while (not found) and ($k <$ max iterations) **do**
    $k \leftarrow k + 1$; Solve $(\mathbf{A} + \mu\mathbf{I})\mathbf{h} = \mathbf{g}$
    if $\|\mathbf{h}\| < \epsilon_2(\|\boldsymbol{\theta}\| + \epsilon_2)$ **then**
      found $\leftarrow true$
    else
      $\boldsymbol{\theta}_{new} \leftarrow \boldsymbol{\theta} + \mathbf{h}$
      $\rho \leftarrow (\|\mathbf{e}\|^2 - \|\mathbf{W}(\mathbf{y} - \mathbf{f}(\boldsymbol{\theta}_{new}))\|^2)/(\mathbf{h}^T(\mu\mathbf{h} + \mathbf{g}))$
      if $\rho > 0$ **then**
        $\boldsymbol{\theta} \leftarrow \boldsymbol{\theta}_{new}$
        $\mathbf{J}(\boldsymbol{\theta}) \leftarrow \mathbf{W}\mathbf{J}(\boldsymbol{\theta})$
        $\mathbf{A} \leftarrow \mathbf{J}(\boldsymbol{\theta})^T\mathbf{J}(\boldsymbol{\theta}); \mathbf{e} \leftarrow \mathbf{W}(\mathbf{y} - \mathbf{f}(\boldsymbol{\theta})); \mathbf{g} \leftarrow \mathbf{J}(\boldsymbol{\theta})^T\mathbf{e}$
        found $\leftarrow (\|\mathbf{g}\|_\infty \leq \epsilon_1)$
        $\mu \leftarrow \mu \max(1/3, 1 - (2\rho - 1)^3); \eta \leftarrow 2$
      else
        $\mu \leftarrow \mu\eta; \eta \leftarrow 2\eta$
      end if
    end if
  end while
  Update weights $w_i \leftarrow \lambda \frac{\nu+1}{\nu+(\mathbf{y}_i - \mathbf{f}_i(\boldsymbol{\theta}))^2}$
  Update $\lambda \leftarrow \frac{1}{N}\sum_{i=1}^{N} w_i$
  Update ν using (6.24)
  $l \leftarrow l + 1$
end while
return $\boldsymbol{\theta}$

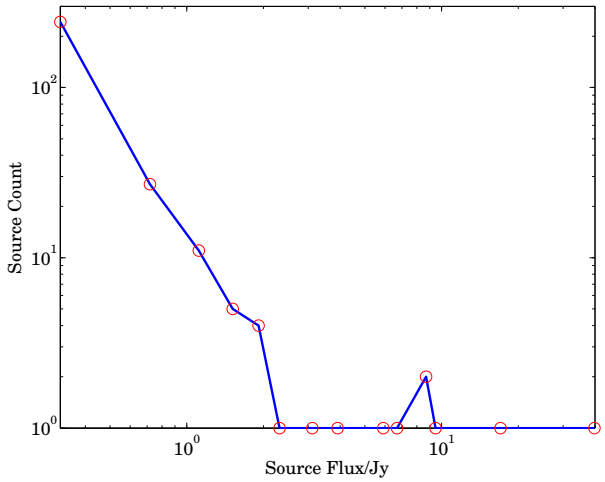

Figure 6.2: Histogram of the fluxes of the 300 simulated sources. The peak flux is 40 Jy.

6.5 Simulation Results

In this section, we provide results based on simulations to convince the robustness of our proposed calibration approach. We simulate an interferometric array with $R = 47$ stations, with the longest baseline of about 30 km. We simulate an observation centered at the north celestial pole (NCP), with a duration of 6 hours at 150 MHz. The integration time for each data sample is kept at 10 s. For the full duration of the observation, there are 2160 data points. Each data point consists of 1081 baselines and 8 real values corresponding to the 2×2 complex visibility matrix.

The sky is simulated to have 300 sources, uniformly distributed over a field of view of 12×12 degrees. The intensities of the sources are drawn using a power law distribution, with the peak intensity at 40 Jy. In Fig. 6.2, we show the histogram of the intensities of the sources. Our intention is to compare the fluxes of the weak sources, i.e. the sources with intensities less than or equal to 1 Jy, after directional calibration is performed. In order to do that we corrupt the visibilities of the bright sources with directional errors that vary slowly with time. We consider three scenarios here: we only corrupt the signals of the sources that have intensities greater than (i) 1 Jy, (ii) 2 Jy and (iii) 5 Jy. For the simulated sky model, there are 28, 11 and 7 sources that have fluxes greater than 1 Jy, 2 Jy and 5 Jy, respectively. Note that in each case, we do not corrupt the signals of the weak sources as our only objective is to find the recovered flux after directional calibration and subtraction of the bright sources from the data, although in reality all sources will be corrupted by similar directional errors. Finally, we add zero mean white Gaussian noise to the simulated data, with the signal to noise ratio (SNR) defined as

$$\mathrm{SNR} \triangleq 10 \log_{10} \left(\frac{\sum_{p,q} \|\mathbf{V}_{pq}\|^2}{\sum_{p,q} \|\mathbf{N}_{pq}\|^2} \right) \ \mathrm{dB}. \tag{6.26}$$

In all simulations, we have kept the SNR at 5 dB.

In Fig. 6.3, we show some of the weak sources (with intensities less than 1 Jy) over a 4×4 degrees of the field of view. In Fig. 6.4, we have also added the bright sources with slowly varying

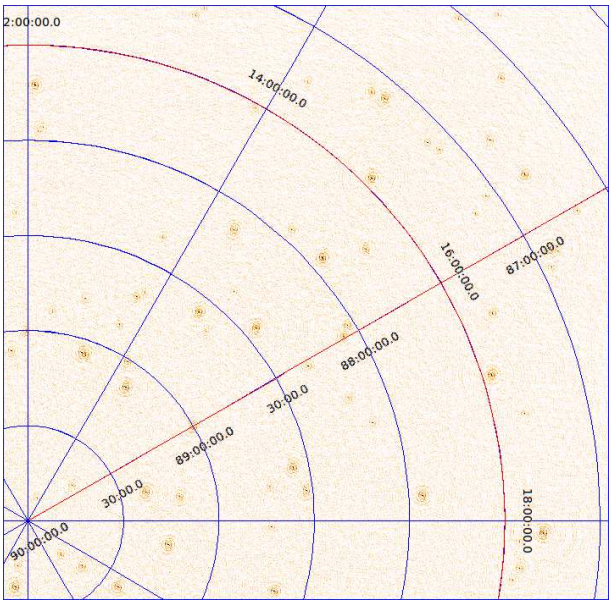

Figure 6.3: Simulated image of 4×4 degrees of the sky, showing only weak sources with intensities less than 1 Jy.

directional errors. Note that in order to recover Fig. 6.3 from Fig. 6.4, directional calibration is essential.

In Fig. 6.5, we show the image after directional calibration along the bright sources and subtraction of their contribution from the data, using traditional calibration based on a Gaussian noise model. On the other hand, in Fig. 6.6, we show the image after directional calibration and subtraction using a robust noise model. With respect to the subtraction of the bright sources from the data, both normal calibration and robust calibration show equal performance as seen from Figs. 6.5 and 6.6.

We perform Monte Carlo simulations with different directional gain and additive noise realizations for each scenario (i), (ii) and (iii) as outlined previously. For each realization, we image the data after subtraction of the bright sources and compare the flux recovered for the weak sources before and after directional calibration. The directional calibration is performed for every 10 time samples (every 100 s duration). Therefore, the number of data points used for each calibration (N) is $10 \times 1081 \times 8 = 86480$ and the number of real parameters estimated are $47 \times 8 \times 28 = 10528$, $47 \times 8 \times 11 = 4136$ and $47 \times 8 \times 7 = 2632$, respectively for scenarios (i),(ii) and (iii). For each scenario (i), (ii) and (iii), we perform 100 Monte Carlo simulations.

Our performance metric is the ratio between the recovered peak flux of the weak sources compared to the original flux of each source. We calculate the average ratio (recovered flux / original flux) over all Monte Carlo simulations. In Figs. 6.7, 6.8 and 6.9, we show the results obtained for scenario (i),(ii) and (iii), respectively.

We observe two major characteristics in Figs. 6.7, 6.8 and 6.9. First, we see that as we calibrate over an increasing number of directions (and subtract an increasing number of sources), the recovered flux is reduced. Second, in all scenarios, robust calibration recovers more flux

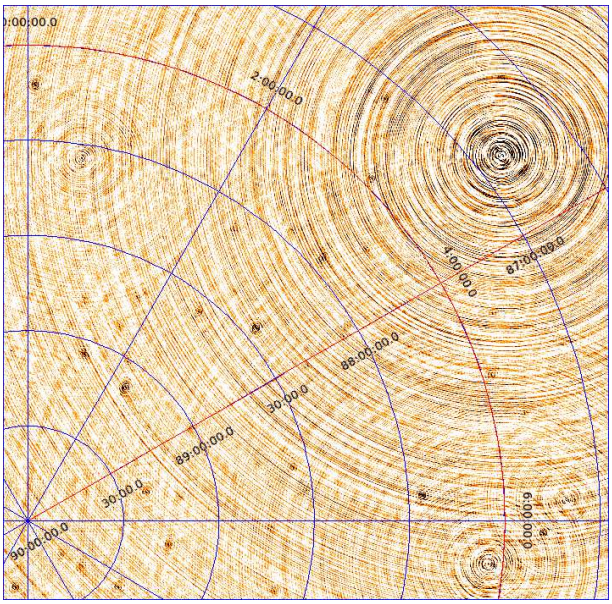

Figure 6.4: Simulated image of the sky where bright sources with fluxes greater than 1 Jy have been corrupted with directional errors. Due to these errors, there are artefacts throughout the image that makes it difficult to study the fainter background sources.

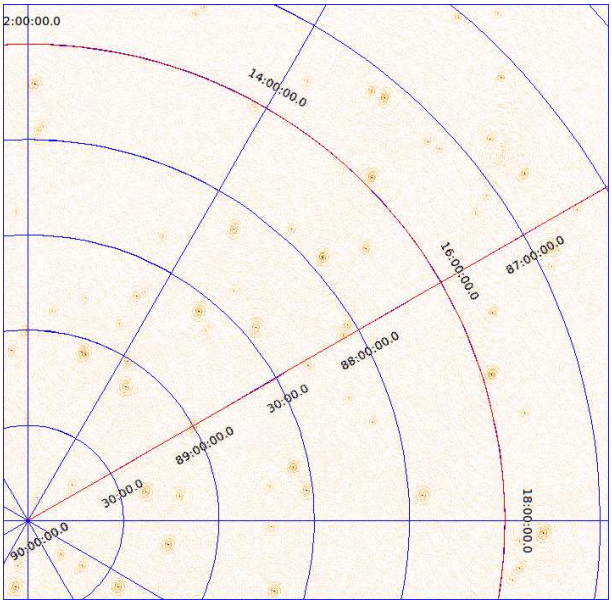

Figure 6.5: Image of the sky where the bright sources have been calibrated and subtracted from the data to reveal the fainter background sources. The traditional calibration based on a Gaussian noise model is applied.

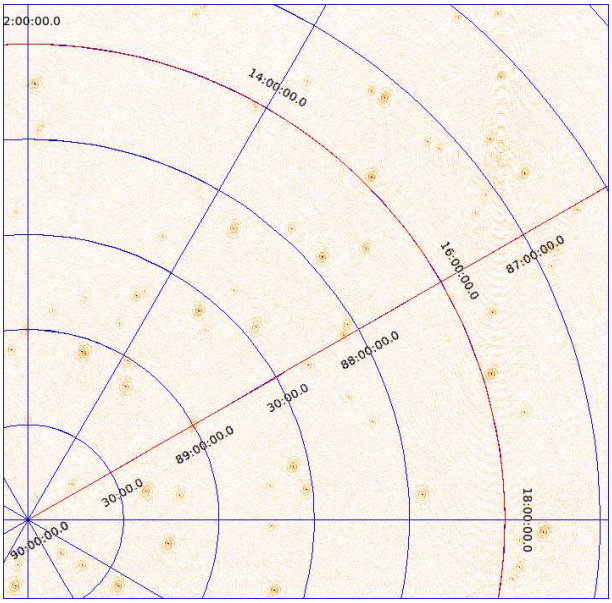

Figure 6.6: Image of the sky where the bright sources have been calibrated and subtracted from the data to reveal the fainter background sources. The robust calibration proposed in this chapter is applied.

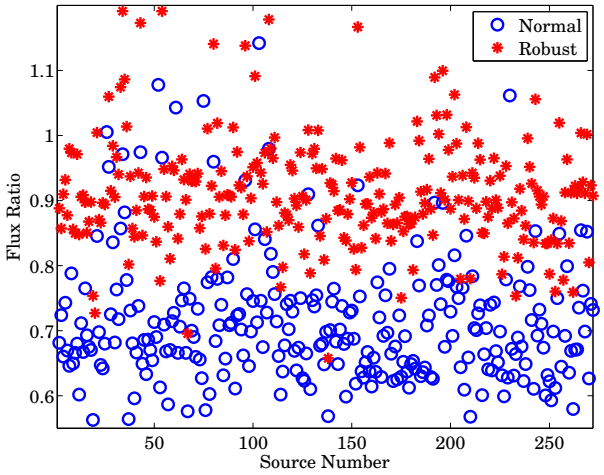

Figure 6.7: Ratio between the recovered flux and the original flux of each of the weak sources, when bright sources ($>$ 1 Jy) are subtracted.

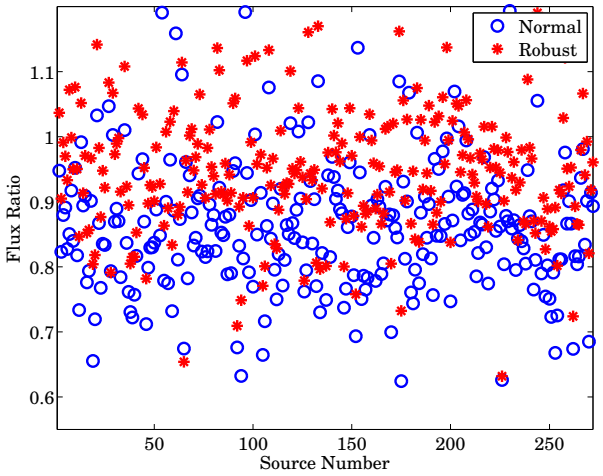

Figure 6.8: Ratio between the recovered flux and the original flux of each of the weak sources, when bright sources (> 2 Jy) are subtracted.

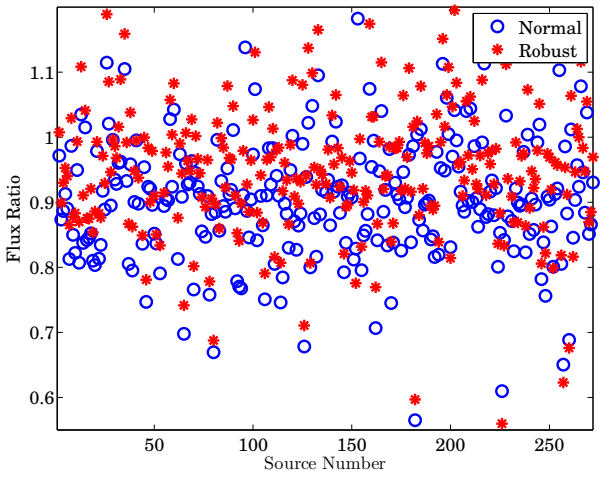

Figure 6.9: Ratio between the recovered flux and the original flux of each of the weak sources, when bright sources (> 5 Jy) are subtracted.

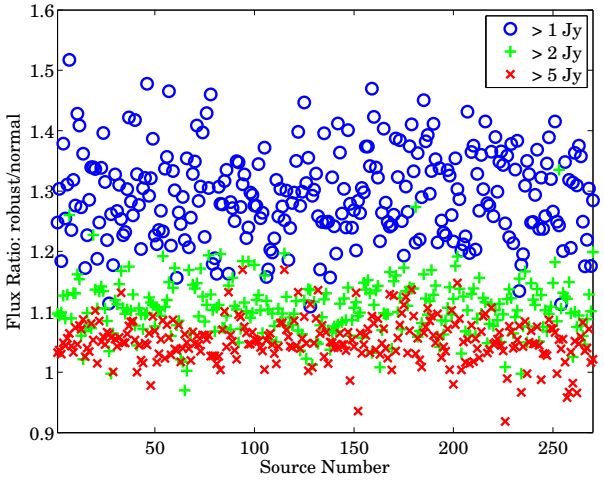

Figure 6.10: Ratio between the recovered flux using robust calibration and the recovered flux using normal calibration. Almost always, robust calibration recovers more flux compared with normal calibration. The different colours indicate different scenarios where the number of bright sources subtracted is varied.

No. of sources calibrated and subtracted	Lowest flux of the subtracted sources (Jy)	Average reduction of the flux of weak background sources (%)	
		Normal Calibration	Robust Calibration
28	1	28.7	8.2
11	2	12.3	3.2
7	5	7.9	3.1

Table 6.1: Comparison of the reduction of flux of the weak background sources with normal and robust calibration.

compared to normal calibration. To illustrate this point, we also plot in Fig. 6.10, the ratio between the recovered flux using robust calibration and the recovered flux using normal calibration. As we see from Fig. 6.10, we almost always get a value greater than 1 for this ratio, indicating that we recover more flux using robust calibration.

We summarize our findings in Table 6.1. We see that at worst case, the performance of normal calibration gives a flux reduction of about 20% compared to robust calibration.

Up to now, we have only considered the sky to consist of only point sources. In reality, there is diffuse structure in the sky. This diffuse structure is seldom incorporated into the sky model during calibration either because it is too faint or because of the complexity of modeling it accurately. We have also done simulations where there is faint diffuse structure in the sky and only the bright foreground sources are calibrated and subtracted. We have chosen scenario (i) in the previous simulation except that we have replaced the sources below 1 Jy with Gaussian sources with peak intensities below 1 Jy and with random shapes and orientations.

In Fig. 6.11, we have shown the residual image of a 6×6 degrees area in the sky after

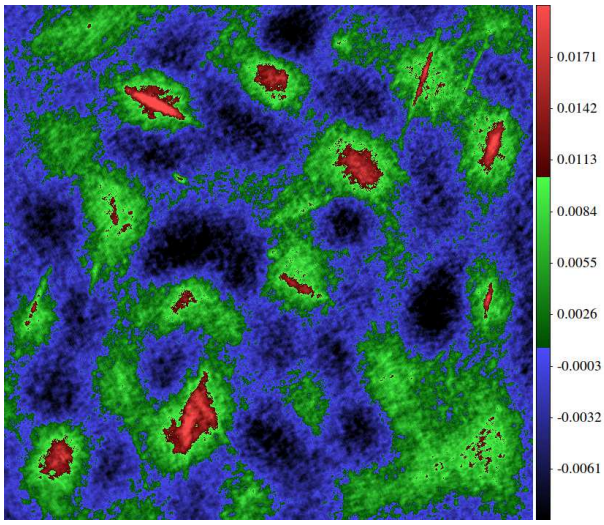

Figure 6.11: Average residual image of the diffuse structure after subtracting the bright sources by normal calibration. The colour scale is in Jy/PSF.

removing all sources brighter than 1 Jy. The residual image is obtained by averaging 100 Monte Carlo simulations. The equivalent image for robust calibration is given in Fig. 6.12.

As seen from Figs. 6.11 and 6.12, there is more flux in the diffuse structure after robust calibration. This is clearly seen in the bottom right hand corner of both figures where Fig. 6.12 has more positive flux than in Fig. 6.11.

6.6 Conclusions

We have presented the use of Student's t distribution in radio interferometric calibration. Compared with traditional calibration that has an underlying Gaussian noise model, robust calibration using Student's t distribution can handle situations where there are model errors or outliers in the data. Moreover, by automatically selecting the number of degrees of freedom ν during calibration, we have the flexibility of choosing the appropriate distribution even when no outliers are present and the noise is perfectly Gaussian. For the specific case considered in this chapter, i.e. the loss of coherency or flux of unmodeled sources, we have given simulation results that show the significantly improved flux preservation with robust calibration. Future work would focus on adopting this for pipeline processing of massive datasets from new and upcoming radio telescopes.

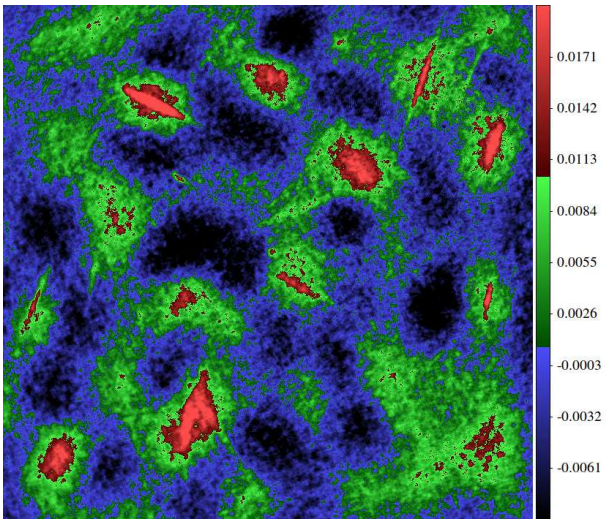

Figure 6.12: Average residual image of the diffuse structure after subtracting the bright sources by robust calibration. The colour scale is in Jy/PSF and is the same as in Fig. 6.11.

Chapter 7

Summary and FutureWork

7.1 Summary

For any radio interferometric telescope, the image quality depends on the convergence of its calibration as well as how fast one can reach this accuracy. This reflects the importance of the convergence property in calibration algorithms. Since calibration problem is a non-linear optimization problem, it is a great challenge to design calibration techniques which guarantee a stable convergence. Moreover, in practice, we do not run calibration algorithms to convergence and usually stop algorithms long before that. The reason is that we are limited by computational time as well as memory consumption in order to keep track of origins of the observed signals. Therefore, developing convergent calibration algorithms with fast speeds of convergence is of an essential importance.

We have developed novel statistical calibration algorithms and investigated their properties in order to obtain optimal solutions by running the algorithms to convergence. This resulted in several contributions to the literature: Kazemi et al. (2011); Kazemi & Yatawatta (2012); Yatawatta et al. (2012); Kazemi et al. (2012, 2011, 2013b,a,c); Kazemi & Yatawatta (2013), which are grouped into three major categories:

1. **Speeding up the procedure of ML estimation in calibration**:

   We applied the SAGE (Space Alternating Generalized Expectation Maximization) algorithm (Fessler & Hero, 1994) to radio interferometric calibration in Kazemi et al. (2011). As it is explained in chapter 1, SAGE is one of the EM (Expectation Maximization, Dempster et al. (1977)) variants which guarantees a fast and stable convergence. The key to success of the algorithm is breaking the calibration's ML (Maximum Likelihood) estimation problem into ML estimation sub-problems which are defined for partitions of parameters. In addition, in Kazemi et al. (2012) and Kazemi et al. (2013c), we have even sped up the standard SAGE calibration algorithm by utilizing OS (Ordered Subsets) scheme (Hudson & Larkin, 1994) which accelerates the iterative procedure of ML estimation for every sub-problem of the SAGE calibration. The reason behind this acceleration is that for Jacobian computations, OS uses only a few percent of the observed data instead of the whole. Thus, OS-SAGE calibration can significantly accelerate the speed of convergence at the initial iterations of the SAGE calibration method. However, since it usually does not converge, we

recommend shifting to a standard SAGE calibration after getting close enough to an optimal solution.

2. **Developing clustered calibration scheme to calibrate for groups of sources**:

   We developed clustered calibration in Kazemi et al. (2011, 2013b) to calibrate for groups of sources when the SNR is not high enough to calibrate for every source individually. Clustered calibration calibrates for every source group as an individual source whose coherency is equal to the summation of coherencies of the cluster's members. In Kazemi & Yatawatta (2012) we presented performance analysis of the scheme and showed that the method has a higher speed of convergence compared to un-clustered calibration when the SNR (Signal to Noise Ratio) is low. This is due to two reasons: (i) Clustered calibration solves for one direction per source cluster. Thus, the number of unknowns is decreased which leads to less computations. (ii) Clustered calibration needs less number of iterations to converge since because it uses strong signal of source clusters rather than signals of weak individual sources to calculate ML estimations. Following the introduction of the calibration, in Kazemi et al. (2013a), we proposed the use of soft (fuzzy) clustering rather than hard clustering for the clustered calibration technique which provides an even faster convergence rate compared to the standard clustered calibration.

3. **Applying robust data modeling into calibration problem**:

   Finally by Yatawatta et al. (2012) and Kazemi & Yatawatta (2013) we recommended the use of Student's t noise model instead of the Gaussian noise model in order to improve the robustness of calibration. When there are model errors or outliers in the data, Gaussian noise model is no more efficient and robust calibration provides a faster speed of convergence compared to the traditional calibration using the Gaussian noise model.

To summarize, In this thesis,

- we propose the use of SAGE calibration instead of standard LS (Least Squares) calibration.
- we propose the use of OS-SAGE calibration at initial iterations in order to obtain a faster convergence rate.
- we propose clustered calibration rather than the standard (un-clustered) calibration for low SNRs.
- we propose to use the clustered calibration via a fuzzy clustering of sources to improve the convergence rate.
- we propose robust calibration via a Student's t noise model for a faster recovery of weak signals when there are outliers in data.

We developed simulated and real experiences and showed that the above expressions are reasonably accurate.

7.2 Future work

- Throughout this thesis, we developed calibration algorithms based on the measurement equation given by Hamaker et al. (1996). However, it is still an open problem if the model

corresponds to all the systematics or not, and if not, then how this model mismatch will affect the reconstruction methods presented in this thesis. For example, how much could it affect the convergence properties of the introduced calibrations.

- We tested the faster convergence rate of SAGE calibration compared to LS calibration using LRT (Likelihood Ratio Test, Graves (1978)). It would be desirable to perform the same comparison between SAGE and robust calibrations performances.
- In chapter 3, we introduced OS calibration without proposing any specific partitioning of data. Finding the smallest possible data partitions whose Jacobian is the best estimate for the Jacobian of the complete data set is addressed in future work. We also explained that OS calibration usually gets to a convergence problem, that is, we proposed to run non-OS calibrations after the OS calibration execution. However, whether this is the best solution or not must be examined. And if it is the best, the effectiveness of the use of SAGE calibration in particular as that non-OS calibration scheme needs to be checked. Moreover, we can perform Monte Carlo experiments to see after how many iterations OS calibration usually gets to a sub-optimal limit cycle.
- Another challenging question is whether we can utilize the incremental EM algorithm for radio interferometric calibration or not. It is proved that the algorithm benefits from a faster convergent rate than the SAGE method. However, the modeling applicability of the method for radio interferometric calibration needs to be examined.
- In clustered calibration, clustering of sources is done manually once before the calibration's execution. However, in future work, we address updating source clusters at several iterations of the calibration procedure using the latest obtained solutions. On top of automating all the clustered calibration procedure, this can improve the accuracy of the clustered calibration using eventually the most efficient clusters design.
- For the standard clustered calibration, we constructed a performance analysis using CRLB (Cramer-Rao Lower Bounds, Kay (1993)). It is natural to extend the analysis for fuzzy clustered calibration as well.
- It will be an interesting question whether the use of the Student's t noise model is the best for improving the robustness of calibration. To answer this question, the statistical characteristic of the noise must be studied in more details and implemented in the calibration ML estimation scheme.
- In chapter 5, the performance of fuzzy clustered calibration is shown only for simulations. We need to assess the superiority of the method in terms of its speed of convergence compared to the standard clustered calibration for real observations as well.
- The use of solutions obtained via calibration for building instrumental models is still and open problem. Extension of works like Yatawatta (2013); van der Tol et al. (2007); Intema et al. (2009) is needed.
- We developed new calibration algorithms in this dissertation. Some of these algorithms have already been implemented (SAGECal) and are already being used in LOFAR data processing pipelines. However, we are still seeking better algorithms that are simpler in implementations and faster in convergence.

Bibliography

Ahn S., Convergent algorithms for statistical image reconstruction in emission tomography, 2004, PhD thesis, University of Michigan

Akaike H., Information theory and an extension of the maximum likelihood principle, 1973, Proceedings of the 2nd International Symposium on Information Theory, eds. B.N.Petrov and F. Csaki, 267

Aravkin A., Friedlander M., van Leeuwen T., Robust inversion via semistochastic dimensionality reduction, 2012, Proceedings of the IEEE International Conference on Acoustics, Speech and Signal Processing (ICASSP), 5425

Baldwin J., Warner P., Aperture synthesis without phase measurements, 1976, MNRAS, 175, 345

—, Phaseless aperture synthesis, 1978, MNRAS, 182, 411

Bartkowiak A., Should normal distribution be normal? The student's t alternative, 2007, Proceedings of the 6th International Conference on Computer Information Systems and Industrial Management Applications (CISIM'07), 3

Bates D. M., Watts D. G., 2007, Nonlinear regression analysis and its applications. Wiley-Interscience

Bernardi G., et al., Subtraction of point sources from interferometric radio images through an algebraic forward modelling scheme, 2011, MNRAS, 413, 411

Bezdek J. C., 1981, Pattern recognition with fuzzy objective function algorithms. Kluwer Academic Publishers, Norwell, MA, USA

Bilmes J., A Gentle tutorial of the EM algorithm and its application to parameter estimation for Gaussian mixture and hidden Markov models, 1998, U.C. Berkely, TR-97-02

Boonstra A., van der Veen A., Gain calibration methods for radio telescope arrays, 2003, IEEE Transactions on Signal Processing, 51, 25

Born M., Wolf E., 1999, Principles of optics. Cambridge University Press

Boyles R. A., On the convergence of the EM algorithm, 1983, Journal of the Royal Statistical Society. Series B (Methodological), 45, 47

Burke B., Graham-Smith F., 2009, An introduction to radio astronomy. Cambridge University Press

Celeux G., Chrétien S., Forbes F., Mkhadri A., 1999, A component-wise EM algorithm for mixtures. Research Report RR-3746, INRIA

Celeux G., Govaert G., A classification EM algorithm for clustering and two stochastic versions, 1992, Computational Statistics & Data Analysis, 14, 315

Condon J. J., Confusion and flux-density error distributions, 1974, ApJ, 188, 279

Conn A. R., Gould N. I. M., Toint P. L., Methods for nonlinear constraints in optimization calculations, 1997, in The state of the Art in Numerical Analysis, Duff I. S., Watson A., eds., Oxford University Press, pp. 363–390

Cornwell T., Fomalont E. B., Synthesis imaging in radio astronomy II, 1999, Astronomical Society of the Pacific Conference Series, 180, 187

Cornwell T. J., Wilkinson P. N., A new method for making maps with unstable radio interferometers , 1981, MNRAS, 196, 1067

Dempster A. P., Laird N. M., Rubin D. B., Maximum likelihood from incomplete data via the EM algorithm, 1977, Journal of the Royal Statistical Society: Series B, 39, 1, with discussion

Diestel R., 2012, Graph theory, Graduate Texts in Mathematics. Springer

Erdogan H., Fessler J. A., Ordered subsets algorithms for transmission tomography, 1999, Physics in Medicine and Biology, 44, 2835

Feder M., Weinstein E., Parameter estimation of superimposed signals using the EM algorithm , 1988, Acoustics, Speech and Signal Processing, IEEE Transactions on, 36, 477

Fessler J. A., Hero A. O., New complete-data spaces and faster algorithms for penalized- likelihood emission tomography, 1993, IEEE Conference Record of Nuclear Science Symposium and Medical Imaging Conference, 3, 1897

—, Space-alternating generalized expectation-maximization algorithm, 1994, IEEE Transactions on Signal Processing, 42, 2664

Fisher R. A., Theory of statistical estimation, 1925, Mathematical Proceedings of the Cambridge Philosophical Society, 22, 700

Fridman P. A., Baan W. A., RFI mitigation methods in radio astronomy, 2001, A&A, 378, 327

Gallant A. R., Nonlinear regression, 1975, The American Statistician, 29, 73

Gini F., Reggiannini R., On the use of Cramer-Rao-like bounds in the presence of random nuisance parameters, 2000, IEEE Transactions on Communications, 48, 2120

Gini F., Reggiannini R., Mengali U., The modified Cramer-Rao bound in vector parameter estimation, 1998, IEEE Transactions on Communications, 46, 52

Gosset W., The probable error of mean, 1908, Biometrika, 6, 1

Graves S., On the Neyman-Pearson theory of testing, 1978, British Journal for the Philosophy of Science, 29, 1

Hamaker J. P., Understanding radio polarimetry. V. Making matrix self-calibration work: Processing of a simulated observation, 2006, A&A, 456, 395

Hamaker J. P., Bregman J. D., Sault R. J., Understanding radio polarimetry. I. Mathematical foundations., 1996, A&AS, 117, 137

Högbom J. A., Aperture synthesis with a non-regular distribution of interferometer baselines, 1974, A&AS, 15, 417

Hongqing Z., Huazhong S., Limin L., Jian Z., PET image reconstruction using a modified ordered subsets and sage algorithm, 2004, 11th IEEE International Workshop on Systems, Signals and Image Processing

Hudson H. M., Larkin R. S., Accelerated image reconstruction using ordered subsets of projection data, 1994, IEEE Transactions on Medical Imaging, 13, 601

Intema H. T., et al., Ionospheric calibration of low frequency radio interferometric observations using the peeling scheme. I. Method description and first results, 2009, A&A, 501, 1185

Jamshidian M., Jennrich R. I., Conjugate gradient acceleration of the EM algorithm, 1993, Journal of the American Statistical Association, 88, 221

Jelić V., et al., Foreground simulations for the LOFAR-epoch of reionization experiment, 2008, MNRAS, 389, 1319

Johnson S. C., Hierarchical clustering schemes, 1967, Psychometrika, 32, 241

Kaufman L., Rousseeuw P., 1990, Finding groups in data: An introduction to cluster analysis. Wiley Interscience, Wiley-Interscience, New York

Kay S., 1993, Fundamentals of Statistical Signal Processing: Estimation theory, Prentice Hall signal processing series. Prentice-Hall PTR

Kazemi S., et al., Radio interferometric calibration using the SAGE algorithm, 2011, MNRAS, 414, 1656

Kazemi S., Yatawatta S., Robust radio interferometric calibration using the t-distribution, 2013, MNRAS, 435, 597

Kazemi S., Yatawatta S., Zaroubi S., Clustered radio interferometric calibration, 2011, IEEE Workshop on StatisticalSignal Processing, SSP2011, 414, 597

—, Ordered-subsets acceleration of radio interferometric calibration: OS-SAGE calibration algorithm, 2012, in proc. IEEE International Symposium on Signal Processing and Information Technology (ISSPIT 2012)

—, Application of fuzzy clustering in clustered radio interferometric calibration, 2013a, *under review in* MNRAS

—, Clustered calibration: An improvement to radio interferometric direction-dependent self-calibration, 2013b, MNRAS, 430, 1457

—, Radio interferometric calibration via ordered-subsets algorithms: OS-LS and OS-SAGE calibrations, 2013c, MNRAS, 434, 3130

Kazemi S., Yatawatta S.and Zaroubi S., Performance analysis of clustered radio interferometric calibration, 2012, IEEE International conference on Acoustics, Speech and Signal Processing (ICASSP), 2533

Kerdprasop K., Kerdprasop N., Sattayatham P., Weighted k-means for density-biased clustering, 2005, in Data Warehousing and Knowledge Discovery, Cam L. M. L., Neyman J., eds., Springer-Verlag Berlin Heidelberg, pp. 488–497

Kirkpatrick S., Gelatt C. D. J., Vecchi M. P., Optimization by simulated annealing, 1983, Science, 220, 671

Kullback S., 1997, Information Theory and Statistics. Dover Publications

Lampton M., Damping-undamping strategies for the Levenberg-Marquardt nonlinear least-squares method, 1997, Computers in Physics, 11, 110

Lange K., Little R., Tylor J., Robust statistical modeling using the T distribution, 1989, Journal of the American Statistical Association, 84, 881

Leshem A., van der Veen A.-J., Radio-astronomical imaging in the presence of strong radio interference, 2000, Information Theory, IEEE Transactions on, 46, 1730

Levanda R., Leshem A., Image formation in synthesis radio telescopes, 2010, IEEE Signal Processing Magazine, 27, 14

Levenberg K., A method for the solution of certain non-linear problems in least squares, 1944, Quarterly of Applied Mathematics, 2, 164

Li S., Wang H., Chai T., A t-distribution based particle filter for target tracking, 2006, Proceedings of American Control Conference, 2191

Liu A., Tegmark M., Zaldarriaga M., Will point sources spoil 21-cm tomography?, 2009, MNRAS, 394, 1575

Liu C., Rubin D., ML estimation of the t distribution using EM and its extensions, ECM and ECME, 1995, Statistica Sinica 5, 19

Liu C., Rubin D., Wu Y., Parameter expansion to accelerate EM: The PX-EM algorithm, 1998, Biometrika, 85, 755

Liu C., Rubin D. B., The ECME algorithm: A simple extension of EM and ECM with faster monotone convergence, 1994, Biometrika, 81, 633

Liu L. Y. Y., B. S., Study on ordered subsets-least Square reconstruction of image, 2005, Journal of Image and Graphics, 10, 628

Lonsdale C. J., et al., The Murchison widefield array: Design overview, 2009, Proceedings of the IEEE Special Issue: Advances in Radio Telescopes, 97, 1497

Lourakis M., Levenberg-Marquardt nonlinear least squares algorithms in C/C++, 2004, Technical report, Institute of Computer Science, Foundation for Research and Technology, Hellas (FORTH)

MacQueen J. B., Some methods for classification and analysis of multiVariate observations, 1967, in Proceedings of the fifth Berkeley Symposium on Mathematical Statistics and Probability, Cam L. M. L., Neyman J., eds., Vol. 1, University of California Press, pp. 281–297

Madsen K., Nielsen H., Tingleff O., Methods for non-linear least squares problems, 2004, Technical report, Technical University of Denmark

Marquardt D. W., An algorithm for least-squares estimation of nonlinear parameters, 1963, Journal of the Society for Industrial and Applied Mathematics, 11, 431

Martí-Vidal I., et al., Methods for non-linear least squares problems, 2010, A&A, 515, A53

Martí-Vidal I., Marcaide J., Spurious source generation in mapping from noisy phase-self-calibrated data, 2008, A&A, 480, 289

McKendrick A. G., Applications of mathematics to medical problems, 1925, Proceedings of the Edinburgh Mathematical Society, 44, 98

Meng X.-L., Dyk D. v., The EM algorithm-an old folk-song sung to a fast new tune, 1997, Journal of the Royal Statistical Society: Series B (Statistical Methodology), 59, 511

Meng X.-L., Rubin D. B., Maximum likelihood estimation via the ECM algorithm: A general framework, 1993, Biometrika, 80, 267

Moon T., The expectation-maximization algorithm, 1996, IEEE Signal Processing Magazine, 13, 47

Moran J. M., et al., Very long baseline interferometric observations of the H_2O sources in W49N, W3(OH), Orion A, and VY Canis Majoris., 1973, ApJ, 185, 535

Neal R. M., Hinton G. E., Learning in graphical models, 1999, MIT Press, Cambridge, MA, USA, pp. 355–368

Noordam J., de Bruyn A., High dynamic-range mapping of strong radio-sources, with application to 3C84, 1982, Nature, 600, 299

Offringa A. R., et al., A LOFAR RFI detection pipeline and its first results, 2010a, eprint 1007.2089 in http://ArXiv.org

—, Post-correlation radio frequency interference classification methods, 2010b, MNRAS, 405, 155

Parsons A. R., et al., The precision array for probing the epoch of re-ionization: Eight station results, 2010, AJ, 139, 1468

Pearson T. J., Readhead A. C. S., Image formation by self-calibration in radio astronomy, 1984, ARA&A, 22, 97

Pindor B., et al., Subtraction of Bright Point Sources from Synthesis Images of the Epoch of Reionization, 2010, PASA, 28, 46

Redner R. A., Walker H. F., Mixture densities, maximum likelihood and the EM algorithm, 1984, SIAM Review, 26, 195

Reid M. J., et al., The structure of interstellar hydroxyl masers - VLBI synthesis observations of W3/OH/, 1980, ApJ, 239, 89

Roche A., 2003, EM algorithm and variants: An informal tutorial. Tech. rep., CEA

Sanroma M., Estalella R., Hybrid mapping using the maximum entropy method, 1984, A&A, 133, 299

Schwab F., Robust solution for antenna gains, 1982, VLA Scientific Memorandum, 136, 1

Smirnov O. M., Revisiting the radio interferometer measurement equation. III. Addressing direction-dependent effects in 21 cm WSRT observations of 3C 147, 2011, A&A, 527, 12

Thompson A. R., Moran J. M., Swenson Jr. G. W., 2001, Interferometry and synthesis in radio astronomy. John Wiley & Sons

van der Tol S., Jeffs B., van der Veen A., Self-calibration for the LOFAR radio astronomical array, 2007, Signal Processing, IEEE Transactions on, 55, 4497

van der Veen A. J., Leshem A., Boonstra A. J., Array signal processing for radio astronomy, 2004, Experimental Astronomy, 17, 231

van Haarlem M. P., et al., LOFAR: The LOw-Frequency ARray, 2013, A&A, 556, A2

Walker R. C., et al., VLBI aperture synthesis observations of H2O masers associated with molecular clouds, 1978, ApJ, 226, 95

Wan R., Yan X., Su X., A weighted fuzzy clustering algorithm for data stream, 2008, in Proceedings of the 2008 ISECS International Colloquium on Computing, Communication, Control, and Management - Volume 01, CCCM '08, IEEE Computer Society, Washington, DC, USA, pp. 360–364

Wax M., Kailath T., Detection of signals by information theoretic criteria, 1985, IEEE Transactions on Acoustics, Speech and Signal Processing, 33, 387

Whiting M. T., Duchamp: A 3D source finder for spectral-line data, 2012, MNRAS, 421, 3242

Wijnholds S., Fish-eye observing with phased array radio telescopes, 2010, PhD thesis, Delft University of Technology, Delft, The Netherlands

Wijnholds S., van der Veen A.-J., Multisource self-calibration for sensor arrays, 2009, IEEE Transactions on Signal Processing, 57, 3512

Willott C. J., et al., The radio luminosity function from the low-frequency 3CRR, 6CE and 7CRS complete samples, 2001, MNRAS, 322, 536

Xu L., Jordan M. I., On convergence properties of the EM algorithm for Gaussian mixtures, 1995, Neural Computation, 8, 129

Xu R., Wunsch D., 2008, Clustering. John Wiley and Sons

Yatawatta S., On the interpolation of calibration solutions obtained in radio interferometry, 2013, MNRAS, 428, 828

Yatawatta S., et al., Radio interferometric calibration using the SAGE algorithm, 2009, IEEE 13th Digital Signal Processing Workshop and 5th IEEE Signal Processing Education Workshop, IEEE, Piscataway, NJ, USA, 150

—, Initial deep LOFAR observations of epoch of reionization windows. I. The north celestial pole, 2013, A&A, 550, A136

Yatawatta S., Kazemi S., Zaroubi S., Robust radio interferometric calibration using the t-distribution, 2012, in IEEE International Symposium on Signal Processing and Information Technology, Ho Chi Minh City, Vietnam.

Nederlandse samenvatting

Optische telescopen hebben detectoren die gevoelig zijn voor individuele fotonen die het detectoroppervlak raken. Hiermee kan de helderheid van een lichtbron aan de hemel gemeten worden. Optische telescopen zijn gevoelig voor fotonen met een golflengte tussen de 400 nanometer (paars) en 700 nanometer (rood), maar ook op andere golflengtes zijn fascinerende dingen aan de hemel zichtbaar. Om ook straling op andere golflengtes waar te nemen, waaronder rontgenstraling, gammastraling, ultraviolet, infrarood en radiogolven, gebruiken astronomen verschillende andere typen telescopen.

Van al deze typen straling beslaat het radiogebied het grootste golflengtebereik, van ongeveer 1 millimeter tot honderden meters (zie figuur 7.1). Radiogolflengtes worden waargenomen met radiotelescopen, waarmee astronomische kennis kan worden vergaard die ontoegankelijk is op elk ander golflengtegebied. Een voorbeeld hiervan is de vorming van de eerste objecten in het vroege universum en hun invloed op het intergalactisch medium, iets wat zelfs met de meest geavanceerde optische telescopen niet kan worden waargenomen. Zodoende spelen radiotelescopen een cruciale rol in fundamenteel astronomisch onderzoek en hebben bijgedragen aan de ontdekking van quasars, pulsars, zwarte gate en vele andere astronomische objecten.

De eerst radio antenne ontvanger werd in 1933 geconstrueerd door de Amerikaanse elektrotechnisch ingenieur Karl Jansky, met als doel het opsporen van bronnen voor telefooninterferentie. Hij ontdekte een radiosignaal met onbekende bron dat zichzelf dagelijks herhaalde, waarmee hij uiteindelijk het centrum van de Melkweg kon traceren. Voortbouwend op zijn werk werden vele schotelvormige radiotelescopen ontworpen, de eerste daarvan was een schotel van 9 meter in 1935 gemaakt door Grote Reber, een andere Amerikaanse elektrotechnisch ingenieur.

Toenemende eisen aan de resolutie maakte schotelvormige antennes onpraktisch, waarmee de weg werd vrijgemaakt voor radio-interferometrische telescopen met meerdere ontvangers. Elk van deze ontvangers was nog steeds een schotelvormige radiotelescoop, maar door een array van zulke telescopen te linken ontstaat een virtuele telescoop die veel groter is dan elk van de aparte schotels. Het gebruik van een array van antennes heeft als extra voordeel dat door slim combineren van de signalen van de aparte antennes de hoeveelheid ruis drastisch kan worden gereduceerd.

De eerste radio-interferometer werd in 1946 geconstrueerd door Marin Ryle en had slechts twee stuurbare dipoolantennes wiens onderlinge afstand kon variĂ≪ren tussen de 17 en 240 meter. Sindsdien zijn er vele radio-interferometers gebouwd. Prominente voorbeelden zijn de Very Long Baseline Array (VLBA, zie figuur 7.2), een van 's werelds grootste radio-interferometers met 25 meter grote schotelvormige ontvangers in voornamelijk Noord Amerika en de LOw Frequency ARray (LOFAR, zie figuur 7.3), een array van ongeveer 1000 kilometer met bijna 20000 dipool antenne-ontvangers verspreid over voornamelijk Nederland.

De door radio-interferometers gemaakte observaties bestaan uit een combinatie van radiosig-

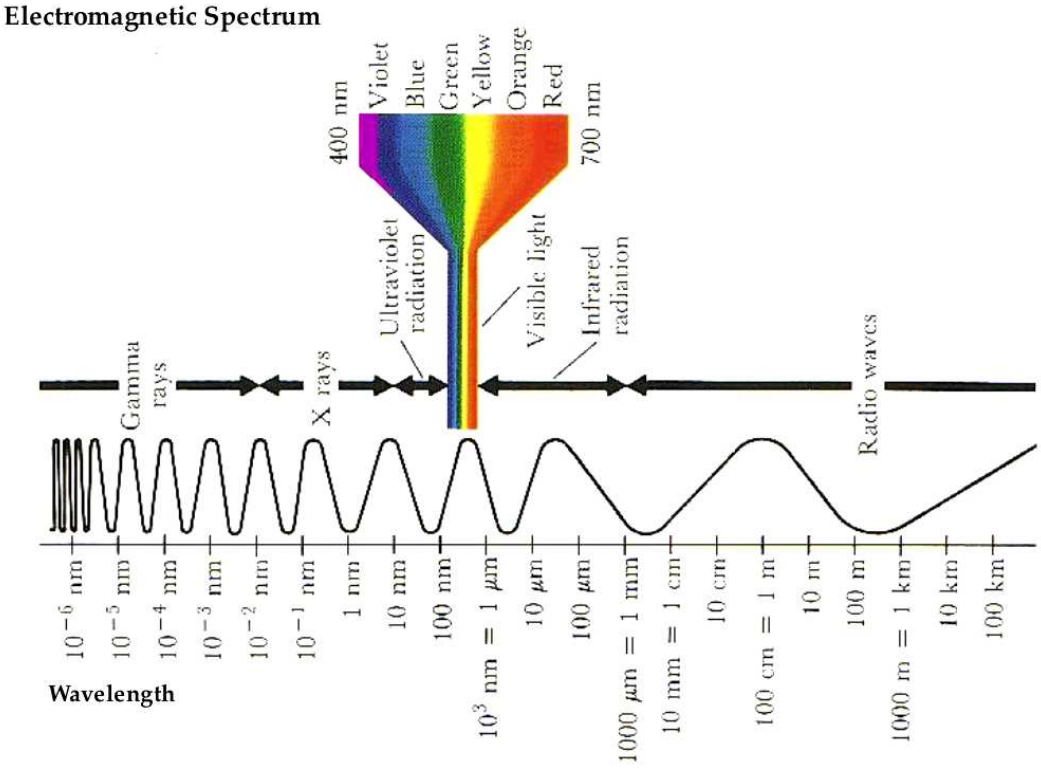

Figuur 7.1: Het elektromagnetisch spectrum: de “kleur” van het licht met de bijbehorende golflengte (http://www.lib.utexas.edu/chem/info/spectrum.html).

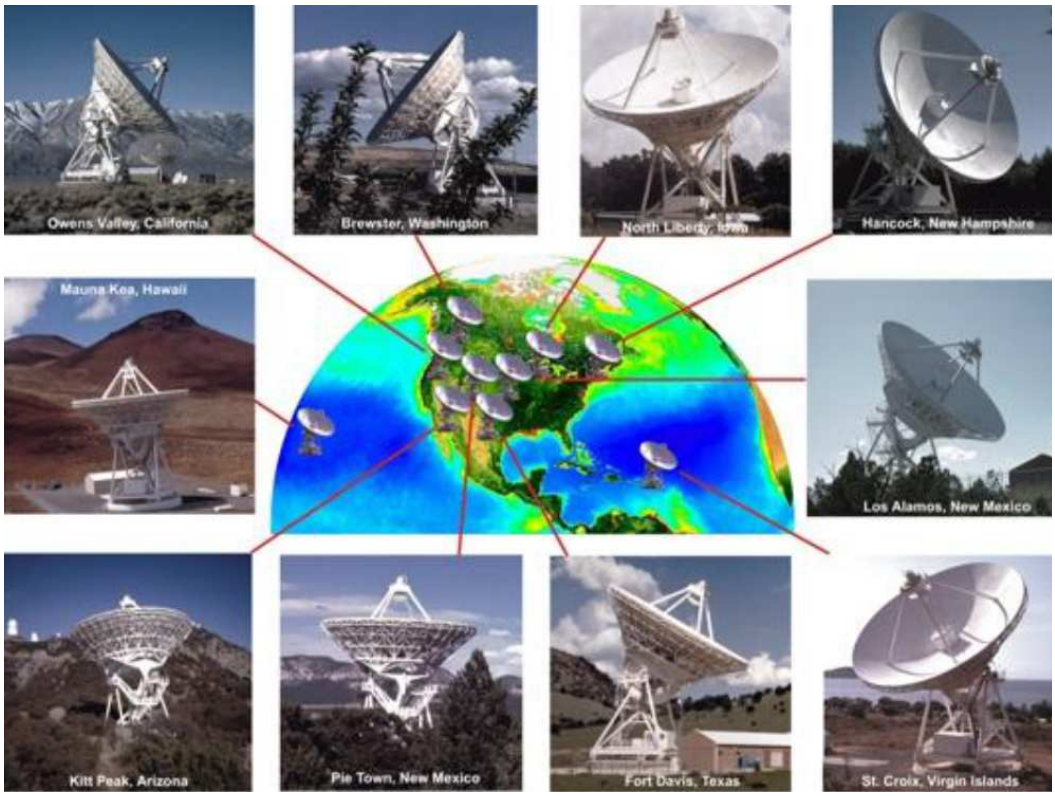

Figuur 7.2: VLBA, een van 's werelds grootste radio-interferometers met 25 meter grote schotelvormige antennes die tezamen een array van 8611 meter vormen. De antennes staan met name in Noord Amerika (http://www.vlba.nrao.edu).

Figuur 7.3: LOFAR gebruikt bijna 20000 dipool antenne-ontvangers. De ontvangers vormen een array van 1000 kilometer en staan grotendeels in Nederland (http://www.lofar.org).

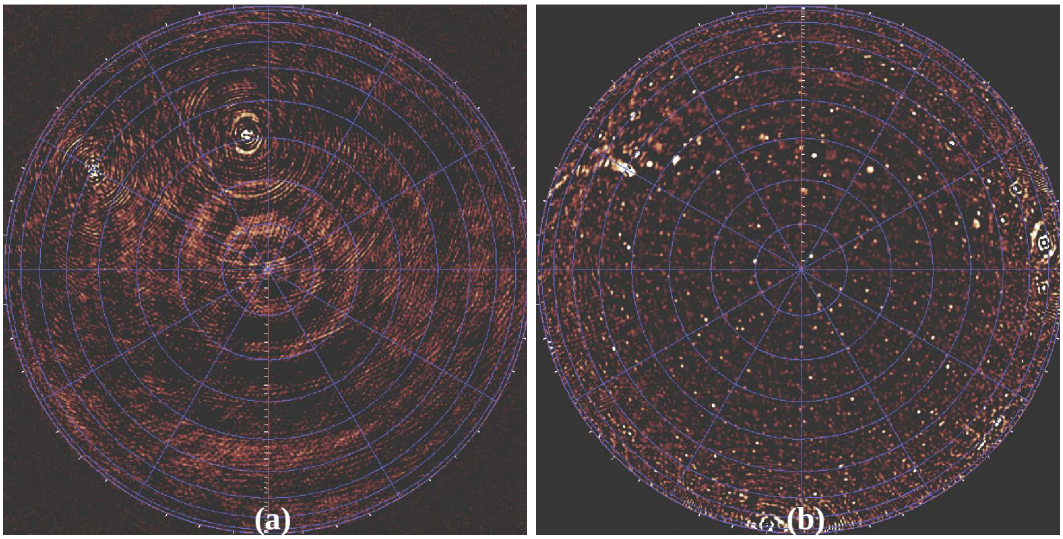

Figuur 7.4: Een beeld van de volledige hemel gemaakt met LOFAR voor (a) en na (b) kalibratie. Kalibratie heeft gezorgd voor een significante verbetering van beeldkwaliteit. Het ongekalibreerde beeld (a) bevat een grote hoeveelheid verstoringen en de radiobronnen zijn wazig. In het gekalibreerde beeld (b) zijn de verstoringen veel zwakker en de radiobronnen scherper. Bovendien zijn er nieuwe radiobronnen zichtbaar die geheel niet te zien waren in het ongekalibreerde beeld (a).

nalen van astronomische bronnen verstoord door de atmosfeer en ruis van de telescoop zelf. Telescopen detecteren ook ongewenste signalen, voornamelijk kunstmatige bronnen zoals signalen van televisie, luchtverkeersleiding en mobiele telefoons. Deze ongewenste signalen worden samen Radio Frequentie Interferentie (RFI) genoemd.

Het schatten en verwijderen van verstoringen en ongewenste signalen wordt “kalibratie” genoemd (zie figuur 7.4). In andere woorden, kalibratie is de procedure waarmee radioastronomen ruis en ongewenste bronnen uit de data verwijderen en zo alleen de signalen van astronomische bronnen overhouden. Kalibratie is de meest belangrijke stap om de gewenste nauwkeurigheid voor een radio-interferometer te behalen, in het bijzonder voor de nieuwste generatie van radiosynthese arrays. Omdat deze nieuwste generatie radio-interferometers een enorme hoeveelheid zeer precieze data waarnemen, is het uitermate belangrijk nieuwe kalibratietechnieken te ontwikkelen die de kwaliteit van de data waarborgen. Het ontwerpen van zulke kalibratietechnieken is het voornaamste onderwerp van deze dissertatie.

In deze dissertatie worden nieuwe statistische kalibratiealgoritmes ontwikkeld en hun eigenschappen onderzocht om de hoogst mogelijke computationele snelheid de beste kwaliteit waarnemingen te krijgen. Het resultaat zijn algoritmes die ordegroottes sneller zijn dan voorheen. De vooruitgang van deze algoritmes ten opzichte van bestaande algoritmes wordt geillustreerd aan de hand van zowel gesimuleerde als waargenomen data.

Ondanks de significante vooruitgang die deze nieuwe algoritmes qua beeldkwaliteit bieden, wordt nog steeds onderzoek gedaan naar verder geoptimaliseerde kalibratie-algoritmes die eenvoudiger te implementeren zijn en sneller convergeren. Signaalverwerking, het onderdeel van de wiskunde waaronder het ontwerpen van dit soort algoritmes valt, kan ook in de toekomst nog veel bijdragen aan de kalibratie van radio-interferometers.

Appendix A: The EM and the SAGE algorithms

A.1 EM algorithm

Considering the complete data $\mathbf{x} = [\mathbf{x}_1^T\ \mathbf{x}_2^T \dots \mathbf{x}_K^T]^T$, where $\mathbf{x}_i$s are defined as (2.8), its PDF will be equal to

$$f_X(\mathbf{x};\boldsymbol{\theta}) = \frac{1}{\pi^{(KM)}|\boldsymbol{\Sigma}|}\exp\{-(\mathbf{x}-\mathbf{s}(\boldsymbol{\theta}))^H\boldsymbol{\Sigma}^{-1}(\mathbf{x}-\mathbf{s}(\boldsymbol{\theta}))\}. \tag{1}$$

In (1) we have

$$\mathbf{s}(\boldsymbol{\theta}) = [\mathbf{s}_1(\boldsymbol{\theta}_1)^T\ \mathbf{s}_2(\boldsymbol{\theta}_2)^T \dots \mathbf{s}_K(\boldsymbol{\theta}_K)^T]^T, \tag{2}$$

and

$$\boldsymbol{\Sigma} = \begin{bmatrix} \beta_1\boldsymbol{\Pi} & O & \dots & O \\ O & \beta_2\boldsymbol{\Pi} & \dots & O \\ \vdots & \vdots & \ddots & \vdots \\ O & O & \dots & \beta_K\boldsymbol{\Pi} \end{bmatrix}. \tag{3}$$

Therefore, the log-likelihood of the complete data $\mathbf{x}$ is derived from

$$\log f_X(\mathbf{x};\boldsymbol{\theta}) = c - \{(\mathbf{x}-\mathbf{s}(\boldsymbol{\theta}))^H\boldsymbol{\Sigma}^{-1}(\mathbf{x}-\mathbf{s}(\boldsymbol{\theta}))\}, \tag{4}$$

where

$$c = -\log\{\pi^{(KM)}|\boldsymbol{\Sigma}|\}.$$

Substituting (2) and (3) in (4), we can rewrite (4) as

$$\begin{aligned} &\log f_X(\mathbf{x};\boldsymbol{\theta}) = c \\ &-\textstyle\sum_{i=1}^{K}\{(\mathbf{x}_i-\mathbf{s}_i(\boldsymbol{\theta}_i))^H(\beta_i\boldsymbol{\Pi})^{-1}(\mathbf{x_i}-\mathbf{s_i}(\boldsymbol{\theta}_i))\}. \end{aligned} \tag{5}$$

Moreover, the complete data $\mathbf{x}$ and the observed data $\mathbf{y}$ are related by the below linear transformation

$$\mathbf{y} = [\mathbf{I}\,\mathbf{I}\dots\mathbf{I}]\mathbf{x} = \mathbf{G}\mathbf{x}, \tag{6}$$

where $\mathbf{G}$ is a block matrix consisting of the identity matrix $\mathbf{I}$ for K times. Thus, they are jointly Gaussian and for a parameter value $\boldsymbol{\theta}'$ we have

$$\widehat{\mathbf{x}} = \mathrm{E}\{\mathbf{x}|\mathbf{y};\boldsymbol{\theta}'\} = \mathbf{s}(\boldsymbol{\theta}') + \Sigma\mathbf{G}^H[\mathbf{G}\Sigma\mathbf{G}^H]^{-1}[\mathbf{y}-\mathbf{G}\mathbf{s}(\boldsymbol{\theta}')]. \tag{7}$$

(7) gives us

$$\widehat{\mathbf{x}}_i = \mathbf{s}_i(\boldsymbol{\theta}_i') + \beta_i[\mathbf{y} - \sum_{l=1}^{K} \mathbf{s}_l(\boldsymbol{\theta}_l')]. \tag{8}$$

as the i-th element of the vector $\widehat{\mathbf{x}}$.

In applying the EM algorithm, at $k+1$-th iteration we would like to find the parameter vector $\boldsymbol{\theta}^{k+1}$ such that maximizes $\mathrm{E}\{\log f_X(\mathbf{x};\boldsymbol{\theta})|Y=\mathbf{y};\boldsymbol{\theta}^k\}$, where $\boldsymbol{\theta}^k$ is the estimation of $\boldsymbol{\theta}$ obtained at k-th iteration. According to (5) it is exactly equivalent to find $\boldsymbol{\theta}_i^{k+1}$ for each $i \in \{1,2,\ldots,K\}$ such that minimizes $\mathrm{E}\{(\mathbf{x}_i - \mathbf{s}_i(\boldsymbol{\theta}_i))^H(\beta_i\mathbf{\Pi})^{-1}(\mathbf{x_i} - \mathbf{s_i}(\boldsymbol{\theta}_i))|Y=\mathbf{y};\boldsymbol{\theta}^k\}$. Therefore, at the $k+1$-th iteration of the algorithm we have

E Step: Calculate

$$\widehat{\mathbf{x}}_i^k = \mathbf{s}_i(\boldsymbol{\theta}_i^k) + \beta_i[\mathbf{y} - \sum_{l=1}^{K} \mathbf{s}_l(\boldsymbol{\theta}_l^k)]. \tag{9}$$

M Step: Compute

$$\boldsymbol{\theta}_i^{k+1} = \arg\min_{\boldsymbol{\theta}_i} ||[\widehat{\mathbf{x}}_i^k - \mathbf{s}_i(\boldsymbol{\theta}_i)]^H(\beta_i\mathbf{\Pi})^{-\frac{1}{2}}||^2, \tag{10}$$

for $i \in \{1,2,\ldots,K\}$.

A.2 SAGE algorithm

Since in the SAGE algorithm the complete data $\mathbf{x}_{W_i}$ is defined as (2.21), we have

$$\begin{aligned} &\log f_{X_{W_i}}(\mathbf{x}_{W_i};\boldsymbol{\theta}_{W_i}) = -\log\{\pi^M|\mathbf{\Pi}|\} \\ &-\{(\mathbf{x}_{W_i} - \textstyle\sum_{l\in W_i}\mathbf{s}_l(\boldsymbol{\theta}_{W_i}))^H\mathbf{\Pi}^{-1}(\mathbf{x}_{W_i} - \textstyle\sum_{l\in W_i}\mathbf{s}_l(\boldsymbol{\theta}_{W_i}))\}. \end{aligned} \tag{11}$$

At $k+1$-th iteration of the algorithm we should calculate the parameter vector $\boldsymbol{\theta}_{W_i}^{k+1}$ which is maximizing $\mathrm{E}\{\log f_{X_{W_i}}(\mathbf{x}_{W_i};\boldsymbol{\theta}_{W_i})|Y=\mathbf{y};\boldsymbol{\theta}^k\}$. Having (11), $\boldsymbol{\theta}_{W_i}^{k+1}$ can be derived by minimizing $\mathrm{E}\{(\mathbf{x}_{W_i} - \sum_{l\in W_i}\mathbf{s}_l(\boldsymbol{\theta}_{W_i}))^H\mathbf{\Pi}^{-1}(\mathbf{x}_{W_i} - \sum_{l\in W_i}\mathbf{s}_l(\boldsymbol{\theta}_{W_i}))|Y=\mathbf{y};\boldsymbol{\theta}^k\}$ with respect to $\boldsymbol{\theta}_{W_i}$. Therefore, the SAGE algorithm's steps at the $k+1$-th iteration would be written as

SAGE E Step: Calculate

$$\widehat{\mathbf{x}}_{W_i}^k = \mathrm{E}\{\mathbf{x}_{W_i}|\mathbf{y},\boldsymbol{\theta}^k\} = \mathbf{y} - \sum_{\substack{j=1\\ j\neq i}}^{m}\sum_{l\in W_j}\mathbf{s}_l(\boldsymbol{\theta}_{W_j}^k), \tag{12}$$

which is derived from (2.23).

SAGE M Step: Compute

$$\boldsymbol{\theta}_{W_i}^{k+1} = \arg\min_{\boldsymbol{\theta}_{W_i}} ||[\widehat{\mathbf{x}}_{W_i}^k - \sum_{l\in W_i}\mathbf{s}_l(\boldsymbol{\theta}_{W_i})]^H(\mathbf{\Pi})^{-\frac{1}{2}}||^2, \tag{13}$$

for $i \in \{1,2,\ldots,K\}$.

Acknowledgements

I would like to sincerely acknowledge my advisors, Saleem Zaroubi and Ger de Bruyn, for their guidance and support. Their advice, and assistance during my doctoral research have been invaluable and working under their supervision was an honor. I would also like to express my deepest gratitude to Sarod Yatawatta. I feel so lucky that I had the chance to work with him and I appreciate all his contributions of time and ideas to this thesis. Furthermore, I would like to gratefully thank Wim Brouw, Alle-Jan van der Veen, and Amir Leshem in my committee for their valuable and insightful comments.

I extend my gratitude to all my colleagues in Kapteyn Astronomical Institute, specially to LOFAR-EoR group members, and to Edwin Valentijn. I would also like to acknowledge Johan Hamaker from who I have learned a lot.

My sincere thanks also goes to Gergo Popping, Katinka Gereb, and Parisa Noorishad for their friendship. I am deeply indebted to Keimpe Nevenzeel and Sandra de Jong for all the wonderful time that we had together. And I would like to sincerely thank Wim Zwitser for all his kindness.

I owe my very special thanks to Niyaz Bashiri Behmiri and Mehmet Aygun, for their encouragement, and support. They have always been there for me, and they meant more to me than I could ever express in words.

Finally, I would like to sincerely thank my beloved parents, Ezat Nasrollahzadeh and Iraj Kazemi, for their motivation, love, and patience. They always were my inspiration and my driving force, and I owe them everything.

This work was supported by NWO grant 436040.